Effect of Cooling Rate on Aluminium-Containing High-Entropy Alloys

Ahmed Nassar

Submitted in accordance with the requirements for the degree of Doctor of Philosophy

The University of Leeds

School of Chemical and Process Engineering

MAY, 2022

The candidate confirms that the work submitted is his/her own, except where work which has formed part of jointly-authored publications has been included. The contribution of the candidate and the other authors to this work has been explicitly indicated below. The candidate confirms that appropriate credit has been given within the thesis where reference has been made to the work of others.

The following is a list of article publications and conference presentations that have been made based on material contained in Chapters 2 and 3 of this work. The citations for these publications are as follows:

Published papers:

- A.E. Nassar, A.M. Mullis, Rapid screening of high-entropy alloys using neural networks and constituent elements, Comput. Mater. Sci. 199 (2021) 110755.
- A. Nassar, A. Mullis, R. Cochrane, Z. Aslam, S. Micklethwaite, L. Cao, Rapid solidification of AlCoCrFeNi2.1 High-entropy Alloy, J. Alloys Compd. 900 (2022).

Published conference proceedings:

- Cao, Lei Gang, Peng Yu Hou, Ahmed Nassar, and Andrew M. Mullis. "Dendritic Growth of Rapid-Solidified Eutectic High-Entropy Alloy." In *Materials Science Forum*, vol. 1035, pp. 46-50. Trans Tech Publications Ltd, 2021.

Acknowledgements

I would like to express my gratitude to Professor Andrew M. Mullis and Dr. Robert F. Cochrane, whose guidance, support and patience were unwavering throughout the course of this project. Their encouragement and trust granted me the confidence to pursue the questions that most piqued my interest, which in turn allowed me to enjoy this journey as a researcher. I am also thankful to the staff without whom neither my journey nor that of most researchers at the University of Leeds would be possible. I would like to thank Diane Cochrane, Robert Simpson, Stuart Micklethwaite, John Harrington, Dr. Zabeada Aslam, Mohammed Javed, Dr. Faye Esat, Dr. Timothy Bigg and the rest who contribute to the operation of our laboratories.

I would also like to thank my parents, whose support I simply could never repay.

Thank you,

Ahmed Nassar

Abstract

In this work, a HEA system is devised based on the outcome of neural network models. The most successful neural network in this work achieves a testing accuracy of 92%. This neural network operates solely on the compositional data of alloys, as opposed to the orthodox approach of using Hume-Rothery (HR) data. Considering that an alloy's composition is always known for certain (unlike HR features that are dependent on estimates), this approach is expected to enable the average researcher to rapidly screen potential HEA compositions. The outcome of the neural network model led to the study of the $Al_xCrCuFeNi$ system, whereby $x = 1.4$ was predicted to be the limit of the alloy's solid-solution window. The $x = 1.0$, $x = 1.3$, $x = 1.5$ and $x = 2.0$ compositions were manufactured using an arc-melter to confirm the prediction, whereby noticeable microstructural complexities are observed in the $x = 1.5$ system that are not observed in the $x = 1.0$ and $x = 1.3$ systems. 'Chinese Script' and 'Sunflower' structures are observed in the $x = 1.5$ system, whereas the $x = 2.0$ system displayed a microstructure dominated by intermetallics and very brittle mechanical behaviour.

The $x = 1.0$ and $x = 1.3$ alloys showed Al-Ni intermetallic needles in their interdendritic regions which adhere closely to dendrite peripheries. The $x = 1.0$ alloy was processed for rapid solidification using a 6.5 m long drop-tube facility. This is in order to explore the possibility of suppressing intermetallic growth and achieving a single-phase simple solid solution. The sizes of the retrieved powders ranged from > 850 μm to 38 μm, with a corresponding range of cooling rates from 112 K/s to 1.13×10^6 K/s. With higher cooling rates, simpler microstructures are obtained and at the highest cooling rate of around 1.13×10^6 K/s, a microstructure free of intermetallics is observed in powders of the 38 – 53 μm size fraction.

The effect of rapid cooling is also studied in the eutectic HEA (EHEA) that is $AlCoCrFeNi_{2.1}$. In equilibrium conditions, $AlCoCrFeNi_{2.1}$ is dual-phase $L1_2$/B2. By processing $AlCoCrFeNi_{2.1}$ using the drop-tube facility, rapidly-solidified powders were achieved with sizes from 850 μm $\leq d <$ 1000–38 μm $\leq d <$ 53 μm with corresponding estimated cooling rates of 114 K/s to 1.75×10^6 K/s respectively. Average interlamellar

spacing was found to decrease from 2.10 μm in the as-cast alloy to 348 nm in the powders of the $38\ \mu m < d < 53\ \mu m$ size fraction. Although decreased interlamellar spacing is expected to enhance microhardness, such a relation was surprisingly not as strong as expected, as microhardness of the powders was found to vary only slightly from an average value of 340 $Hv_{0.03}$. This unexpected result is explained via the observation of disorder trapping and increased FCC volume fraction. With increasing cooling rate, the microstructure of $AlCoCrFeNi_{2.1}$ was found to evolve gradually from regular eutectic to colony eutectic, followed by dendritic with eutectic the interdendritic regions. In some instances at the highest cooling rate, dendritic structures may be observed with no eutectic observed in the interdendritic region. In particles of size $d < 212\ \mu m$ BCC dendrites were observed, either dominating the structure or coexisting with FCC dendrites.

Table of Contents

Acknowledgements ..... **ii**
Abstract ..... **iii**
Table of Contents ..... **v**
List of Tables ..... **vii**
List of Figures ..... **viii**
Abbreviations ..... **xiv**
Introduction **1**
1. Literature review **4**
1.1 High Entropy Alloys (HEAs) 4
1.1.1 The emergence of HEAs 4
1.1.2 HEA core effects 8
1.2 HEA design 11
1.2.1 Formation criteria 11
1.2.2 Design towards desired structures 14
1.3 HEA properties 16
1.3.1 Yield strength 16
1.3.2 Hardness 18
1.3.3 Other properties 21
1.4 Spinodal decomposition 26
1.4.1 Fundamentals 26
1.4.2 Spinodal Decomposition in High Entropy Alloys 31
1.5 Rapid solidification 37
1.5.1 Fundamentals 37
1.5.2 Rapid solidification of High Entropy Alloys 40
1.6 Machine-learning techniques in HEA discovery 48
2. Equipment and methodology **51**
2.1 Arc-Melter 51
2.2 Drop-Tube 53
2.3 Sample Characterisation 56
2.3.1 Optical Microscopy 56
2.3.2 Scanning Electron Microscopy and Energy Dispersive X-Ray Spectroscopy 57
2.3.3 X-Ray Diffraction 59
2.4 Vickers Microhardness 60

2.5 Transmission Electron Microscopy 61
2.6 Machine learning 63
2.6.1 Data compilation and curation 63
2.6.2 Neural networks 64
3. Experimental results 67
3.1 HEA screening using Machine Learning methods 67
3.1.1 Gradient descent with multi-variate linear regression 67
3.1.2 Neural networks 71
3.1.3 Validation 75
3.1.4 Discussion 84
3.2 Rapid solidification of AlCrCuFeNi 87
3.2.1 Microstructure development 87
3.2.2 Microhardness 109
3.2.3 Discussion 113
3.3 Rapid solidification of $AlCoCrFeNi_{2.1}$ 117
3.3.1 Microstructure development 117
3.3.2 Microhardness 139
3.3.3 Discussion 140
4. Conclusions 145
Future work 149
References 151
Appendix 172

List of Tables

Table 1.1 Eutectic compositions of Ta binary with each of Cr, Co, Fe and Ni [64]....15

Table 1.2 Microstructures and hardness of AlCoCrCuFeNi with variations in composition [38]……...……..17

Table 2.1 Masses of elements in intermediate alloys to reach equimolar AlCuCrFeNi……...……53

Table 2.2 Thermophysical properties of N_2 and $AlCoCrFeNi_{2.1}$ HEA…..…….....55

Table 3.1 Elemental analysis of as-cast AlCrCuFeNi master alloy……90

List of Figures

Figure 1.1 Number of publications including the term 'HEA' from 2004 to 2019....5
Figure 1.2 Diffusion coefficients of Co, Cr, Fe, Mn and Ni in different alloys at varying temperatures, highlighting slower diffusion in the CoCrFeMnNi HEA [44]. 9
Figure 3 Schematic of the lattice distortion effect in AlCoCuNiFe HEA [11]. 10
Figure 1.4 Correlation between VEC and the BCC FCC phase stability for HEAs [20]. 13
Figure 1.5 Yield strength versus density of HEAs – serves as a visual representation of average strength in BCC HEAs being higher than FCC HEAs [66].....18
Figure 1.6 Phase diagram of AlxFeCoCrNi showing system's crystal structure tending towards ordered BCC with increased Al content [79]. 19
Figure 1.7 XRD patterns of AlxFeCoCrNi HEA for x=0.3 and x=1.8. The symbols α, α', and β represent disordered BCC, ordered BCC (B2) and FCC phases respectively [80]. 20
Figure 1.8 Comparison of toughness and strength combination in HEAs with other metallic alloys, ceramics and glasses [82].....21
Figure 1.9a Wear resistance versus hardness in the AlxCo1.5CrFeNi1.5Tiy alloy with Al00Ti05, Al02Ti05, Al00Ti10 and Al02Ti10 being Co1.5CrFeNi1.5Ti0.5, Al0.2Co1.5CrFeNi1.5Ti0.5, Co1.5CrFeNi1.5Ti and Al0.2Co1.5CrFeNi1.5Ti respectively Figure 1.9b Wear resitance versus hardness in CuCoNiCrAl0.5FeBx alloy with Boron molar fraction increased from zero to one [84].....22
Figure 1.10 Hardness of HEAs (irradiated and unirradiated) at 300 nm indentation depth. Vanadium is used as a control sample [88]. 24
Figure 1.11 Showing $L1_2$ ordering in $Al_{0.3}$CoCrFeNi post irradiation [32]. 25
Figure 1.12a Schematic Phase diagram outlining composition X_0 which lies within the chemical spinodal and where SD is expected to occur Figure 1.12b Gibbs free energy at quenched temperature, showing spontaneous reduction in free energy with small composition fluctuation [111]. 30
Figure 1.13a Composition profile as an alloy is quenched from T_1 to T_2 at composition X_0 Figure 1.13b as alloy is quenched outside the spinodal region (refer to Figure 1.12) [111]. 31
Figure 1.14 a Compositional fluctuations of Al and Cr in dendritic region of AlCoCrFeNi and Figure 1.14 b in ID region [105].....33
Figure 1.15 High magnification micrograph of sunflower-like microstructure found in Al_2CrCuFeNi_2 as a result of SD [106]. 34
Figure 1.17 Wavelength and amplitude evolution of SD features in FeCoCuMnNi as a function of annealing time [98]. 36
Figure 1.16 Backscatter electron image of HfZrTi$Ta_{0.53}$ with TEM bright field image from selected region and corresponding SAD pattern [96].....36
Figure 1.18 Secondary arm spacing versus solidification time for Al-4.5 wt% Cu alloy [111].....38

Figure 1.19 Interdiffusion between α and β phases as the eutectic front grows with a velocity V [111] 40
Figure 1.20 Gas-atomised powders of CrFeNiMn HEA [122]. 41
Figure 1.21 Cooling rate as a function of droplet diameter in $Al_{0.6}$CoCrFeNi [123]. 42
Figure 1.22 Stress-strain curve of undercooled CoCrFeNi [126]. 43
Figure 1.23 Increasing microhardness in CoCrFeNi as undercooling is gradually increased [127]. 44
Figure 1.24 In situ observation of nucleation in undercooled CoCrFeNi HEA [128]……..……..46
Figure 1.25 Delay time between nucleation of FCC and metastable BCC at different undercooling scenarios [128]…….….46
Figure 1.26 Hardness as a function of undercooling in three HEAs [118]……47
Figure 1.27 EDS maps of CoFeNiCu at various values of undercooling, showing improved homogeneity as undercooling is increased [135]……..48
Figure 1.28 Schematic of NN architecture showing five input features, three hidden layers, and three outputs classifying the alloys as SS, IM or SS + IM [143]…….50
Figure 2.1 Copper-hearth showing different mould shapes…….52
Figure 2.2 Schematic of Drop-Tube apparatus used in this work [152]……56
Figure 2.3 X-Ray diffraction in crystal structure [153]……...60
Figure 2.4 5-row print of the data set used in NN2. 'Z' denotes the difference in atomic radii and 'Ed' the difference in Pauling electronegativity. The SS/IM column indicates the HEA's phase, with 1 indicating (SS) or (SS+IM) and 0 indicating a (AM), (IM) or (AM+IM). Only 7 of the 37 elements present in the database are shown. A small arbitrary value (-0.05) was chosen to indicate the absence of an element……....64
Figure 2.5a Rectified Linear Unit Figure 2.5b Sigmoid activation functions……....66
Figure 3.1a Cost vs Epochs for LRGD model with random initiation point Figure 3.1b iteration starting point obtained using the matrix method from Equation 23...70
Figure 3.2a Schematics of NN1 and Figure 3.2b NN2 architectures. Number of hidden layers and number of units per layer shown are not representative of the true models but help in visualising the networks. The output layer in both architectures is shown as a Sigmoid activation function with binary output……....72

Figure 3.3 Training loss and accuracy for NN1. Between each set of plots, the data is shuffled and 70% of the data is taken for training……..…….73
Figure 3.4 Training loss and accuracy for NN2. Between each set of plots, the data is shuffled and 70% of the data is taken for training……...74
Figure 3.5 XRD scans of x = 1.0, x = 1.3, x = 1.5 and x = 2.0 alloys in the $Al_xCuCrFeNi$ system……...…...76
Figure 3.6a Micrograph of $Al_{1.0}CrCuFeNi$ showing dendritic structure Figure 3.6b Appearance of needle-like IM only observable at higher magnifications……..77
Figure 3.7a Micrograph of $Al_{1.3}CrCuFeNi$ showing dendritic structure Figure 3.7b higher magnification micrograph of $Al_{1.3}CrCuFeNi$, showing increased presence of IM phase relative to the x = 1.0 composition……..……..78
Figure 3.8 Micrograph of $Al_{1.5}CrCuFeNi$ showing increased presence of IM in the ID matrix……..80
Figure 3.9a Micrograph of $Al_{1.5}CrCuFeNi$ showing "Chinese script" IM structure in the ID matrix at low magnification Figure 3.9b Higher magnification of the Chinese Script structure in $Al_{1.5}CrCuFeNi$……...81
Figure 3.10a "Sunflower" structure in $Al_{1.5}CrCuFeNi$ showing matrix dominated by intermetallics Figure 3.10b Higher magnification focusing on lamellar region…....82
Figure 3.11a Micro-cracks in microstructure of $Al_{2.0}CrCuFeNi$ outlining the brittle nature of the alloy Figure 3.11b Overall microstructure of $Al_{2.0}CrCuFeNi$ showing coarse sphere-like and needle intermetallics in its matrix……..……....83
Figure 3.12 Estimated cooling rates of AlCrCuFeNi powders versus mean powder diameter……...……...87
Figure 3.13 XRD patterns of AlCrCuFeNi as-cast alloy and powders……....89
Figure 3.14 Backscatter SEM image of as-cast equimolar AlCrCuFeNi microstructure……..…….90
Figure 3.15 Microstructure of AlCrCuFeNi powder cooled at an estimated 112 K/s (d > 850 μm)…….91
Figure 3.16 High magnification backscatter images of AlCrCuFeNi powder from d > 850 μm size-fraction…….92
Figure 3.17 Microstructure of AlCrCuFeNi powder cooled at an estimated 432 K/s (500 – 850 μm)……..94

Figure 3.18 AlCrCuFeNi powder from 300 – 500 μm size-fraction (1716 K/s)……95
Figure 3.19a AlCrCuFeNi powder from 212 – 300 μm size-fraction (4599 K/s) Figure 3.19b AlCrCuFeNi powder from 150 – 212 μm size-fraction (1.28×10^4 K/s).....96
Figure 3.20 Low-magnification back-scattered SEM migrograph of AlCrCuFeNi powder from 106 – 150 μm size-fraction (3.74×10^4 K/s)……97
Figure 3.21 Higher magnification backscatter micrographs of AlCrCuFeNi powder from 106 – 150 μm size-fraction (3.74×10^4 K/s)……99
Figure 3.22 AlCrCuFeNi powder from 75 – 106 μm size-fraction (1.13×10^5 K/s)…….……...100
Figure 3.23 AlCrCuFeNi powder from 53 – 75 μm size-fraction (3.60×10^5 K/s)……....101
Figure 3.24 AlCrCuFeNi powder from 38 – 53 μm size-fraction (1.13×10^6 K/s)……....102
Figure 3.25a ID region from the as-cast alloy, including IM phases. Figure 2.35b [-2 2 0] SAED pattern from ID phase showing FCC structure. Figure 3.25c [0 -2 3] SAED pattern from 'needle-like' phase showing B2 ordering, where the red circles highlight the superlattice spots……104
Figure 3.26a SAD pattern from ID region [011] zone axis, Figure 3.26b SAD pattern from IM [011] zone axis Figure 3.26c HAADF image Figure 3.26d-h elemental distribution from ID and IM regions in d > 850 μm sample……105
Figure 3.27a Dendritic region from droplet of the d < 850 µm size-fraction Figure 3.27b [0 0 -1] SAD pattern of precipitates within the dendrite Figure 3.27c [-2 2 0] SAD pattern of precipitate-free region within the dendrite……106
Figure 3.28 HAADF image and elemental distribution of dendritic region in AlCrCuFeNi powder of d > 850 μm size fraction……107
Figure 3.29 HAADF image and elemental distribution images from ID region in AlCrCuFeNi powder of d > 850 μm size fraction. …….……108
Figure 3.30 Equivalent diameter of fragmented dendrites against cooling rate…..111
Figure 3.31 Microhardness of AlCrCuFeNi powders as a function of $A^{-0.25}$ in a Hall-Petch plot…….112

Figure 3.32 Microhardness of AlCrCuFeNi powders as a function of average cooling rate……113

Figure 3.33a Microstructure of as-cast AlCoCrFeNi2.1 EHEA – Where A is the BCC phase and B is the FCC phase; Figure 3.33b Line-scan of as-cast $AlCoCrFeNi_{2.1}$ showing Al-Ni rich phase and Cr rich phase……....118

Figure 3.34a regular eutectic structure of the arc-melted AlCoCrFeNi2.1 alloy Figure 3.34b and Figure 3.34c SAED patterns of the regions labeled 1 and 2, showing ordered B2 and ordered L12 structures, respectively……119

Figure 3.35 XRD patterns for $AlCoCrFeNi_{2.1}$ powders obtained via drop-tube processing……..…120

Figure 3.36 Estimated cooling rates of $AlCoCrFeNi_{2.1}$ powders as a function of powder diameter…….121

Figure 3.37a Microstructure of particle from 850 – 1000 size fraction and Figure 3.37 b) particle from 500 – 850 size fraction……124

Figure 3.38a Appearance of cellular eutectic in the 150 – 212 sieve fraction and Figure 3.38b A more dominant cellular structure of particle in 106 – 150 sieve fraction…….125

Figure 3.39 Primary FCC nucleation in particle from 106 – 150 sieve fraction…126

Figure 3.40 $AlCoCrFeNi_{2.1}$ morphology as powder size decreases, showing increasing volume fraction of FCC phase. Powders from a) to e) are taken from powder size fractions 150 – 212 µm, 106 – 150 µm, 75 – 106 µm, 53 – 75 µm and 38 – 53 µm, respectively……..129

Figure 3.41 Increasing dendritic volume fraction with increasing cooling rate..…130

Figure 3.42 Particle from 38 – 53 µm size fraction with eutectic microstructure retained in the interdendritic region……..131

Figure 3.43 Particle from 75 – 106 µm size fraction with clear nucleation point leading to dendritic region. Colony and regular eutectic regions are also visible…132

Figure 3.44 Interlamellar spacing versus cooling rate for $AlCoCrFeNi_{2.1}$ powders…….133

Figure 3.45 a) Lamellar region from 500 - 850µm size particle, with corresponding SAED patterns showing ordered B2 and disordered FCC structures in regions labelled 1 and 2, respectively. Figure 3.45 b) Irregular lamellae from 38 – 53 µm

size particle, with corresponding SAED patterns showing disordered BCC and disordered FCC structures in regions labelled as 3 and 4, respectively……136
Figure 3.46 a) BCC dendrites observed within particles of 75 – 106 µm size fraction
Figure 3.46 b) BCC dendrites extending beyond localized region and occupying full microstructure…….136
Figure 3.47 Al and Ni rich (BCC) dendrites of parasite-like phase observed within the 106 µm < d < 150 µm and 150 µm < d < 212 µm powder-size fractions……..137
Figure 3.48 Al and Ni depleted (FCC) dendrite observed within a particle from the smallest powder-size fraction (38 µm < d < 53µm)…….....138
Figure 3.49 Microhardness of $AlCoCrFeNi_{2.1}$ powders as a function of lamellar spacing in a Hall-Petch plot……139
Figure 3.50 Backscattered SEM image of annealed particle from 150 - 212 µm size-fraction…….…….140

Abbreviations

HEA – High Entropy Alloy

MPEA – Multi-Principal Element Alloy

EHEA – Eutectic High Entropy Alloy

RHEA – Refractory High Entropy Alloy

HR – Hume-Rothery

IM – Intermetallic

SEM – Scanning Electron Microscopy

XRD – X-Ray Diffraction

EDX – Energy Dispersive X-Ray

BSE – Backscattered Electron

SE – Secondary Electron

CFE – Cold-Field Emission

FIB – Focused Ion Beam

OM – Optical Microscopy

TEM – Transmission Electron Microscopy

DTA – Differential Thermal Analysis

DSC – Differential Scanning Calorimetry

SS – Solid Solution

VEC – Valence Electron Concentration

FCC – Disordered Face-Centred Cubic structure

BCC – Disordered Body-Centred Cubic structure

A2 – Disordered Body-Centred Cubic structure

$L1_2$ – Ordered FCC structure

B2 – Ordered BCC structure

HCP – Hexagonal Close-Packed structure

ML – Machine Learning

NN – Neural Network

GD – Gradient Descent

LRGD – Linear Regression with Gradient Descent

AM – Additive Manufacturing

SD – Spinodal Decomposition

RSP – Rapid Solidification Processing

TRL – Technology Readiness Level

CET – Columnar-to-Equiaxed Transition

SLM – Selective Laser Melting

VLM – Vacuum Levitation Melting

BF – Bright-Field

APB – Anti-Phase Boundary

DPA – Displacement Per Atom

Introduction

The search for lighter and stronger materials that perform in extreme environments has played a crucial role in the development of many of today's modern industries (aerospace, automotive, energy generation and so forth). Naturally, such a pursuit is dependent on the development and discovery of new metals. The development of superalloys marked the beginning of a new metallic era and a big leap towards materials more suited for gas turbines, reactor cores etc. Around a century since their discovery, knowledge of superalloys is now well-established, and their composition spaces have been largely explored. As such, further significant discoveries depend on academic attention being shifted from conventional and superalloys towards new alloy types.

High Entropy Alloys (HEAs) are a new family of alloys - discovered circa 2002 - which are bound to play a key role in the future of alloy development [1]. Typically containing a minimum of five elements in near-equiatomic composition [2], HEAs provide a large uncharted space for alloy discovery. Multi-principal element alloys (MPEAs) in general have been overlooked in past years due to the general belief that their microstructures are overly complex (containing many intermetallic phases). Contrary to this opinion, the first reported HEA ($Co_{20}Cr_{20}Fe_{20}Mn_{20}Ni_{20}$) showed a single-phase FCC structure [3]. Since then, single-phase FCC [4], BCC [5,6] and HCP [7] HEAs have been discovered and have proven to have exceptional properties [8].

As the high entropy of mixing in HEAs (brought about by their equiatomic compositions) leads to reduced Gibbs free energy, it is a main factor leading to their simple solid-solution microstructures [9]. In fact, for an alloy to be classified as an HEA, it is widely agreed that its entropy of mixing must be no less than $1.5R$, where R is the gas constant. High entropy forms part of the four *core effects* which are characteristic to HEAs; these are: high-entropy, sluggish diffusion, lattice distortion, and the cocktail effect [10,11]. These four effects appear consistently in HEAs and have proven useful in understanding the nature and behaviour of HEAs. These core effects and their significance will be discussed in Chapter 1.

Although single-phase HEAs received the initial spotlight, HEAs do not have to be single-phase to be deemed worthy of attention. In recent years, significant effort has been dedicated to the development of duplex and eutectic HEAs [12]. The aim of this is to design alloys which contain a balance of desired properties from any two phases [13]. The first eutectic HEA (EHEA) was reported in 2014 [14], proving that tapping the potential of HEAs lies not only within a trial-and-error approach to obtain single-phase alloys, but also in a more design-oriented approach. Nevertheless, HEAs are still in their early days and the systematic discovery of new HEAs using already-promising combinations of elements is still very much relevant.

To date, thermodynamic databases are far from accurately predicting HEA phases. Mainly, this is due to the large composition space HEAs offer and the fact that generally up to today, the central areas of phase diagrams have been largely ignored. With no knowledge of central areas of multi-principal element alloys, there is no foundation to build on to predict the central areas of HEAs. With relation to industry, one of the challenges HEAs face is their poor castability (due to the chemical inhomogeneity and composition segregation), complicating the production of large ingots [15]. Assessing the properties of HEAs and the effects of thermo-mechanical operations on them is crucial in their integration into industrial applications. Generally, HEA properties have shown to be promising with refractory HEAs proving to have exceptional performance at high temperatures [16], eutectic HEAs showing unmatched strength-to-ductility ratios [17] and aluminium-containing HEAs showing unique combinations of low-density and high hardness/strength [18].

The work within focuses on Aluminium-containing HEAs. Investigating such HEAs is important due to their particularly low densities, giving them the potential for aerospace and automobile applications. Aluminium added to all or four of Cu, Cr, Fe, Ni and Co has been the most studied system to date. As aforementioned, within these six elements there exists a plethora of combinations to be studied. However, with this system as with other HEAs in general, there exists a lack of investigations on the effect of rapid solidification on HEA microstructure evolution and HEA properties. Using a drop-tube facility, this work produced HEA powders with cooling rates ranging from orders of 10^2 to 10^6 Ks^{-1}.

Chapter 1 presents a literature review on the core effects which have become characteristic to HEAs, the range of HEA microstructures to-date, a summary of the mechanical properties of HEAs (with a particular focus on Aluminium-containing HEAs), rapid-solidification processing of HEAs and machine-learning methods for HEA design. Chapter 2 covers the methodology and equipment used in this work. Chapter 3 presents the results obtained throughout this research, covering the machine-learning component of this project in its first section, followed by the rapid-solidification processing of the AlCrCuFeNi and $AlCoCrFeNi_{2.1}$ alloys in its second and third sections, respectively. Finally, Chapter 4 presents the main conclusions which were drawn from this work.

1. Literature review

The aim of this chapter is to situate this project in relation to existing HEA knowledge. The emergence of HEAs and the four *core effects* of HEAs are briefly explained to aid the reader in developing a broad intuition for the topic. This is followed by a summary of HEA formation criteria and methods of achieving HEAs with desired properties. Spinodal decomposition cases in HEAs are then outlined, highlighting the point that HEA microstructures need not be simple solid solutions without exception. Rapid solidification studies of HEAs are then summarised and criticised where need be. Finally, a review of HEA discovery is presented, highlighting the stark shift in recent years from the use of bounded criteria to the use of machine learning (ML) methods.

1.1 High Entropy Alloys (HEAs)

1.1.1 The emergence of HEAs

Up to the early 2000s, multi-principal element alloys (MPEAs) were viewed with little-to-no chance of having microstructures comprising simple solid-solutions. Agreement among the scientific metallurgical community was mainly that the microstructures of such alloys would comprise complex and brittle phases, rendering the entirety of MPEAs to be unworthy of attention. This belief was disrupted by the discovery of the Cantor Alloy (CoCrFeMnNi) around 2002, which was found to be single-phase FCC [19]. The Cantor alloy led to great academic attention being diverted towards MPEA exploration and the investigation of MPEA properties. Soon after, the characteristic high entropy of mixing in these MPEAs was noted and the term High Entropy Alloys was coined. Due to the large number of elements, the liquid or random solid solution states of MPEAs have higher configurational possibilities. Namely, the effect of entropy is much more significant in MPEAs than in conventional alloys. As such, this led to the explanation that it is the high configurational entropy of MPEAs which reduces the Gibb's free energy of their simple solid solutions, thus allowing their formation [9,20]. This intuition is aided

by Equation 1.1, where it can be seen that a larger entropy, *S*, leads to a reduction in the Gibbs' free energy (*G*) of the system.

$$G = H - TS \tag{1.1}$$

Where *G* is Gibbs' free energy, *H* is the total enthalpy of the system, *T* is temperature and *S* is the system's total entropy.

Circa 2005, the superior mechanical properties of HEAs gained popularity across the metallurgical field and steadily amassed attention within the community. Vast potential applications of HEAs were being anticipated, creating a compounding effect which further accelerated HEA research. In 2006, key characteristics of HEAs were outlined by Jien-Wei Yeh [21], which initiated wider interest not only in the mechanical behaviour of HEAs but also in their intrinsic properties. The bar chart in Figure 1.1 shows how the number of HEA-related studies since 2004 has been increasing in an exponential manner [22].

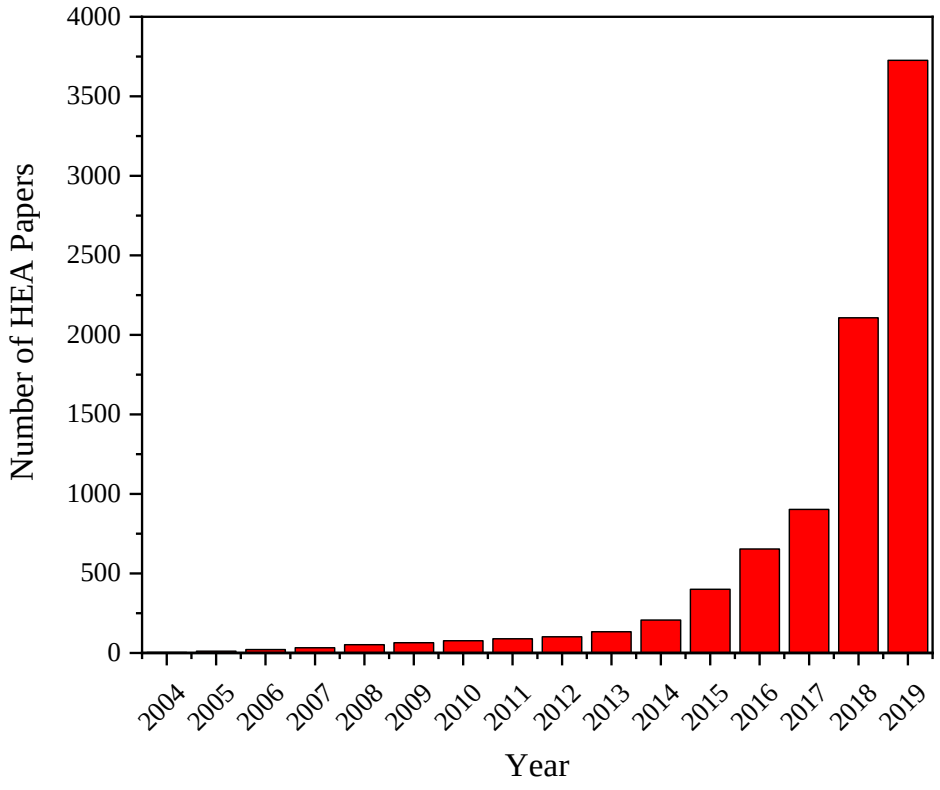

Figure 1.1 Number of publications including the term 'HEA' from 2004 to 2019 [22]

In 2007, criteria for HEA formation were outlined [2] which placed limits on the differences in enthalpies and entropies of mixing, differences in atomic radii and differences in the valence electron concentration between the HEA's constituent elements. Although these criteria were drawn from the well-established Hume-Rothery (HR) parameters [23], experimental efforts soon made it evident that more was needed to better predict HEA formation. This was further affirmed in 2013, when it was shown by Otto *et* al. [9] that HEAs with the same number of elements and similar HR properties may show single-phase structures or, by contrast, rather complex structures containing multiple phases and intermetallics. Although doubts were always present that HR-based parameters alone may not be sufficient, this 2013 study by Otto *et al*. led to significant shifts in the modus operandi of HEA discovery. Due to such studies, combined with HEAs becoming a topic of significant attention, the exploration of new and more accurate predictive parameters became a major segment of research and many predictive parameters devised during the 2013 – 2015 period are still used today in guiding HEA prediction and design.

In 2018, the first attempts were made to employ machine learning (ML) methods in discovering new HEA compositions and designing HEAs with desired properties [24]. Recent attempts with ML methods have been promising and varied in nature, with some works focusing on designing HEAs with targeted properties such as Young's modulus [25] and hardness [26], or predicting solid-solution windows [27] and eutectic compositions of multi-component systems [28]. ML methods are expected to play a crucial role in the future of HEA development, especially as our databases of HEA compositions and properties grow and become more sophisticated.

Until today however, most HEA systems which have been investigated stem from already promising systems – the AlCoCrFeMnNi is one of the most relevant examples. The opportunities within discovering entirely new systems is naturally limited by the fact that many elements present challenges relating to scarcity, toxicity and difficulty in processing. However, although such challenges are unlikely to change with time, better deployment of already discovered systems is still a task that holds many promising prospects. As progress is made in small-scale HEA production and HEA discovery, bridging the gap between scientific investigations and industrial practise is a major

obstacle at the forefront of HEAs. As of today, investigations on the macro-scale production of HEAs are rather limited and most HEAs are not yet suitable for large-scale casting, as they can show significant inhomogeneity and poor liquidity [17]. This is a problem which eutectic HEAs (EHEAs) seem to show promise in overcoming due to their duplex structures and potential balance between ductility and hardness. Some efforts have shown that industrial-scale EHEA ingots can be prepared without facing the issues around poor castability and inhomogeneity [17,29], although objectively, the challenge of scaling HEA usability continues to overshadow the progress in the field.

Almost two decades since Yeh [1] defined HEAs to comprise single phase solid solutions, various MPEAs have been fabricated to date which are multi-phase [30] or even comprise intermetallics [31]. As the field has progressed, the original definition of HEAs has become less at the centre of discussions and in turn, this has made way for more constructive research which revolves around HEA properties, fabrication, and applications. So far, HEAs have been proposed in several applications ranging from nuclear [32] and biomaterials [33] to civil structures [34] and aerospace parts [35].

Moving forward, methods of HEA manufacturing are expected to be just as important as HEA discovery, especially as this will be key to their successful integration in industrial practices. In recent years, a wider variety of methods have been investigated, ranging from more novel techniques such as Selective Laser Melting (SLM) [36] to more traditional methods such as melt spinning and casting. This demonstrates that there remains a need for substantial scientific efforts to continue unravelling new HEA compositions and applications, but more importantly, to allow their macro-scale production to be realised.

1.1.2 HEA core effects

Some characteristics of HEAs are uncommon in other alloys and are referred to in literature as the ‘core effects’ of HEAs. These effects, of which there are four, describe HEA behaviours and metallurgical properties.

The first and arguably most relevant core effect is known as the high entropy effect. Mainly, the high entropy effect states that the high configurational entropy resulting from the equimolar composition of 5 (or more) elements mainly leads to Solid Solution (SS) phases rather than intermetallic (IM) phases [37]. This is contrary to the previous rationale that alloys comprising several principal elements lead to overly complex microstructures that are likely to comprise brittle phases. Many HEAs do have more than one phase, and some also have intermetallic (IM) phases [38]. However, these IM phases generally include many elements and their degree of ordering is greatly reduced. To understand the significance of entropy on the formation of solid-solution phases (rather than the competing intermetallic and elemental phases), reference must be made to Equation 1.1.

The second law of thermodynamics states that the within several possible states in a system, the state of lowest Gibbs free energy will be the equilibrium state. Therefore, it can be seen from Equation 1.1 that a high entropy of mixing can overshadow the effect of the enthalpy of mixing (which when largely positive leads to segregations and when largely negative leads to formation of IM phases). Entropy of mixing is hence a main contributor in the formation of solid solution phases. However, a growing number of studies has shown that the assumption that a high entropy of mixing is the only criteria for forming solid-solution HEAs is inaccurate [39].

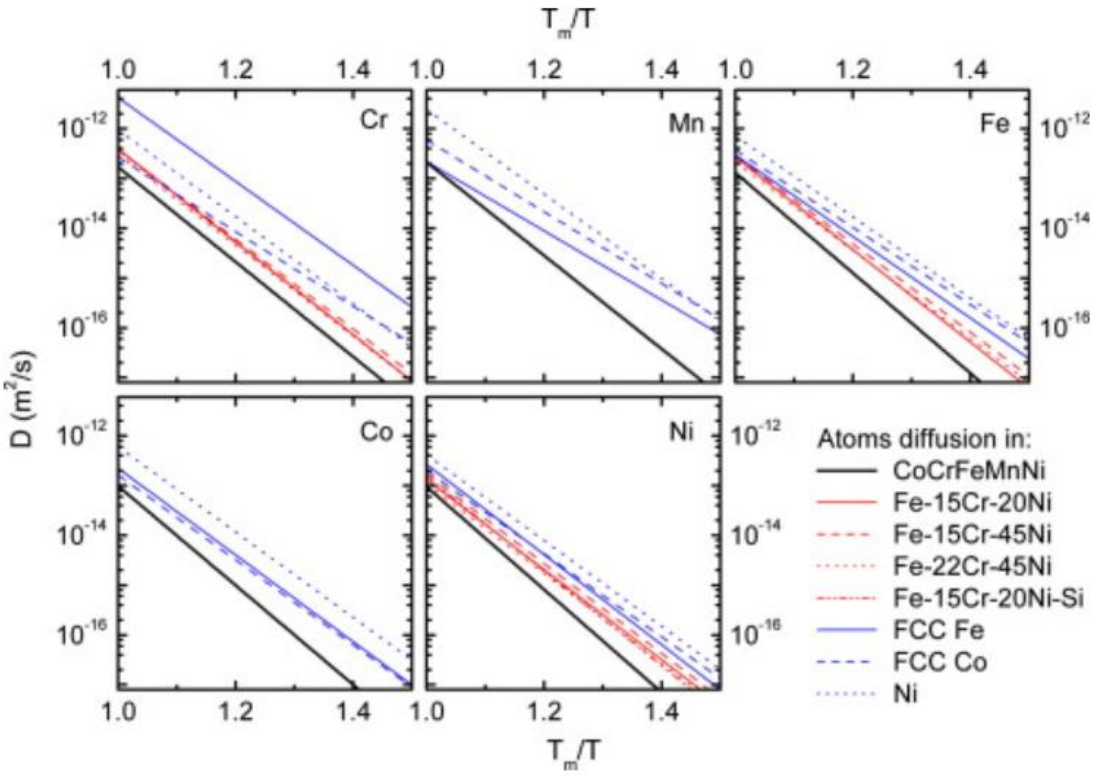

Figure 1.2 Diffusion coefficients of Co, Cr, Fe, Mn and Ni in different alloys at varying temperatures, highlighting slower diffusion in the CoCrFeMnNi HEA [44].

The second core effect is known as the sluggish diffusion effect. This term is used to describe the slow atomic movement in HEAs relative to conventional and superalloys [40,41]. Although this intrinsic feature of HEAs is partly responsible for their unique properties (mainly stability and strength at high temperatures) [42], it is difficult to model and has never been probed directly [43]. Due to the fact that no single element dominates the solid-solution in a HEA, each lattice site is naturally surrounded by different bonds, causing significant variations in potential energy around the lattice [44,45]. There appears to be consensus that fluctuations in lattice potential energy increase the probability that activation energies across the lattice exceed migration enthalpies (which must be overcome for diffusion to occur), thus resulting in a "trapping effect" which slows down diffusion [45]. Figure 1.2 takes the CoCrFeMnNi HEA as an example to highlight the effect of sluggish diffusion, where the diffusion coefficients of several elements are probed and shown to be smaller in CoCrFeMnNi when compared to other alloys.

The third core characteristic of HEAs is known as the lattice distortion effect. The nature of the multi-component solid solution in HEAs leads to every atom being surrounded by different types of atoms [46]. As such, these notable size differences between neighbouring atoms leads to strains in the lattice which lead to a distortion effect. A schematic of this effect is presented in Figure 1.3. These distortions in HEAs are much larger than in conventional alloys that are based on one major element [44,47], meaning that the atoms in HEAs deviate from their ideal locations in a more significant manner [48]. This lattice distortion reduces the effect of thermal strain on HEAs [49] as essentially, the lattice distortion induced by the increased kinetic energy of the system due to a temperature rise is considered small relative to the magnitude of the already existing distortion. The lattice distortion effect in HEAs is also partly responsible for their exceptional hardness and strength [50].

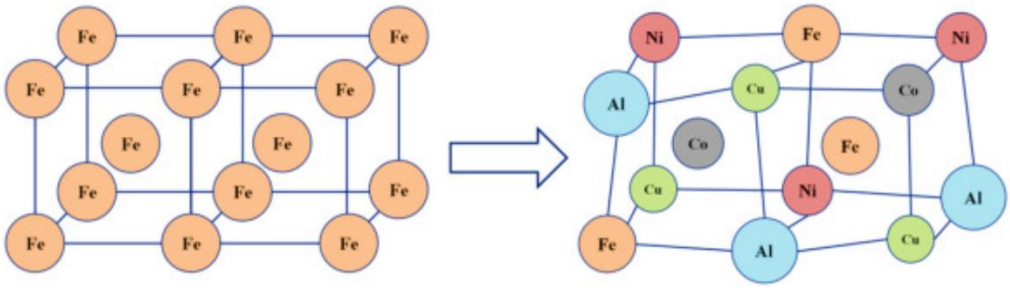

Figure 1.3 Schematic of the lattice distortion effect in AlCoCuNiFe HEA [11].

The fourth and final core characteristic of HEAs is the cocktail effect. The cocktail effect is a mere reminder of the fact that unexpected properties arise from a multi-principal element system. Namely, the cocktail effect is the umbrella term to which any HEA properties that do not adhere to the 'sum of the parts reasoning' (expressed in Equation 1.2) are attributed [51].

$$\bar{a} = \sum c_i a_i \tag{1.2}$$

Where a is any given property whose average value, $\bar{a}$, is to be calculated (to obtain an estimate for the expected value of a in the HEA). c_i is the atomic fraction of element i in the HEA.

1.2 HEA design

1.2.1 Formation criteria

Defining the formation criteria of HEAs requires the consideration of several factors, most of which are based on a set of rules describing the conditions needed for solid solution (SS) formation (Hume-Rothery rules). Placing criteria on HR features involves minimising differences in electronegativities, atomic sizes and valence electron concentrations between elements in the HEA [52], whereas thermodynamic criteria for HEA formation have involved placing limits on the enthalpy of mixing ΔH_{mix} and the ideal entropy of mixing ΔS_{mix}. The most widely considered factor in HEA formation is ΔS_{mix}, where the main consensus since the birth of HEAs has been that for the formation of an HEA, ΔS_{mix} of the constituent elements must be no less than 1.5R, where R is the gas constant. The ideal entropy of mixing is calculated as per Equation 1.3 below:

$$\Delta S_{mix} = -R \sum_{i=1}^{n} x_i \ln(x_i) \tag{1.3}$$

Where R is the gas constant (8.31 $JK^{-1}mol^{-1}$), n is the number of elements in the HEA and x is the atomic fraction of element i.

From the second law of thermodynamics – refer to Equation 1.1 – it is seen that a large value of entropy reduces the Gibbs free energy of a system. This idea provides the main rationale for placing a lower limit of 1.5R on the ideal entropy of mixing and seeking its maximum. It can be seen from Equation 1.4 that maximum entropy is achieved at equimolar composition, namely at $x_i = \frac{1}{n}$. Therefore, the ideal entropy of mixing can be written as per Equation 1.5:

$$\therefore (\Delta S_{mix})_{max} = -R \left[n \cdot \frac{1}{n} \ln \left(\frac{1}{n} \right) \right] \tag{1.4}$$

$$\therefore (\Delta S_{mix})_{max} = R[\ln(n)] \tag{1.5}$$

As Equation 1.5 shows, entropy initially increases rapidly with *n* as more elements are added in equimolar proportion, but the rate of increase slows as *n* increases.

A further criterion for HEA formation is placed to limit atomic misfit between the constituent elements of the HEA. This criterion, δr, expresses the average radius difference between the constituent elements of the HEA (see Equation 1.6). Generally, for HEA formation a δr value of less than 6.5% is required, whereas for single phase HEAs, the required value is as low as 3.8% [53].

$$\delta r = \sqrt{\sum_i x_i \left(1 - \frac{r_i}{\bar{r}}\right)^2} \tag{1.6}$$

Where *x* is the atomic fraction of element *i*, r_i is the element's atomic radius, $\bar{r}$ is the weighted average radius and δr is the radius difference criterion.

Valence Electron Concentration (VEC) is another HR criterion which apart from being useful in aiding HEA formation, is also useful in predicting their crystal structure. For instance, this criterion has shown that FCC stability is enhanced at VEC values greater than 8, while BCC stability is enhanced at VEC values of less than 7 [54]. Between these two VEC values, many duplex (FCC+BCC) HEAs exist, providing a useful screening method to aid in designing EHEAs. Generally, however, VEC is to remain between 5 and 10 for HEA formation. Figure 1.4 shows a multitude of HEAs and the correlation between their VEC values and their crystal structures. Pauling electronegativity is also considered an important HR parameter for HEA formation, where its limits lay between 1.6 and 2.0 for HEA formation [55].

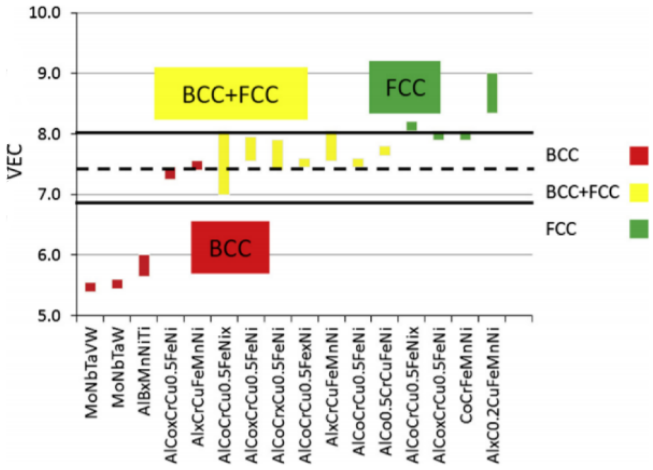

Figure 1.4 Correlation between VEC and the BCC FCC phase stability for HEAs [20].

Finally, Ω is a thermodynamic criterion (given by Equation 1.7) which is recommended to exceed 1.1 for HEA formation [56]. As seen from Equation 1.7, $T_m \Delta S_{mix}$ must be greater than $|\Delta H_{mix}|$ for this criterion to be met, meaning that the contribution of entropy to the free energy of the system should be dominant.

$$\Omega = \frac{\left(\sum_i x_i T_{m,i}\right)\Delta S_{mix}}{|\Delta H_{mix}|} \tag{1.7}$$

Where x_i is the atomic fraction of element *i* and $T_{m,i}$ is the melting point of the element.

In summary, Hume-Rothery rules state that to favour the formation of solid solutions, the constituent elements must have similar atomic diameters, electronegativities and valence electron concentrations (VECs) [57]. Other practical criteria are also worth considering for HEA formation. Similar melting points of the constituent elements is one such example, as with large variance in melting temperatures the fabrication of the HEA becomes more complicated. Finally, a common rationale used today is that elements sharing the same crystal structures are more likely to adhere to the Hume-Rothery rules. However, this is a somewhat limiting methodology as it defies a more daring approach towards HEA exploration.

1.2.2 Design towards desired structures

Notwithstanding the criteria based on HR parameters, there are further methods for designing HEAs of desired structures. A common method lies in studying the binary phase diagrams of the HEA's constituent elements. This method is applied to deduce the compositions at which a certain phase would be most likely to form. Such a method has been proven in multiple instances for unveiling EHEAS. For instance, the work of Jiang et al. applies this method to develop EHEAs [58], whereby eutectic binary alloys are used to form part of the five-component HEA while ensuring that the entropy of mixing lies within the range specified in section 1.2.1. Via this method four new EHEAs were discovered – $CoCrFeNiNb_{0.45}$, $CoCrFeNiTa_{0.40}$, $CoCrFeNiZr_{0.55}$ and $CoCrFeNiHf_{0.4}$. Seeing that Niobium can form a eutectic structure with each of Iron [59], Cobalt [60], Nickel [61] and Chromium [62], the rationale of adding Nb to the base elements (CoCrFeNi) of this EHEA family becomes clearer. As the atomic radius of Niobium is significantly larger the radii of Co, Cr, Fe and Ni, the addition of Nb intensifies the lattice distortion effect resulting in further strengthening of the base alloy [63]. As for Ta, Zr and Hf, the same rationale was used in their design, in that eutectic compositions were sought in the binaries of each of these elements with elements from the CoCrFeNi 'base'. The eutectics of all the alloys in this EHEA family comprised alternating FCC and Laves phases [58].

This strategy of looking for eutectic compositions in binary phase diagrams to develop a EHEA was also implemented to develop the $CoCrFeNiTa_{0.47}$ EHEA [64]. This method simply lists the eutectic compositions of Ta with each of the elements from the base alloy (in this case CoCrFeNi). The average of molar fraction of the eutectic compositions with Ta is calculated (see Table 1.1), to give the eutectic composition of the five-element alloy such that $(CoCrFeNi)_{89.45}Ta_{10.55}$ is the determined EHEA, empirically simplifying to $CoCrFeNiTa_{0.47}$.

This method is surely not limited to unveiling EHEAs. A similar approach of analysing binary phase diagrams was used by Zhang et al. to understand the microstructure of Cantor alloy (CoCrFeMnNi, known to be single-phase FCC) [50]. Taking the Cantor alloy as a case study and observing that only one (Ni) of its constituent elements has an FCC structure at room temperature, it seems unexpected that this HEA possesses a single-phase FCC structure. However, looking at the constituent binaries clarifies that a single-phase FCC structure is the most common among the binary phase diagrams over a large range of temperatures and compositions [50]. This method can therefore be extended to search for single-phase HEAs by comparing binaries which show large regions of a single-phase crystal structure. Finally, it can be said that the same rationale – which is arguably the essence of the cocktail effect – can be applied in designing HEAs of desired physical properties.

Table 1.1 Eutectic compositions of Ta binary with each of Cr, Co, Fe and Ni [64].

Element	Eutectic molar fraction	Element	Eutectic molar fraction
Cr	87	Ta	13
Fe	92.5	Ta	7.5
Ni	86.3	Ta	13.7
Co	92	Ta	8
Avg. molar fraction	89.45	Avg. molar fraction	10.55

1.3 HEA properties

1.3.1 Yield strength

A topic very much at the heart of HEA research is the strength versus ductility trade-off. Generally, BCC phases have higher yield strengths than FCC phases (see Figure 1.5) but are brittle, whereas FCC structures are usually more ductile but have lower yield strength and hardness [65]. Table 1.2 lists some HEAs that have been chosen to intentionally highlight the strength versus ductility trade-off in relation to their constituent phases [66]. To address the balance between strength and ductility, the ability to design HEAs with a specific structure (as mentioned in section 1.2.2) is of great importance. EHEAs in particular offer a large part of the solution, as the balance in properties of their constituent phases (taking FCC + BCC as an example) limits the between strength and ductility.

One such EHEA with alternating FCC + BCC phases is $AlCoCrFeNi_{2.1}$ which has attracted a great amount of academic attention since its discovery in 2014 [14]. The $AlCoCrFeNi_{2.1}$ alloy shows a better strength-ductility balance compared to most single phase HEAs reported to date – with a yield stress value of 620 MPa and elongation to failure of 17 % [67]. Cold rolling this alloy to 90 % and annealing at 800 °C for one hour increased this alloy's yield strength to 1100 MPa, albeit decreasing its elongation to 12 % [67]. Another EHEA showing an exceptional strength-ductility balance is $Fe_{28.2}Ni_{18.8}Mn_{32.9}Al_{14.1}Cr_6$ with a yield strength of 680 MPa and ductility of 18 %. Post cold-rolling to 60 % and annealing at 1000 °C for one hour, the alloy's yield strength decreased by 80 MPa in return for a 2 % increase in ductility [68].

Although dual-phase HEAs with a HCP structure as one of their phases are much less common than FCC+BCC HEAs [66], they have exceptional ductility and yield strength values that are also relatively high [69], [70]. $Fe_{50}Mn_{30}Co_{10}Cr_{10}$ is a dual phase ($FCC_{0.7}HCP_{0.3}$) alloy with a yield strength of 375 MPa and a ductility of 73% [70]. NbTaTiVW is another dual-phase HEA with a HCP structure as one of its phases (BCC + HCP) and has a yield strength of 1420 MPa and a ductility of 20 % [69].

It is also important to understand the effects of varying a particular element in the MPEA system. For instance, Al is a BCC stabilizer in the AlCoCrCuFeNi based system and as a general rule, increasing its molar fraction leads to an increase in the alloy's yield strength [71]. One of many examples is the increase in the yield strength of the Al_xCoCrCuFeNi alloy when *x* (molar ratio of Aluminium) is increased. This alloy has yield strength values of 400MPa, 950MPa and 1600 MPa when *x* is 0.5, 1 and 2 respectively [72]. This effect is very well documented, but the case of the Al_xCoCrFeMnNi system is used as an additional example, where an increase in *x* from 0.2 to 0.6 results in an increase in yield strength from 220MPa to 833MPa [73].

Table 1.2 Microstructures and hardness of AlCoCrCuFeNi with variations in composition [38].

Alloy	Structure	Hardness (HV)
$AlCo_{0.5}CrCuFeNi$	FCC + BCC	473
$AlCoCrCu_{0.5}FeNi$	BCC	458
$AlCoCrCuFeNi_{0.5}$	FCC + BCC	423
AlCoCrCuFeNi	FCC + BCC	420
$AlCoCrCuFe_{0.5}Ni$	FCC + BCC	418
$AlCoCr_{0.5}CuFeNi$	FCC + BCC	367
$Al_{0.5}CoCrCuFeNi$	FCC	208

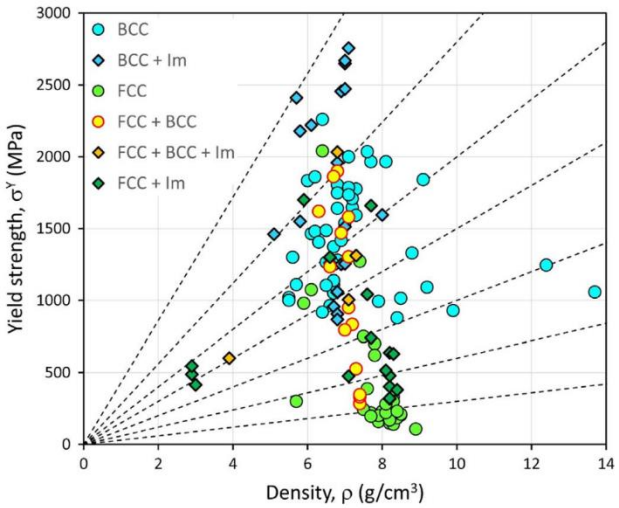

Figure 1.5 Yield strength versus density of HEAs – serves as a visual representation of average strength in BCC HEAs being higher than FCC HEAs [66].

1.3.2 Hardness

Varying the composition of a certain element in a HEA can balance volume fractions between FCC and BCC phases, offering a solution to the strength-ductility trade-off and achieving an optimal hardness value [74]. Hardness in single-phase FCC HEAs generally lies within the ranges of 100-200 HV [37], whereas in single-phase BCC alloys it is usually greater than 600 HV [75].

For example, the as-cast $Al_{0.5}FeCoCrNi$ (single-phase FCC) alloy has a Vickers hardness of 247 HV, whereas annealed samples of the same alloy had an average hardness 33 HV greater than the as-cast sample [76]. As BCC phases are harder than FCC phases, the growth of a BCC phase is expected in the annealed samples and is indeed observed [76]. Expectedly due to annealing however, a drop in the hardness (roughly back to the as-cast value) was observed in the sample annealed at 950 °C despite the continued existence of the BCC phase. This is as the expected outcome upon annealing is to reduce the density

of dislocations by recrystallization, which in turn reduces the work hardening of the metal [77].

The AlFeCoCrNi alloy was also investigated by varying the ratio of Aluminium to Nickel [78]. The alloy with high Aluminium content ($Al_{1.7}FeCoCrNi_{0.3}$) showed a BCC structure, while the high Nickel alloy ($Al_{0.3}FeCoCrNi_{1.7}$) showed an FCC structure. Expectedly, the high Aluminium alloy had a higher Vickers hardness (671 HV) than the high Nickel alloy (163 HV). Although both Aluminium and Nickel possess FCC crystal structures at room temperature, the BCC structure of the $Al_{1.7}FeCoCrNi_{0.3}$ alloy is explained by Aluminium's large atomic radius which inhibits the formation of a close-packed structure, thus resulting in a BCC lattice [78]. The tendency of Aluminium to initiate BCC growth in the AlFeCoCrNi alloy has been confirmed in many works; the thermodynamic calculations found in the work of Zhang et al. [79] (see Figure 1.6) and in the experimental work of Wang et al. [80] (see Figure 1.7) are just a few.

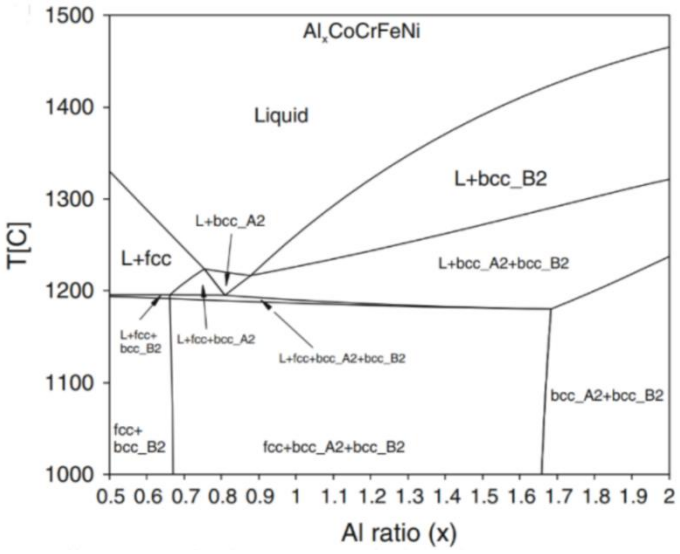

Figure 1.6 Phase diagram of AlxFeCoCrNi showing system's crystal structure tending towards ordered BCC with increased Al content [79].

Varying Chromium content in the $AlFeCoCr_xNi$ alloy has a similar effect to that of Aluminium – namely, increasing the molar fraction of Chromium from 0.2 to 1.0 has the effect of increasing the alloy's hardness from 268 HV to 526.6 HV [81]. However, unlike

the case of Aluminium, increasing the Chromium molar fraction beyond unity (i.e. equimolar composition) results in a small decline in the alloy's hardness [81]. Although no XRD analysis was done by Geanta et al. in this study to investigate the growth of a BCC phase, the increase in hardness was attributed to the formation of intermetallic compounds as Chromium content was increased.

Typically, increasing Aluminium content in HEAs of the AlCoCrCuFeNi type increases the alloy's hardness due to a transition from a single-phase FCC structure, to a BCC + FCC structure and eventually to a single-phase BCC structure [72]. For instance, as-cast equimolar AlCoCrCuFeNi hardness increased from 133 HV to 655 HV as Al molar fraction was increased from 0.0 to 3.0, with the increase being largely linear [72].

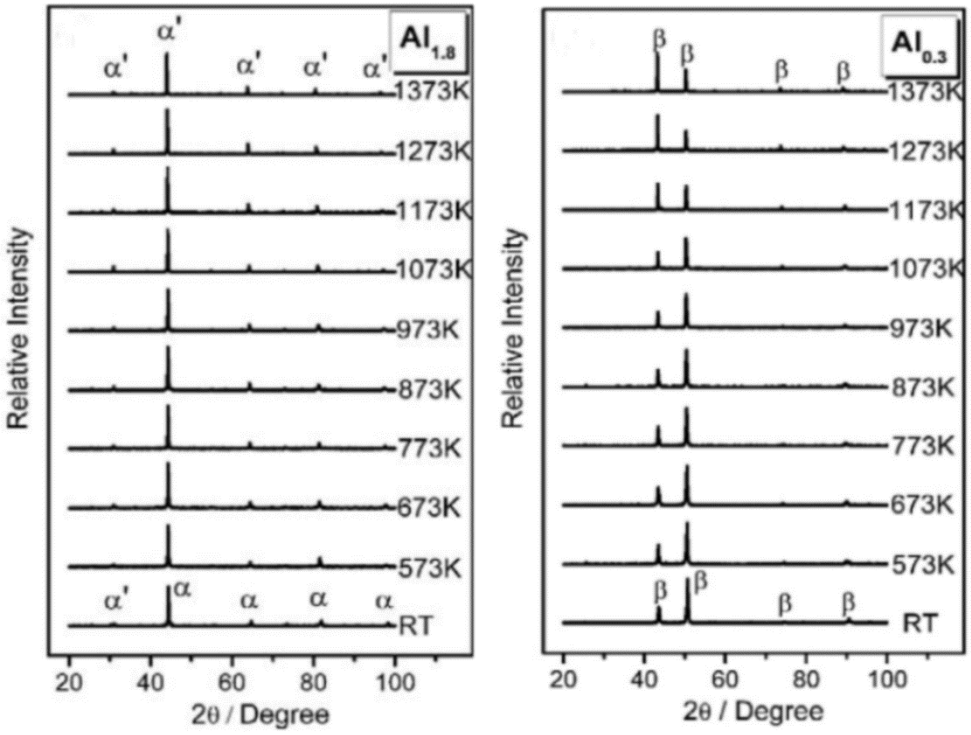

Figure 1.7 XRD patterns of AlxFeCoCrNi HEA for x=0.3 and x=1.8. The symbols α, α', and β represent disordered BCC, ordered BCC (B2) and FCC phases respectively [80].

1.3.3 Other properties

High-entropy alloys display unique properties in more than just strength, hardness and thermal stability. When considering a combination of fracture toughness with yield strength, HEAs appear to be superior to other alloys (superalloys and conventional alloys), ceramics and glasses (see Figure 1.8) [82]. A few HEAs have also been tailored towards wear resistance and perform well when compared with proven anti-wear materials such as SUJ2 (bearing steel), SKH51 (high-speed steel), SKD61 (high-chromium steel) and 316 and 17-4 steels. One such example is the $Al_xCo_{1.5}CrFeNi_{1.5}Ti_y$ alloy, where cases in which $x = 0$, $y = 1$ and $x = 0.2$, $y = 1$ had better wear resistance than the materials used as references for anti-wear (SUJ2 and SKH51) in that study (see Figure 1.9a) [83]. Although this study does not attempt more combinations to search for an optimal Ti/Al ratio, it makes clear that HEAs have the potential to perform well under high wear.

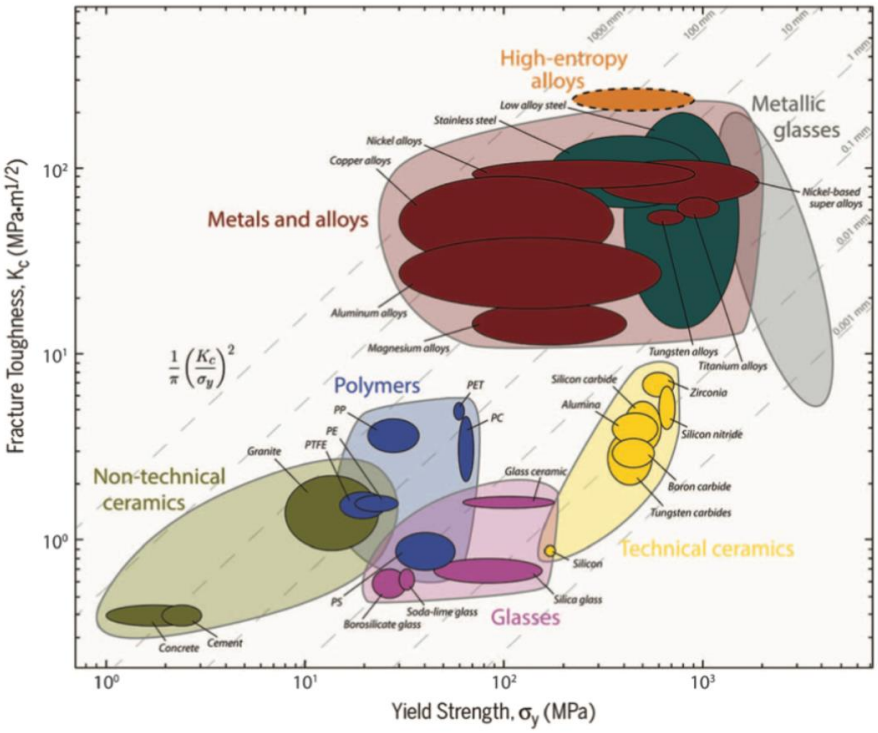

Figure 1.8 Comparison of toughness and strength combination in HEAs with other metallic alloys, ceramics and glasses [82].

Another HEA with wear-resistance characteristics that compare well to the aforementioned steels is $CuCoNiCrAl_{0.5}FeB_x$ [84]. Although this alloy does not perform as well as the $Al_{0.2}Co_{1.5}CrFeNi_{1.5}Ti$ and $Co_{1.5}CrFeNi_{1.5}Ti$ alloys, it still competes with cobalt-based superalloy Stellite and the steel with highest wear resistance (SUJ2) (see Figure 1.9b). As the Boron molar fraction is increased from 0.0 to 1.0, the wear resistance of this alloy increases almost linearly from 0.9 m/mm^3 to 1.7 m/mm^3 – outperforming SUJ2's wear resistance by 0.18 m/mm^3 [84].

A final property of HEAs worthy of reviewing is irradiation resistance. Although irradiation resistance in HEAs appears to be one of the least explored topics in the field, sluggish solute diffusion in HEAs (relative to other alloys) has made HEAs potential candidates in nuclear power systems and particularly in fission and fusion reactors. The lack of studies in this topic is likely due to the difficulty in conducting representative experiments where high temperatures and high radiation (doses of several hundreds of displacement per atom) are required. However, studies thus far have shown that relative to conventional nuclear materials, HEAs tend to show less phase changes and volume-swelling which can be induced due to irradiation [85].

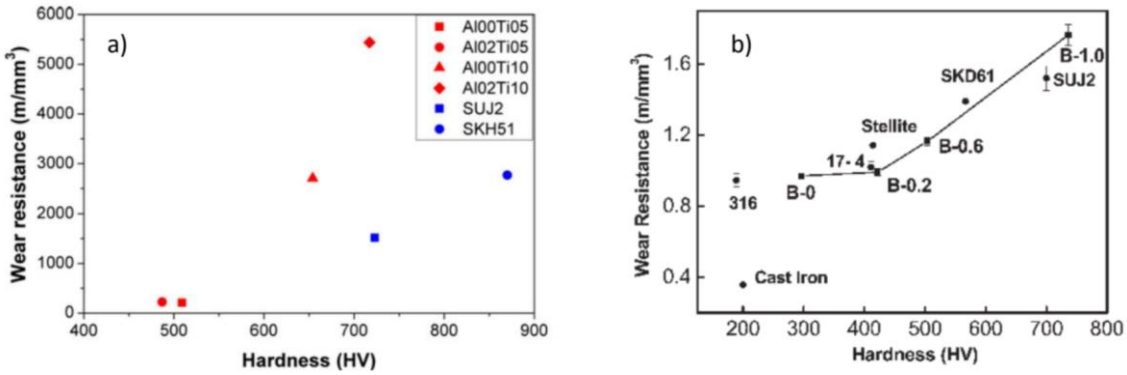

Figure 1.9a Wear resistance versus hardness in the AlxCo1.5CrFeNi1.5Tiy alloy with Al00Ti05, Al02Ti05, Al00Ti10 and Al02Ti10 being Co1.5CrFeNi1.5Ti0.5, Al0.2Co1.5CrFeNi1.5Ti0.5, Co1.5CrFeNi1.5Ti and Al0.2Co1.5CrFeNi1.5Ti respectively **Figure 1.9b** Wear resitance versus hardness in CuCoNiCrAl0.5FeBx alloy with Boron molar fraction increased from zero to one [84].

Xia et al. study the irradiation behavior of the $Al_xCoCrFeNi$ system (where x = 0.1, 0.75 and 1.5) by exposing the fabricated alloys to Au ion irradiation of 3 MeV [86]. It is observed in this study that as the BCC volume fraction increases with increasing Al content, the alloys become more sensitive towards irradiation and display larger volume swelling. A maximum volume swelling of 6.5% is observed in the x = 1.5 alloy exposed to 50 dpa. Nonetheless, a more conventional material for fission reactors such as $Fe_{15}Cr_{20}Ni$ that is exposed to a similar dpa shows volume swelling of around 30%. Considering the x = 0.1 alloy, the maximum volume swelling observed is 1.25 % at 65 dpa. Although the work of Xia et al. shows that HEAs are relatively insensitive towards irradiation, a larger range of dpa scenarios would be beneficial in forming a better understanding. As the maximum dpa reached in their study is 65 dpa and realistic operating conditions may reach several hundreds of dpa [85], the results may not be entirely conclusive about HEA deployment in the nuclear industry. However, to further affirm the suitability of HEAs in such applications, it was also shown (using TEM analysis) that the crystal structure of the alloys is unaffected by the radiation.

Further, Lu et al. show that the single phase BCC HEA $Ti_2ZrHfV_{0.5}Mo_{0.2}$ shows high stability under He ion irradiation [87], whereby its crystal structure post-irradiation is unaffected. It is further shown that the nanohardness of $Ti_2ZrHfV_{0.5}Mo_{0.2}$ is unaffected by He ion irradation, whereas it is common in conventional alloys that irradiation hardening is observed. Kareer et al. have also shown that the BCC alloys TiVNbTa, TiVZrTa and TiVCrTa are promising candidates for HEA applications and show almost no irradiation hardening (see Figure 1.10) [88]. This point of difference on BCC performance highlights the need for further irradiation studies in HEAs.

Finally, although in the larger scheme there is little doubt about the suitability of HEAs to nuclear applications, some studies have shown contrasting results. One such study is that of Chen et al. which investigated the effect of 1 MeV Kr ion irradiation on the $Al_{0.3}CoCrFeNi$ and CoCrMnFeNi HEAs. Chen et al. show that at 300 ℃, irradiation hardening experienced by the HEAs is larger than that observed in 316H steel [32]. It was also shown in this study that the crystal structure of $Al_{0.3}CoCrFeNi$ after irradiation changes from being FCC to ordered $L1_2$, whereas the CoCrMnFeNi and 316H alloys

remain stable (see SAD patterns in Figure 1.11). This result is not in accord with the aforementioned study of Xia et al., which concluded that the crystal structure of $Al_{0.1}$CoCrFeNi is stable under Au ion irradiation. Nevertheless, the irradiation tests of Xia et al. were conducted at room temperature [86], as opposed to those of Chen et al. on $Al_{0.3}$CoCrFeNi which were conducted at 300 ℃, making it difficult to make conclusive remarks by comparing both studies.

This example highlights the importance of using conditions (temperature and dpa) which are representative of those in reactor cores before nominating HEAs for use in nuclear applications. In a follow up study, Chen et al. investigate the same alloys under the same irradiation conditions but at a higher temperature of 500 ℃. This study confirmed that the formation of ordered $L1_2$ in $Al_{0.1}$CoCrFeNi is due to irradiation rather than an annealing effect, as an annealed $Al_{0.1}$CoCrFeNi sample showed no ordering [89]. Irrespective of such conflicting results, it may well be argued that nuclear applications may be where HEAs are most needed, as current commercial alloys in the industry have often failed under the extreme temperature, irradiation and corrosion conditions found in nuclear reactors [90].

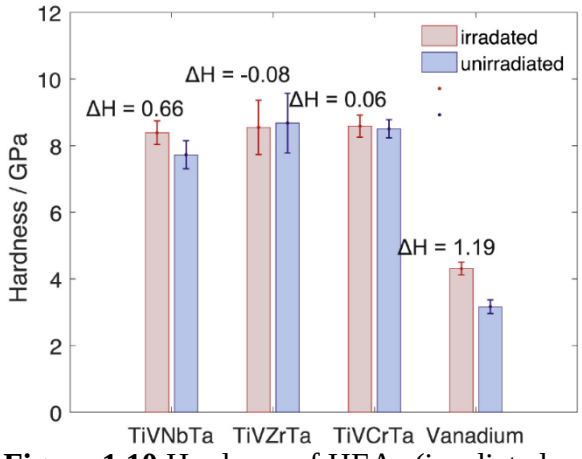

Figure 1.10 Hardness of HEAs (irradiated and unirradiated) at 300 nm indentation depth. Vanadium is used as a control sample [88].

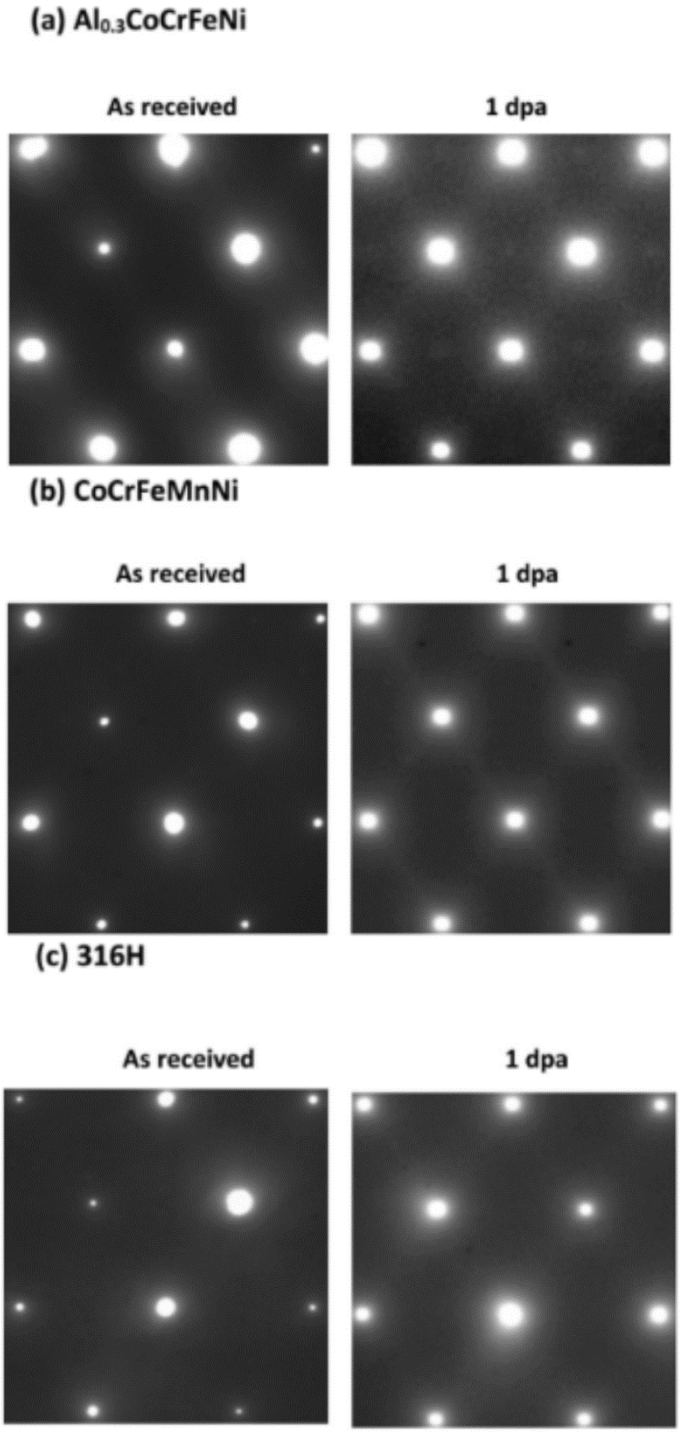

Figure 1.11 Showing $L1_2$ ordering in $Al_{0.3}$CoCrFeN*i* post irradiation [32].

1.4 Spinodal decomposition

1.4.1 Fundamentals

According to classical solidification theory, a degree of undercooling below equilibrium temperature is required for nucleation to occur. Unlike classical nucleation however, Spinodal Decomposition (SD) is a process that occurs without a nucleation barrier [91]. To understand the conditions needed for SD, reference may be made to a phase diagram with a miscibility gap such as that seen in Figure 1.12a. For an alloy of composition X_0 that is quenched from a temperature T_1 to a temperature T_2, the quenched state lies within the miscibility gap such that the homogenous α phase decomposes into α_1 and α_2 ($\alpha \rightarrow \alpha_1 + \alpha_2$).

As seen in Figure 1.12b, the composition X_0 lies within a region where there is a negative curvature in the Gibb's free energy curve for T_2. It can be seen that this is an unstable region, as small fluctuations in composition will lead to a reduction in free energy from G_0. Therefore, the free energy will reduce spontaneously through chemical decomposition, as the segregation of the two phases achieves a more stable configuration [92]. Namely, A-rich regions become further enriched in A atoms and B-rich further become further enriched in B atoms – this phenomenon is commonly referred to as 'uphill diffusion' [93]. This process of 'uphill diffusion' continues to take place until equilibrium is reached, leading to two phases of composition X_1 and X_2. The two resulting phases have the same crystal structure but different lattice parameters and compositions [94]. It can be said that the second derivative of an alloy's free energy at the quenched state, with respect to the solute's molar ratio, must be negative for SD to occur – as shown in Equation 1.8.

$$\frac{d^2G}{dx^2} < 0 \tag{1.8}$$

Where *G* is the free energy of the system and *x* is composition.

Considering a small composition fluctuation such that the free energy of the system after the fluctuation is G_0', the relation between the change in free energy and the composition fluctuation can be shown as per Equations 1.9 – 1.11:

$$G_0' = \frac{1}{2}\left[G_0 + \frac{dG}{dx}\Delta x + \frac{1}{2}\frac{d^2G}{dx^2}(\Delta x^2)\right] + \frac{1}{2}\left[G_0 - \frac{dG}{dx}\Delta x + \frac{1}{2}\frac{d^2G}{dx^2}(\Delta x^2)\right] \quad (1.9)$$

$$\therefore\ G_0' = G_0 + \frac{1}{2}\frac{d^2G}{dx^2}(\Delta x^2) \quad (1.10)$$

$$\therefore\ \Delta G = \frac{1}{2}\frac{d^2G}{dx^2}(\Delta x^2) \quad (1.11)$$

It can therefore be observed that when the condition from Equation 1.8 is met, ΔG, the change in chemical energy, will also be negative, leading to spontaneous decomposition.

However, the above calculation neglects interfacial energy and geometric misfit between the A-rich regions and B-rich regions. To calculate the condition for SD more accurately, chemical and coherent strain energy terms must be accounted for. Accounting for these additional energy terms leads to more representative models and in turn, leads to the narrowing of the composition range for SD [95]. Once these additional energy terms are accounted for, a final spinodal may be deduced (known as the coherent spinodal), resulting in a region where the homogenous α phase is unstable and SD occurs. It may therefore be said that the chemical spinodal (the spinodal deduced without accounting for additional energy terms) is of no practical importance.

The chemical energy and coherent strain terms are expressed in Equations 1.12 and 1.13, respectively.

$$\Delta G_\gamma = K\left(\frac{\Delta x}{\lambda}\right)^2 \quad (1.12)$$

Where ΔG_γ is interfacial chemical energy term, *K* is a proportionality constant and λ is the wavelength of composition modulation.

$$\Delta G_s = \eta^2 (\Delta x)^2 \frac{E}{1-\upsilon} V_m \tag{1.13}$$

Where ΔG_s is the interfacial coherent strain energy term, *E* is Young's modulus, υ is Poisson's ratio, V_m is the molar volume and η is expressed as:

$$\eta = \frac{1}{a}\left(\frac{da}{dx}\right) \tag{1.14}$$

Where *a* is the lattice parameter.

As such, the total change in free energy can be expressed as the sum of equations 1.11, 1.12 and 1.13, leading to:

$$\Delta G_T = \frac{1}{2}\frac{d^2G}{dx^2}(\Delta x^2) + K\left(\frac{\Delta x}{\lambda}\right)^2 + \eta^2 (\Delta x)^2 \frac{E}{1-\upsilon} V_m \tag{1.15}$$

$$\therefore \Delta G_T = \left[\frac{d^2G}{dx^2} + \frac{2K}{\lambda^2} + 2\eta^2 \frac{E}{1-\upsilon} V_m\right] \frac{(\Delta x)^2}{2} \tag{1.16}$$

Where ΔG_T is the total change in Gibbs free energy.

For SD to occur, ΔG_T must be negative, and therefore:

$$\frac{d^2G}{dx^2} + \frac{2K}{\lambda^2} + 2\eta^2 \frac{E}{1-\upsilon} V_m < 0 \tag{1.17}$$

From Equation 1.17, the minimum wavelength (λ) for spinodal decomposition may be deduced, such that:

$$\frac{2K}{\lambda^2} < -\left(\frac{d^2G}{dx^2} + 2\eta^2 \frac{E}{1-\upsilon} V_m\right) \tag{1.18}$$

$$\therefore \lambda^2 > -\frac{2K}{\left(\frac{d^2G}{dx^2} + 2\eta^2 \frac{E}{1-\upsilon} V_m\right)} \tag{1.19}$$

Outside the coherent spinodal, the initial free energy of the system is still higher than equilibrium free energy, although a slight composition variation leads to an increase in free energy. In this case, SD will not occur and rather, a nucleation process occurs whereby the composition of the resulting nuclei varies significantly from that of the matrix. This process therefore takes place via downhill (conventional) diffusion. The comparison between routes of spontaneous separation (SD) and conventional diffusion is seen in Figures 1.13a and 1.13b, respectively.

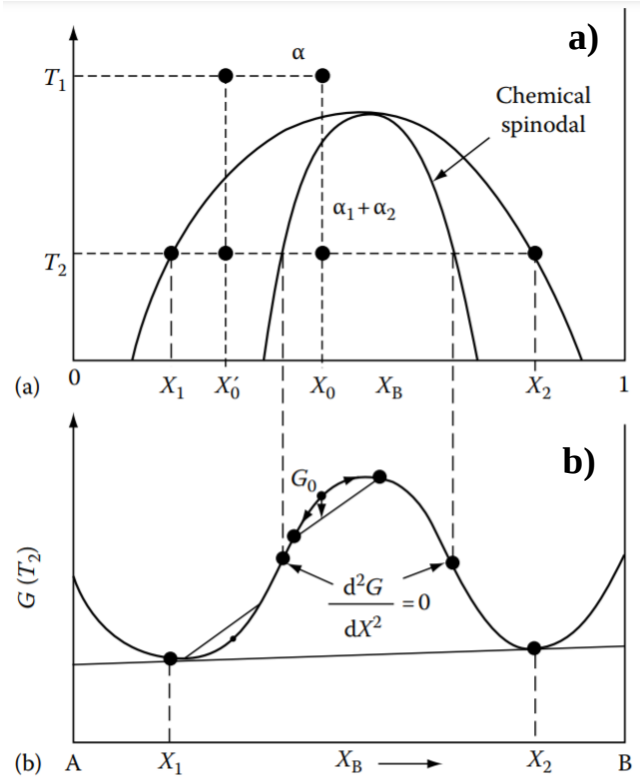

Figure 1.12a Schematic Phase diagram outlining composition X_0 which lies within the chemical spinodal and where SD is expected to occur **Figure 1.12b** Gibbs free energy at quenched temperature, showing spontaneous reduction in free energy with small composition fluctuation [111].

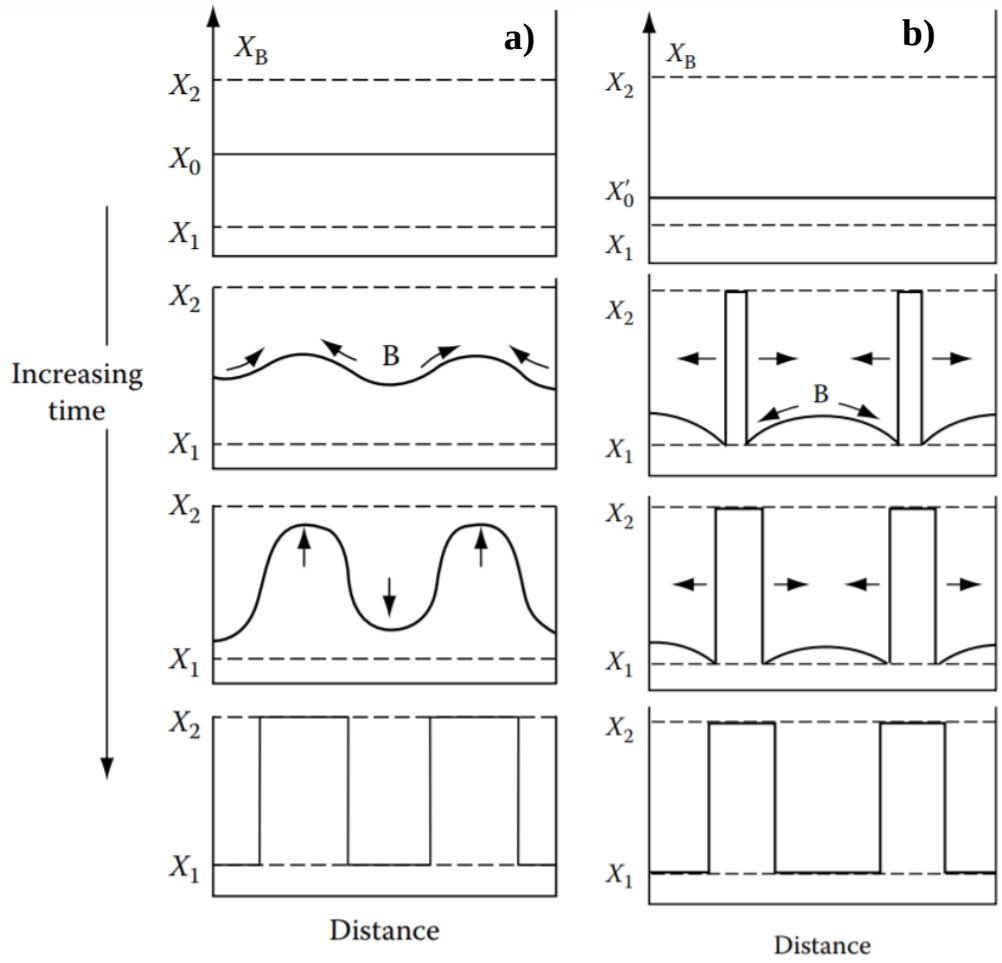

Figure 1.13a Composition profile as an alloy is quenched from T_1 to T_2 at composition X_0 **Figure 1.13b** as alloy is quenched outside the spinodal region (refer to Figure 1.12) [111].

1.4.2 Spinodal Decomposition in High Entropy Alloys

Spinodal Decomposition (SD) in HEAs has become a topic of academic interest only in recent years. The delay in exploring the occurrence of SD in HEAs is perhaps owed to the early emphasis placed on simple solid-solutions. Nevertheless, as the field advances and various HEAs with SD are unveiled, academic attention has evolved towards understanding the effect of SD on the properties of MPEA systems. In recent years, increasing academic efforts have taken bold steps in achieving SD in HEAs tailored for specific applications. From a mechanical perspective, it is well established that SD can be advantageous due to its hardening effects that derive from modulated structures or

precipitates interfering with dislocations. SD has been observed to lead to strengthening effects in various HEAs [96,97], and its effect on the magnetic properties of HEAs has also been explored and shown to have potential benefits such as increasing Curie temperature [98]. Moreover, structures from spinodal decomposition, when quenched in at high cooling rate, give very fine microstructures (of the order of the critical wavelength, Equation 1.19) [99].

The most thoroughly explored case of SD in HEAs is in systems comprising at least four of Al, Co, Cr, Cu, Fe and Ni. The work of Tong et al. explores the $Al_xCoCrCuFeNi$ system by varying the Al molar fraction from 0.0 to 3.0 in varying increments. In this study SD is observed in the ID region as A2 and B2 modulated plates [100] at values of x between 1.0 and 1.3. Although Tong et al. do not observe SD at compositions below $x = 1.0$, a study by Pickering et al. shows that SD occurs in the dendritic region of the $Al_{0.5}CoCrCuFeNi$ alloy which leads to two FCC phases [101]. Although the observation of Pickering et al. contradicts that of Tong et al., it also outlines the difficulty that is often encountered in observing nanoscale phase separation.

Nevertheless, the modulated plates observed by Tong et al. in the ID region of equimolar AlCoCrCuFeNi have been repetitively observed in alloys of a similar base. Zhang et al. also study equimolar AlCoCrCuFeNi and are in agreement with Tong et al. in that modular A2 and B2 plates (Cr-Fe rich and Al-Ni rich, respectively) form in the ID region as a result of SD [102]. However, Zhang et al. explore the phase separation of Cu in the ID region to a further extent (although both studies observe Cu segregation in the ID region). Due to its positive enthalpies of mixing with the other elements [103], Cu segregation is a commonly observed phenomenon in Cu-containing HEAs. In equimolar AlCoCrCuFeNi Cu content in the ID region is observed to be as high as 77% [102]. As such, Zhang et al. observe Cu-rich nanoprecipitates in the alloy's ID regions and grain boundaries which remain up to cooling rates of 10^7 K/s observed via melt-spinning.

In the Cu-free system of equimolar AlCoCrFeNi, Wang et al. observe that SD occurs in the ID region in the same manner observed in the equimolar AlCoCrCuFeNi alloy such that modulated A2 (Cr-Fe rich) and B2 (Al-Ni rich) plates are formed [80]. Although Wang et al. make no mention of SD occurring in the dendritic regions, Manzoni et al.

observe SD in the dendritic regions of equimolar AlCoCrFeNi which also results in a modulated A2 + B2 structure [104]. Tian et al. confirm this observation in AlCoCrFeNi, noting a modulated SD structure in not only the ID region of the alloy but also in the dendrites [105]. Figure 1.14 from the work of Tian et al. shows the fluctuations in atomic concentration of Al and Cr in both the dendritic and ID regions of AlCoCrFeNi. The fluctuations in concentration reflect the modulated nature of the spinodally-decomposed plates. Figure 1.14 also shows that the plates comprise an Al-rich phase and a Cr-rich phase, which are established to be B2 structured Al-Ni and A2 structured Cr-Fe.

SD has also been observed in the $Al_2CrCuFeNi_2$ alloy where it forms part of an interesting 'sunflower' structure. First observed by Guo et al., the petals of the sunflower structure were identified to be a eutectic of a Ni-Al-rich B2 phase and a Cr-rich A2 phase [106]. The internal section of the structure is considered to be where the primary B2 phase originates from and within this region, fine BCC precipitates form as a result of SD (see Figure 1.15). This sunflower structure was confirmed in $Al_2CrCuFeNi_2$ in a separate study which investigates the effect of increasing Al content, and was found to exist up to $Al_{2.5}CrCuFeNi_2$.

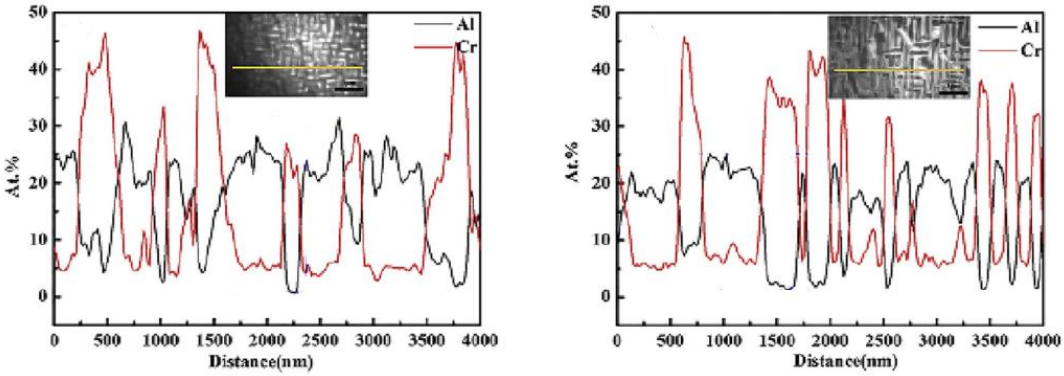

Figure 1.14 a) Compositional fluctuations of Al and Cr in dendritic region of AlCoCrFeNi and **Figure 1.14 b)** in ID region [105].

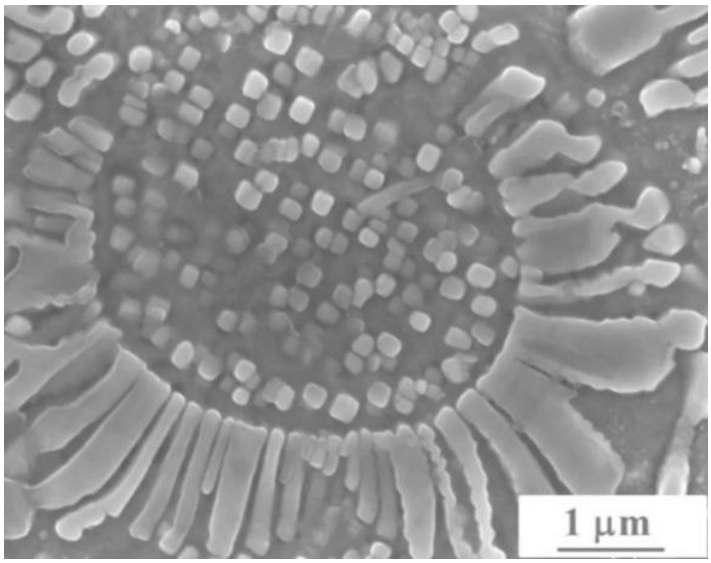

Figure 1.15 High magnification micrograph of sunflower-like microstructure found in $Al_2CrCuFeNi_2$ as a result of SD [106].

Deviating from the relatively well-explored systems discussed so far, SD has also has been observed in other MPEAs including refractory HEAs. Zhang et al. study the $HfZrTiTa_{0.53}$ HEA which undergoes SD resulting in modulated plates of finer structure than those observed in the AlCoCrFeNi system [96]. The spinodally-decomposed structure in $HfZrTiTa_{0.53}$ is shown in Figure 1.16. This modulated structure is made of two BCC phases, with one phase being lean in Ta content and the other rich in Ta content. Zhang et al. make an important observation in the fact that SD is observed in the binary phase diagrams of Hf-Ta and Zr-Ta. In reference to the method used by Jiang et al. (mentioned in section 1.2.2) to develop EHEAs by observing eutectic compositions in the constituent binaries [58], Zhang et al. show that this is a technique which can serve useful in HEA design in a more general sense. Additionally, it is observed that Ta has positive mixing enthalpies with Hf, Zr and Ti [96]. Together, these observations explain the occurrence of SD in $HfZrTiTa_{0.53}$ and the fluctuations in Ta concentration across the spinodal structure. Although Zhang et al. make no mention of how the precise atomic fraction of Ta was deduced, it is most likely that reference was made to the compositions which lie in the miscibility gaps of the constituent binary diagrams. Another refractory HEA which undergoes SD is HfNbTiV [107], showing modulations of two different disordered BCC phases. The composition fluctuations in this HEA are such that one BCC phase is rich in Hf and V, while the other is rich in Nb and Ti. Observing the mixing

enthalpy pairs of the alloy, the segregation occurs as expected as Hf-V and Nb-Ti are the two lowest enthalpies of mixing observed in the available permutations. The resultant phases have very similar lattice parameters such that the Hf-V enriched phase has a lattice parameter of 0.3295 nm and that of the Nb-Ti enriched phase is 0.3313 nm.

Finally, as the effect of sluggish diffusion in HEAs on SD would be interesting to consider, the study of Rao et al. is highlighted to conclude this section. In their study on FeCoNiMnCu which investigates the effect of different annealing conditions on the alloy, Rao et al. observe SD becomes more pronounced as annealing time is increased (see Figure 1.17) [98]. Due to the sluggish atomic diffusion in HEAs, the amplitudes of the spinodally-decomposed phases require sufficient annealing time to increase, as indeed is observed in Figure 1.17. The SD in FeCoNiMnCu leads to Fe-Co enriched regions and Cu-rich regions, both which are disordered FCC structures. Contradictory to the idea of sluggish diffusion however, is the observation of Zhang et al. which has been mentioned briefly in this section [102]. That Zhang et al. observe fine spinodally-decomposed structures in AlCoCrCuFeNi despite achieving cooling rates of the order 10^7 K/s indicates that atomic diffusion in HEAs cannot have as sluggish a nature as is often emphasised. The annealing results of Rao et al. and the rapid-cooling results of Zhang et al. serve as a perfect example to show that although current suspicions about sluggish diffusion in HEAs are valid, a conclusive statement is hard to make.

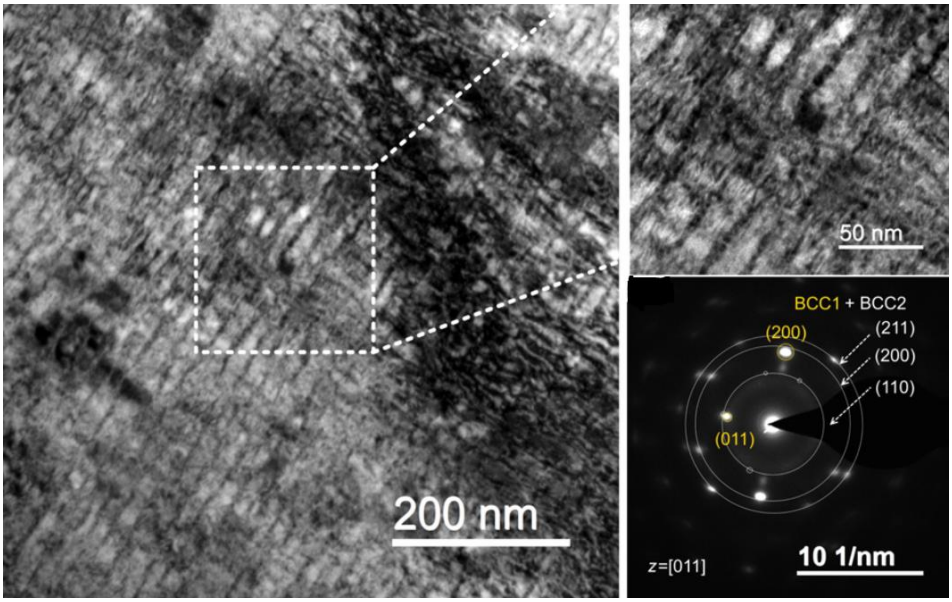

Figure 1.17 Backscatter electron image of $HfZrTiTa_{0.53}$ with TEM bright field image from selected region and corresponding SAD pattern [96].

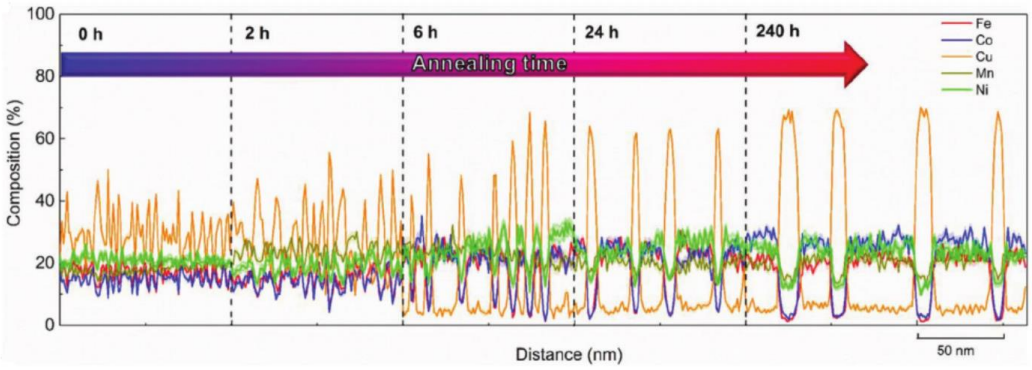

Figure 1.16 Wavelength and amplitude evolution of SD features in FeCoCuMnNi as a function of annealing time [98].

1.5 Rapid solidification

1.5.1 Fundamentals

Rapid Solidification Processing (RSP) is the process that refers to the rapid extraction of heat from metals in molten state bringing them to their solid state. Generally, rapid solidification is defined to be in the range of cooling rates larger than 10^3 K/s [108]. However, although it is important to define a lower limit on the cooling rate which defines RSP, observing a significant difference between the microstructures of the rapidly-cooled and conventional samples is often most useful. The primary advantage of RSP lies in achieving desirable features in a material's microstructure that may not be achieved by conventional processing. Namely, RSP offers the possibility of extending solid solubility and revealing non-equilibrium phases. A further advantage of RSP stems from grain refinement which is likely to lead to improved features of the processed material.

RSP can be achieved using a variety of techniques, some of which rely on rapid heat extraction during solidification, and others which attain large undercooling prior to nucleation. The former relies on maximising the release of heat from the liquid via conduction, convection and radiation and as such, comprises quenching processes such as melt-spinning, gas atomisation and spray casting. For the latter, undercooling must be achieved by suppressing heterogeneous nucleation such that the molten state of the metal is retained beyond freezing point [109]. To avoid heterogeneous nucleation, techniques to achieve undercooling usually rely on containerless solidification in order to avoid nucleation induced by foreign substances. Most commonly, undercooling is achieved by glass fluxing, electrostatic/magnetic levitation and drop tube techniques.

In relation to dendritic structures, solidification time and the extent of undercooling are known to influence the overall morphology of the solidified structure. Secondary arm spacing, λ_2, is the distance between adjacent dendrite branches stemming from the primary dendrite and is strongly dependent on cooling rate [110]. Figure 1.18 shows the correlation between secondary arm spacing and solidification time for an Al-Cu alloy, where the spacing is proportional to the cube root of solidification time [111].

Furthermore, dendrite tip radius is also part of dendritic morphology which is strongly affected by RSP [111]. Namely, dendrite tip radius is determined by undercooling during the growth phase and remains fixed thereafter.

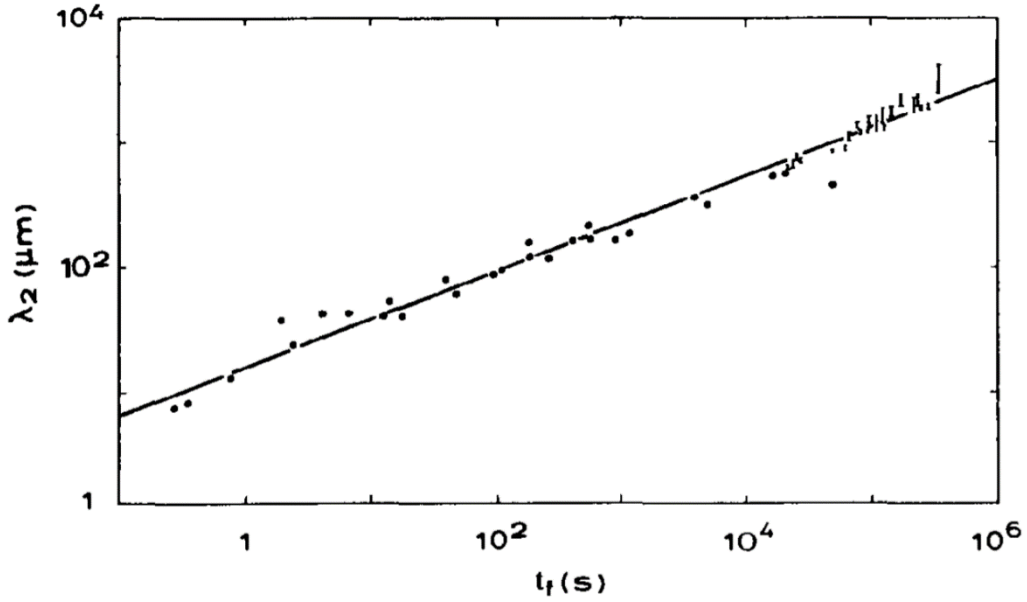

Figure 1.18 Secondary arm spacing versus solidification time for Al-4.5 wt% Cu alloy [111]

In the solidification of eutectic alloys, two solid phases are formed cooperatively [112]. The two solid phases could appear as alternating lamellae or as a rod-like structure. A lamellar structure is developed when the volume fractions of the two phases are roughly equal, whereas rod eutectics are seen when the volume fraction of one phase is much smaller than the other – whereby the minor phase forms rods in the matrix of the major phase [113]. The growth of lamellar eutectics depends on the interlamellar spacing (marked as λ in Figure 1.19) as this spacing determines the rate of diffusion of atoms from one phase to another – smaller interlamellar spacing therefore leads to faster growth [112]. A lower limit exists for λ however, such that enough interfacial energy is present to sustain the interface between the two phases (α and β) [114].

A general understanding for the effect of RSP on eutectic morphology may be acquired using Equation 1.20 [115].

$$\lambda \Delta T = constant \tag{1.20}$$

Where λ is the interlamellar spacing and ΔT is undercooling.

From Equation 1.20 it can be seen that undercooling and interlamellar spacing are inversely proportional, meaning that a finer lamellar structure is obtained at larger undercoolings. If sufficient undercooling is reached during RSP, the eutectic(lc structure can no longer form, as the interfacial energy between the α and β phases will not suffice. Namely, the interface cannot be maintained beyond a critical growth velocity. Therefore as undercooling increases and the critical value of λ is reached, the eutectic morphology will be lost.

Another important way which RSP provides enhanced structures is by inhibiting the formation of intermetallic compounds [116]. This is promising in achieving simple structures from MPEA systems which are originally complex at equilibrium. As the initial preoccupation of the metallurgical community about MPEA development was mainly related to the formation of complex compounds, inhibiting the formation of intermetallics via RSP directly addresses this point and provides further opportunities for HEA development.

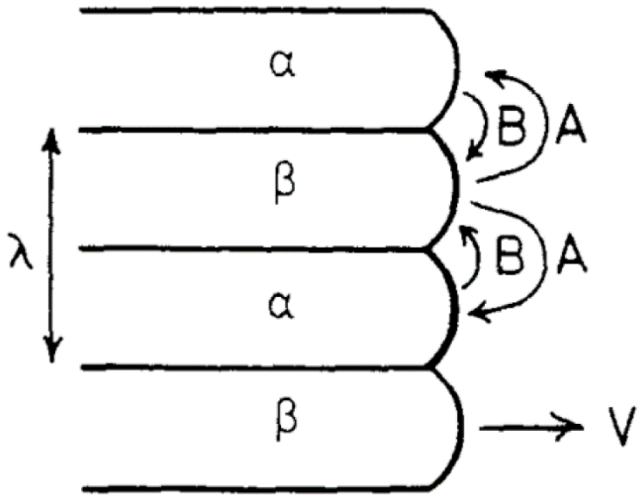

Figure 1.19 Interdiffusion between α and β phases as the eutectic front grows with a velocity *V* [111]

1.5.2 Rapid solidification of High Entropy Alloys

Rapid solidification of HEAs creates an opportunity for investigating the evolution of their microstructures and mechanical properties with cooling rate. With sluggish diffusion being a main characteristic in HEAs, the rate of coarsening at elevated temperatures is minimal, leading to excellent retention of fine microstructures. As such, RSP of HEAs is important in exploring not only the possibility of extending their solid solutions and inhibiting the formation of complex phases but also the enhancement of their mechanical properties.

RSP of HEAs to date has been attempted using methods such as gas atomisation [117], glass fluxing [118], melt-spinning [119], vacuum levitation melting (VLM) [120] and selective laser melting (SLM) [121]. Although the undercoolings and cooling rates attained by the different methods do vary, the motivation is to explore the effect of non-equilibrium solidification on HEAs.

Although gas atomisation experiments on HEAs cannot be found in abundance, the available studies have shown that rapidly solidified HEA powders can be achieved in sizes as fine as < 20 μm. Figure 1.20 shows fine powders from the CrFeNiMn HEA achieved by gas atomisation [122], where it was found that despite the duplex (FCC + BCC) nature of furnace-cooled CrFeNiMn, the powders showed a nearly single phase FCC structure. As different size fractions of powders are often obtained from processes such as gas atomisation, differences in structures and morphologies between the different sized powders are expected. In the case of CrFeNiMn, Lehtonen et al. found that the volume fraction of the BCC phase increases with cooling rate, up to 5.5 % in the smallest size powders [122]. Although cooling rate estimates are not presented in the work of Lehtonen et al., a gas atomisation study by Zhou et al. [123] on the $Al_{0.6}$CoCrFeNi HEA obtains powders of similar size and estimates a cooling rate of around 6×10^6 K/s. The differences in constituent elements between both alloys will affect the cooling rate due to the differences in properties. However, the cooling rate estimated by Zhou et al. can be taken as an estimate especially given that both studies use an Ar atmosphere. Between the largest size powders (90 – 150 μm) and the smallest size powders (< 20 μm) of the CrFeNiMn HEA, Lehtonen et al. find that nanohardness increases from 3.95 GPa to 4.25 GPa. This increase can be largely attributed to grain refinement (as observed grain size decreases from 6 μm to 2.5 μm), although the slight increase in BCC phase may also be a contributing factor.

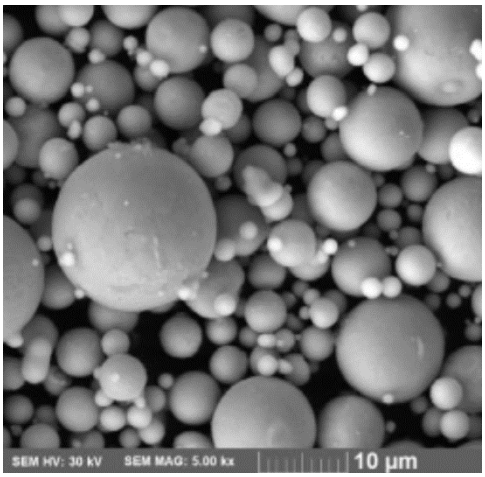

Figure 1.20 Gas-atomised powders of CrFeNiMn HEA [122].

Gas atomisation of the $AlCoCrFeNi_{2.1}$ EHEA has also been applied, in which Ding et al. observed a blocky dendritic structure of FCC dendrites with an FCC/BCC interdendritic eutectic [117]. As large cooling rates tend to favour dendritic growth, gas atomised $AlCoCrFeNi_{2.1}$ powders showing dendritic growth is a somewhat expected observation. Centrifugally cast $AlCoCrFeNi_{2.1}$, cooled at 450 K/s, showed an almost identical structure of FCC dendrites with a eutectic interdendritic region [124], albeit that the dendrites were somewhat better developed than those in the gas atomisation study. Further confirming this departure from eutectic growth at high cooling rates is the work of Nagase et al., where melt-spun $AlCoCrFeNi_{2.1}$ was shown to lose its lamellar structure and form precipitates on the grain boundaries [125]. Although in EHEAs, the eutectic is expected to be inhibited at high cooling rates, in $AlCoCrFeNi_{2.1}$ a small eutectic volume fraction remains in its gas atomised powders despite the cooling rate range of around 10^4 – 10^5 K/s. However, in the $Al_{0.6}CoCrFeNi$ alloy (which shows a FCC + BCC eutectic in equilibrium conditions) the eutectic structure is indeed inhibited in its gas-atomsised powders cooled at 1.45×10^5 K/s. In the case of the $Al_{0.6}CoCrFeNi$ powders it is the growth of the FCC which is suppressed [123]. Figure 1.21 shows the estimated cooling rates of these powders with respect to droplet diameter.

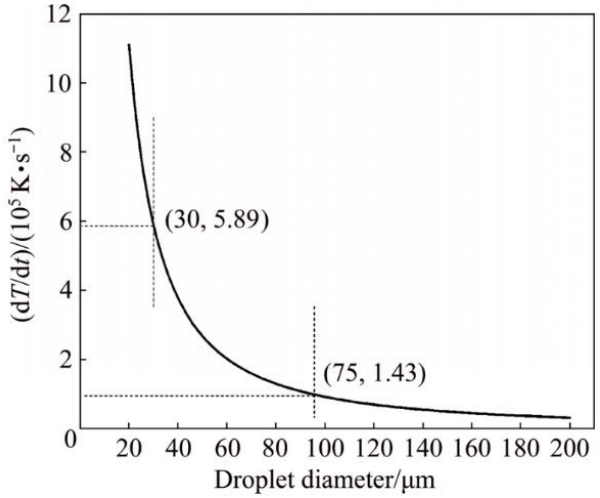

Figure 1.21 Cooling rate as a function of droplet diameter in $Al_{0.6}CoCrFeNi$ [123].

Other RSP techniques such as glass fluxing and levitation methods have shown to achieve undercoolings (ΔT) of up to 380 K [118] in HEAs and significant improvements in mechanical properties. For instance, CoCrFeNi undercooled by 300 K using a glass fluxing method showed an increase in compressive yield strength from 137 MPa to 455 MPa (see Figure 1.22) [126]. Similar to the aforementioned outcome of enhanced nanohardness in gas-atomised CrFeNiMn powders, the increase in yield strength of undercooled CoCrFeNi is attributed to grain refinement. Unlike the study of Lehtonen et al. however, where no mention was made of the BCC phase contributing to increased hardness, Li et al. in their study of glass-fluxed CoCrFeNi do highlight the role played by the observed BCC precipitates in enhancing the yield strength of the alloy. It is therefore evident that in HEAs of this base, it is not uncommon that BCC growth is observed with higher growth velocities. Wang et al. also study CoCrFeNi undercooled by glass fluxing method and achieve similar undercoolings as the study by Li et al. Similar observations are made in both studies and their appears to be unison in the fact that grain refinement and BCC growth are observed. Wang et al. study a wider range of undercoolings and as such, are able to present the enhanced microhardness with increased undercooling in a gradual fashion [127]. Figure 1.23 shows the enhanced microhardness in CoCrFeNi as undercooling is increased by increments of 50 K.

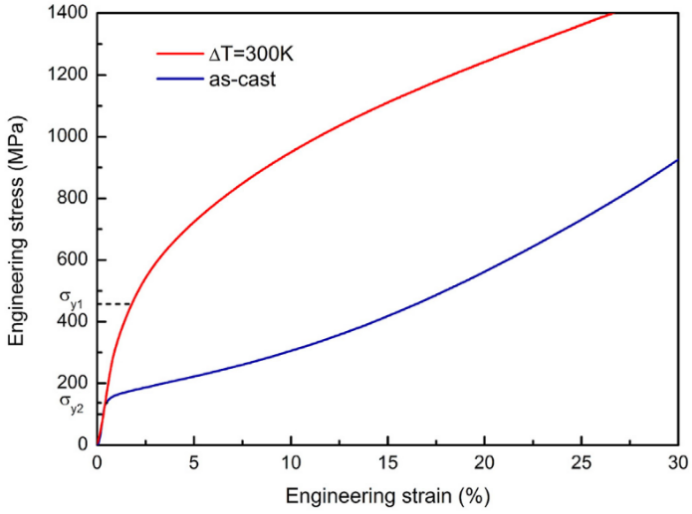

Figure 1.22 Stress-strain curve of undercooled CoCrFeNi [126].

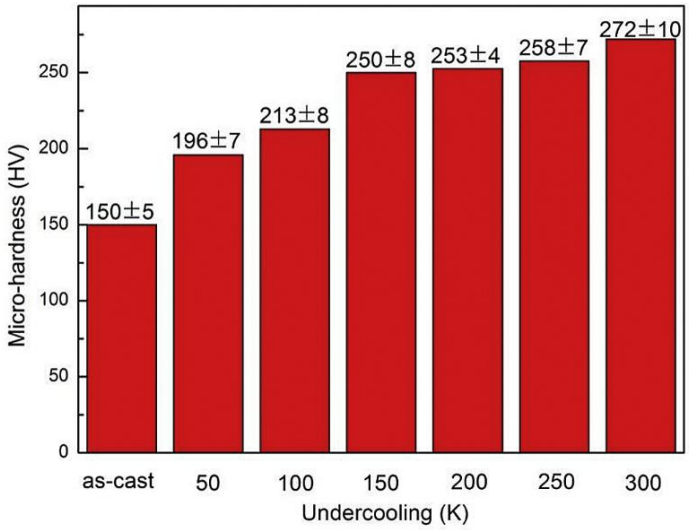

Figure 1.23 Increasing microhardness in CoCrFeNi as undercooling is gradually increased [127].

Vacuum Levitation Melting (VLM) has shown to obtain comparable undercoolings in HEAs and have similar effects on the properties of the alloys. Andreoli et al. studied the solidification behaviour of CoCrFeNi post achieving undercoolings of up to 150 K [128]. In this in situ study, insightful observations are made on the effect of different undercoolings using high-speed imaging techniques. As mentioned above, gas-atomised CoCrFeNi shows a predominantly FCC structure although at higher growth velocities a small BCC volume fraction (around 5 %) develops. In the in situ VLM study of Andreoli et al. on CoCrFeNi with 120 K of undercooling, a stable FCC phase nucleates and gives result to a single-phase FCC structure. However, an image series shows that at a higher undercooling of 150 K, a BCC phase nucleates first and that an FCC phase nucleates thereafter (see Figure 1.24), allowing the conclusion to be made that the BCC phase is metastable. Nevertheless, the BCC can presumably be nucleated in favour in favour of FCC, as the recalescence images indicate the undercooling with respect to the BCC phase is lower than the undercooling with respect to the FCC phase. However, it is also clear that once both phases are nucleated, FCC will outgrow BCC. Figure 1.25 shows the delay time between the nucleation of the BCC and FCC phases. Naturally, the delay time is expected to shrink with higher undercooling (as growth velocity increases with undercooling) and this is indeed observed in Figure 1.25. Generally, this observation of

BCC nucleation at high undecooling is in accord with the aforementioned gas atomisation studies on CoCrFeNi, which showed BCC presence only in the smallest size powders (those with highest cooling rates).

In a study on supercooled, equimolar MoNbReTaW, Hu et al. observed that an undercooling of 500 K (achieved by electrostatic levitation) leads to disorder trapping and the growth of a single BCC structure [129]. As with previous studies, the rapidly-solidified MoNbReTaW sample showed improved hardness (20% increase from the as-cast alloy). Disorder trapping is expected to occur in rapidly-solidified HEAs not only due to the high cooling rates but also due to their characteristic sluggish atomic diffusion, and it is argued by Ding et al. that disorder trapping also occurs in gas-atomised powders of the $AlCoCrFeNi_{2.1}$ alloy [117].

Likely due to its higher technology readiness level (TRL) relative to other techniques, selective laser melting (SLM) is the most explored form of RSP in HEAs. In fact, by and large the focus of gas atomisation and other powder metallurgy studies of HEAs is to produce powders for additive manufacturing (AM) purposes. Although SLM does not achieve supercooling comparable to that of fluxing and levitation techniques (as heterogeneous nucleation is instant), SLM can achieve cooling rates of up to 10^7 K/s [130], depending on laser energy density. However, the layer-by-layer nature of AM results in columnar grain growth, leading to anisotropic properties in the fabricated alloys [131]. This is no different in HEAs as the issue has been observed in several AM-fabricated HEAs [132,133]. Such alloys with anisotropic mechanical properties find few applications in the real world. As such, the topic of columnar-to-equiaxed transitioning (CET) of the resulting dendrites is a topic that is rightly attracting intensive attention. Despite these barriers that AM faces, it is worth remembering that HEAs are not industry-ready in any case as yet. As such, attempts to produce AM-fabricated HEAs as well as explorations of achieving CET in HEAs [134] should be considered with a positive outlook.

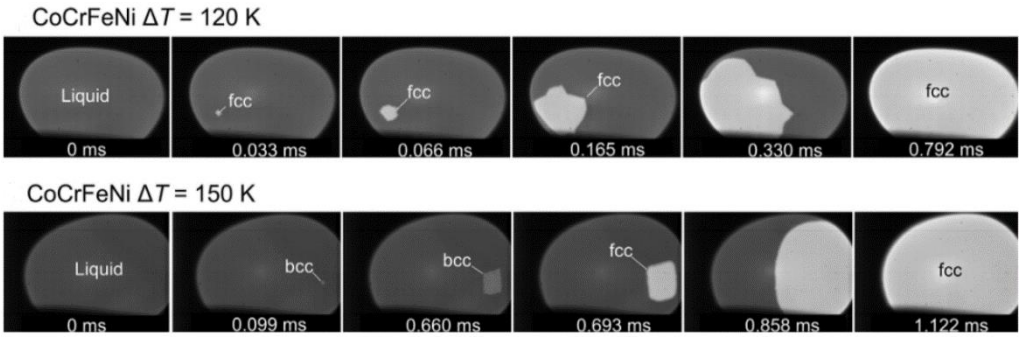

Figure 1.24 In situ observation of nucleation in undercooled CoCrFeNi HEA [128].

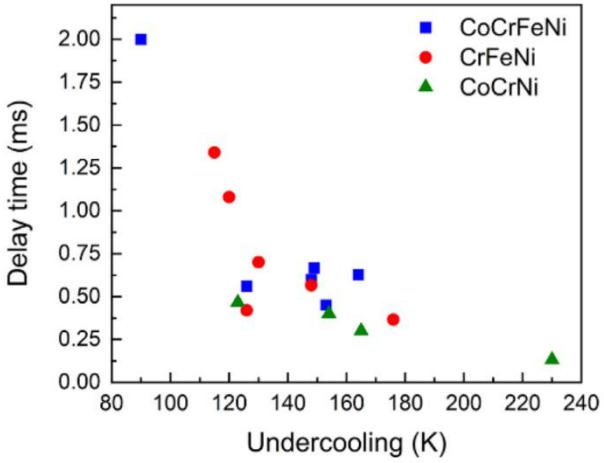

Figure 1.25 Delay time between nucleation of FCC and metastable BCC at different undercooling scenarios [128]

To conclude this section, it is worth reminding the reader that improvements in mechanical properties are not a granted outcome of RSP. For example, Wang and Kong demonstrate that $CoCrFeNiCu_2$ supercooled via glass fluxing showed improved microhardness as undercooling increased but declined at a critical undercooling of 236 K (see Figure 1.26) due to phase separation [118]. This phase separation is often observed in similar alloys containing Cu, where a Cu-depleted primary phase is formed and a Cu-rich phase forms in the interdendritic region. As mentioned in section 1.4.2, this phenomenon is owed to the positive enthalpy of mixing between Cu and the other elements. It is important to stress, however, that this is not always the outcome when Cu forms part of a MPEA. In fact, the same study shows that phase separation subsides in the CoCrFeNiCu alloy at high undercoolings and its microhardness increases monotically

as expected. This is also confirmed by Cui et al. [135], who show that Cu segregation steadily decreases until it is almost unobservable in a sample that experiences an undercooling of 226 K (see EDS maps in Figure 1.27). It may therefore be said that the atomic fraction of Cu in the $CoCrFeNiCu_2$ alloy causes phase separation that is too strong to be mitigated by large supercooling.

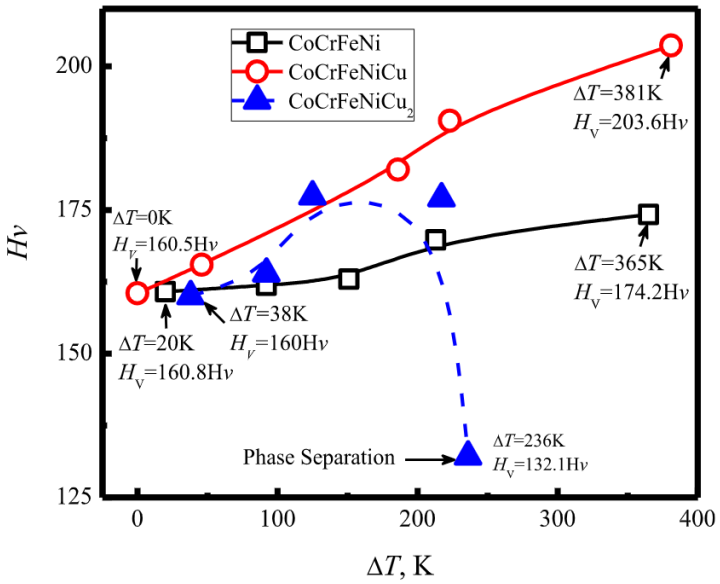

Figure 1.26 Hardness as a function of undercooling in three HEAs [118].

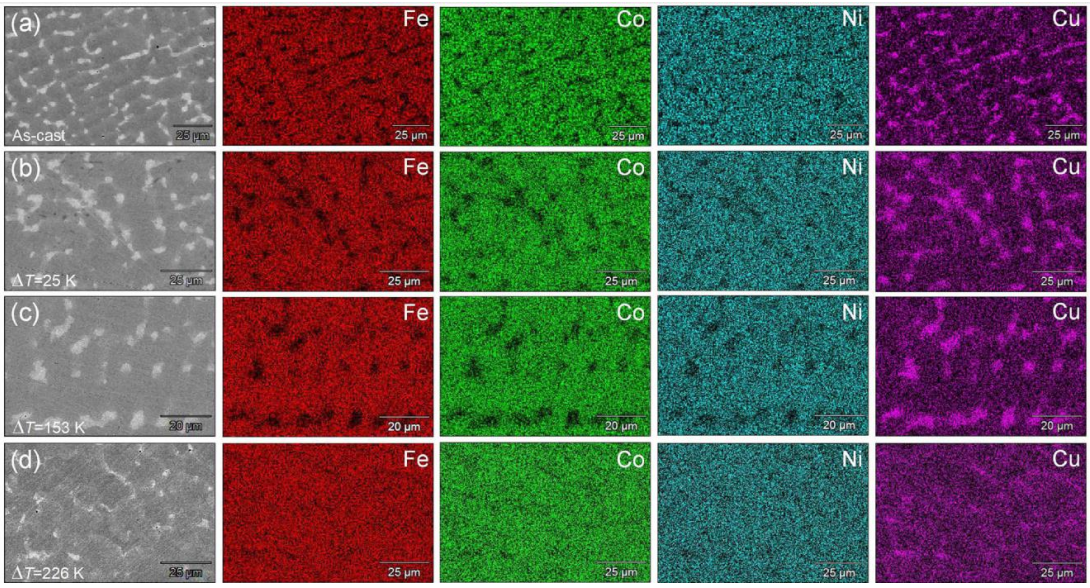

Figure 1.27 EDS maps of CoFeNiCu at various values of undercooling, showing improved homogeneity as undercooling is increased [135].

1.6 Machine-learning techniques in HEA discovery

It was discussed in Section 1.2 how HEA formation criteria have stirred constant debate since HEA discovery. This has given HEA researchers the incentive to turn to ML methods in predicting HEAs with desired structures [136] and properties [137]. The first attempts in employing ML for HEA discovery were made in 2018, and judging by the surge in such attempts over the past year, it is evident that ML methods will play an integral part in shaping the future of HEA research.

Since 2018, various ML approaches have been applied to HEA phase selection, although artificial neural networks have seen the most success amongst the algorithms and are the most widely applied [138]. HR features are typically used as the inputs to the NN (as shown in Figure 1.28), with the outputs typically being a combination of SS, SS + IM, IM and AM; where SS, IM and AM are solid solution, intermetallic and amorphous structures, respectively. In general, there appears to be agreement that beyond 4 to 5 input features, diminishing returns in accuracy of the NNs are observed [139–141], although debate remains on the most effective HR features to be used for optimal results. For

instance, Dai et al. [142] show (using ML methods) VEC to be the most important parameter in HEA phase prediction and ΔS_{mix} to be the least important, whereas in the ML-based study of Huang et al., δ is concluded to be the most relevant parameter [143]. A study by Zhang et al. deploys ML with extended Miedema theory and concludes that formation enthalpy and δ are the most relevant parameters in HEA prediction [144]. Despite these differences, ML-driven progress has not been halted and ML models have been improving in accuracies in a yearly manner, with reported accuracies today constantly ranging between 90 – 95 % [145,146].

Examples of successful HEA design using ML models include the work of Wen et al., where a database containing $Al_xCo_yCr_zCu_uFe_vNi_w$ HEAs and their hardness values was used to train a ML (NN) model [147]. In this work, Wen et al. report two alloys with hardness values 10 % larger than the maximum value found in the database. The alloys reported are $Al_{43}Co_{22}Cr_{23}Fe_7Ni_5$ and $Al_{47}Co_{20}Cr_{18}Cu_5Fe_5Ni_5$, both of which were shown to comprise a disordered BCC structure and an ordered B2 structure. Bhandari et al. pursue a similar approach using a database of refractory HEAs and their hardness values. In this study, Bhandari et al. uncover a novel RHEA in $C_{0.1}Cr_3Mo_{11.9}Nb_{20}Re_{15}Ta_{30}W_{20}$ with a predicted hardness value of 695 HV [148]. The alloy was then manufactured to experimentally confirm the predicted value, which was found to align within a 15 % error margin. It is therefore a matter of time before the use of NN becomes mainstream amongst HEA researchers and studies such as those of Wen et al. [147] and Bhandari et al. [148] become implementable with ease. In fact, Yan et al. predict 10 single-phase RHEAs (comprising combinations between Al, Mo, Nb, Cr, W and Ti) using several ML algorithms and confirm their predictions experimentally [149]. Although it is not mentioned how many of the studied alloys are novel, Yan et al.'s experiment certainly makes a statement in proving the applicability and scalability of ML in alloy discovery.

As ML models rely heavily on HEA databases, a foreseeable problem halting their progress is the lack of systematic recording of HEAs and their properties. For example, the impacts which processing methods have on an alloy's properties are often not considered when documenting HEAs. It is often the case that a given property of the same alloy can have two different reported values; these discrepancies are most likely attributed to differences in processing methods which have not been recorded. Some examples are

the $AlCoCrCu_{0.5}FeNi$ alloy with hardness values reported to be 458 HV, 563 HV and 665HV [147], and the $Al_3FeNiCoCrCu$ alloy with a microstructure reported to be intermetallic (IM) [150] and solid-solution (SS) [151]. Generally, to achieve maximal results from a NN, the size of the data set should be as large as possible, with only alloys with high uncertainty being omitted. As such, in order for the HEA community to excel in applied ML, HEA databases need to be put together with clear outlines of the processing techniques used to manufacture them.

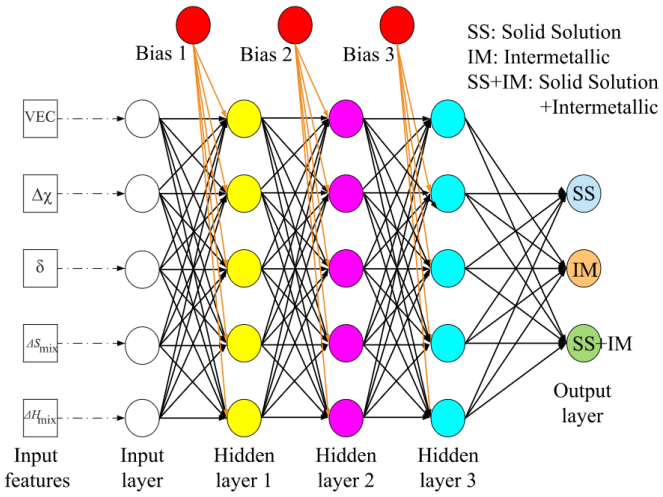

Figure 1.28 Schematic of NN architecture showing five input features, three hidden layers, and three outputs classifying the alloys as SS, IM or SS + IM [143].

2. Equipment and methodology

This chapter summarises the experimental methods and equipment used in this project. HEA ingots were produced using an arc-melter and melted several times to ensure homogeneity. Titanium was used as a getter in the arc-melter furnace to limit oxidation. As the HEAs produced in this work all contain Aluminium, this was an important aspect during ingot preparation. Rapidly solidified droplets were then produced from these HEA ingots using the drop-tube facility. To analyse the powders and as-cast samples, a range of testing methods were used including optical microscopy, scanning electron microscopy (SEM), energy-dispersive X-ray (EDX), X-ray diffraction (XRD), transmission electron microscopy (TEM), focused ion beam (FIB) and Vickers-microhardness. This equipment is explained in more detail within this chapter.

2.1 Arc-Melter

An arc-melter was used to produce the HEAs studied in this work. The arc-melter's vacuum chamber (evacuated down to 5×10^{-2} mbar) along with a Titanium getter produced an inert atmosphere for element mixing to take place without oxidisation. For the addition of Aluminium however, the drop-tube was employed as a furnace as it provides a more inert atmosphere. Aluminium's high oxygen affinity poses difficulties in mixing it with other elements using the arc-melter without oxidisation taking place.

For a melt to be carried out successfully using the arc-melter, the following components of the arc-melter need to be in check: a copper hearth, non-consumable Tungsten electrode, melting/vacuum chamber, rod for arc-control, UV shield and valves controlling pressure in the melting chamber. In addition, an electrical power system is needed for generating the arc, a coolant system (water) to keep lower the hearth's temperature, a vacuum pump and an Argon (inert gas) cylinder connected to melting chamber.

The vacuum pump used with this arc-melter is a two-stage stage oil sealed pump. Before melting a sample, the chamber is evacuated to pressures of the order 10^{-2}mbar and backfilled with about 50 mbar of Argon at least five times. Although all the melting was performed in the round-shaped moulds (for better mixing), the final melt of each HEA

was done in a square mould (see Figure 2.1) to make the sectioning of the alloy more manageable during sample preparation.

The splashing of material during an arc-melting experiment is normal and usually results in a small weight-loss – this was deemed negligible in this project. To minimise the splash, certain precautions can be taken such as ensuring a safe distance between the electrode and the sample and ensuring that the contact time between the arc and the sample is not too long (15 seconds is sufficient in most melts). Ensuring a distance between the electrode and the sample is important to avoid Tungsten contamination in the sample.

Ensuring homogeneity is important for any arc-melted sample and is especially important in producing HEAs. For this reason, each sample was turned over and melted four times at each stage. For example, if the stages of forming an alloy of ABCD, the stages would be AB, CD and ABCD. Table 2.1 gives an example of the melting stages in achieving the AlCuCrFeNi alloy.

Figure 2.1 Copper-hearth showing different mould shapes.

Table 2.1 Masses of elements in intermediate alloys to reach equimolar AlCuCrFeNi

Alloy	Element mass (g)					Arc-melted/Drop-tube furnace
	Al	Cu	Cr	Fe	Ni	
AlCu	2.5	5.8	-	-	-	Drop-tube
FeNi	-	-	-	5.1	5.4	Arc-melted
AlCuFeNi	2.5	5.8	-	5.1	5.4	Arc-melted
AlCuCrFeNi	2.5	5.8	4.8	5.1	5.4	Arc-melted

2.2 Drop-Tube

The HEAs prepared in the arc-melter were transferred to the drop-tube for rapid solidification. A schematic of the 6.5m long drop-tube used in this work is shown in Figure 2.2. The HEA ingot is placed in a tri-hole alumina crucible and mounted such that the crucible's centre is coincident with that of the RF coil. Before melting the alloy, the drop-tube's atmosphere must be inert and oxygen-free. The vacuum in the drop-tube (order of 10^{-6} mbar) is reached via two pumping stages. The first stage employs a rough pump (placed at the bottom of the drop-tube), which reaches vacuums of roughly 7×10^{-3} mbar. This pump is used to carry out three flushes, with 500mbar of Nitrogen gas used to backfill the drop-tube between each flush. A turbo-molecular pump (placed in the mezzanine floor) is then used to reach lower vacuums down to roughly 8×10^{-6} mbar.

Once the desired vacuum is reached, the drop-tube is backfilled with Nitrogen gas up to 500 mbar and the melting stage is then ready to take place. An RF power generator (found on top-floor) is used to elevate the alloy's temperature to its melting point. Once the ingot is completely melted, N_2 gas is used to create a differential pressure of 4 Bar to eject it downwards. Mostly, the droplets solidify containerlessly and are collected in the drop-tube's catch-pot (lower ground). To monitor the alloy's temperature during the melting

stage, an R-type thermocouple is used. Water supply is used cool the structure of the drop-tube during the melting stage.

The resulting powders from the ejection are then sieved into 10 standard diameter ranges: ≥ 850 μm, 850–500 μm, 500–300 μm, 300–212 μm, 212–150 μm, 150–106 μm, 106–75 μm, 75–53 μm, 53–38 μm and ≤ 38 μm. A heat balance for a droplet in free fall is used in order to calculate the cooling rate of each powder size fraction. This heat balance considers heat transfer via convection, conduction and radiation from the droplet to its environment. This heat balance is expressed as shown below in Equation 2.1.

$$\frac{dT_d}{dt}\left[c_l(1-f)+c_s f - L\frac{df}{dt}\right] = \frac{6h}{\rho d}\left(T_d - T_g\right) + \frac{6\varepsilon\sigma_b}{\rho d}\left(T_d^4 - T_g^4\right) \qquad (2.1)$$

where T_g is the temperature of the gas (N_2) used to flush the apparatus, T_d is the instantaneous temperature of the particle, c_s and c_l are the specific heat of the metal in the solid and liquid states respectively; f is the solid fraction, ρ is the density of the metal, d the diameter of the droplet, ε the emissivity of the droplet surface, σ_b the Stefan–Boltzman constant and h is the heat transfer coefficient estimated using:

$$h = \frac{\kappa_g}{d}\left(2 + 0.6\sqrt{Re}\sqrt[3]{Pr}\right) \qquad (2.2)$$

Where κ_g is the thermal conductivity of the gas (given in Table 2.2) and Re and Pr are the Reynold and Prandtl numbers for the flow respectively, given by:

$$Pr = \frac{c_{pg}\mu}{\kappa_g}, \quad Re = \frac{\rho_g d}{\mu}\left|v_d - v_g\right| \qquad (2.3)$$

Where d is the particle diameter and c_{pg} and μ are the specific heat capacity and kinematic viscosity of the gas respectively. The velocity differential between the droplet and the gas is $\left|v_d - v_g\right|$ and can be assumed to be the terminal velocity, v_T. v_T is given as:

$$\left|v_d - v_g\right| = v_T = \sqrt{\frac{4gd}{3C_d}\left(\frac{\rho - \rho_g}{\rho_g}\right)} \qquad (2.4)$$

where, g is acceleration due to gravity, ρ_g is the density of the gas, and C_d is the drag coefficient, estimated from:

$$C_d Re^2 = \frac{4mg\rho_g}{\pi\mu^2} \tag{2.5}$$

Where m is the initial mass of the sample.

As the sample properties (c_l, ρ and L) are undocumented for the HEAs studied in this work, estimates were made using properties of the constituent elements and their mass ratios. Nevertheless, T_m was determined by DTA analysis as this would give a more accurate value than the average of T_m value between constituent elements. The density as for each HEA using Archimedes' principle. Table 2.2 summarises these values as well as the properties of N_2 gas.

Table 2.2 Thermophysical properties of N_2 and $AlCoCrFeNi_{2.1}$ HEA

Material	Parameter	Value
N_2 Gas	c_{pg}	$1039\ J\ kg^{-1}K^{-1}$
	μ	$1.78 \times 10^{-5}\ N\ s\ m^{-2}$
	κ_g	$2.6 \times 10^{-2}\ Wm^{-1}K^{-1}$
	ρ_g	$1.16\ kg\ m^{-3}$
$AlCoCrFeNi_{2.1}$	c_l	$811.16\ J\ kg^{-1}\ K^{-1}$
	ρ	$7380\ kg\ m^{-3}$
	L	$3.07 \times 10^5\ J\ K^{-1}$

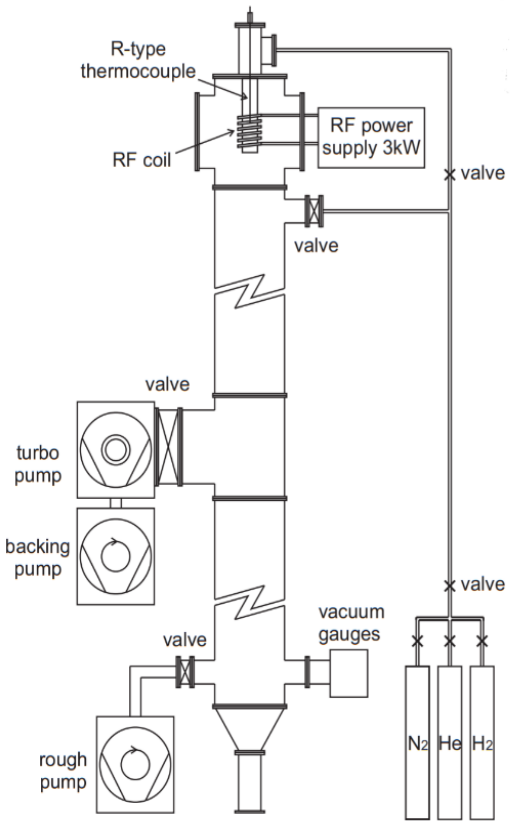

Figure 2.2 Schematic of Drop-Tube apparatus used in this work [152].

2.3 Sample Preparation and Characterisation

2.3.1 Optical Microscopy

An Olympus BX51 microscope was used as the first stage in revealing a sample's microstructure. To observe the manufactured alloy microstructures, a section of the as-cast samples is cut using a precision saw (Beuhler, Isomet 5000). The sample was then mounted automatically using the Beuhler Simplimet 1000 mounting press with Transoptic resin. The mounted samples were then ground in the order of P240, P600, P1200 and P2500 grinding paper. The sample was then polished (on cloth) using diamond pastes in the sequence of 6µm, 3µm and 1µm. The grinding and polishing sequences are

mentioned in more detail in Table 2.3. The samples were then etched using aqua regia solution (HCl and HNO3 in 3:1 ratio) for 10 seconds.

Table 2.3. Grinding and polishing sequences.

	1ST Grind	2nd Grind	3rd Grind	4th Grind	5th Grind
Paper	P240	P600	P800	P1200	P2500
Suspension	Water				
Time (mins)	2-7				
Disc speed (rpm)	100-200				
Rotation direction	Contra				
Polishing					
	1st Polish	2nd Polish	3rd Polish		
Paper	Cloth	Cloth	Cloth		
Suspension	6µm diamond paste	3µm diamond paste	1µm diamond paste		
Time (mins)	4-8	4-8	4-8		
Disc speed (rpm)	70-90	70-90	70-90		
Rotation direction	Contra	Contra	Contra		

2.3.2 Scanning Electron Microscopy and Energy Dispersive X-Ray Spectroscopy

For further and more sophisticated microstructure examination, the samples were examined under the Hitachi SU8230 SEM coupled with the Oxford Instruments Aztec Energy Dispersive X-Ray spectrometry (EDX). Backscattered-electron (BSE) detection and secondary-electron (SE) detection are the two main modes in which the SEM was operated in this work. Backscatter detection is useful for phase contrast analysis as heavier elements result in higher intensity electron backscattering in comparison to lighter elements, resulting in the regions with heavier elements appearing to be brighter. Secondary electrons are low energy electrons obtained via inelastic scattering with the surface of the material. Secondary electron scattering allows features such as grain boundaries and precipitates to be identified. Deciding on which mode of detection to be used depends on the objective of the analysis. For instance, SE imaging has a higher resolution than BSE imaging due to the lower energy of SE electrons, creating a smaller interaction volume. As such, SE imaging is used when the objective is to capture sharp

features in a sample, such as topographical contrast or faceted surfaces. On the other hand, BSE detection reveals differences between areas which are chemically different.

Any SEM is dependent on the concept of firing an electron beam at the specimen's surface. Typically, the source of the electron beam is a cathode (Tungsten hairpin filament) to which a strong electric field is applied. However, the Hitachi SU8230 SEM utilises cold-field-emission (CFE) technology, whereby a sharpened cathode is used rather than a hairpin filament. Field emission in general provides beams with higher intensity than hairpin filaments, and the ultra-high vacuum achieved by CFE further improves the electron density of the generated beam (due to the improved absorption of gas molecules at the cathode tip). As such, the energy spread in CFE operated SEM's is at least half that of SEMs with Schottky emitters (0.25 eV versus 0.70 eV respectively). The Hitachi SU8230 has a dedicated backscatter detector which is designed to use higher energy signals, hence resulting in higher resolution images. To obtain quality images, BSE analysis was carried out using an accelerating voltage of 20kV. Although voltages as little as 5kV could also lead to good images, it was found that for the samples involved in this work, 20kV was the best operating mode.

EDX was used for quantitative elemental analysis of the alloys. For such analysis, a given volume in the sample is bombarded by the SEM's electron beam. During this bombardment, electrons in the lower energy levels of the atoms at the sample's surface are ejected. As such, electron vacancies are created are then filled by electrons from higher states. As an electron moves to a lower state, an X-ray is emitted to balance the energy difference between the two energy levels. Each element has an X-ray of a characteristic wavelength which is omitted during this process, allowing the element to be identified.

Upon striking the detector, an X-Ray creates a charge which is proportional to its energy. The relative abundance of the X-Rays is then measured versus their energy, allowing a spectrum of X-Ray energy versus counts to be deduced and as such, reveal the sampled volume's elemental composition. To reduce the interaction volume, low accelerating voltages (5kV) were opted for during EDX analysis. EDX analysis was carried out at specific points, along manually drawn lines or on a selected area. A range of

magnifications was also used during the EDX analysis. For instance, for checking the overall homogeneity of a sample, small magnifications were used such that a larger area is covered. In such a case, higher accelerating voltages were used (15kV). However, in cases which required a more localised analysis such as identifying the components dominating a particular phase, smaller magnifications were used with 5kV as the accelerating voltage.

2.3.3 X-Ray Diffraction

X-Ray Diffraction (XRD) is a non-destructive method used to analyse the structure of crystalline phases present in a material. XRD analysis is carried out by directing an x-ray beam from a source (cathode ray tube) at a sample and measuring the scattered intensity as a function of the angle at which the X-Rays are emitted. Once the beam is separated, the scatter, also called a diffraction pattern, indicates the sample's crystalline structure. The Rietveld refinement technique is then used to characterize the crystal structure which most likely provided the observed pattern. Diffraction occurs when the path difference between the scattered and incident beams is a multiple of the wavelength of the X-ray (a schematic of this is displayed in Figure 2.3). This relation is known as Bragg's law (given in Equation 2.6)

$$n\lambda = 2dsin\theta \tag{2.6}$$

Where n is an integer representing the order of reflection, d is the distance between adjacent planes, λ is the wavelength of the incident beam and θ is the diffraction angle of the beam.

Current XRD databases are limited in characterising HEAs. This is due to the fact that lattice spacing data for FCC and BCC solid solutions of multicomponent alloys is lacking. Mainly, this can be explained due to the large internal strains within the lattice, which as seen in Section 1.2, makes it difficult to predict the lattice structures of HEAs. Therefore, the XRD peaks in this project were characteristed manually by using the d-spacing of each peak and finding the matching miller indices. In this work, monochromatic Cu Kα1

X-Rays with wavelength λ= 1.54056 Å were used with a scanning range (2θ) between 20° to 100° and a step size of 0.03.

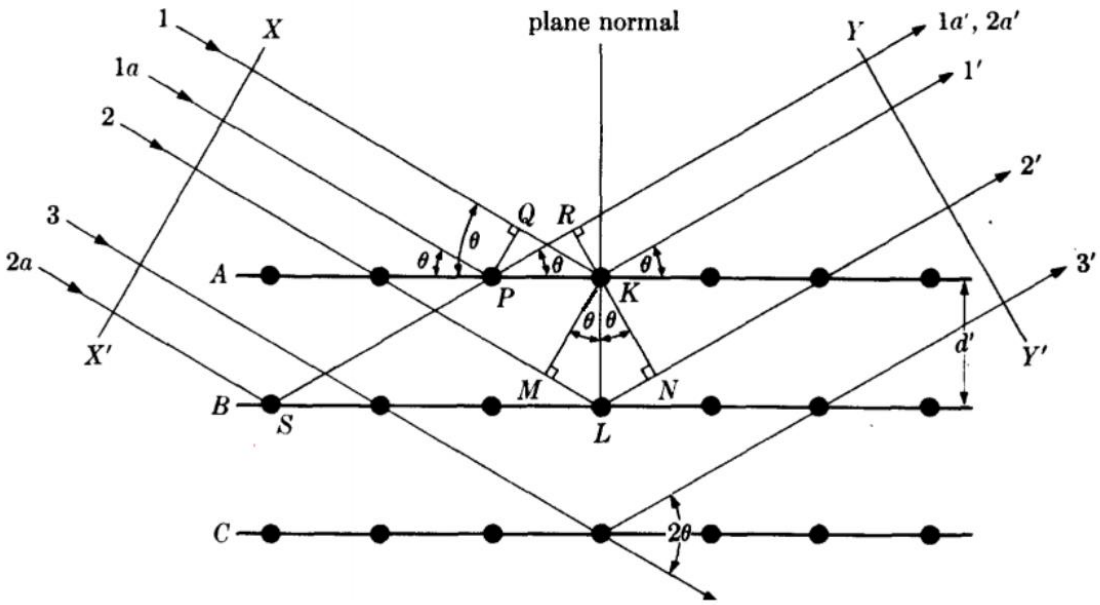

Figure 2.3 X-Ray diffraction in crystal structure [153]

2.4 Vickers Microhardness

For each HEA, Vickers microhardness tests were carried out on its as-cast form as well as its rapidly solidified powders. Performing microhardness tests on powders from all size fractions allowed the effect of cooling rate to be deduced. A Tukon 1202 Wilson Vickers micro-hardness tester was used while keeping the load and dwell-time constant across all size fractions in order for fair comparisons to be made. A 0.05kg load was used in all tests with a dwell-time of 10 seconds. The final microhardness value of each powder size fraction was taken as an average of at least 10 individual measurements in order to minimise the standard error. For lamellar samples, it is acknowledged that the value of microhardness measurements may vary significantly between the two phases. However, as at least 10 measurements were made, it is assumed that the final average of the measurements is a fair representation of the sample's microhardness.

2.5 Focused Ion Bean and Transmission Electron Microscopy

Transmission electron microscopy (TEM) is used to determine the crystallographic structures, composition and phase compositions of the materials fabricated in this work. TEM analysis provides a more detailed level of understanding of the samples than other techniques such as SEM. Namely, TEM technique requires thin specimens in order to probe internal structures, whereas SEM provides information about surface features. Nonetheless, both TEM and SEM use similar methods for beaming electrons, which involve condenser lenses and an electron gun within a vacuum system. As the electron beam passes through a thin specimen (prepared via Focused Ion Beam method, FIB), electrons are diffracted in different intensities allowing the microstructure to be characterised. As TEM requires samples of around 50 -100 nm thickness, FIB (FEI Helios G4 CX DualBeam) is used to prepare the TEM sample. The sample is Platinum coated prior to the use of FIB and thereafter, accelerated Gallium ions are used to section the region of interest in the sample. A sample carrier is then welded onto the sectioned sample in order to retrieve it whereby it is ready for TEM.

Not limited to high-resolution imaging, TEM also allows diffraction patterns to be obtained from a selected region – this is known as Selected Area Diffraction (SAD). In the case of crystalline materials (as with the work in this research), the SAD patterns comprise distinct spots from which lattice parameters can be calculated. The diffraction angle θ in TEM can be proved to be very small using Equations 2.7 to 2.11, showing that the electron beams from crystal planes are almost parallel to the electron beam from the source.

According to Bragg's law,

$$sin\theta = \frac{\lambda}{2d_{hkl}} \tag{2.7}$$

For small θ, $sin\theta \approx \theta$ and therefore,

$$\theta = \frac{\lambda}{2d_{hkl}} \tag{2.8}$$

Where θ is the diffraction angle, λ is the wavelength of the incident electron beam and d_{hkl} is the distance between successive planes.

λ can be deduced using Equation 2.9,

$$\lambda = \frac{h}{2meV(1 + \frac{eV}{2mc^2})} \tag{2.9}$$

Where h is Planck's constant, m is the mass of the electron, eV is the electron's charge and c is the speed of light.

Given that a FEI Titan3 Themis 300 operating at 300 kV was employed:

$$\lambda = \frac{h}{2meV(1 + \frac{eV}{2mc^2})} \tag{2.10}$$

Assuming a lattice d-spacing of 0.5 nm, θ can be deduced such that:

$$\theta = \frac{\lambda}{2d_{hkl}} = 0.13° \tag{2.11}$$

As the beam passes through a crystalline specimen, there will be a distance of 1/dhkl between these diffraction spots which in turn allows the phase to be identified as per Equations 2.12 and 2.13 (for a cubic system).

$$cos\theta = \frac{h_1h_2 + k_1k_2 + l_1l_2}{\sqrt{\left({h_1}^2 + {k_1}^2 + {l_1}^2\right)\left({h_2}^2 + {k_2}^2 + {l_2}^2\right)}} \tag{2.12}$$

$$\frac{1}{{d_{hkl}}^2} = \frac{h^2 + k^2 + l^2}{a^2} \tag{2.13}$$

2.6 Machine learning

2.6.1 Data compilation and curation

The data on phases and HR features of the alloys was collected using references [27,150,151]. These datasets were expanded on by adding the composition data for each alloy. As such, a column dedicated to each element present in the database was initiated, with cells pertaining to absent elements in any given HEA being populated with an arbitrary, small number (-0.05 chosen in this work). These cells were not populated with zeros in order to avoid large error gradients in the weight calculations. Figure 2.4 shows a 5-row print of the data including composition as part of the input features. Finally, the output prediction from each of the models is either a 1 or a 0. The data was arranged such that a "1" correlates to a solid-solution (SS) or a SS with intermetallic (SS+IM). This choice was made as many accepted HEAs have minor IM phases and the orthodox definition that a HEA must strictly comprise a single-phase SS is evolving. In turn, a "0" signals an amorphous (AM) structure, an IM or (AM + IM). Although data in references [27,150,151] contained binary alloys, these were omitted in this work. However, the final database contained ternary alloys as well as MPEAs. Omitting the binary alloys was done in order to avoid their presence in the testing sets, which would lead to inflated accuracies. On the other hand, ternary alloys were retained as they aid the NN in developing connections between certain elements, yet are not as predictable as binaries. The data was shuffled to avoid the formation of patterns and bias and finally, feature scaling was implemented such that each instant in the column of a given HR parameter was divided by the maximum value in the column (see Equation 2.14). Feature scaling was not applied to composition columns, as maintaining the sum of each row to be around 100 and maintaining the constant arbitrary value of -0.05 influences the NN performance.

$$x_{i,new} = \frac{x_i}{x_{max}} \tag{2.14}$$

Where x_i is instance number *i* in feature *x* and x_{max} is the largest value in feature *x*. $x_{i,new}$ is the updated value of x_i.

	Alloy	Z	dH	dS	VEC	Ed	SS/IM	Al	Ni	Co	Cr	Fe	Cu	Ti	...
0	Al0.5CoCrCuFeNiTi1.4	0.59	0.51	0.58	0.69	0.42	0	7.25	14.49	14.49	14.49	14.49	14.49	20.29	
1	AlCoCrCu0.5FeNi2	0.44	0.66	0.35	0.76	0.33	1	15.38	30.77	15.38	15.38	15.38	7.69	-0.05	
2	Cu0.5NiCoCrAl0.5Fe2	0.34	0.78	0.32	0.78	0.28	1	8.33	16.67	16.67	16.67	33.33	8.33	-0.05	
3	Al0.5CrCuFeMnNi	0.39	0.82	0.42	0.76	0.39	1	9.09	18.18	-0.05	18.18	18.18	18.18	-0.05	
4	WNbMoTaV	0.25	0.75	0.24	0.39	0.94	1	-0.05	-0.05	-0.05	-0.05	-0.05	-0.05	-0.05	

Figure 2.4 5-row print of the data set used in NN2. 'Z' denotes the difference in atomic radii and 'Ed' the difference in Pauling electronegativity. The SS/IM column indicates the HEA's phase, with 1 indicating (SS) or (SS+IM) and 0 indicating a (AM), (IM) or (AM+IM). Only 7 of the 37 elements present in the database are shown. A small arbitrary value (-0.05) was chosen to indicate the absence of an element.

2.6.2 Neural networks

The neural networks were constructed using the Keras API in the Google Collaboratory environment, with the Pandas library used to import the final data set of 391 alloys. A 70/30 split was used between the training and testing data respectively for each of the NNs. To assess the average prediction accuracies of the neural networks the data was shuffled and fed back to the models three times. Choosing the right hyperparameters for the neural networks is of vital importance in maximising their performance. NN1 (neural network including elemental composition data only) is the main focus of this work as it uses a dataset which, to the best of the authors' knowledge, has not been used to this scale before. The optimal hyperparameters for NN1 were found to be: learning rate = 0.3, batch size = 3, number of hidden layers = 9 and the maximum number of units in a hidden layer = 192. The input dimension for NN1 is 37, in accordance with the number of elements in the database, while the output layer comprises 1 unit. Each of the above parameters was chosen as the best value by iterating through a pre-defined range. For instance, in determining the best learning rate, a range of values from 0.1 to 1 were probed, with the value leading to best predictive accuracy being chosen.

The activation function chosen for the hidden layers was the Rectified Linear Unit (ReLU) activation function, as it yielded the best results when compared to other activation functions. The ReLU activation function maintains the value being passed to a unit in the hidden layer unless the value is negative, in which case the value is made equal to zero [154] (see Figure 2.5a). This simple calculation keeps its computational cost to a minimum making it a very frequently used function. For the output layer the logarithmic sigmoid (logsig) activation function was used as this generates outputs of either 0 or 1 (see Figure 2.5b). As the NN is classifying binary features, this is the optimal activation function for this purpose.

The sigmoid activation function is described as per Equation 2.15.

$$S(x) = \frac{1}{1 + e^{-x}} \tag{2.15}$$

Where *x* is any input value which is forced to a zero or one output denoted as *S(x)*.

To predict the phase of a previously uninvestigated HEA using the NNs designed in this work, the HEA's five features (ΔS_{mix}, ΔH_{mix}, VEC, δ and $\Delta\chi$) must first be calculated, allowing the HEA to be added to the database. The atomic percentages of the alloy's elements must also be calculated in a manner that is consistent with the database. Upon adding the HEA to the database, the cell indicating the HEA's phase can be randomly chosen (0 or 1), as this will not affect the NN's prediction. The HEA of unknown phase is then intentionally made to be the only alloy in the "testing set", as the rest of the alloys (all 391) in this case are used in the training set to enhance the NN's learning. In this work, this process was applied for the Al_xCuCrFeNi alloys, yielding predictions which were verified.

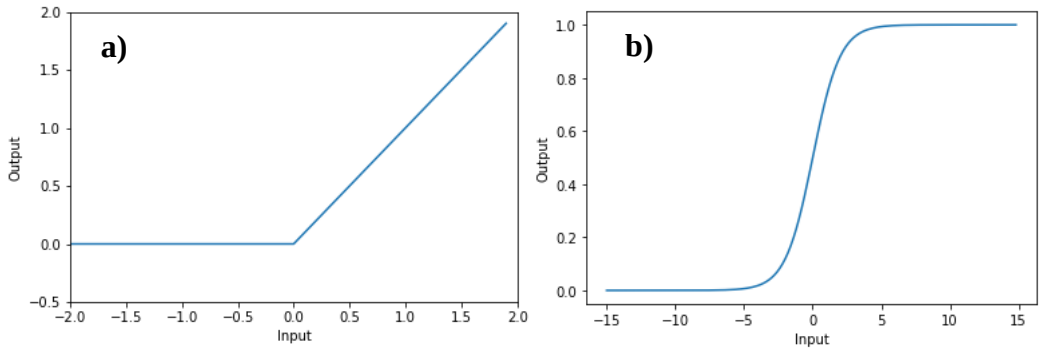

Figure 2.5a Rectified Linear Unit **Figure 2.5b** Sigmoid activation functions.

3. Experimental results

This chapter presents the bulk and powder HEAs fabricated throughout the course of this work. First, a neural network is presented which was developed for the discovery of new HEAs. To validate the neural networks, reference was made to the $Al_xCrCuFeNi$ alloy, to predict composition at which the system transitions towards a microstructure dominated with intermetallics. For each alloy, microstructural development with increased cooling rate is discussed. XRD, SEM and TEM are used as characterisation methods of the samples, while microhardness measurements are made to develop an idea for the evolution of the mechanical properties of the alloy with cooling rate. Finally, the eutectic HEA $AlCoCrFeNi_{2.1}$ is presented, followed by a more in-depth analysis of the equimolar AlCrCuFeNi HEA.

3.1 HEA screening using Machine Learning methods

3.1.1 Gradient descent with multi-variate linear regression

To predict novel HEA compositions, this work begins with multivariate linear regression implemented with the gradient descent algorithm (LRGD). The LRGD model is designed to set an initial standard upon which the neural networks developed later in this work will be measured. The inputs to the LRGD model are entropy of mixing, enthalpy of mixing, valence electron concentration, atomic radius difference and Pauling electronegativity difference (ΔS_{mix}, ΔH_{mix}, VEC, δ and $\Delta\chi$ respectively). Using these input features, the LRGD model was applied using standard gradient descent equations, shown as Equations 3.1 – 3.3 below [155]. The database used for this work is presented in Appendix 1.

$$h_\theta(x) = \boldsymbol{\theta}^T \boldsymbol{x} \tag{3.1}$$

$$J(\theta_j) = \frac{1}{2m}\sum_{i=1}^{m}(h_\theta(x^i) - y^i)^2 \tag{3.2}$$

$$\theta_j := \theta_j - \alpha\frac{\partial}{\partial\theta_j}J(\theta_j) \tag{3.3}$$

Where $h_\theta(x)$ is a hypothesis created to best fit the data and $\boldsymbol{\theta}$ is an (n+1) dimensional vector containing the correlation coefficients (where n is the number of input features). $\boldsymbol{x}$ is an (n+1 by m) array which is a concatenation of all the input features and a dimensional vector of ones. m is the number of instances in the database and $J(\theta_j)$ is the cost function quantifying the error in each coefficient resulting from the generated hypothesis. i denotes the number of the instance and y denotes the output feature (1 or 0), where 1 is a SS/SS+IM structure and 0 is a IM/AM structure. Finally, j is the subscript denoting the coefficient in the $\boldsymbol{\theta}$ vector and α is the learning rate.

To begin the iterations for the LRGD algorithm an initial $\boldsymbol{\theta}$ vector of zeros was chosen. The $\boldsymbol{\theta}$ values then converge towards the correlation coefficients which lead to minimum error. The learning rate, α, was varied using a 'for loop' until an optimal value was found (i.e. a value which reaches minimum cost in shortest number of epochs). The optimal value for learning rate for the explored range between 0.1 and 1 was found to be 0.3. After minimum cost is reached, $\boldsymbol{\theta}^T$ is multiplied with $\boldsymbol{x}$ (vector containing features of a given instance) to form a linear equation which best fits the data.

To confirm the results of the LRGD model, a matrix method was also used to deduce the regression coefficients. The method used is outlined by Scott H. Brown [156] and is applied as shown in Equation 3.4. This method is useful in that it does not use an iterative process in order to deduce the optimal regression coefficients. As such, Equation 3.4 allows the reduction of lowering computational cost. Furthermore, this method obtains results which are independent of learning rate.

$$\boldsymbol{\theta} = (\boldsymbol{x}^T\boldsymbol{x})^{-1}\boldsymbol{x}^T\boldsymbol{y} \tag{3.4}$$

Where $\boldsymbol{\theta}$ is the vector of correlation coefficients, $\boldsymbol{x}$ is the array containing the standard features of the HEAs and $\boldsymbol{y}$ is the vector containing phase data (0 or 1).

Testing the LRGD model's predictive performance in the testing set (set of data it has not seen before) yielded an average accuracy of 73%. As such, a NN is expected to yield results with accuracies higher than 73% to be deemed successful. Figure 3.1a shows the drop in cost, $J(\boldsymbol{\theta})$, as the number of epochs increases. Despite the LRGD model finding the optimal set of correlation coefficients, it is fully expected that the model would mispredict a group of data entries which have unique features not expressed sufficiently in the data set. This is a clear limitation of the LRGD model as with other models which base their predictions on individual HEA features.

In attempt to probe the maximum possible accuracy of the LRGD model, Equation 3.4 was used to find an optimal set of correlation coefficients prior to running the LRGD model. This set of coefficients was then used in the LRGD model as the starting point of the algorithm (i.e. the iterations begin at a point where calculated cost is already close to a minimum). The effect of this can be seen in Figure 3.1b, where the cost at zero epochs is already 0.148. This is then exploited by running the LRGD model to a point of diminishing returns. Combining the matrix method in Equation 3.4 with the LRGD algorithm achieves a 2% increase in the accuracy of the LRGD model, raising its overall accuracy to 75%.

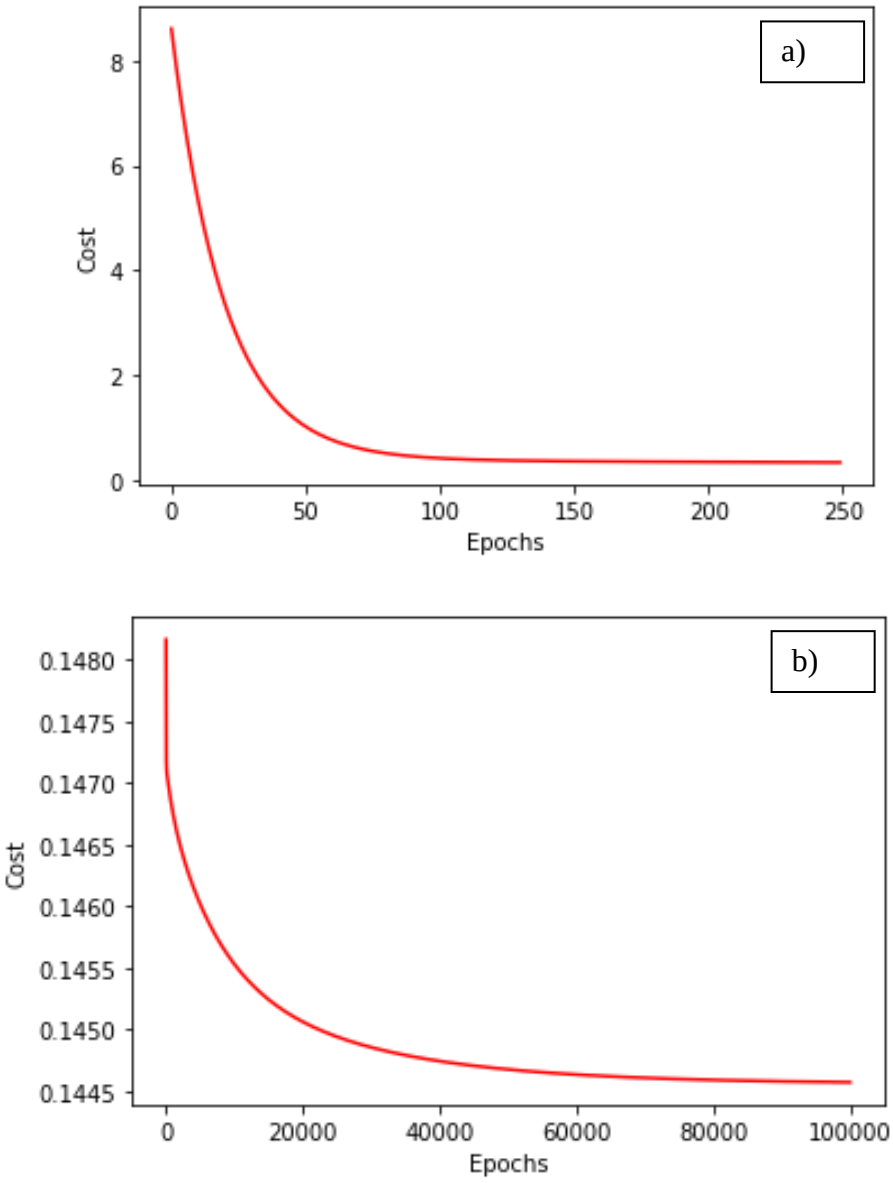

Figure 3.1a Cost vs Epochs for LRGD model with random initiation point **Figure 3.1b** iteration starting point obtained using the matrix method from Equation 23.

3.1.2 Neural networks

Two neural networks are designed in this work, each with different input features. The first neural network (NN1) receives solely composition data (atomic percentages) as inputs. The second neural network (NN2) receives the five input features used for the LRGD model (ΔS_{mix}, ΔH_{mix}, VEC, δ and $\Delta\chi$) in addition to the composition data which NN1 receives. NN1 is designed with the motive that composition is essentially the only information which is known with high accuracy about an HEA, whereas all other possible input features (whether Hume-Rothery or thermodynamic) involve many estimates and calculations of averages. Figure 3.2a and 3.2b show schematics of the architectures used for NN1 and NN2, respectively.

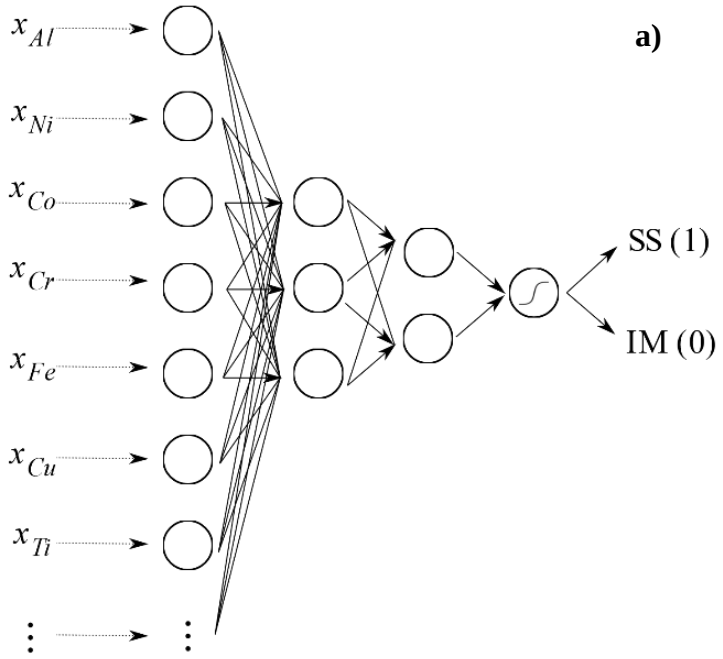

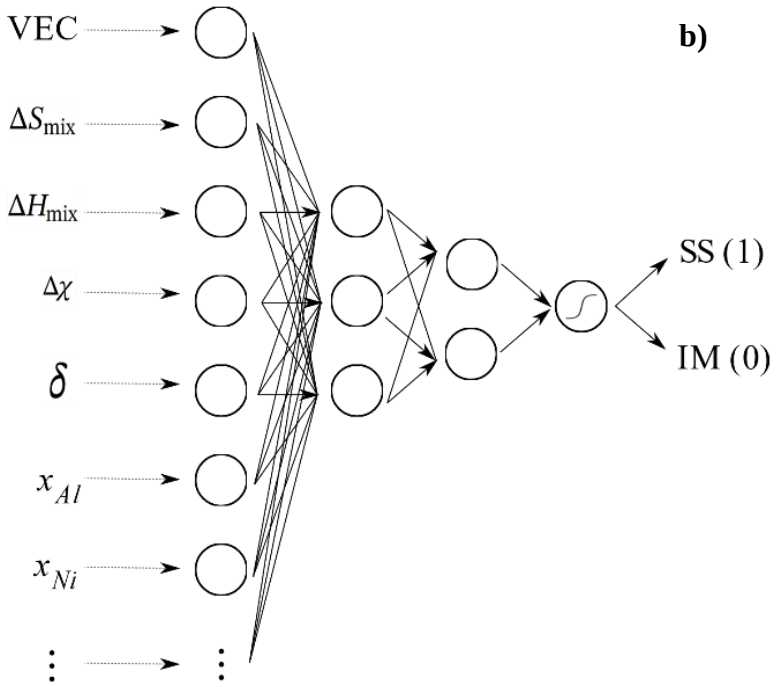

Figure 3.2a Schematics of NN1 and **Figure 3.2b** NN2 architectures. Number of hidden layers and number of units per layer shown are not representative of the true models but help in visualising the networks. The output layer in both architectures is shown as a Sigmoid activation function with binary output.

To assess the neural networks, the original dataset was shuffled and fed to the NNs three times. This ensures that alloy systems which are easier to predict do not inflate the accuracy by consistently appearing in the testing set. Such systems may be tertiary alloys or HEAs which share the same base of elements and differ only slightly in composition. Figure 3.3 and Figure 3.4 show the accuracy and loss plots of NN1 and NN2, respectively, for three different runs between which the data was shuffled. It is important to ensure that the NN's performance is not affected by data shuffling as this confirms that its results are reproducible with other data sets and that its predictions are scalable as the dataset grows. The accuracy the NN achieves in the test set is recorded after each run, with the average accuracy of three runs taken to be the representative value of the NN's accuracy. A NN's accuracy in the test set is calculated by finding the number of correctly predicted instances as a percentage of the total number of instances in the training set.

For predictions on the testing set, NN1 and NN2 achieved average accuracies of 92% and 90%, respectively. To the best of the author's knowledge, the only model exceeding the performance of NN1 was implemented by Lee et al. [145], which achieved a testing accuracy of 93%. Considering that Lee's model uses 13 Hume-Rothery predictive features, NN1 appears to retain the aforementioned advantage of simplicity and scalability. Other notable attempts are those of Huang et al. [143] and Zhang et al. [140] which achieve predictive accuracies of 89% and 91%, respectively. These works also depend heavily on HR data and use between 4 and 20 features in their databases. That NN1 achieves a testing accuracy of 92% has significant implications, as it shows that the

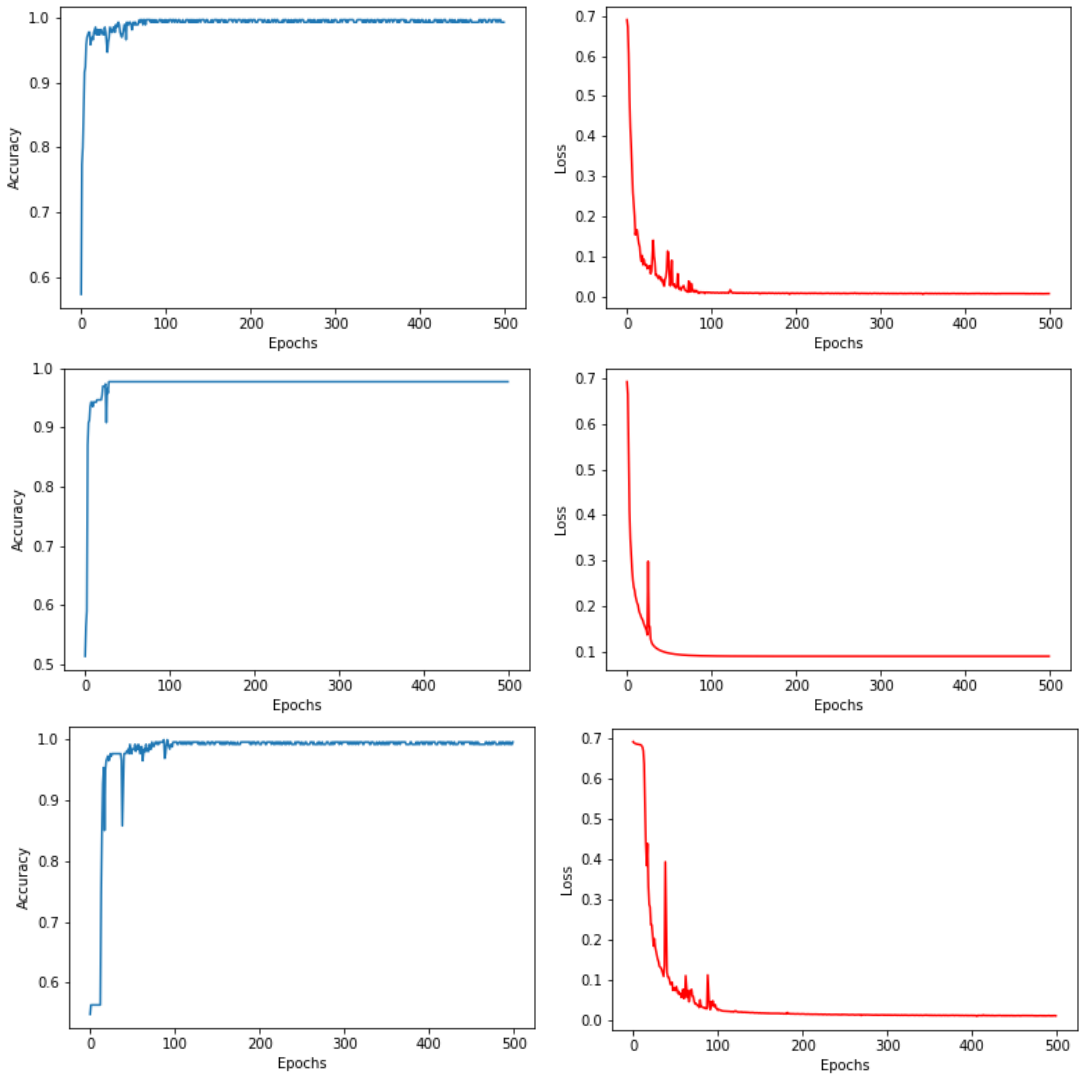

Figure 3.3 Training loss and accuracy for NN1. Between each set of plots, the data is shuffled and 70% of the data is taken for training.

complete abandonment of predictive parameters is not only possible but also advantageous. This result is in some way expected, since atomic percentage data does not require estimations to be made (unlike thermodynamic and HR features), hence leading to datasets that are more consistent and less prone to errors. Although vast efforts have been expended on modifying thermodynamic and HR parameters to capture finer phenomenological details [157–160], the saturation in the number of parameters is rather evident and the leaner approach used by NN1 provides a method with a high potential to scaled for use by the average researcher.

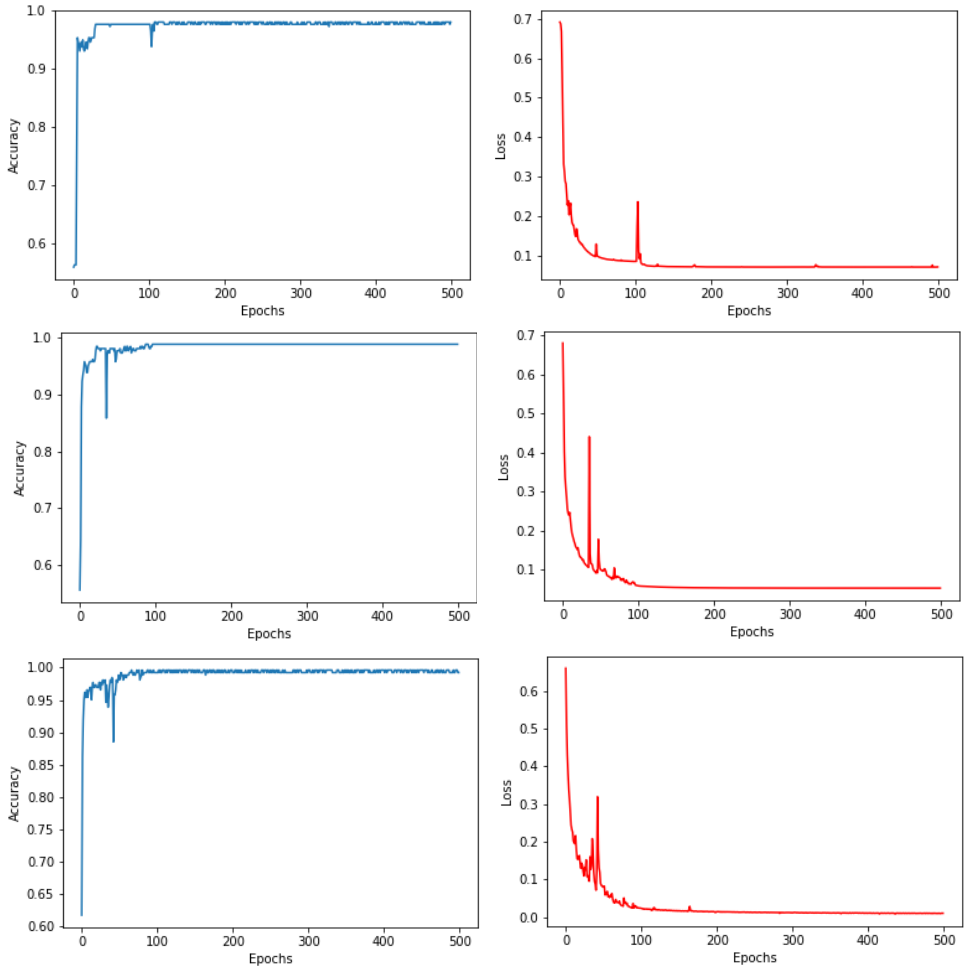

Figure 3.4 Training loss and accuracy for NN2. Between each set of plots, the data is shuffled and 70% of the data is taken for training.

3.1.3 Validation

For validation, NN1 and NN2 are used to predict the solid-solution (SS) limit in $Al_xCuCrFeNi$, beyond which x (atomic percentage of Al) leads to a microstructure occupied by intermetallics. According to the outcome from both NN1 and NN2, $x = 1.4$ is the composition at which the output changes from "1" (SS/SS+IM) to "0" (IM) as x increases. As such, the compositions directly above and below this point were chosen to be manufactured ($x = 1.3$ and $x = 1.5$), as well as compositions further away from this critical point ($x = 1.0$ and $x = 2.0$) in order to confirm the observations. The $x = 1.0$ and $x = 1.3$ compositions corresponded to "1" in binary, whereas the $x = 1.5$ and $x = 2.0$ compositions corresponded to "0" in binary. It is important to distinguish that "1" in binary indicates SS or (SS+IM) structures, and "0" in binary indicates amorphous (AM), IM or (AM +IM) structures. This is since MPEAs comprising (SS/SS+IM) structures have been encoded as "1" entries in the datasets and all other entries have been encoded as "0" entries.

Figure 3.5 shows the XRD traces of the four alloys, where the FCC peak is clearly visible in the $x = 1.0$ alloy, but decreases in intensity in the $x = 1.3$ alloy and is no longer present in $x = 1.5$ and $x = 2.0$. Evidently, the BCC becomes more dominant as Al content is increased, this is a common observation and has been reported in $Al_xCrCoFeNi$ [13], $Al_xCrCoCuFeNi$ [161] and $Al_xCrFeNi$ [162]. The microstructure of the $x = 1.0$ alloy can be seen in Figure 3.6a, where a predominantly dendritic structure is evident. A minor phase is present in the matrix which is more visible at the higher magnification shown in Figure 3.6b. This IM has been previously characterised as $AlNi_{0.77}Fe_{0.23}$ with a volume fraction reported to be 18% (obtained via XRD peak intensity analysis) [163]. Although this IM has been reported with specific atomic fractions for Al and Ni, it is more likely that this IM is $AlNixFe_{1-x}$ where Fe can randomly substitute for Ni at different levels. The $x = 1.3$ alloy displays a very similar morphology to the $x = 1.0$ composition (see Figure 3.7a), where the needle-like intermetallic remains within the dendrites' vicinity but extends further outwards than what is observed in the $x = 1.0$ microstructure (see Figure 3.7b).

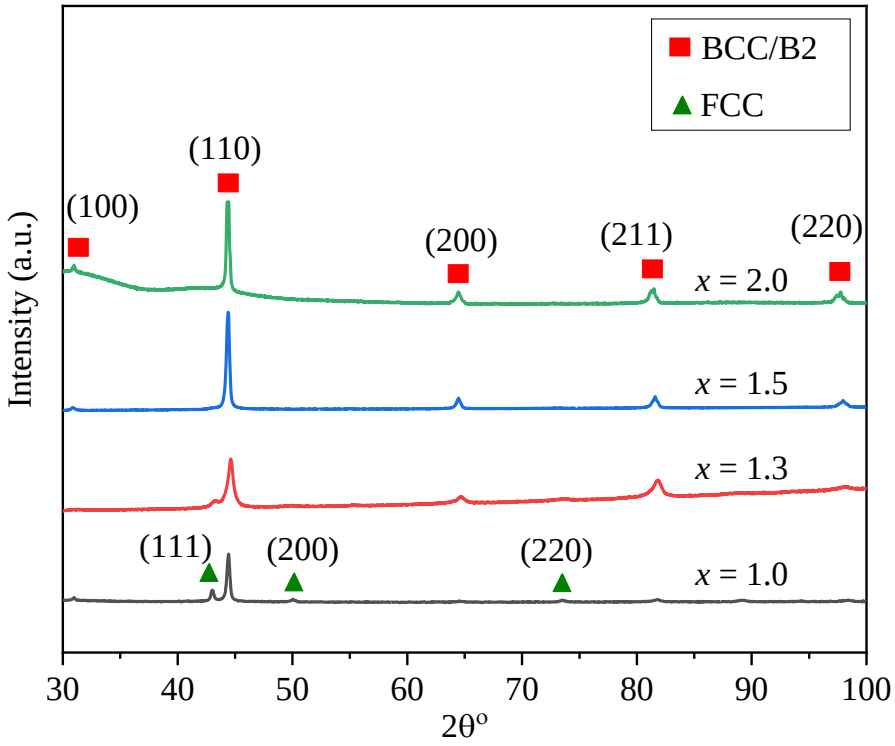

Figure 3.5 XRD scans of $x = 1.0$, $x = 1.3$, $x = 1.5$ and $x = 2.0$ alloys in the $Al_xCuCrFeNi$ system.

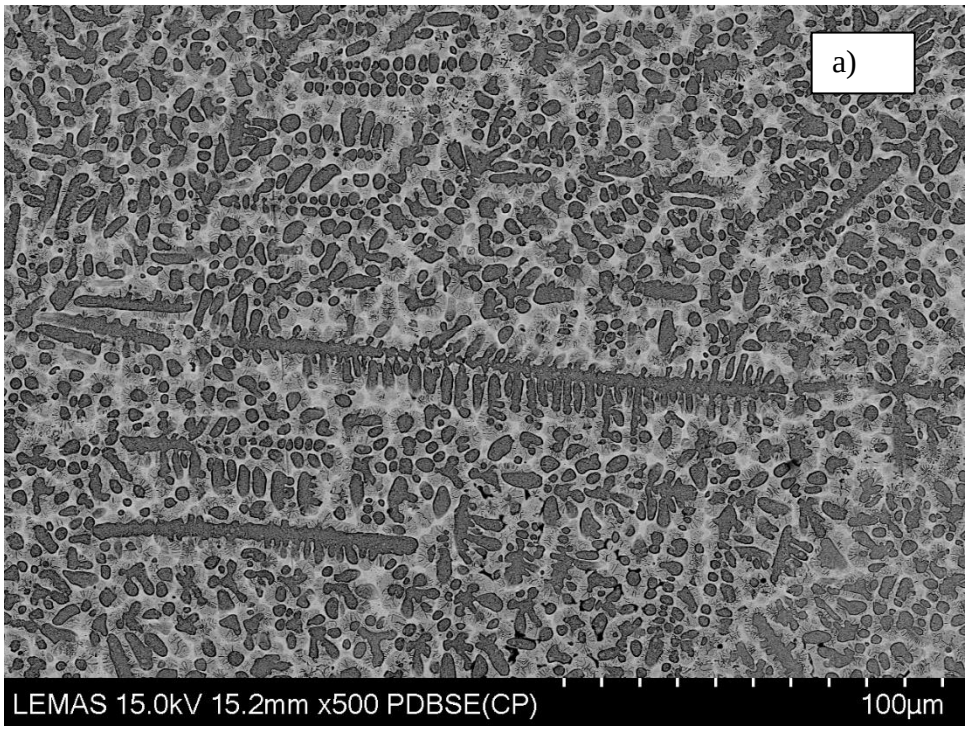

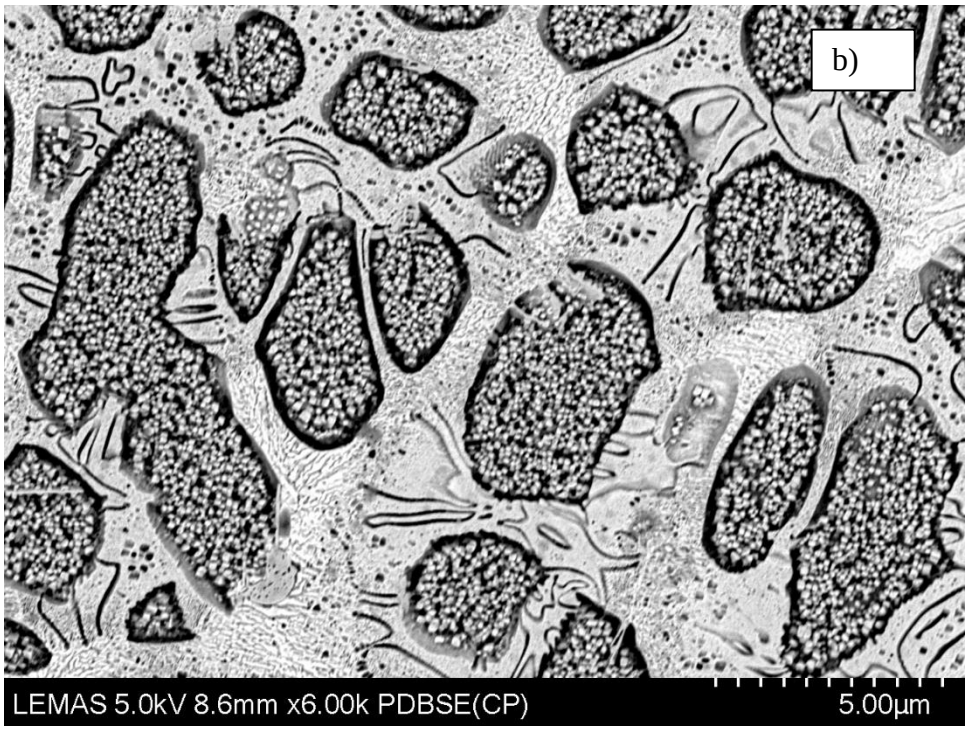

Figure 3.6a Micrograph of $Al_{1.0}CrCuFeNi$ showing dendritic structure **Figure 3.6b** Appearance of needle-like IM only observable at higher magnifications.

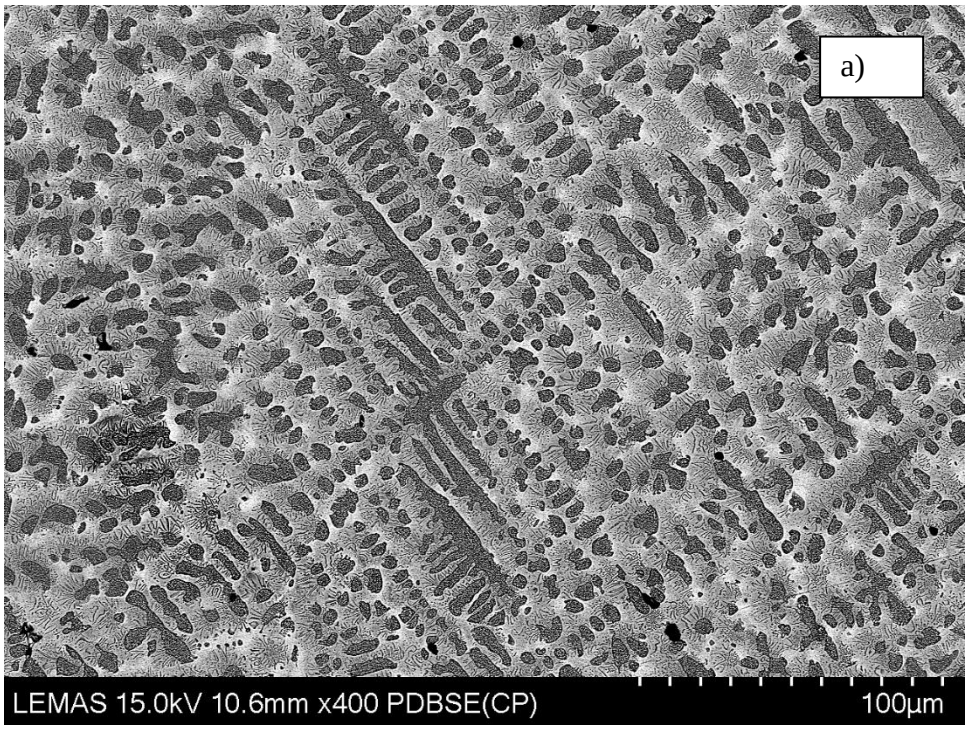

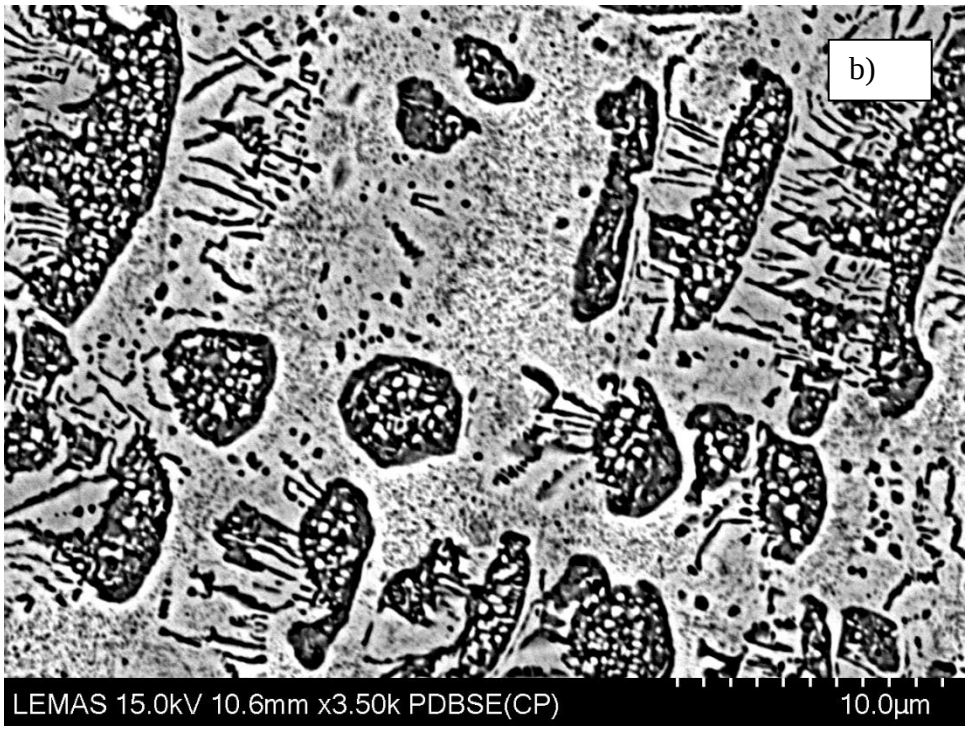

Figure 3.7a Micrograph of $Al_{1.3}CrCuFeNi$ showing dendritic structure **Figure 3.7b** higher magnification micrograph of $Al_{1.3}CrCuFeNi$, showing increased presence of IM phase relative to the $x = 1.0$ composition

The $x = 1.5$ alloy was found to comprise two unique features in its microstructure (both which confirm its classification as an alloy with dominant IM phases). Unlike the $x = 1.0$ and $x = 1.3$ alloys, the IM phase here does not adhere to the local vicinity of the dendrites, as seen in Figure 3.8. One of the unique features in this alloy (shown in Figures 3.9a and 3.9b) is the morphology of the IM phase forming a structure commonly referred to as "Chinese script" [164,165]. Rather, the IM phase forms a Chinese script structure extending into the matrix. The second feature in this alloy (seen in Figures 3.10a and 3.10b) has been observed previously in $Al_2CrCuFeNi_2$, where it is referred to as a "sunflower" structure [106]. In this work, Guo et al. classify the petals of the sunflower structure to be a eutectic of a Ni-Al-rich B2 phase and a Cr-rich BCC phase. The internal section of the structure is considered to be where the primary B2 phase originates from and within this region, fine BCC precipitates form as a result of spinodal decomposition. Finally, the needle-like IM observed in the $x = 1.0$ and $x = 1.3$ compositions is still present at the vicinity of the dendrites.

The $Al_2CrCuFeNi$ alloy has a brittle nature that is notably reflected in its mechanical behavior. Figure 3.11a shows a visible collection of micro-cracks in the surface morphology of the alloy. It is important to note that the cracks shown were not intentionally induced via mechanical operations, but rather as a result of handling of the alloy in standard processes such as mounting, cutting etc. Such cracks further confirm that the prediction made by the models is correct and that the $Al_2CuCrFeNi$ alloy comprises excessive dominance of IM phases in its microstructure. Figure 3.11b shows an SEM micrograph of $Al_2CuCrFeNi$, outlining the presence of coarse spherical precipitates in the interdendritic region, together with much finer spherical and needle shaped precipitates decorating the dendrite boundaries. Although the exact structures of the observed IM phases have not been identified, the study of their morphologies is not the primary objective of this work – the focus within is to confirm the application of the presented rapid-screening method. However, the extremely brittle nature of the alloy indicates that these dominant IM phases are A2/B2 precipitates, as these phases take away from the alloy's ductility and have been shown to grow with increasing aluminium content in alloys such as $Al_xCoCrFeMnNi$ [100].

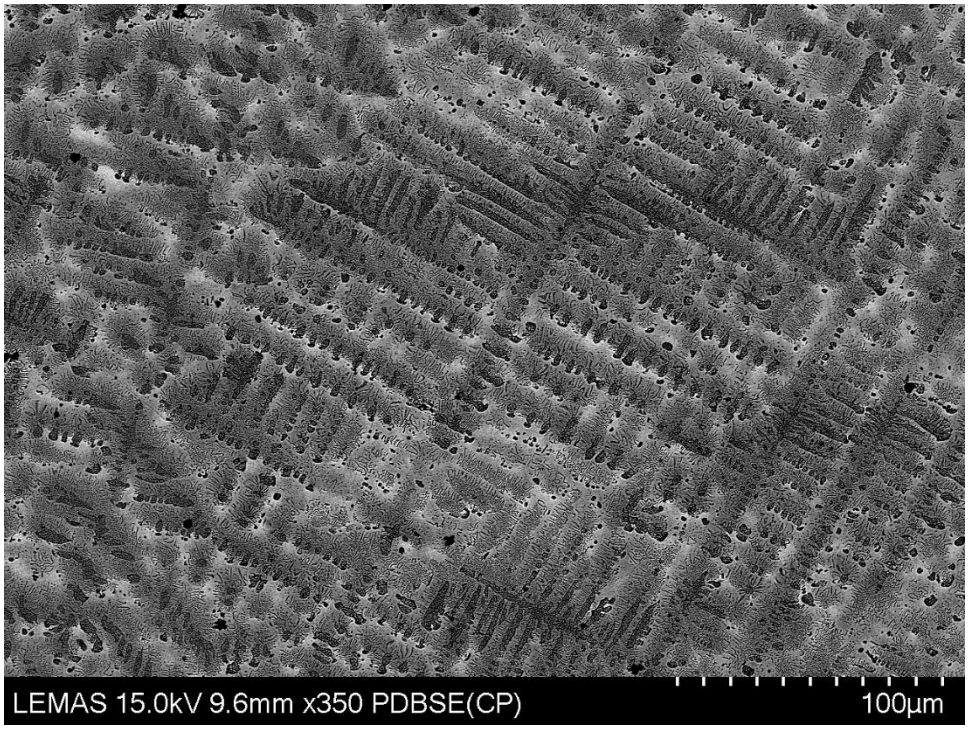

Figure 3.8 Micrograph of $Al_{1.5}CrCuFeNi$ showing increased presence of IM in the ID matrix.

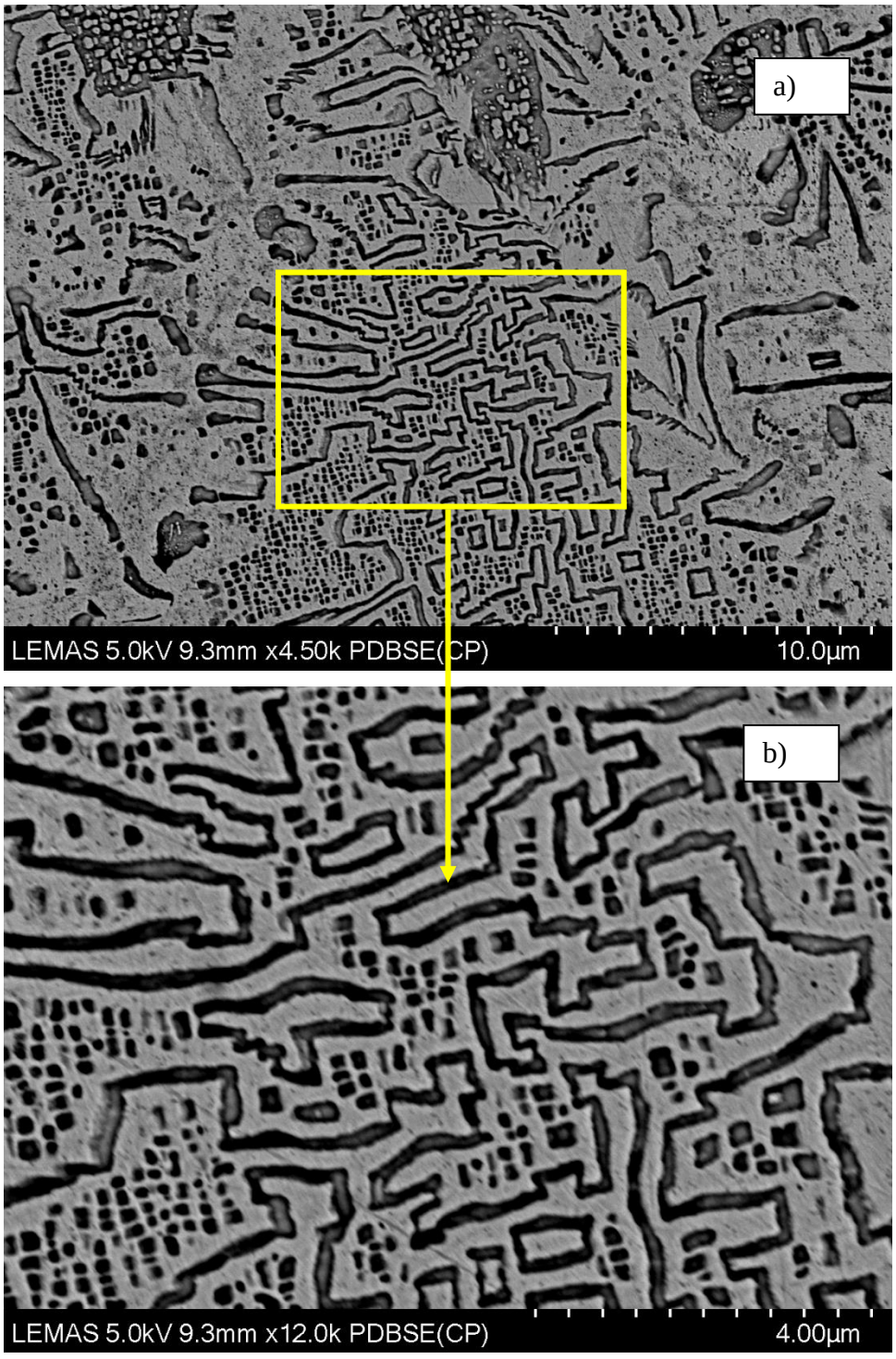

Figure 3.9a Micrograph of $Al_{1.5}CrCuFeNi$ showing "Chinese script" IM structure in the ID matrix at low magnification **Figure 3.9b** Higher magnification of the Chinese Script structure in $Al_{1.5}CrCuFeNi$.

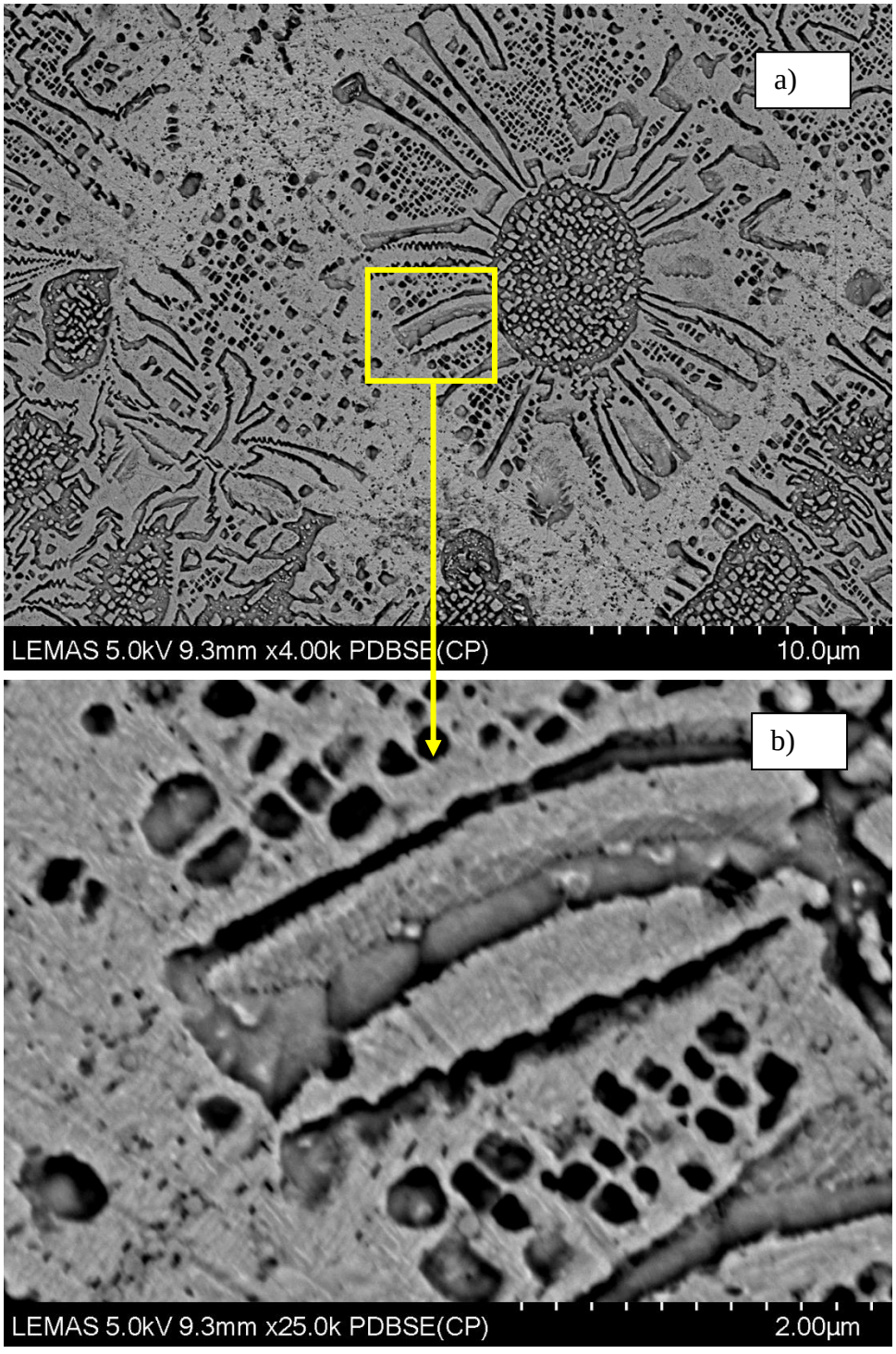

Figure 3.10a "Sunflower" structure in $Al_{1.5}CrCuFeNi$ showing matrix dominated by intermetallics **Figure 3.10b** Higher magnification focusing on lamellar region.

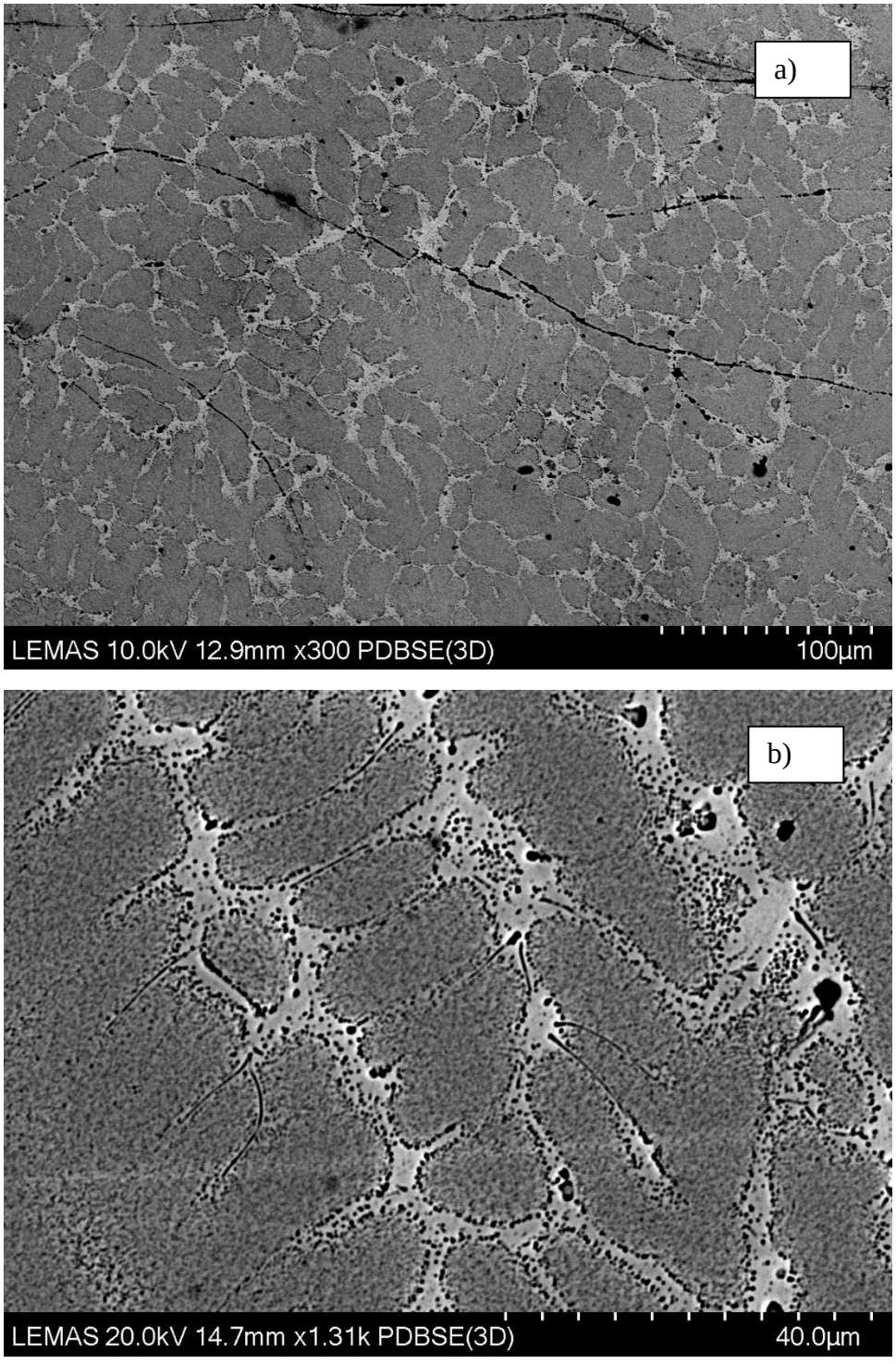

Figure 3.11a Micro-cracks in microstructure of $Al_{2.0}CrCuFeNi$ outlining the brittle nature of the alloy **Figure 3.11b** Overall microstructure of $Al_{2.0}CrCuFeNi$ showing coarse sphere-like and needle intermetallics in its matrix.

3.1.4 Discussion

Although the LRGD model yielded modest accuracies relative to contemporary attempts found in literature, its main objective was mostly to set a standard to which the neural networks would be compared. Combined with Equation 23, the LRGD model proves that a 75% prediction accuracy can be achieved largely due to the similar entries in the database, which vary only slightly by component or atomic fraction. Knowing that the neural networks are expected to achieve more than 75% accuracy, the neural networks NN1 and NN2 were designed to predict HEA phases, achieving average prediction accuracies of 92% and 90%, respectively.

As far as the author is aware, the predictive accuracy of NN1 is only 1% less than the highest accuracy achieved by researchers to date. The fact that NN1 performs with such accuracy has significant implications, as it shows that the elimination of HR features from the database (and relying solely on atomic percentage data) is not only possible but also advantageous. This result is in some way expected, since atomic percentage data does not require estimations to be made (unlike thermodynamic and HR features), leading to datasets that are more consistent and less prone to errors. Given today's debate on the most effective HR features for HEA prediction and the saturation in the number of predictive parameters, a lean and accurate approach such as that of NN1 is useful in achieving models that are scalable for rapid use by researchers.

NN1 and NN2 were used to predict the HEA composition window in the $Al_xCuCrFeNi$ system, yielding a prediction that at $x = 1.4$ the system transitions from a SS/SS+IM to an IM/AM. Therefore, the $x = 1.0$, $x = 1.3$, $x = 1.5$ and $x = 2.0$ compsotions were manufactured to confirm the predictions. The $x = 1.0$ and $x = 1.3$ compositions were confirmed to comprise SS+IM microstructures, with a needle-like IM phase adhering to the vicinity of the dendrites. Observing the fine (nano-scale) precipitates within the dendrites of both alloys, it is likely that they have formed via spinodal decomposition. Comparing these microstructures with some of the single-phase solid-solution HEAs (e.g. Cantor alloy – CoCrFeMnNi), it can be argued that they display overly complex morphologies to be classified as HEAs. However, many multi-phase alloys have been reported over the last decade that have been widely accepted as HEAs [166–168], as long

as the behavior of the MPEA is consistent with HEA properties. Since such MPEAs have been classified as HEAs comprising (SS+IM) structures and encoded as "1" entries in the datasets, it is fully expected that the x = 1.0 and x = 1.3 compositions be predicted accordingly.

The x = 1.5 system showed a significantly more complex microstructure, in which a "Chinese script" IM was observed in the ID region. Visibly, this structure is an extension of the 'needles' seen in the x = 1.0 and x = 1.3 alloys. It may therefore be deduced that increasing Al content promotes the growth of this needle-like structure. A sunflower structure is also observed in the x = 1.5 system, comprising a petal-like arrangement which surrounds nano-scale preciptates that appear to have formed via spinodal decomposition. The sunflower structure in this alloy (see Figure 3.10) has been observed previously in $Al_2CrCuFeNi_2$ [106]. In this work, Guo et al. classify the petals of the structure to be a eutectic of a Ni-Al-rich B2 phase and a Cr-rich BCC phase. The internal section of the structure is considered to be where the primary B2 phase originates from and within this region, fine BCC precipitates form as a result of spinodal decomposition. Despite half the Ni content, the sunflower structure in $Al_2CrCuFeNi$ is shown in our work to contain the same phases and morphology. Although spinodally-decomposed precipitates within the dendrites have been observed in $Al_{1.5}CrCuFeNi$, these precipitates were also observed in the x = 1.0 and x = 1.3 alloys. As such, the main points which distinguish the x = 1.5 system seem to be the stark presence of intermetallics in the ID region. Nevertheless, the prediction of the neural networks is justified upon observing the complexity of the x = 1.5 micrographs relative to those of x = 1.0 and x = 1.3.

Finally, the x = 2 composition yields an alloy that is very brittle in nature and a microstructure showing the presence of coarse, spherical IM precipitates in the interdendritic region. Further, much finer spherical and needle shaped precipitates decorating the dendrite boundaries. Indeed, this alloy was manufactured to confirm IM saturation as x is increased, and this is observed not only in the micrographs of $Al_2CrCuFeNi$, but also in its mechanical behavior.

Based on the outcomes of this section, the $x = 1.0$ composition is chosen for further study. Particularly due to the limited presence of IM phases in $Al_{1.0}CuCrFeNi$, this alloy was chosen for drop-tube-processing to explore the possibility of completely suppressing IM growth via rapid cooling. As such, this section inspires not only the discovery of SS HEAs, but also HEA compositions that are in the 'grey area' that is SS+IM. In that regard, the latter need not be disregarded completely and can be considered for RSP in order to reach simple solid solution HEAs.

3.2 Rapid solidification of AlCrCuFeNi

3.2.1 Microstructure development

This section focuses in more depth on the as-cast, equimolar AlCrCuFeNi system presented in section 3.1. In section 3.1, needle-like intermetallics were observed in the ID region of equimolar AlCrCuFeNi and faceted precipitates were observed within the dendrites. In order to explore the possibility of inhibiting these features using RSP, AlCrCuFeNi is processed using a drop-tube facility, yielding powders with cooling rates from 112 K/s up to 1.13×10^6 K/s. To aid in correlating the powders presented in this work to their respective cooling rates, Figure 3.12 relates droplet size with cooling rate.

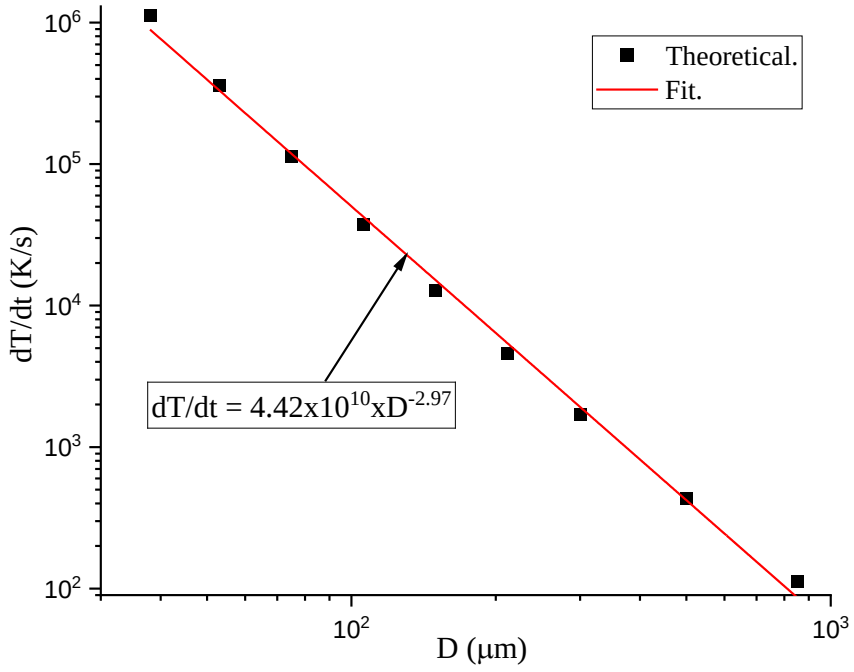

Figure 3.12 Estimated cooling rates of AlCrCuFeNi powders versus mean powder diameter.

The XRD traces of as-cast AlCrCuFeNi and AlCrCuFeNi powders are shown in Figure 3.13, where it can be observed that the FCC peaks seen in the as-cast alloy decrease in intensity and become unobservable in the 38 – 53 μm size fraction. The XRD trace of the 38 – 53 μm droplets therefore suggests a single-phase structure, whereas the traces from 500 – 850 μm down to the 53 – 75 μm size-fraction show that the FCC is not inhibited, though it is heavily restricted. Figure 3.14 shows the SEM backscattered electron image of the as-cast AlCrCuFeNi alloy, where its microstructure is seen to have a dendritic structure that possesses four distinct parts: the dendritic region, precipitates within the dendrites, a needle-like intermetallic (IM) seen along the periphery of the dendrites and deeper within the ID region, and finally, the inter-dendritic (ID) matrix. These are labelled as 1-4 in Figure 3.14 in their respective order.

Although AlCrCuFeNi was also highlighted in section 3.1.3, in this section it is important to revisit its microstructure in order to track its morphology as cooling rate increases. Figure 3.14 also shows that the IM in the ID matrix appears in a spherical form as well as sharp needles of varying complexity. Within the dendrites, precipitates (labelled as 1) appear to be evenly distributed and consistent in size, which appears to be of the nano-scale. An EDS analysis presented in Table 3.1 shows the Cu content in the ID regions of the as-cast alloy to be dominant and particularly higher than the content of Cr and Fe. Note that this does not include EDS data of the IM, as its size makes it difficult to probe using SEM-EDS technique. Considering the relatively large, positive enthalpies of mixing between Cu and each of Cr and Fe (12 kJ mol^{-1} and 13 kJ mol^{-1} respectively) [168], Cu solidification partitioning is expected. This small bonding energy of Cu with Cr and Fe leads to separation in the ID region which, as seen from Table 3.1, leads to an atomic percentage of Cu in the ID region of near 50%. Cu segregation, particularly in a plate-like manner, has previously been observed in several HEAs comprising similar principal elements, such as $Al_{0.5}CrCuFeNi_2$ [169] and $Al_2CoCrCuFeNi$ [100] AlCoCrCuFeNi [170].

Although Al and Ni contribute to the ID region, they also form a significant part of the dendritic region, where they are not expected to form a fully homoegenous structure with Cr and Fe due to the precipitates observed. It is also worth noting the small size of the dendrite fragments seen in Figure 3.14 given the low cooling rate of the as-cast sample

(circa 20 K/s). This is largely due to dendrite fragmentation which is characteristic to this alloy and the aformentioned alloys of a similar base.

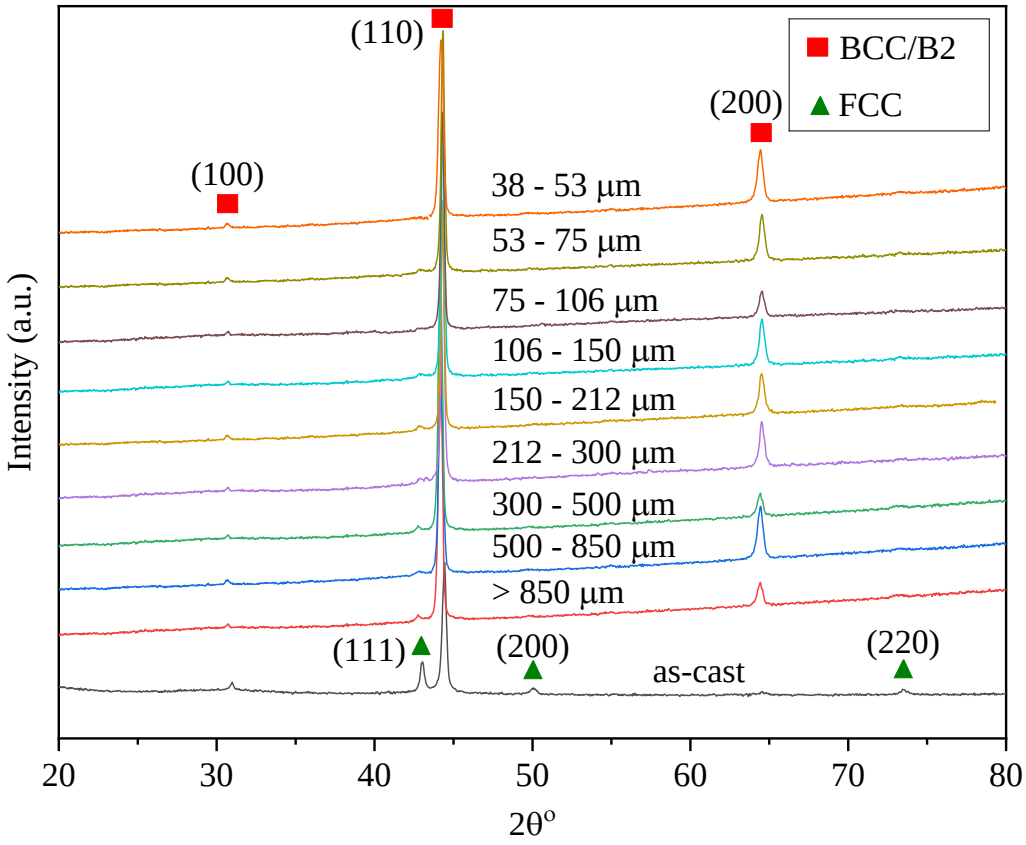

Figure 3.13 XRD patterns of AlCrCuFeNi as-cast alloy and powders.

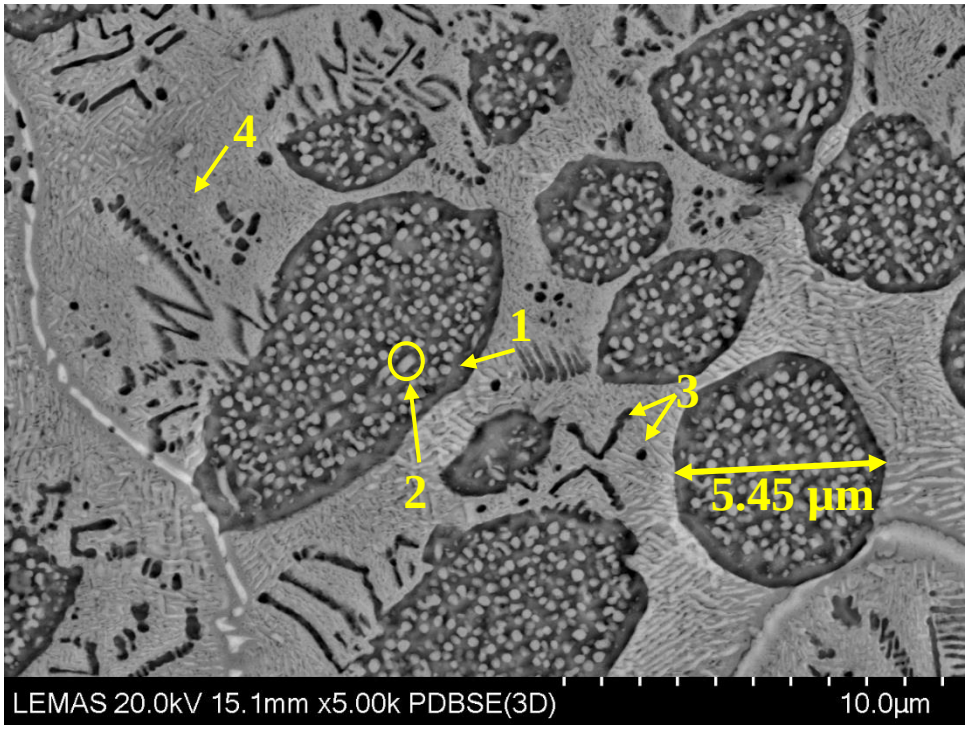

Figure 3.14 Backscatter SEM image of as-cast equimolar AlCrCuFeNi microstructure.

Table 3.1. Elemental analysis of as-cast AlCrCuFeNi master alloy.

Region	Element (at%)				
	Al	Cr	Cu	Fe	Ni
D	12.53	31.00	8.89	30.07	17.51
ID	20.62	3.38	47.28	6.52	21.75

The microstructure of an AlCrCuFeNi droplet from the d > 850 µm size fraction (cooled at an estimated 112 K/s) is presented in Figure 3.15, showing its strong similarity to the as-cast sample. Although the microstructure of the *d* > 850 µm is finer, it is evident that this cooling rate is not high enough to suppress the growth of the needle-like structure and the precipitates within the dendrites. Figure 3.16 presents a higher magnification backscatter image of a *d* > 850 µm particle, showing that the individual precipitates are finer and hence their number density greater than that observed in the as-cast alloy. It is also noticeable that the intermetallics in this particle are more reminiscent of a ribbon-like structure (rather than needle-like) as they typically display a curvature as opposed to the sharp edges seen in the as-cast microstructre. Generally, Figure 3.15 and Figure 3.16 make it clear that particles cooled at 112 K/s have equally complex micrstructures as the as-cast alloy, and that higher cooling rates are required to achieve a simple solid-solution.

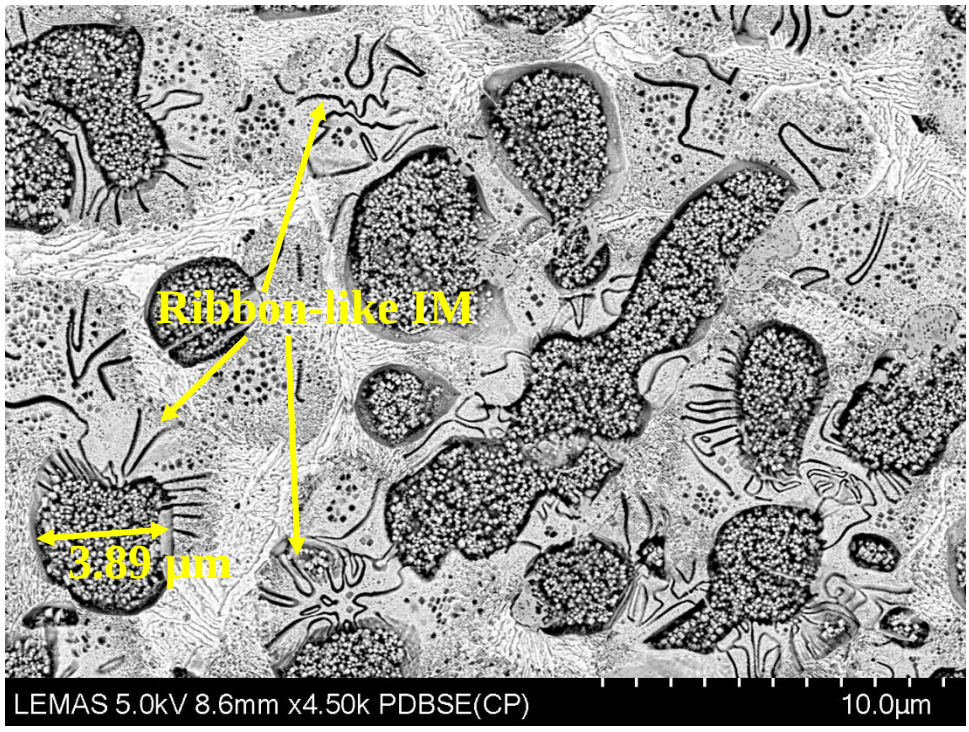

Figure 3.15 Microstructure of AlCrCuFeNi powder cooled at an estimated 112 K/s (*d* > 850 μm).

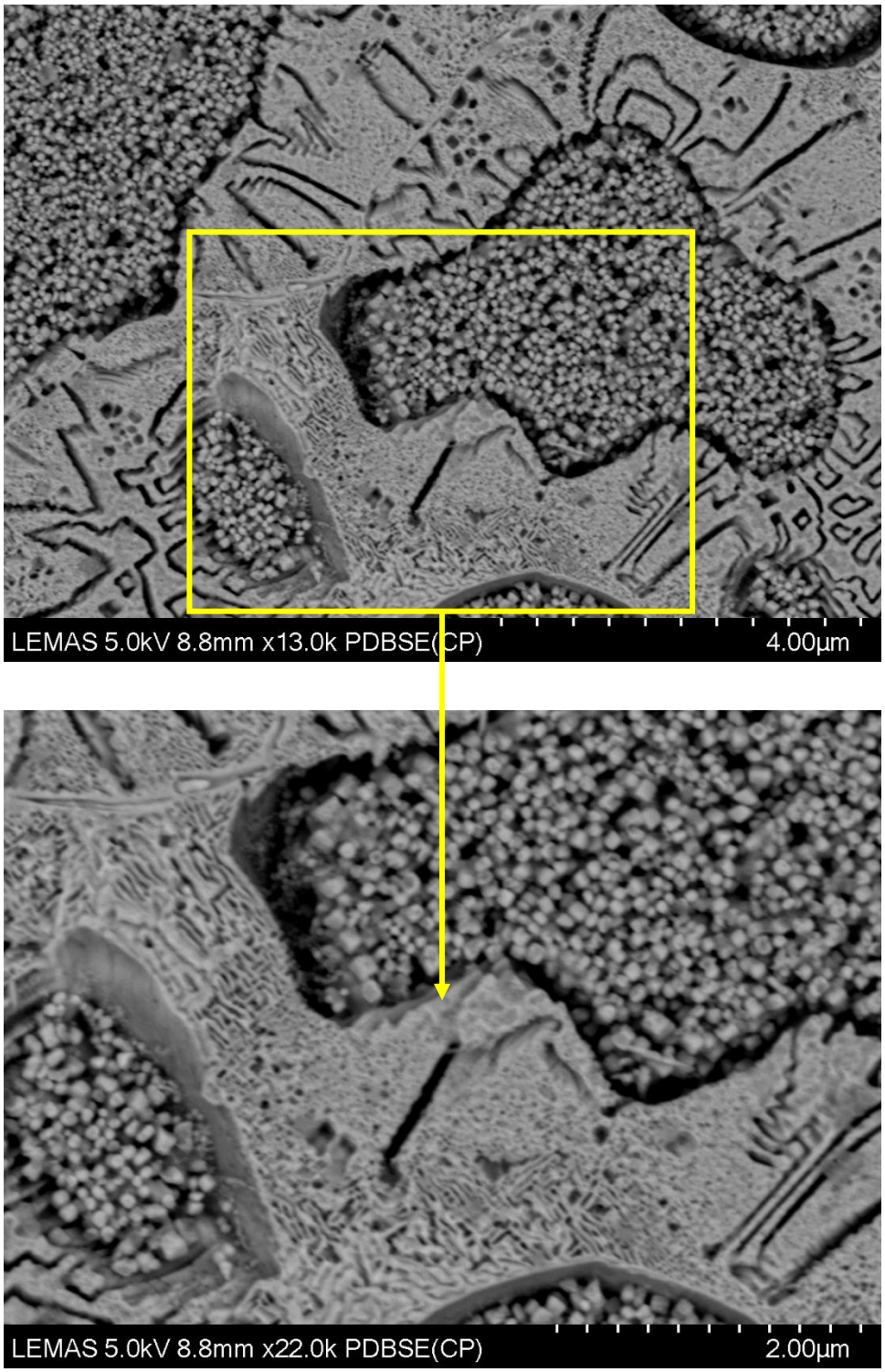

Figure 3.16 High magnification backscatter images of AlCrCuFeNi powder from $d >$ 850 μm size-fraction.

In the smaller particles of the 500 – 850 μm size range (cooled at around 432 K/s), a slight simplification of the microstructure may be observed. With reference to the corresponding XRD trace in Figure 3.13, the intensity of the FCC peak decreases further in this sample. Regarding the sample's microstucture, Figure 3.17 shows that the intermetallic adheres more strictly to the dendrites' peripheries. At the higher cooling rates experienced by the 300 – 500 μm (1716 K/s), 212 – 300 μm (4600 K/s) and 150 – 212 μm (3.74×10^4 K/s) sized powders, the ribbon-like IM and the precipitates within the dendrites persist, indicating that aside from the apparent grain refinement, a significant change in microstructure is not present. The microstructures of the 300 – 500 μm, 212 – 300 μm and 150 – 212 μm particles can be seen in Figure 3.18 and Figure 3.19a and Figure 3.19b, respectively.

The 106 – 150 μm (3.74×10^4 K/s) droplets appear at low magnification to comprise a simple solid-solution structure free of the features seen in larger powders – see Figure 3.20. At higher magnifications, however, it appears that the needle-like aggregates are still very much present, as observed in Figure 3.21. The precipitates within the dendrites are also retained at this cooling rate, with their scale being refined to the order of a few nanometers. Such is also the case with the 53 – 75 μm (3.60×10^5 K/s) and 75 – 106 μm (1.13×10^5 K/s) powders, where it can be seen in Figure 3.22 and Figure 3.23 that the intermetallic features are extremely fine and may only be observed at high magnifications.

Finally, at the highest cooling rate of around 1.13×10^6 K/s, a microstructure free of IM phases is observed in powders of the 38 – 53 μm size-fraction (see Figure 3.24). These microstructures show a much closer resemblance to a typical single-phase solid-solution. Namely, the powders of the 38 – 53 μm size-fraction show a simple dendritic structure, where the critical observations can be made that are the dendrites appear to be free of precipitates, and the ID phase appears to be free of the needle/ribbon structures observed at lower cooling rates. Generally, simple structures such as the one seen in Figure 3.24 are obtained due to the rapid cooling rates which achieve large enough undercoolings to form metastable phases and possibly induce disorder trapping.

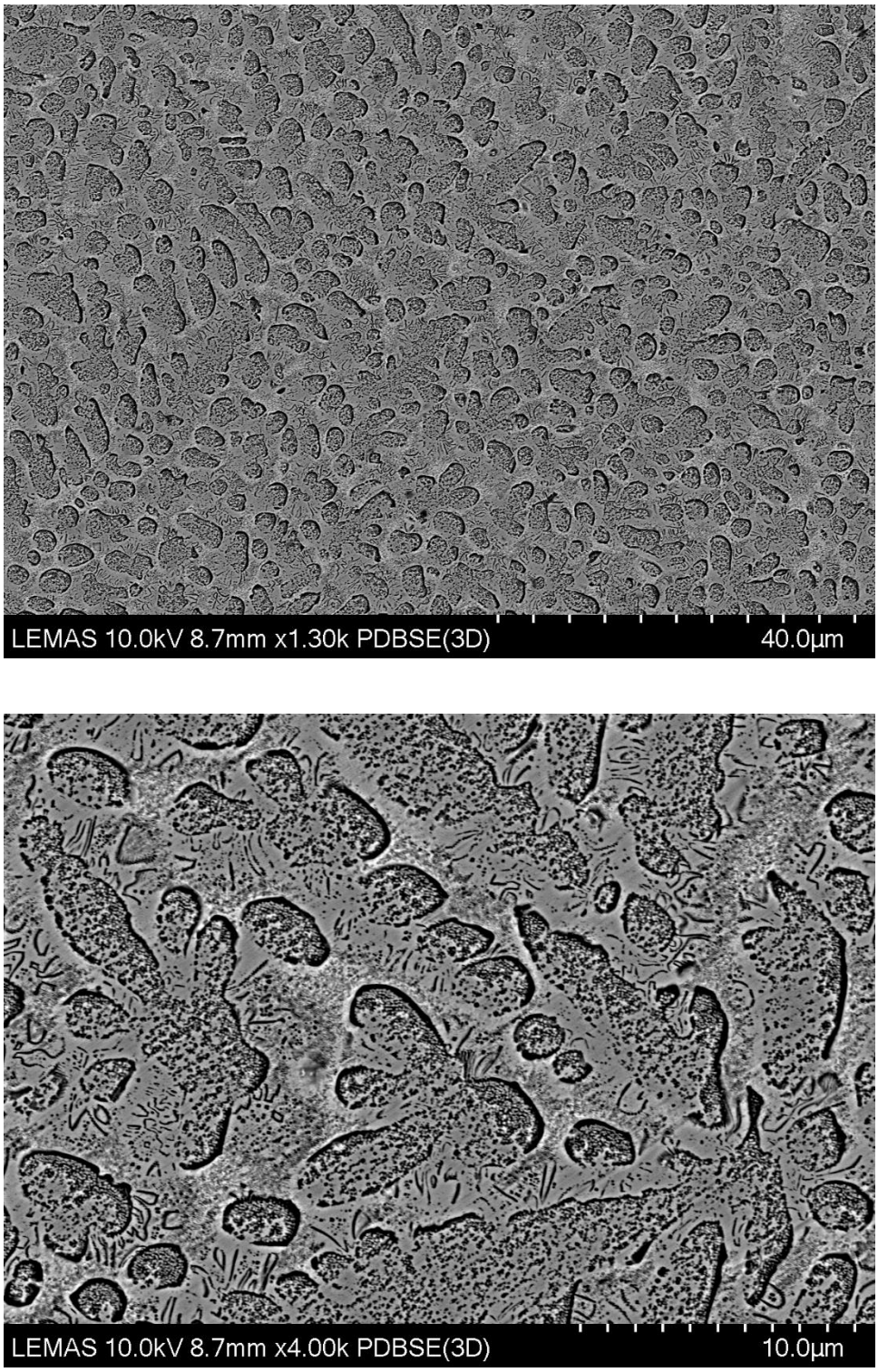

Figure 3.17 Microstructure of AlCrCuFeNi powder cooled at an estimated 432 K/s (500 – 850 μm).

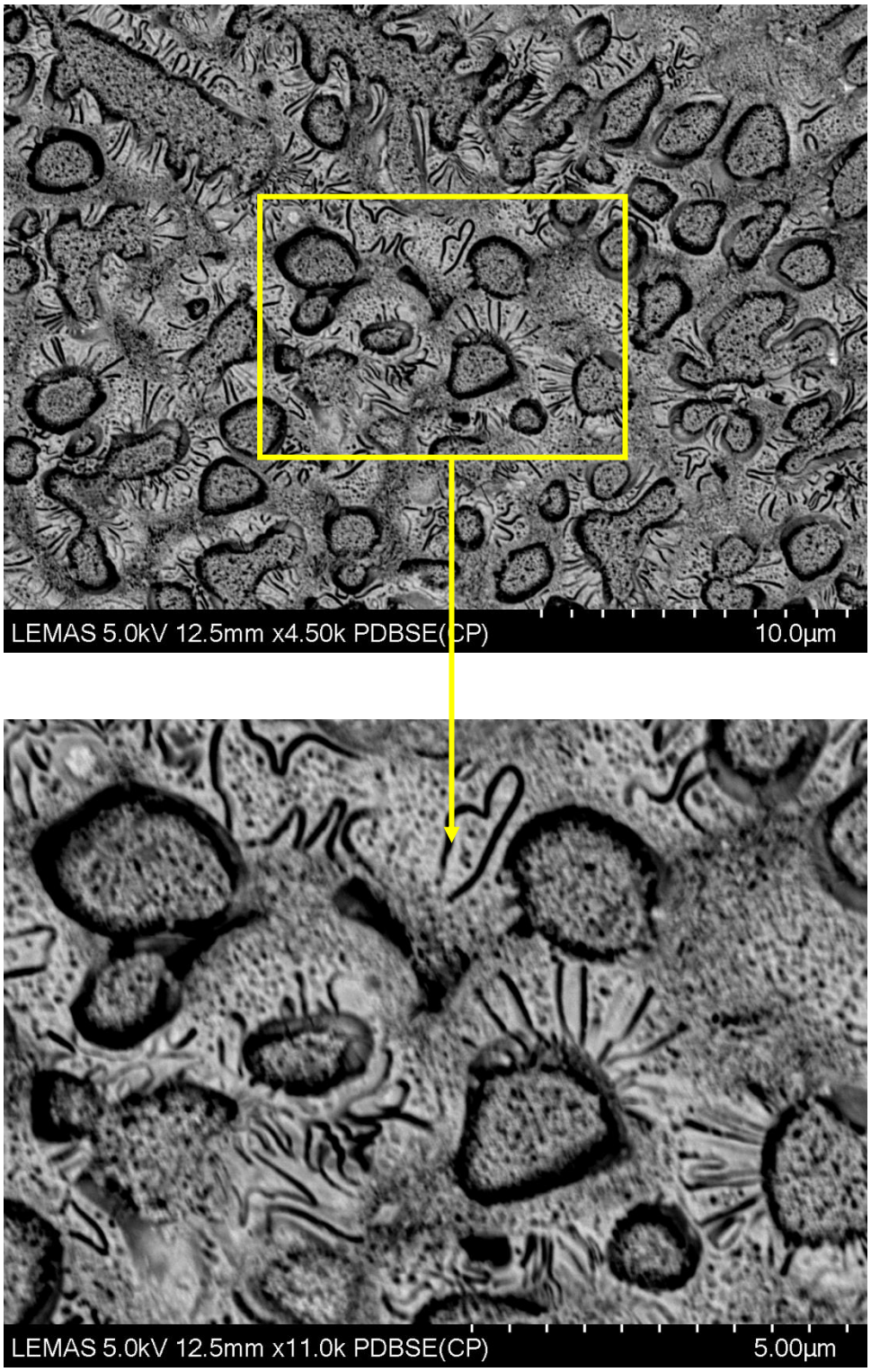

Figure 3.18 AlCrCuFeNi powder from 300 – 500 μm size-fraction (1716 K/s)

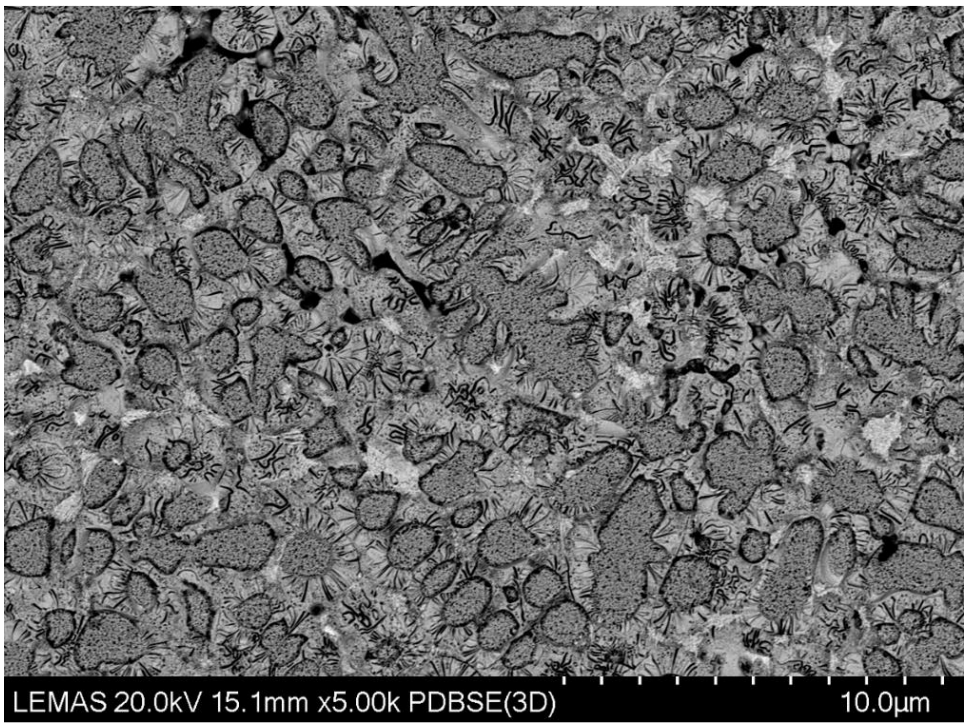

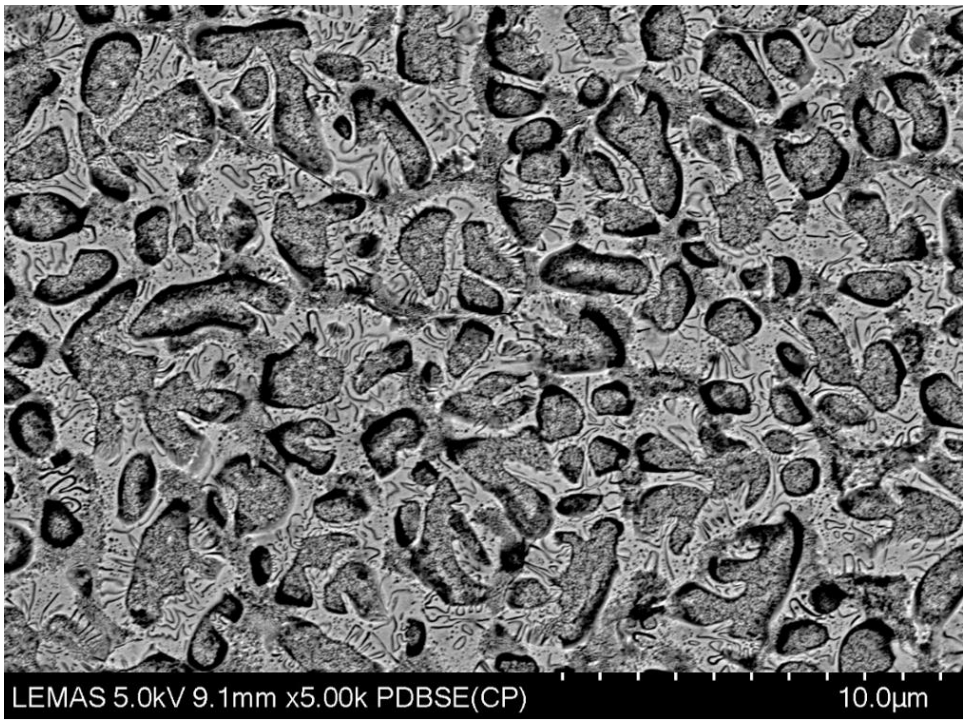

Figure 3.19a AlCrCuFeNi powder from 212 – 300 μm size-fraction (4599 K/s) **Figure 3.19b** AlCrCuFeNi powder from 150 – 212 μm size-fraction (1.28×10^4 K/s)

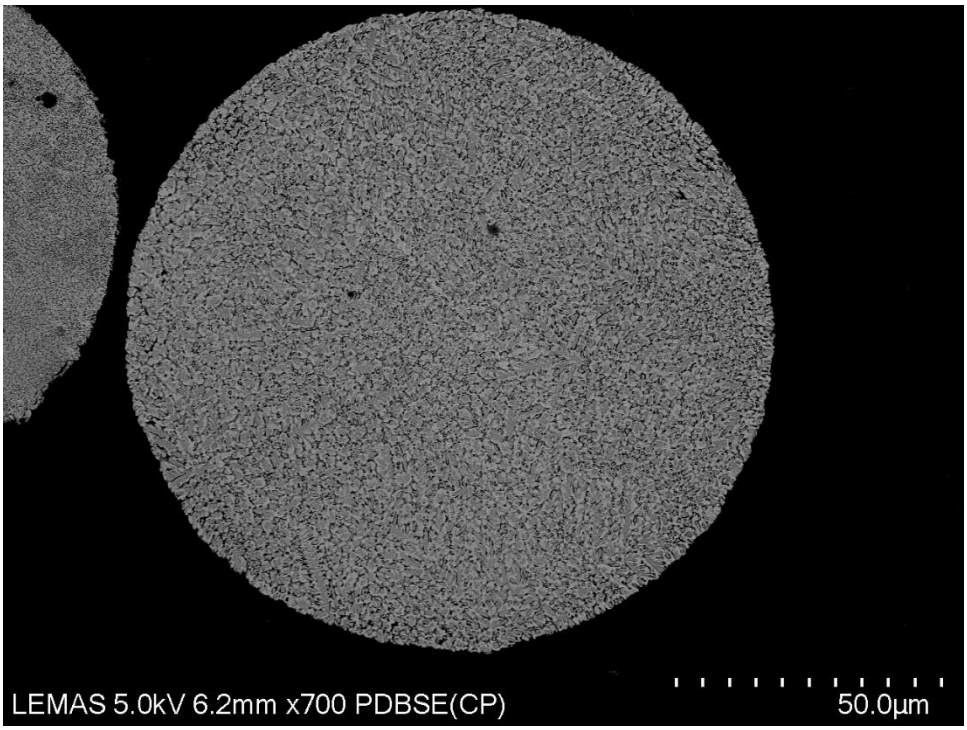

Figure 3.20 Low-magnification back-scattered SEM migrograph of AlCrCuFeNi powder from 106 – 150 µm size-fraction (3.74×10^4 K/s).

Further to SEM backscatter images and XRD, TEM analysis on the as-cast sample confirms the duplex nature of the master alloy. Figure 3.25a shows a Bright-Field (BF) of an inter-dendritic region in the as-cast sample, in where the ID matrix is labelled as '1' and the IM regions are labelled as '2'. The SAD patterns of these phases are presented in Figure 3.25b and Figure 3.25c, where it can be seen that the IM regions are B2 ordered and the ID matrix comprises an FCC structure. These phases have lattice parameters of 2.63 Å and 3.49 Å, respectively.

TEM analysis is also carried out on the $d > 850$ μm powders obtained from the drop-tube experiment. Firstly, the ID region of the sample is analysed as seen in Figure 3.26, which shows that the IM needles are Cr-Fe rich and the ID region is rich in Al-Ni-Cu. Unlike the as-cast sample, the ID region of the $d > 850$ μm droplet is found to comprise an ordered B2 structure (shown by the SAD pattern in Figure 3.26a), indicating that the FCC of the ID region is inhibited at this cooling rate of 112 K/s. This is compatible with the XRD data in Figure 3.13, which shows a significant drop in the intensity of the FCC peak

in the d > 850 μm scan. Judging by the SAD pattern of Figure 3.26b, the B2 ordered structure of the needle-like IM appears to be retained. The SAD pattern of the ID matrix is shown in Figure 3.25. Between the needle-like structures in Figure 3.26, weak intensity bands of Cr and Fe are present which are only observed in TEM EDS mapping. Referred to in Figure 3.26e and Figure 3.26g as inter-needle bands, these bands may represent needle intermetallics which had not developed completely prior to solidification.

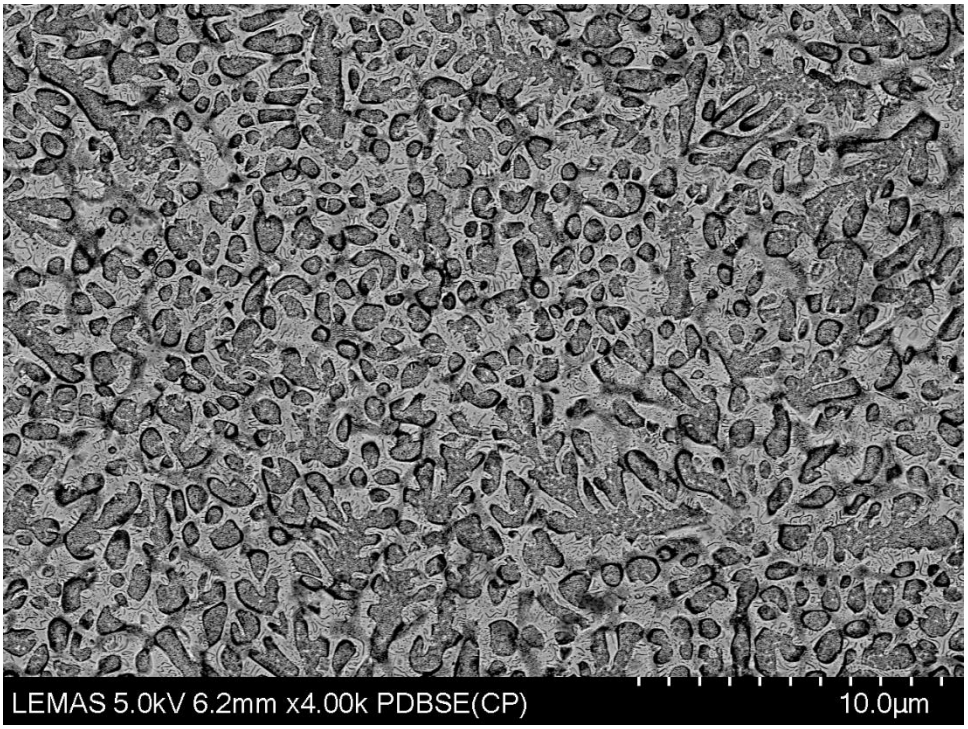

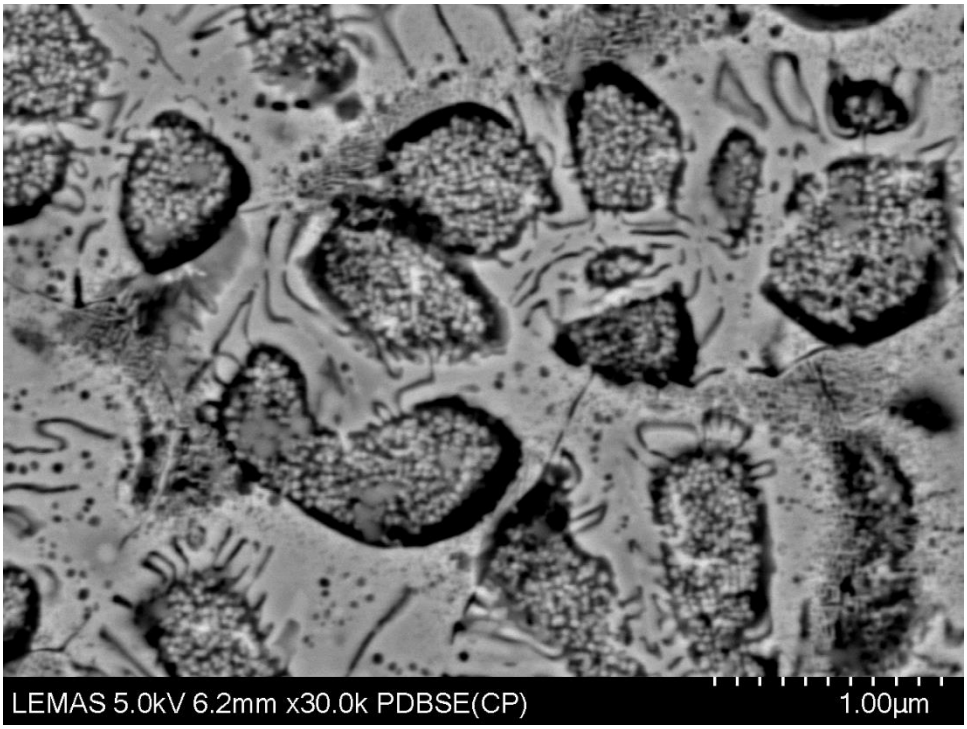

Figure 3.21 Higher magnification backscatter micrographs of AlCrCuFeNi powder from 106 – 150 μm size-fraction (3.74×10^4 K/s).

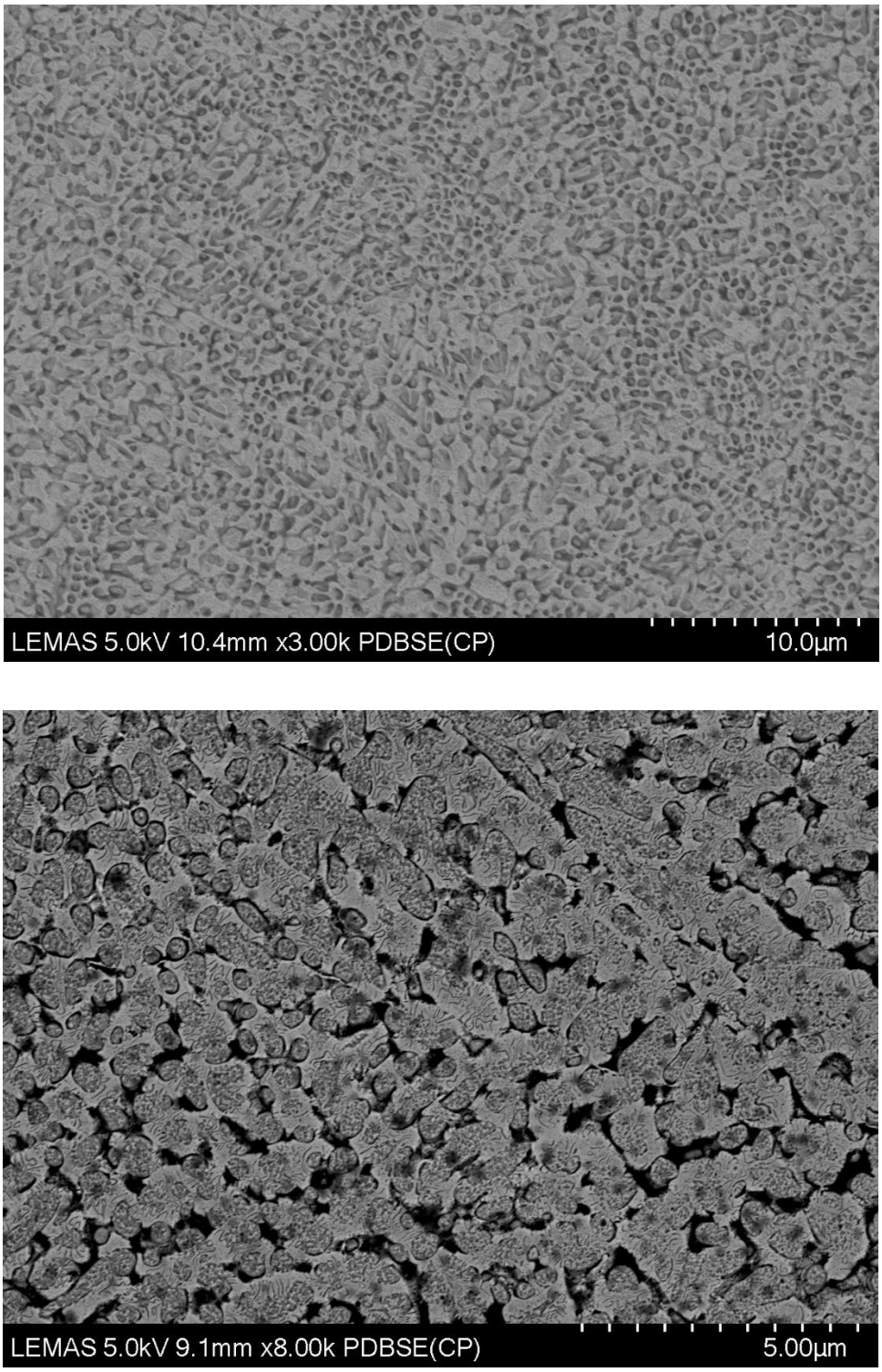

Figure 3.22 AlCrCuFeNi powder from 75 – 106 μm size-fraction (1.13×10^5 K/s)

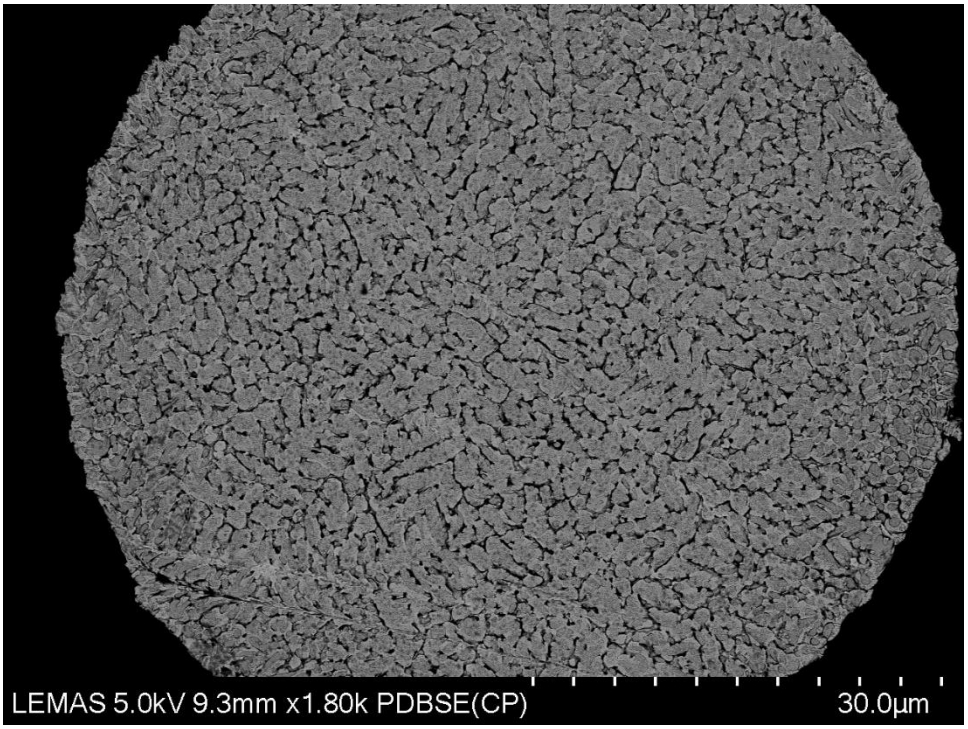

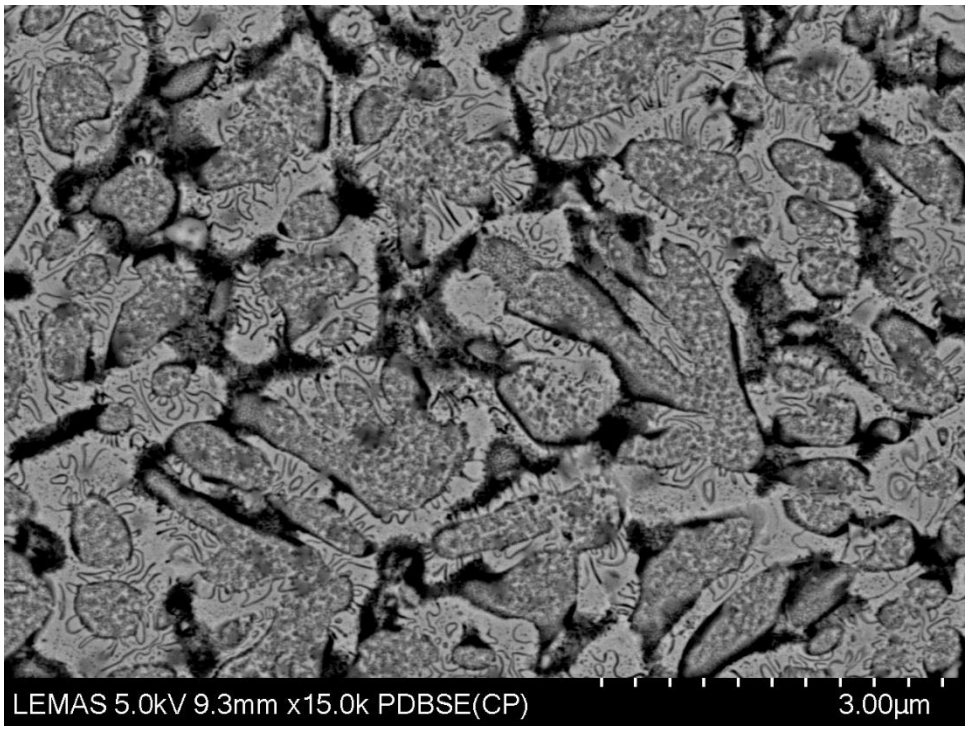

Figure 3.23 AlCrCuFeNi powder from 53 – 75 μm size-fraction (3.60×10^5 K/s)

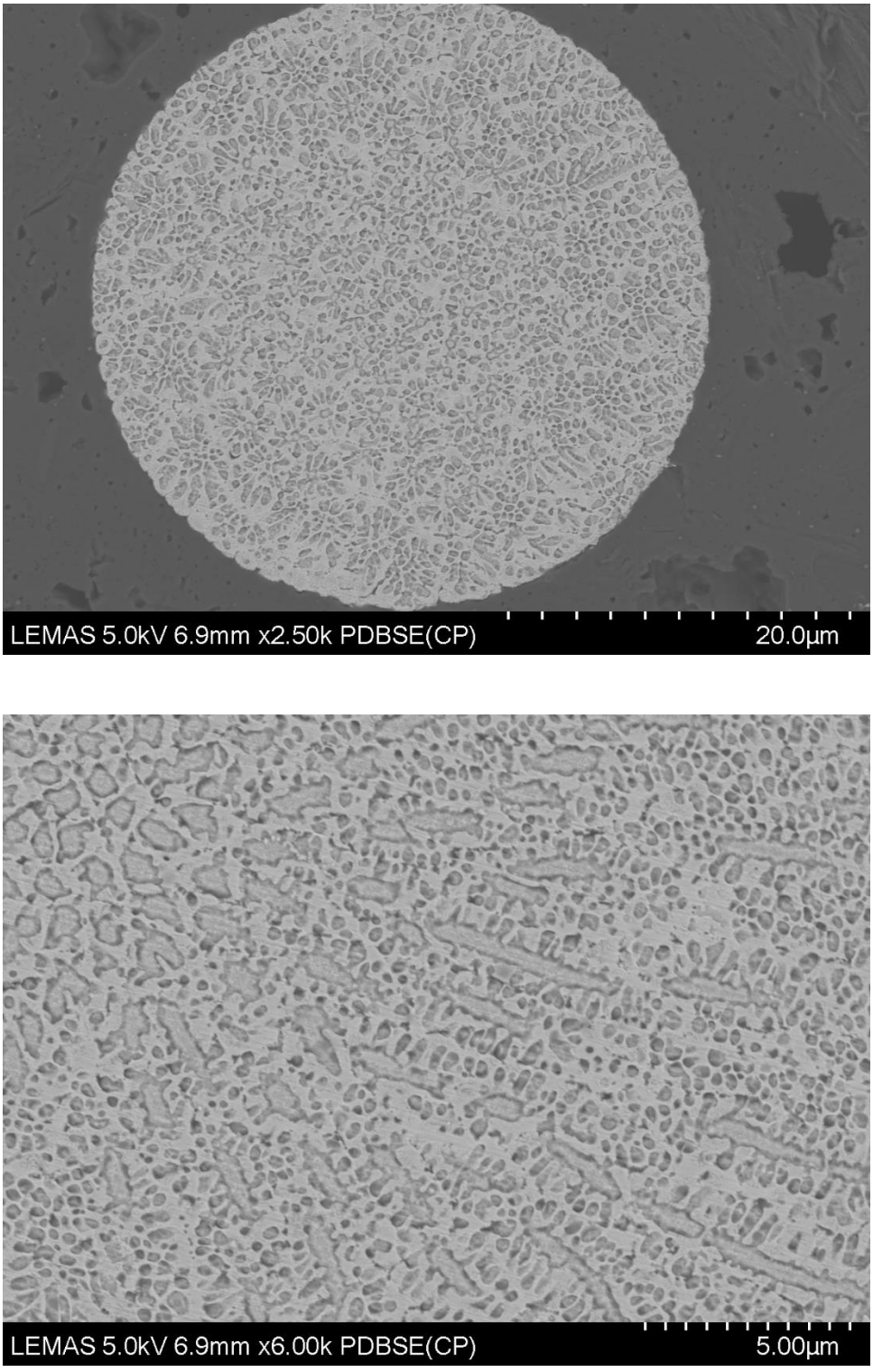

Figure 3.24 AlCrCuFeNi powder from 38 – 53 μm size-fraction (1.13×10^6 K/s)

Figure 3.27a shows a BF image of the dendritic region in the $d > 850\ \mu m$ sample. SAD patterns are taken from the precipitates within the dendrites and from the dendrite itself, showing that both phases comprise ordered B2 structures. These SAD patterns are shown in Figure 3.27b and Figure 3.27c. The lattice parameters of the dendrite and the precipitates (within the dendrites) are found to be 2.43 Å and 2.42 Å, respectively. HAADF imaging and elemental distribution maps of a dendritic region in the same sample are shown in Figure 3.28, where it is evident that the precipitates are rich in Al and Ni and the dendrite mainly comprises Cr and Fe. This is a commonly observed separation of elements due to the favourable, negative enthalpies of mixing between Al-Ni and Cr-Fe. On the dendrite's periphery (in the ID region) plate-like Cu separation is observed which takes place in addition to the bulk segregation of Cu. In addition to these plate-like nano-precipitates, globular Cu precipitates are also observed in the ID region. These are shown in the elemental distribution maps of Figure 3.29.

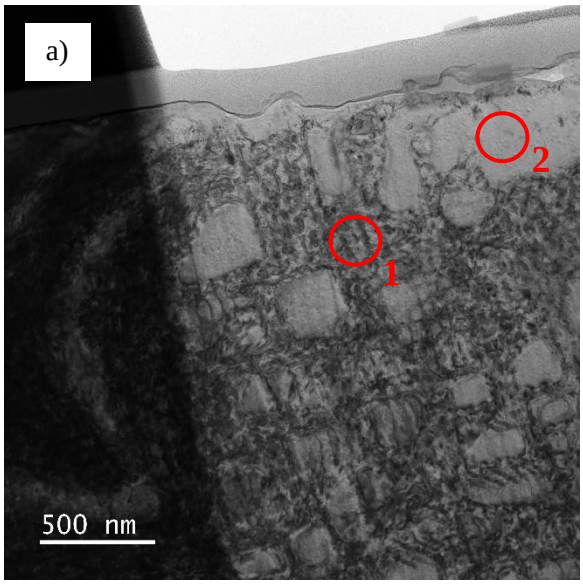

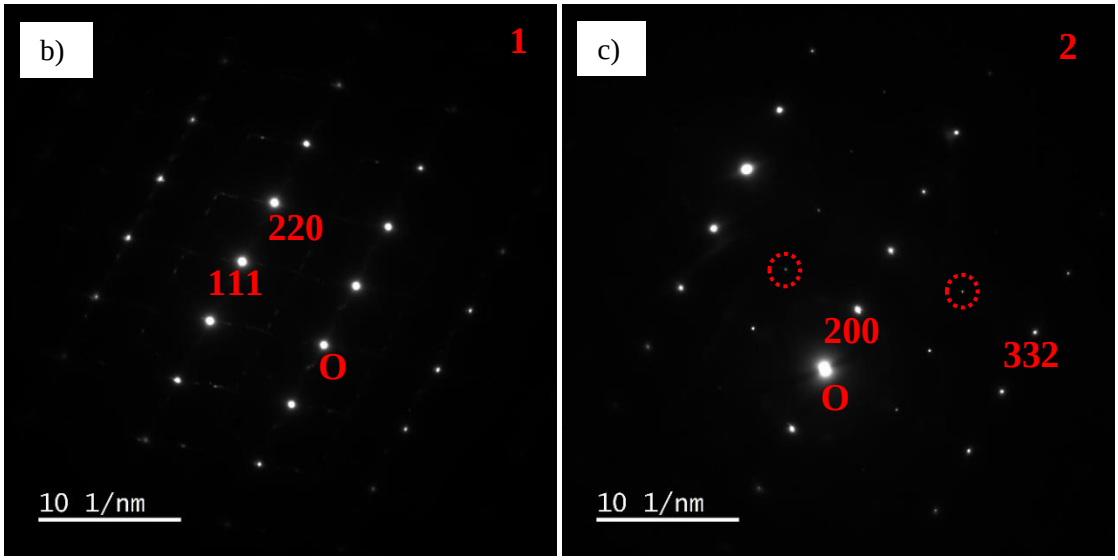

Figure 3.25a ID region from the as-cast alloy, including IM phases**. Figure 2.35b** [-2 2 0] SAED pattern from ID phase showing FCC structure**. Figure 3.25c** [0 -2 3] SAED pattern from 'needle-like' phase showing B2 ordering, where the red circles highlight the superlattice spots.

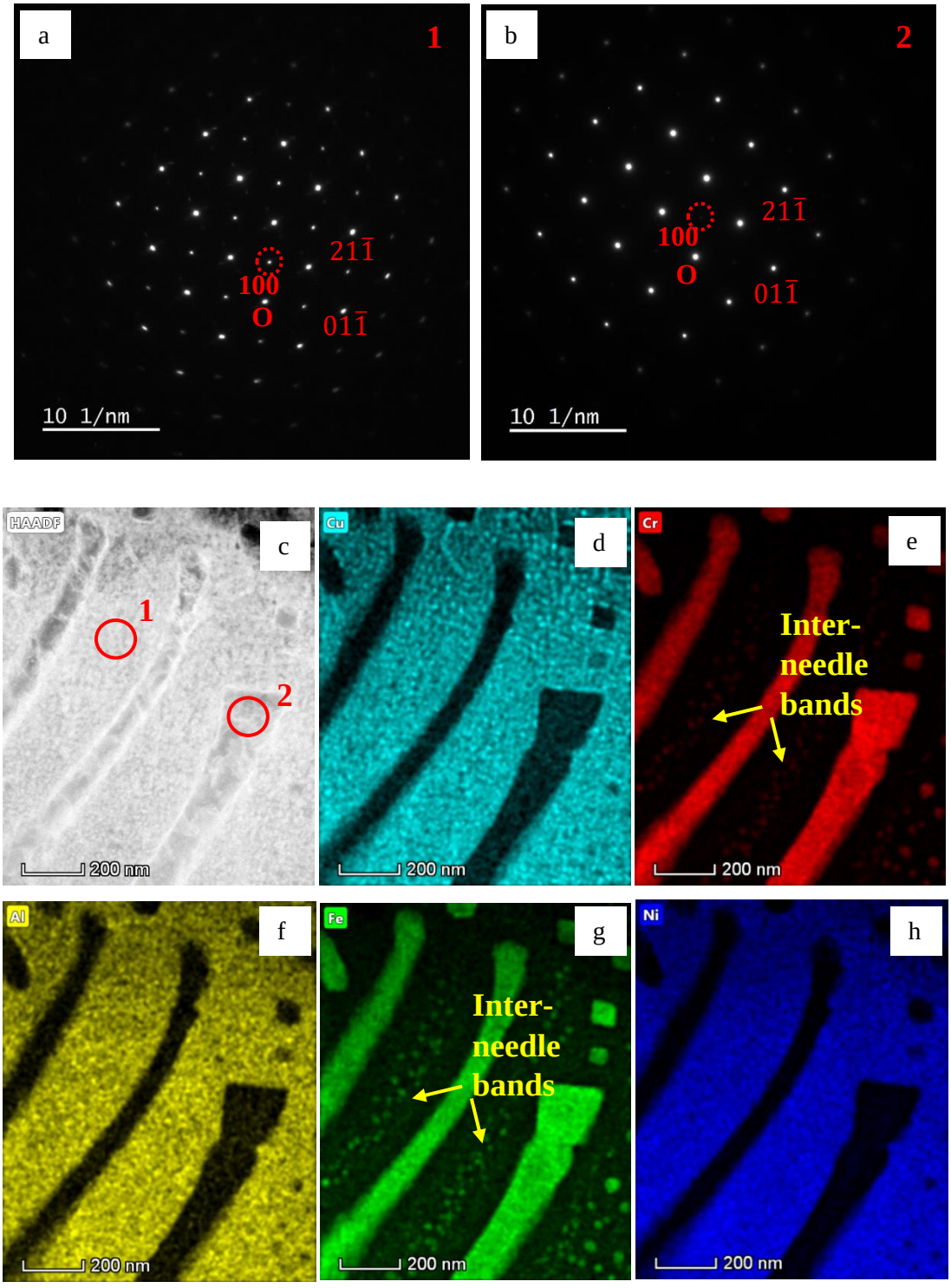

Figure 3.26a SAD pattern from ID region [011] zone axis, **Figure 3.26b** SAD pattern from IM [011] zone axis **Figure 3.26c** HAADF image **Figure 3.26d-h** elemental distribution from ID and IM regions in $d > 850$ μm sample.

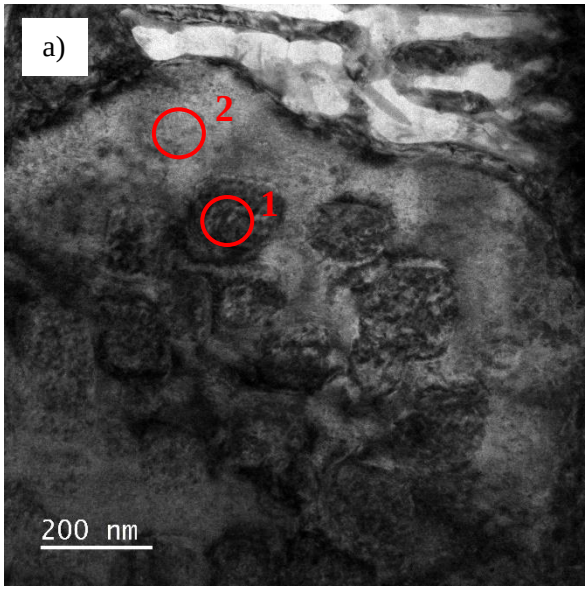

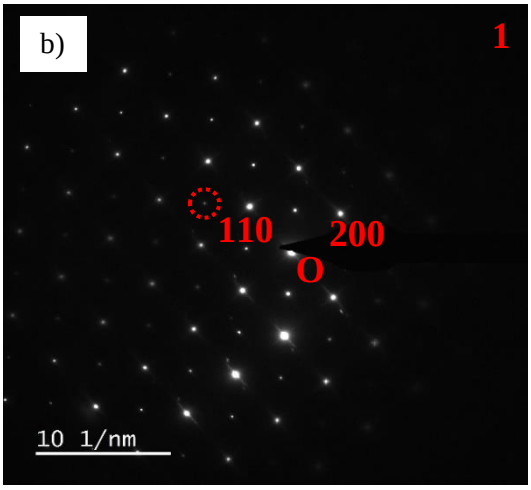

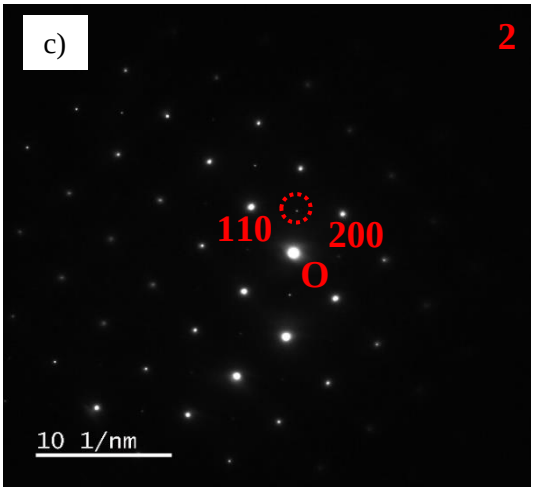

Figure 3.27a Dendritic region from droplet of the d > 850 µm size-fraction **Figure 3.27b** [0 0 -1] SAD pattern of precipitates within the dendrite **Figure 3.27c** [-2 2 0] SAD pattern of precipitate-free region within the dendrite.

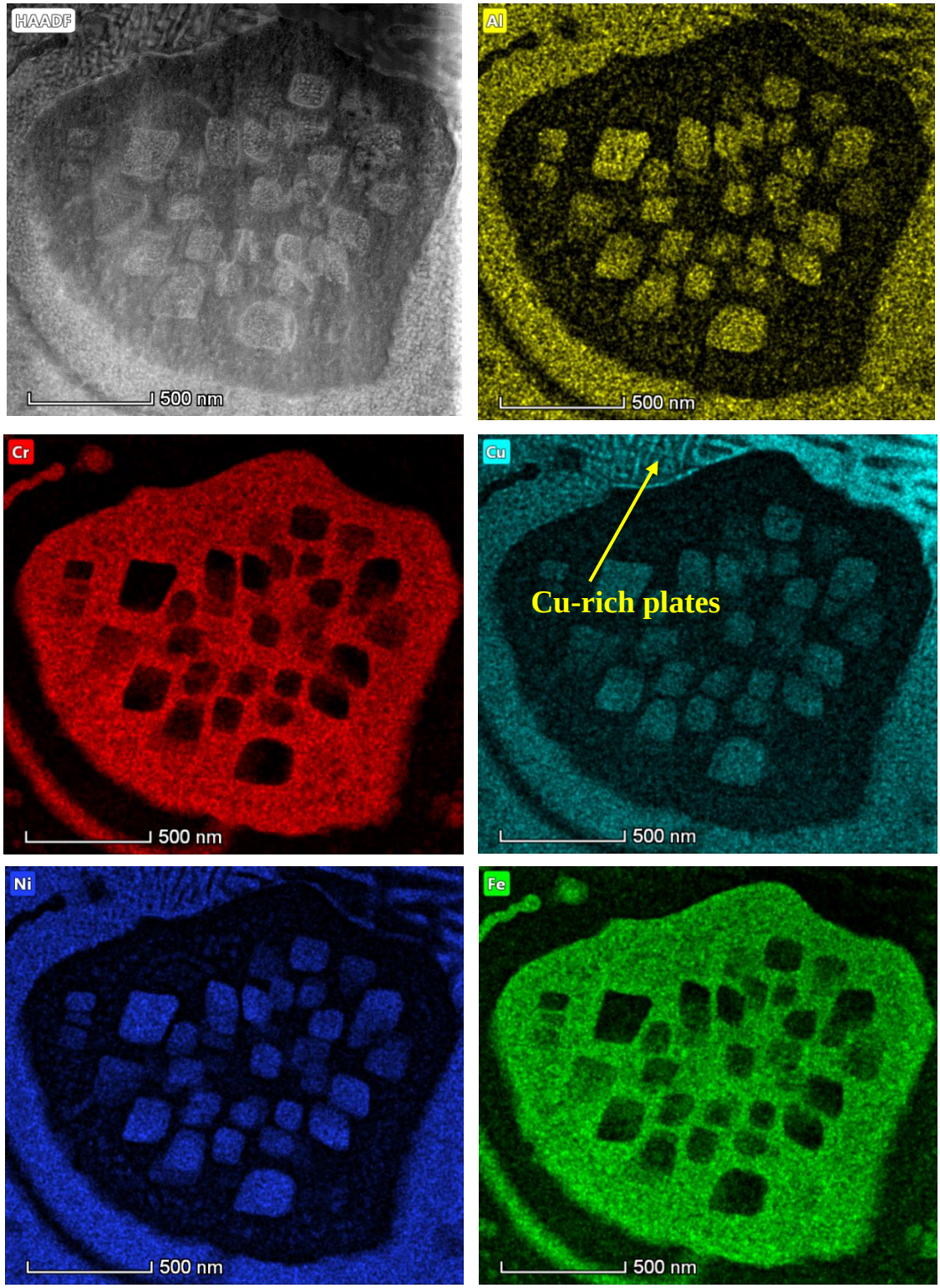

Figure 3.28 HAADF image and elemental distribution of dendritic region in AlCrCuFeNi powder of d > 850 μm size fraction.

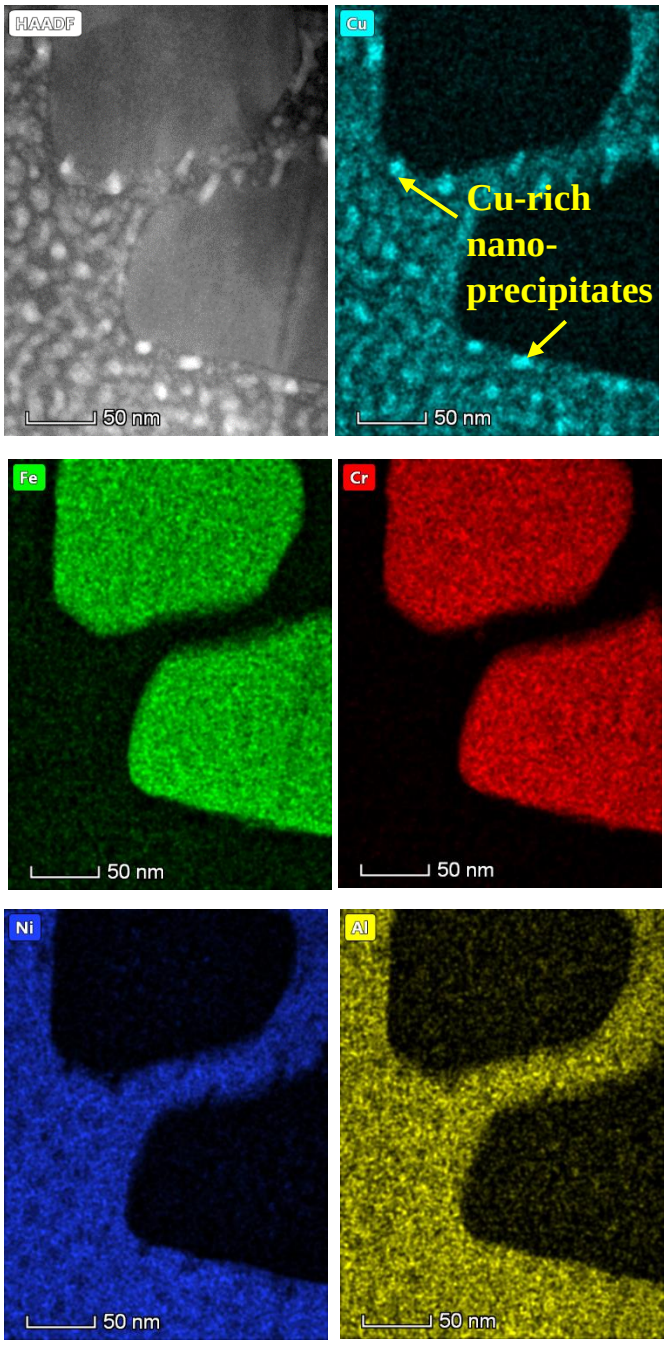

Figure 3.29 HAADF image and elemental distribution images from ID region in AlCrCuFeNi powder of d > 850 μm size fraction.

3.2.2 Microhardness

Grain refinement is observed as cooling rate increases and powder size is reduced. Due to the fragmented nature of the dendrites observed in the AlCrCuFeNi powders, grain refinement due to rapid solidification is measured as a function of dendrite area rather than a more common measure such as secondary dendrite arm spacing. In particular, the square root of the measured area is multiplied by a factor of $\frac{2}{\sqrt{\pi}}$, in order to obtain the equivalent diameter of the (fragmented) dendrite – see Equations 3.5 to 3.8. Figure 3.30 shows the relation between average cooling rate and the equivalent diameter, d_{eq}, of the dendrites. Gradual refinement is observed with increased cooling rate, where d_{eq} decreases from a mean value of 3.86 μm in the d > 850 μm size fraction to 0.47 μm in the 53 – 75 μm size fraction. Data for the smallest size fraction of 38 – 53 μm is not presented as the comparison is made between powders of similar microstructures that differ mainly due to grain refinement.

$$A = \pi \left(\frac{d_{eq}}{2}\right)^2 \tag{3.5}$$

$$A = \pi \frac{{d_{eq}}^2}{4} \tag{3.6}$$

$${d_{eq}}^2 = \frac{4A}{\pi} \tag{3.7}$$

$$d_{eq} = \frac{2\sqrt{A}}{\sqrt{\pi}} \tag{3.8}$$

To understand the effect of rapid cooling on the microhardness of the AlCrCuFeNi HEA, Vickers microhardness measurements were made on the powders obtained from the alloy. In the Hall-Petch plot of Figure 3.31, the alloy shows an overall increase in microhardness

as the dendrites become finer. This confirms the positive effect of grain refinement on the microhardness of the powders. An outlier is observed at $A^{-0.25} = 0.74$, which is explained by the larger FCC residue than other samples, as this is the slowest-cooled powder (it being known that FCC is the softer phase). Further, microhardness is plotted against cooling rate, in order to better correlate microstructure/particle size to microhardness. This plot is seen in Figure 3.32, where the largest powder sieve fraction ($d > 850\ \mu$m) has a microhardness of 519 $HV_{0.03}$ and the smallest powder sieve fraction ($38 - 53\ \mu$m) shows a microhardness of 805 $HV_{0.03}$, confirming the increase in microhardness due to grain refinement. While there is an overall increase, it appears as though there are certain developments in the morphology of the alloy to which the jumps in microhardness are attributed. The micrographs included in Figure 3.32 attempt to explain the jumps in microhardness from the $150 - 212\ \mu$m to the $106 - 150\ \mu$m and from the $53 - 75\ \mu$m to the $38 - 53\ \mu$m size fractions. Naturally, grain refinement is the principal factor in these witnessed increases in microhardness. However, these changes in microstructure are highlighted to allow correlating the alloy structure to its microhardness. It can be seen that from the $150 - 212\ \mu$m to the $106 - 150\ \mu$m size fractions, the morphology changes from being evidently dendritic to a more fragmented appearance, where the dendrites are only observable at higher magnifications – Figure 3.21 in Section 3.2.1 provides a closer look at this morphology. As for the increase seen between the ($53 - 75\ \mu$m) to the ($38 - 53\ \mu$m) size fractions, Figure 3.24 shows that this is the critical point where the microstructure of the powders loses the needle-like structures in the matrix and achieves a simple solid solution. In the regions where microhardness does not vary with cooling rate, it is suspected that the decreasing concentration of nano-precipitates within the dendrites has a negative effect on hardness, cancelling out the effect of grain refinement.

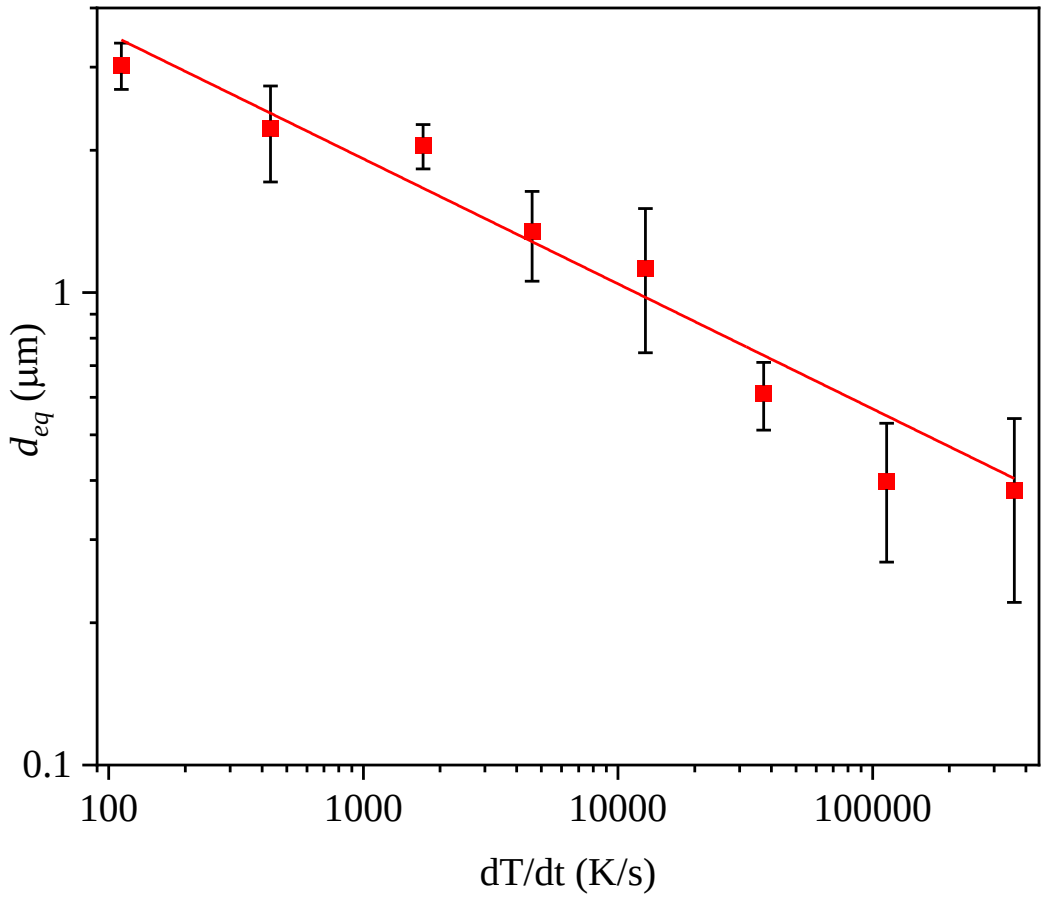

Figure 3.30 Equivalent diameter of fragmented dendrites against cooling rate.

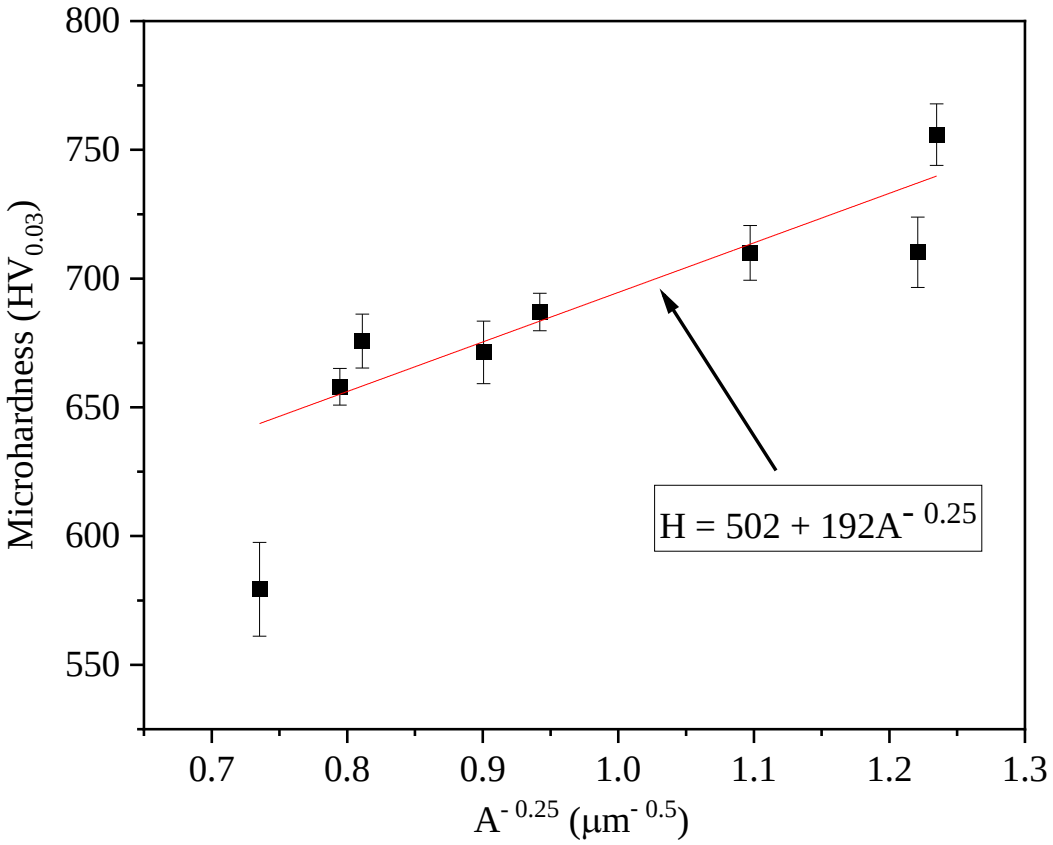

Figure 3.31 Microhardness of AlCrCuFeNi powders as a function of $A^{-0.25}$ in a Hall-Petch plot.

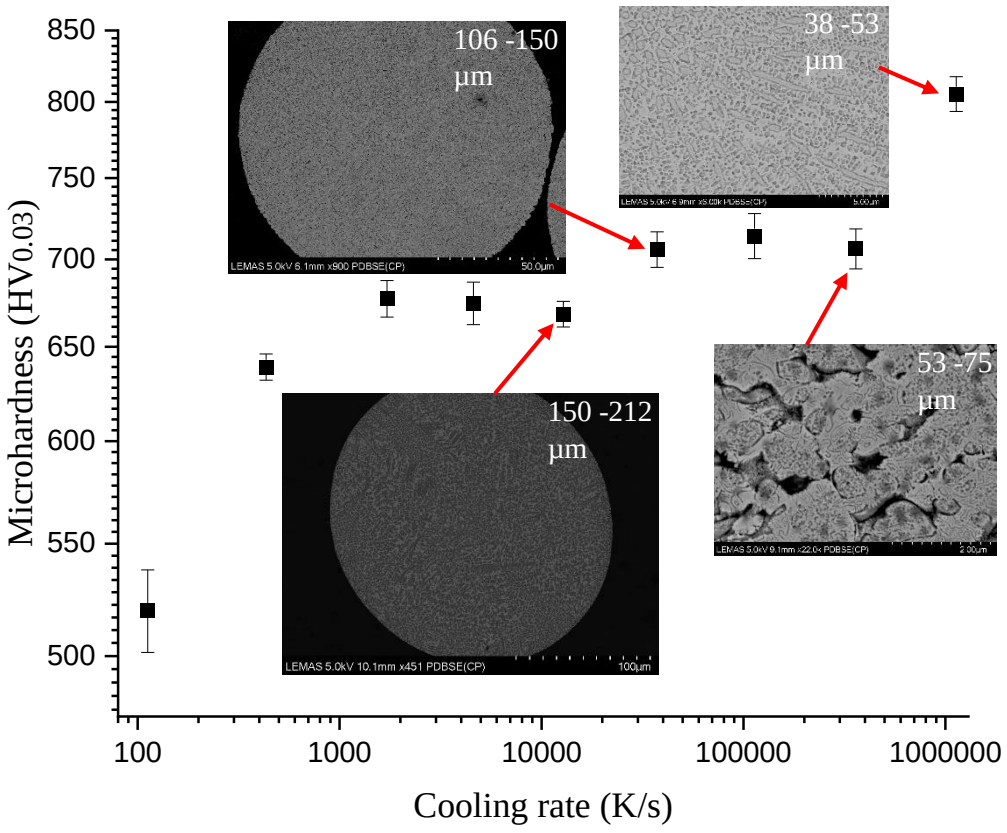

Figure 3.32 Microhardness of AlCrCuFeNi powders as a function of average cooling rate.

3.2.3 Discussion

In this work, non-equilibrium cooling of equimolar AlCrCuFeNi HEA is achieved using a drop-tube facility such that cooling rates between 112 K/s and 1.13×10^6 K/s are attained. As-cast AlCrCuFeNi is also investigated and found to comprise FCC and B2 phases. A needle-like IM phase is observed in the ID region of the as-cast alloy and identified to be a B2 ordered phase, whereas the ID region is FCC ordered. The B2 ordered IM can be seen in Figure 3.14 where it is labelled as phase '3'. From Figure 3.14 it can be argued that the spherical and needle-like structures within the ID region are the same phase (both labelled as '3'), only that the orientation with which the sample is sectioned gives rise to two seemingly distinct morphologies. This argument is supported by the elemental

composition maps presented in Figure 3.26 and Figure 3.29, where the spherical and needle-like structures are shown to be rich in Cr and Fe. Phase separation within the dendrites is also observed in the as-cast alloy. We conclude that the precipitates within the dendrites form via spinodal decomposition in the solid-state due to their nature in appearing consistently in the microstructure's dendrites, their uniform distribution within the dendrites and the consistency of their size. These factors make it likely that these precipitates form due to a spontaneous process such as spinodal decomposition rather than a nucleation process. This argument is further supported by the fact that the precipitates and the dendrites comprise the same crystal structure (both B2 ordered. Spinodal decomposition has also been observed previously in alloys of a similar base, particularly in the AlCoCrCuFeNi system [102].

The TEM analysis shows that the AlCrCuFeNi HEA attains a single B2 structure at cooling rates of 112 K/s and above. The SAD patterns in Figure 3.26 and Figure 3.27 form a full picture of the phases in the sample cooled at 112 K/s, where Figure 3.26 shows the B2 ordering in the IM phase and the ID region, and Figure 3.27 shows the B2 ordering of the dendrite and their precipitates. As such, it is evident that FCC growth is already inhibited at this cooling rate. This is relatively similar to an observation made by R. Wang et al., who show that FCC growth in the duplex (FCC/BCC) AlCoCrFeNi HEA is inhibited due to the cooling rate experienced during laser fabrication [171]. However, although this study does prove the inhibition of FCC growth, there is no mention of the cooling rate at which this occurs. Contrary to our work and the work of R. Wang et al. is the observation made by Y. Wang et al., which claims that in the equimolar AlCoCrCuFeNi HEA, it is the growth of the BCC which is restrained due to selective laser melting (though not completely inhibited), rather than the FCC [172]. Despite the slight difference in constituent elements, it would be expected that the AlCoCrCuFeNi HEA would show the same general behavior as its Cu-free variant. Nevertheless, given that our as-cast is sample expected to have a cooling rate of around 10 – 20 K/s, it can be said that the FCC structure is lost between 20 K/s and around 112 K/s. The XRD traces in Figure 3.13 are in accord with the observation that FCC growth is suppressed, as the intensity of the FCC peak is dramatically reduced and almost unobservable in the powders. The weak FCC peaks which remain are due to the stochastic nature of

nucleation (and hence droplet undercooling), in that the FCC phase is likely being retained in some, but not all droplets. This accounts for the decreased intensity of the FCC peaks in the XRD spectrum (fewer droplets with FCC) and is also consistent with not seeing the FCC phase in the single TEM sample taken in Figure 3.26.

Between the needle-like structures, weak intensity bands of Cr and Fe are present which are only observed in TEM EDS mapping. Referred to in Figure 3.26e and Figure 3.26g as inter-needle bands, these are likely to be 'embryonic' needles, in that the structure solidified prior to forming fully developed needles. It is expected that the SAD pattern from the area between the needles also shows a B2 structure, since both the ID matrix and the needle-like phase are B2 ordered. It is indeed observed in the SAD pattern (Figure 3.26a) of the 'inter-needle region' that there appears to be a slight overlap in patterns between the B2 structure of the ID region with that of the Cr and Fe rich bands. Given that the inter-needle spacing is around 400 nm, it is likely that these have formed via solid-state diffusion rather than growth from the liquid.

At the highest cooling rate of around 1.13×10^6 K/s, a microstructure free of IM phases is observed in powders of the 38 – 53 μm size fraction. A microstructure from this size fraction is displayed in Figure 3.24 and shows a much closer resemblance to a typical single-phase solid-solution. Just as the ID phase appears to be free of the needle/ribbon-like IM observed at lower cooling rates, the dendrites also appear to be free of precipitates. Due to one of the core characteristics of HEAs that is sluggish diffusion, it would be expected that the solid-state spinodal decomposition which gives rise to these precipitates would be suppressed at cooling rates of lower magnitude. Nevertheless, Figure 3.24 shows that with higher cooling rates, simpler microstructures can be obtained and the extension of the solid-solution of HEAs is possible via drop tube rapid-solidification technique.

Grain refinement is observed in the powders and is measured as a function of equivalent diameter (d_{eq}). The fragmented nature of the dendrites makes it impossible to use a more common measure of grain refinement such as secondary arm spacing. Nevertheless, the measurement of d_{eq} gives a clear idea about the grain refinement occurring as cooling

rate increases and particle diameter decreases. Figure 3.30 shows d_{eq} against cooling rate, highlighting a smooth transition in grain refinement as cooling rate increases. Further evidence of grain refinement is observed in Figure 3.31, where a positive Hall-Petch relation is obtain such that $\sigma_y = \sigma_0 + \kappa_H A^{-0.25}$; where σ_y is the yield strength of the material, σ_0 is the friction stress, κ_H is Hall-Petch coefficient and A is the measured area of the dendrites.

Finally, the microhardness of the rapidly cooled samples is probed and found to increase with cooling rate. Although this is a standard observation attributed to grain refinement, another contributing factor which may not be neglected is the suppression of FCC growth. As the FCC is the softer phase in the alloy, its early suppression means that the hardness of the alloy is enhanced. However, it is also clear from Figure 3.32 that between some powder sizes the microhardness remains relatively constant. This is explained by the idea that the refinement of the ordered precipitates within the dendrites is expected to have an adverse effect on microhardness, leading to an apparent stagnation in certain regions of the plot. This non-conventional effect was first highlighted in Ni-based alloys containing significant volume fractions of ordered, Ni_3Al precipitates [173]. Namely, for dislocations to travel through the precipitates they must do so in pairs, as the first dislocation must first overcome the energy barrier to create an anti-phase boundary (APB). The second dislocation follows, removing the APB created by the leading dislocation. As such, the APB energy barrier to be overcome is hence reduced as the precipitates in the AlCrCuFeNi dendrites decrease in size. This effect may be used to explain the stagnant regions in Figure 3.32, where the strengthening due to grain refinement is being counterbalanced. Finally, the clear jumps in microhardness are attributed to developments in morphology whereby the first jump is attributed to increasingly fragmented dendrites, and the second and final jump is attributed to the transition towards a simple solid solution structure.

3.3 Rapid solidification of $AlCoCrFeNi_{2.1}$

3.3.1 Microstructure development

Figure 3.33 shows the microstructure of as-cast $AlCoCrFeNi_{2.1}$ observed using backscatter SEM imaging, where it is evident that the microstructure shows a lamellar eutectic, comprising a dark, Al and Ni rich phase and a light phase that is particularly rich in Cr (see EDX line scan). TEM analysis shown in Figure 3.34 reveals the crystallographic information of the constituent phases (see reflection spots of ordering crystal structures, highlighted by red circles), confirming that the dark and light phases are ordered B2 and $L1_2$ phases, respectively. These results are in accord with other investigations on this EHEA, where it is widely agreed that the equilibrium solidification of $AlCoCrFeNi_{2.1}$ results in a structure of alternating $L1_2$ and B2 phases [174][175]. Emanating facets can also be observed in the microstructure of the as-cast alloy, extending outwards from the regular lamellae and connecting to adjacent lamellar bands. It is obvious that these emanating facets do not retain a particular lamellar spacing. Rather, the lamellae expand radially in a disordered manner until splitting occurs which appears to maintain an upper bound on the spacing.

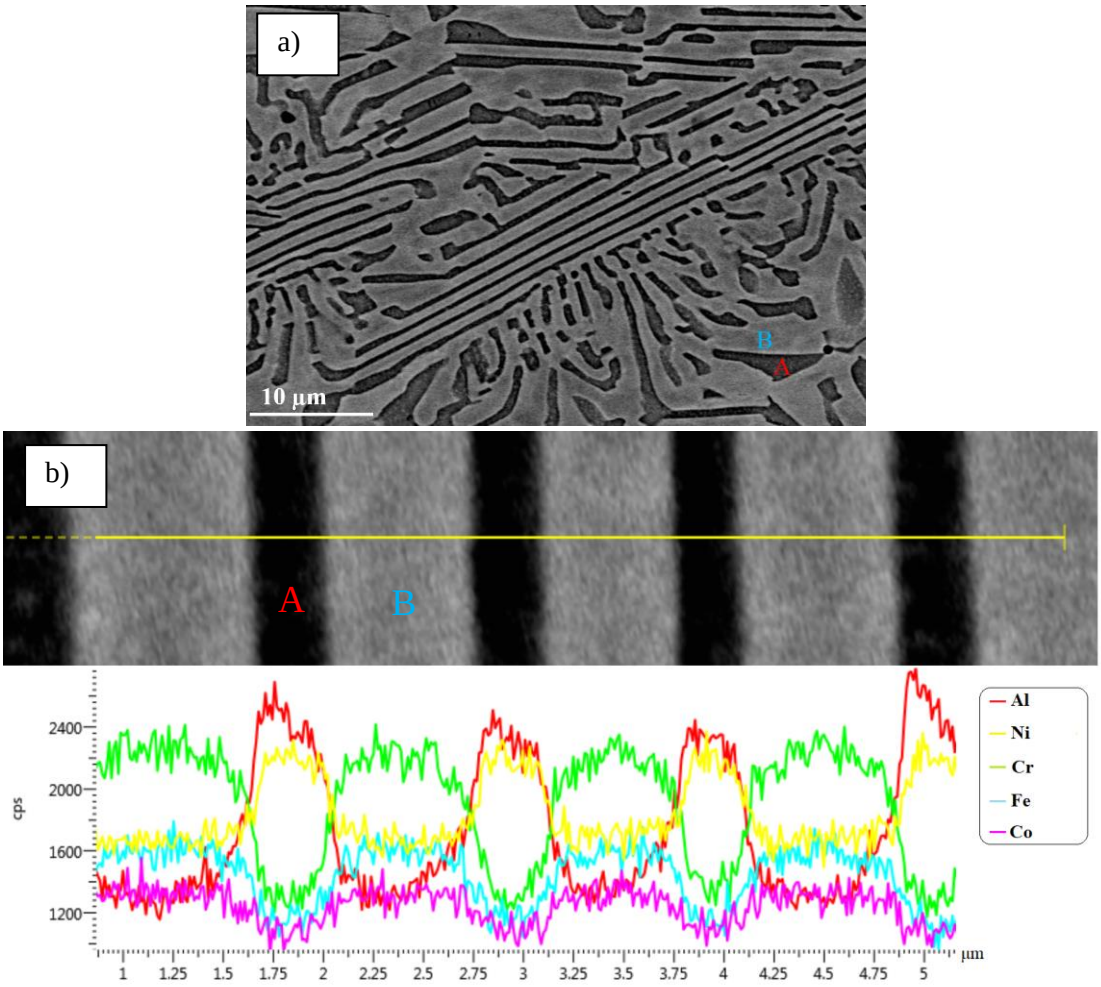

Figure 3.33a Microstructure of as-cast AlCoCrFeNi2.1 EHEA – Where A is the BCC phase and B is the FCC phase; **Figure 3.33b** Line-scan of as-cast $AlCoCrFeNi_{2.1}$ showing Al-Ni rich phase and Cr rich phase.

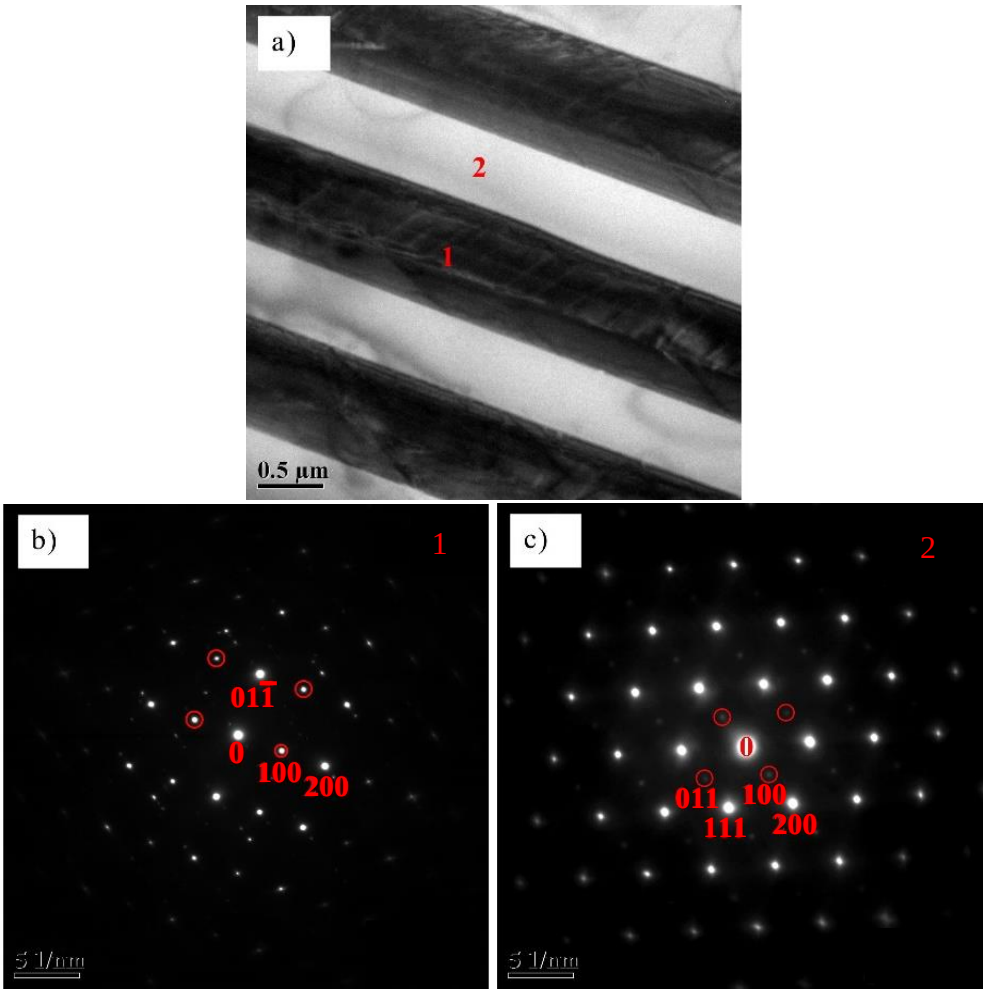

Figure 3.34a Regular eutectic structure of the arc-melted AlCoCrFeNi2.1 alloy [011]. **Figure 3.34b** and **Figure 3.34c** SAED patterns of the regions labeled 1 and 2, showing ordered B2 and ordered L12 structures, respectively [011].

The XRD pattern in Figure 3.35 confirms that the FCC/BCC duality is retained for all rapidly cooled powders, irrespective of cooling rate. However, it must be noted that due to the stochastic nature of nucleation, differences in microstructure exist between particles of the same size fraction albeit they experience similar cooling rates. Figure 3.36 shows the relationship between droplet size and cooling rate, and serves as a good reference in correlating the presented microstructures with their respective cooling rates. The cooling rates presented correspond to the lower bound of the aforementioned powder size fractions.

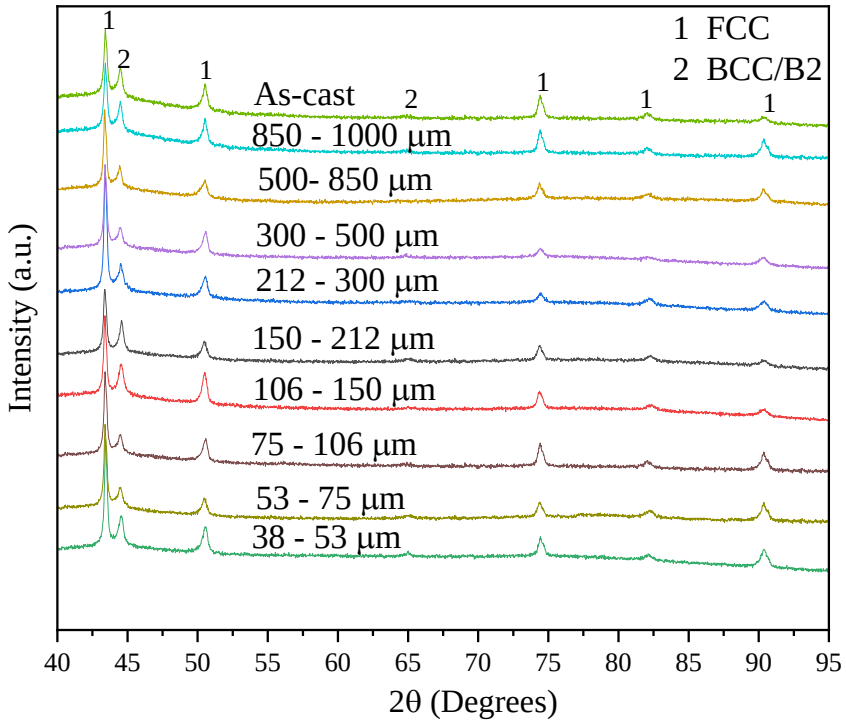

Figure 3.35 XRD patterns for $AlCoCrFeNi_{2.1}$ powders obtained via drop-tube processing.

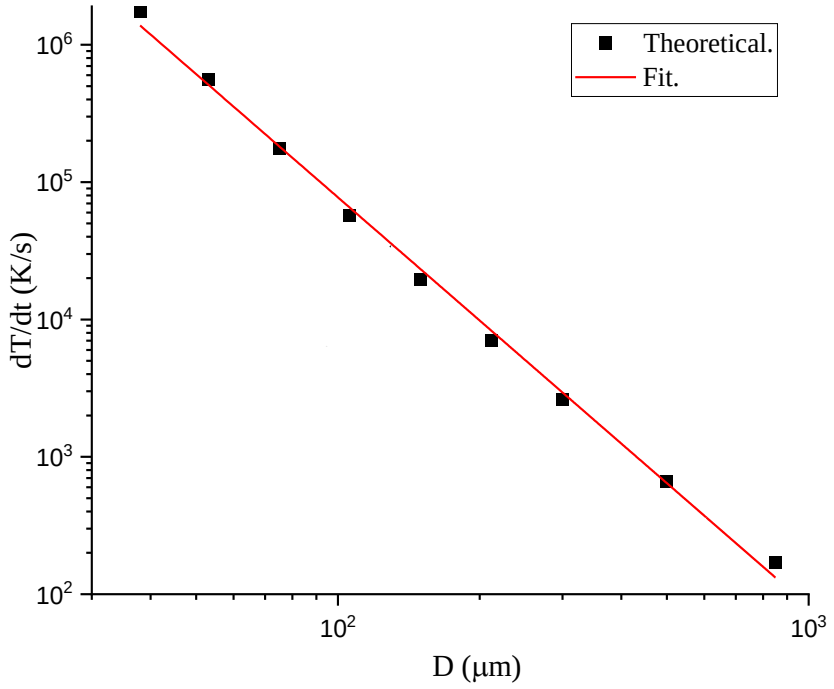

Figure 3.36 Estimated cooling rates of $AlCoCrFeNi_{2.1}$ powders as a function of powder diameter.

Despite solidifying at respective cooling rates of 114 Ks^{-1} and 170 Ks^{-1}, the microstructures of the 850 - 1000 μm and 500 - 850 μm powders are not significantly different from the as-cast microstructure. The structures in these powders are less regular and comprise alternating bands of coarse and fine spacing. In some respects (particularly the big variation in spacing) is reminiscent of an anomalous eutectic. This is evident from Figure 3.33a above, which shows the as-cast microstructure, as well as Figures 3.37a and 3.37b, which show backscatter micrographs of 850 - 1000 μm and 500 - 850 μm particles, respectively. As powder size decreases, two additional features are observed in the $AlCoCrFeNi_{2.1}$ powders – dendritic growth and cellular eutectic colonies.

Cellular eutectic growth is observed in the 150 - 212 μm sieve-fraction, coexisting with a regular eutectic and a dendritic phase (see Figure 3.38a). With increasing cooling rate, however, the cellular eutectic becomes more prevalent than regular lamellae. The higher cooling rate experienced by the 106 – 150 μm sieve-fraction provides evidence for this,

as in some instances, cellular colonies are seen to occupy the entire microstructure, as shown in Figure 3.38b. That dendritic growth can also be observed in Figure 3.38a indicates that sufficient undercooling is achieved in this droplet for a eutectic to dendritic transformation to occur. This is further confirmed in that dendritic growth is observed in each of the smaller sieve-fractions.

Figure 3.39 shows typical dendritic growth in a $AlCoCrFeNi_{2.1}$ particle from the 106 – 150 μm size range. It is evident in this case (due to the marked nucleation point) that with increasing undercooling, the solidification of $AlCoCrFeNi_{2.1}$ transitions from the primary solidification constituent being eutectic to the primary solidification phase being FCC dendritic. This departure from eutectic growth becomes increasingly apparent as cooling rate increases. Figure 3.40 demonstrates, in a visual manner, that the primary FCC volume fraction, and the primary FCC phase in particular, increases with cooling rate. Figure 3.41 confirms and quantifies this observation, showing the increase in volume fraction of the primary (dendritic) FCC phase with increasing cooling rate. It was found that the FCC volume fraction in the largest powders is 63.7 %. Due to the relatively low cooling rate of these powders, this is expectedly similar to the FCC fraction in the as-cast alloy (65.3 %) and in both cases is in accord with the FCC volume fraction reported in the literature [176]. With increasing cooling rate, it is observed that the primary FCC volume fraction increases monotonically, reaching an average maximum of 85% in powders of the 38 - 53 μm size-fraction.

It is worth noting that despite the predominantly dendritic structures in the smaller powders, cellular eutectic regions and even regular lamellae can be observed in their interdendritic regions - Figure 3.42 (from 38 - 53 μm particle) is one such example. Nevertheless, at the highest cooling rates (smallest droplets), particles with a dendritic microstructure and no eutectic in the interdendritic region are observed. This indicates that, in some instances, the residual undercooling following recalescence is sufficient to inhibit eutectic formation. Namely, due to the stochastic nature of nucleation, not all particles in the smaller size-fractions experience the critical undercooling and many retain the eutectic structure in the interdendritic region. All the aforementioned structures (regular eutectic, colony eutectic and dendrites) of the growth morphology are present in one particle (75 - 106 μm) displayed in Figure 3.43, wherein it is evident that the

constituents of the microstructure have become finer relative to the larger powders. Figure 3.44 quantifies this by showing the relation between interlamellar spacing and cooling rate on a logarithmic scale. As expected, interlamellar spacing is refined with higher cooling rates, ranging from 1.63μm to 0.35μm in the largest and smallest powder-size fractions, respectively. Considering that average interlamellar spacing in the as-cast microstructure was found to be 2.1 μm, it can be seen that a refined lamellar spacing may be achieved even at the lowest cooling rate of 114 K/s.

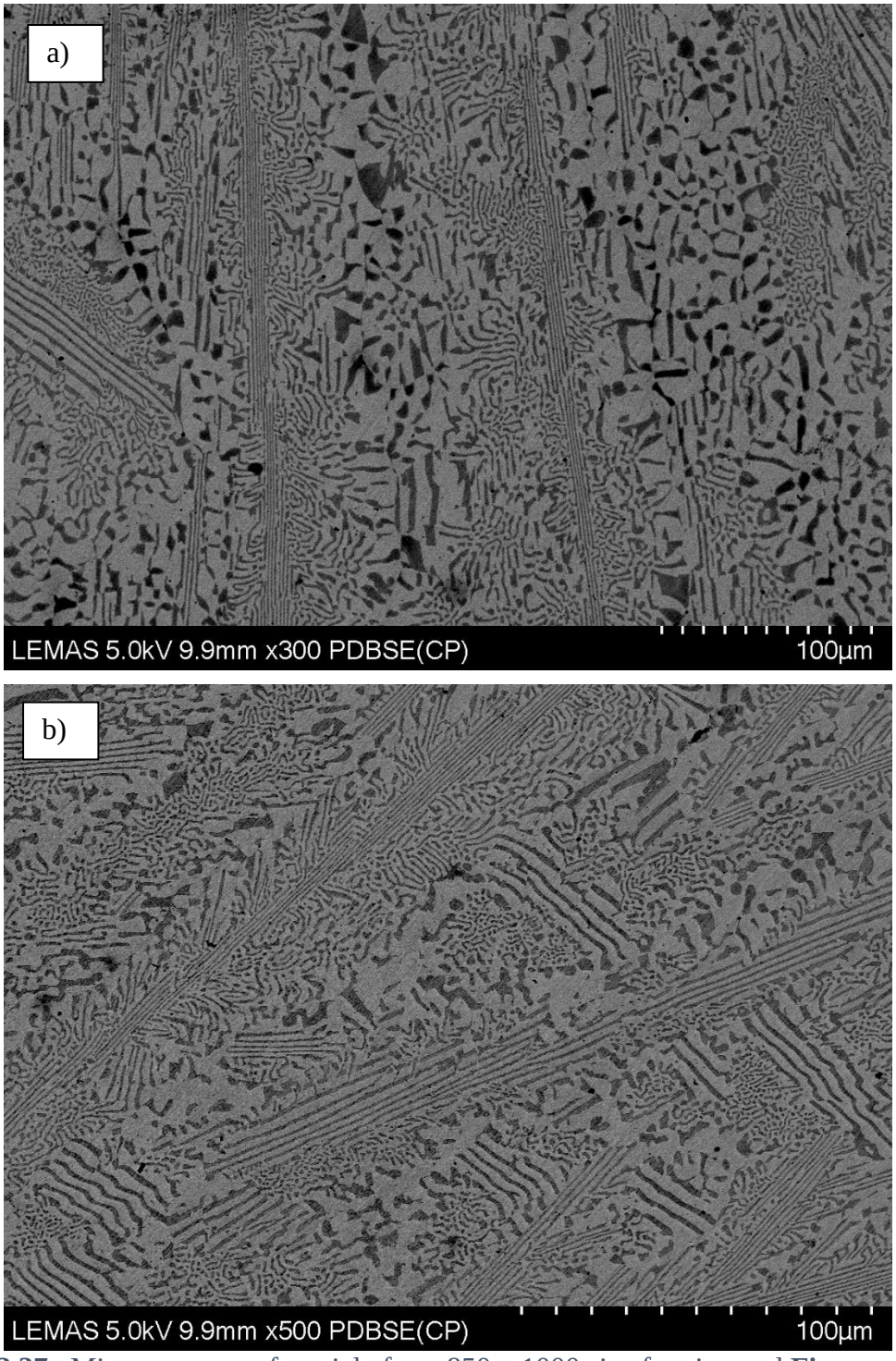

Figure 3.37a Microstructure of particle from 850 – 1000 size fraction and **Figure 3.37b** particle from 500 – 850 size fraction

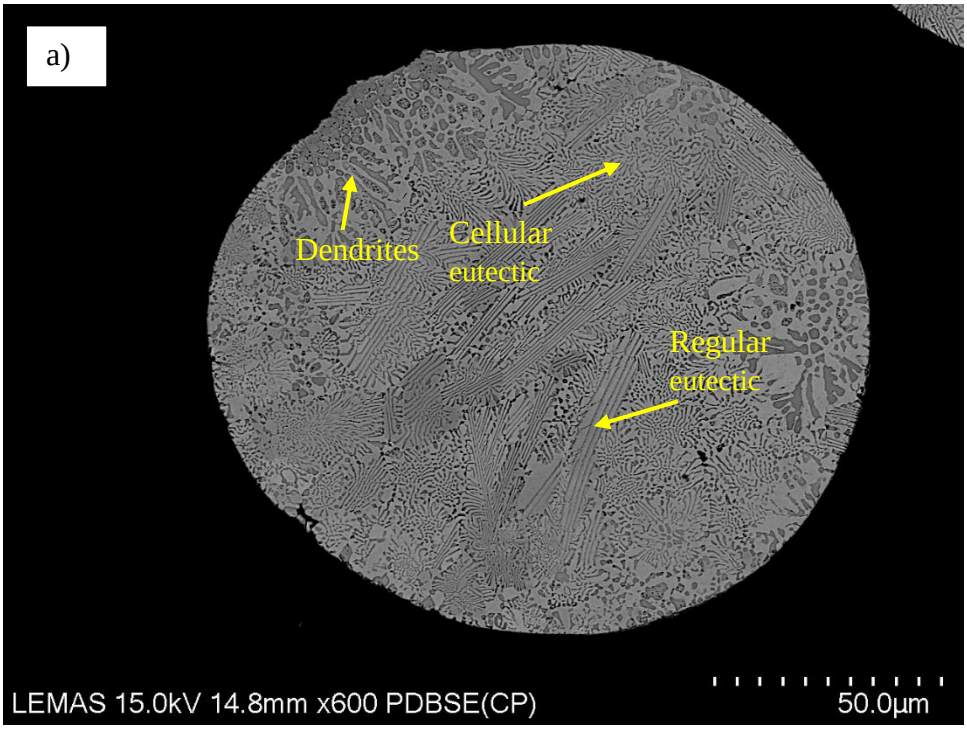

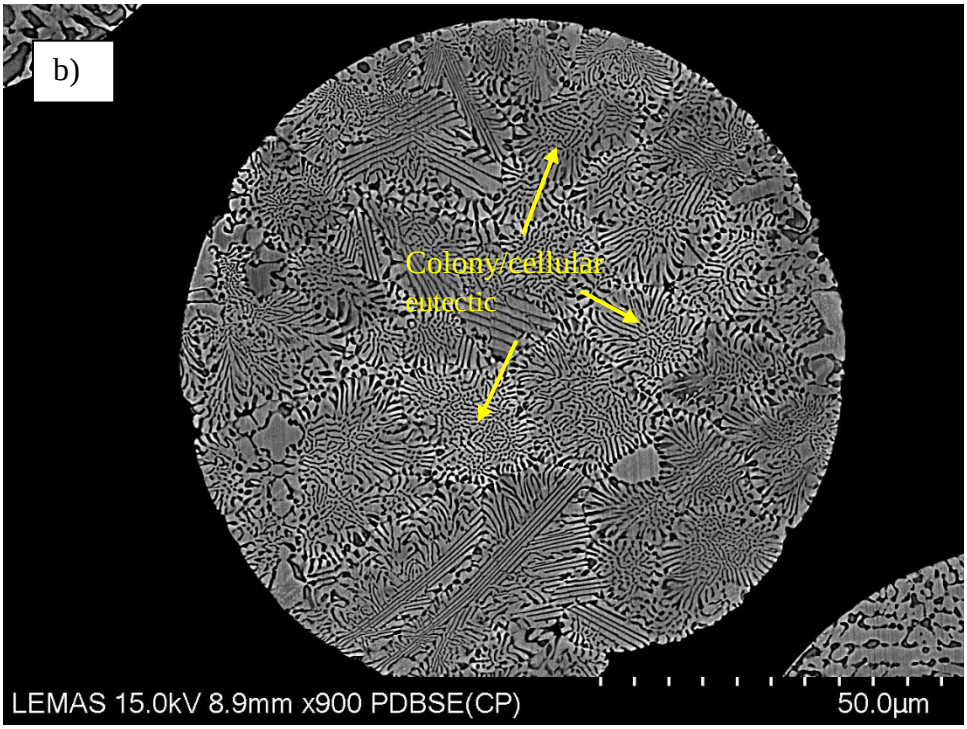

Figure 3.38a Appearance of cellular eutectic in the 150 – 212 sieve fraction and **Figure 3.38b** A more dominant cellular structure of particle in 106 – 150 sieve fraction.

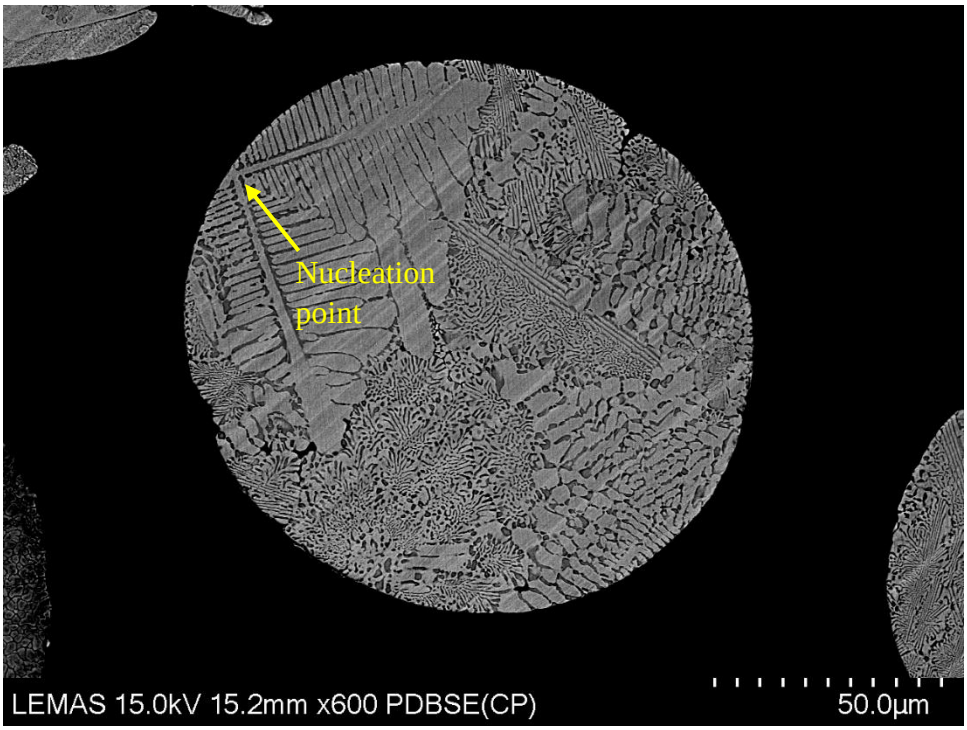

Figure 3.39 Primary FCC nucleation in particle from 106 – 150 sieve fraction.

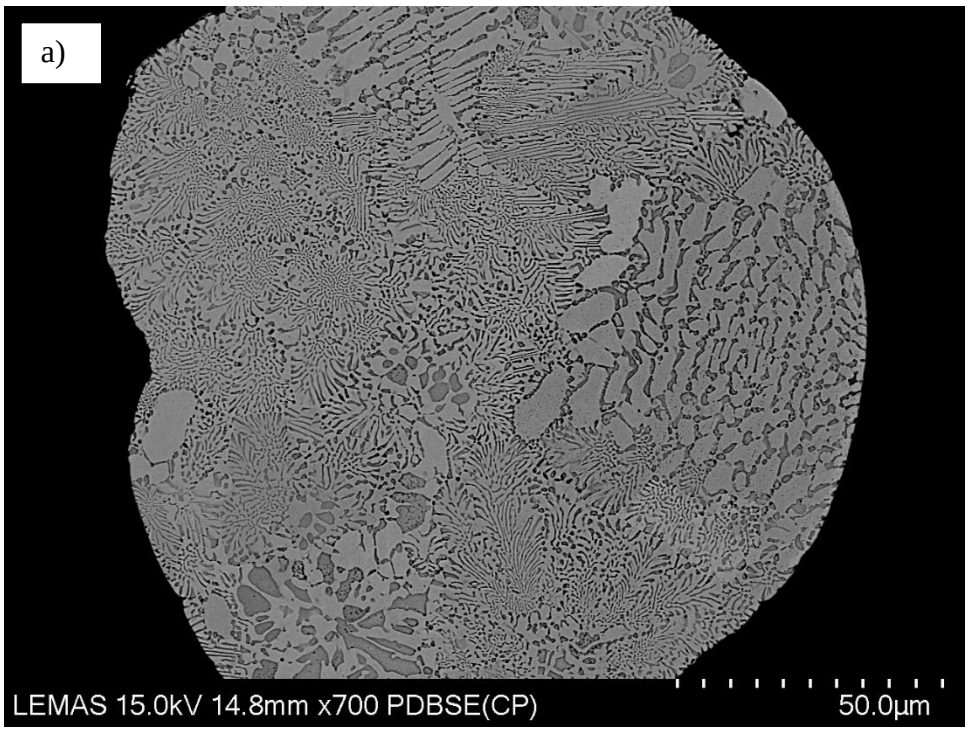
a)
LEMAS 15.0kV 14.8mm x700 PDBSE(CP)
50.0µm

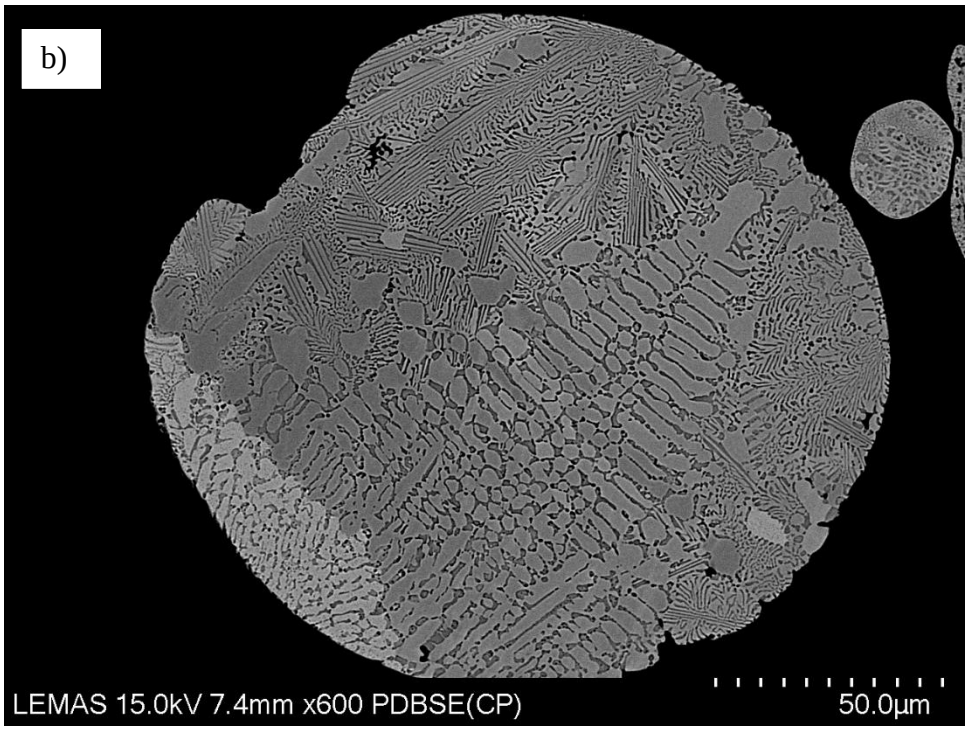
b)
LEMAS 15.0kV 7.4mm x600 PDBSE(CP)
50.0µm

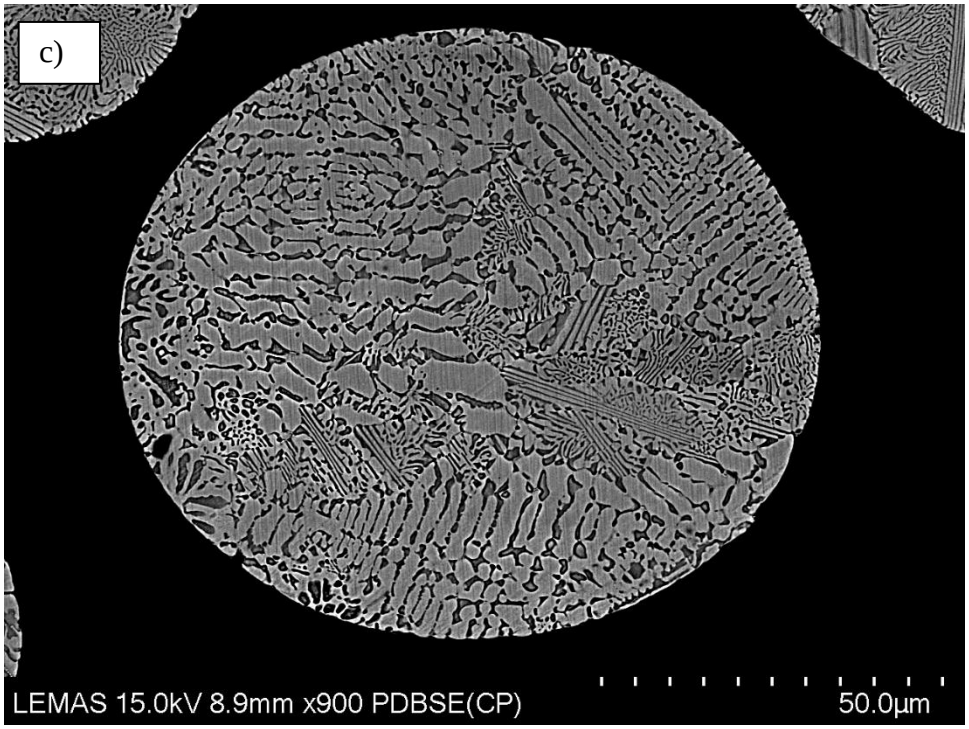
c)
LEMAS 15.0kV 8.9mm x900 PDBSE(CP)
50.0µm

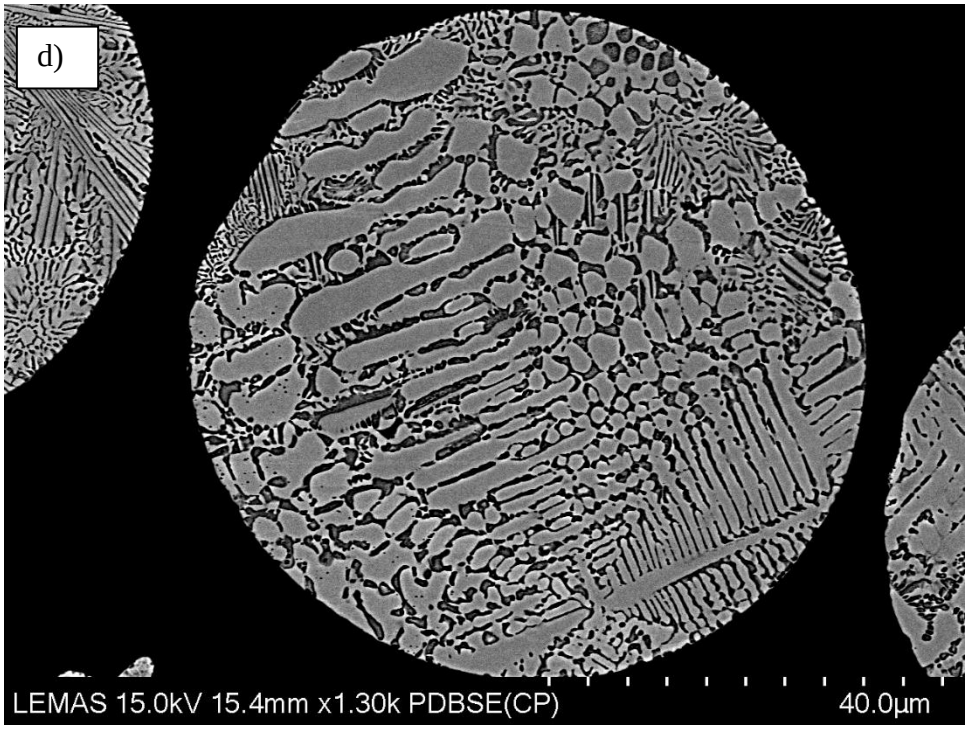
d)
LEMAS 15.0kV 15.4mm x1.30k PDBSE(CP)
40.0µm

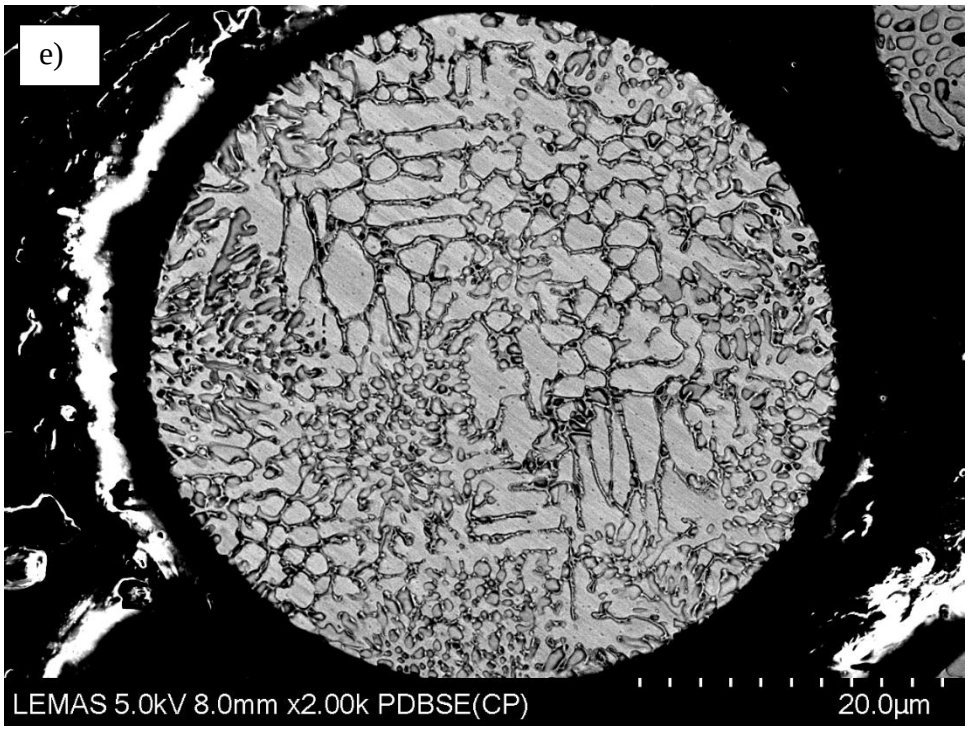

Figure 3.40 $AlCoCrFeNi_{2.1}$ morphology as powder size decreases, showing increasing volume fraction of FCC phase. Powders from **a)** to **e)** are taken from powder size fractions 150 – 212 µm, 106 – 150 µm, 75 – 106 µm, 53 – 75 µm and 38 – 53 µm, respectively.

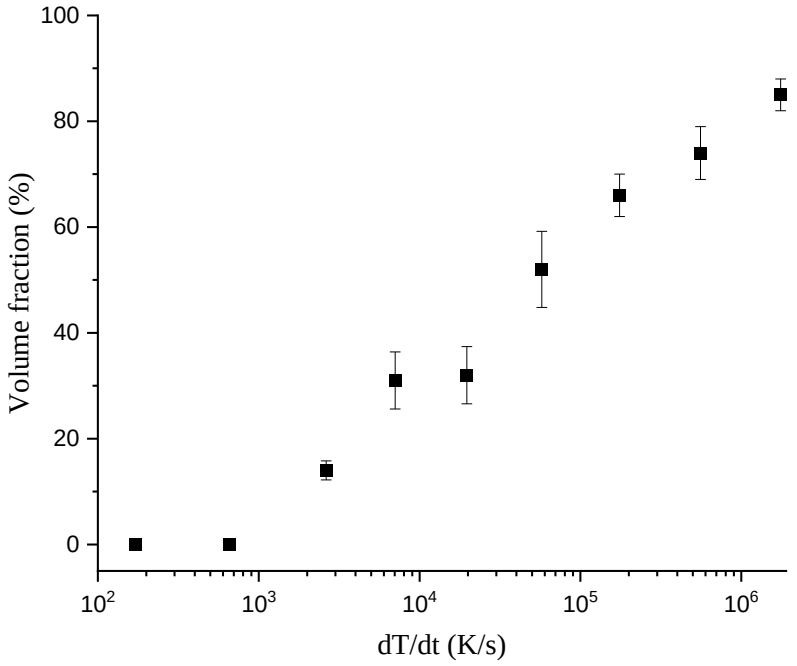

Figure 3.41 Increasing dendritic volume fraction with increasing cooling rate.

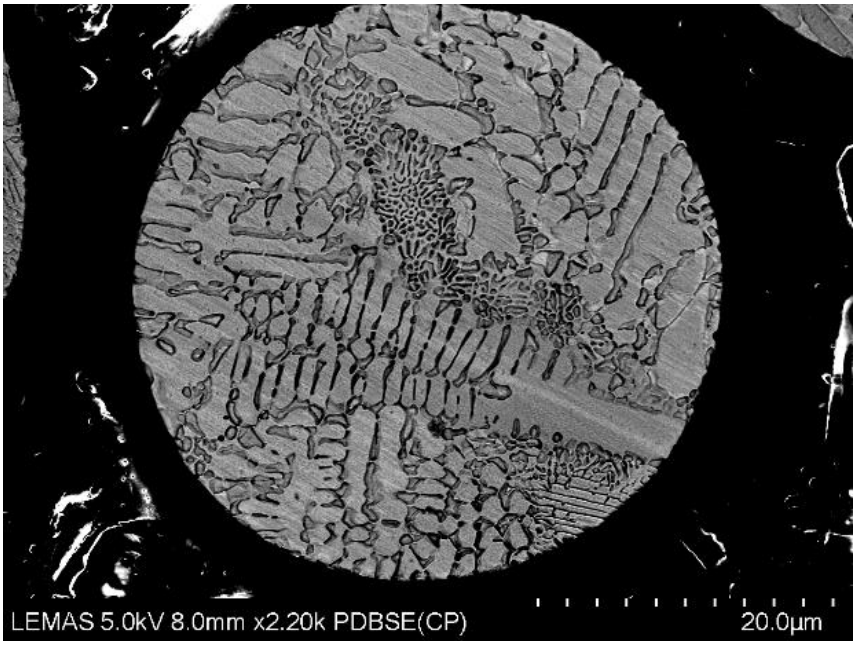

Figure 3.42 Particle from 38 – 53 µm size fraction with eutectic microstructure retained in the interdendritic region.

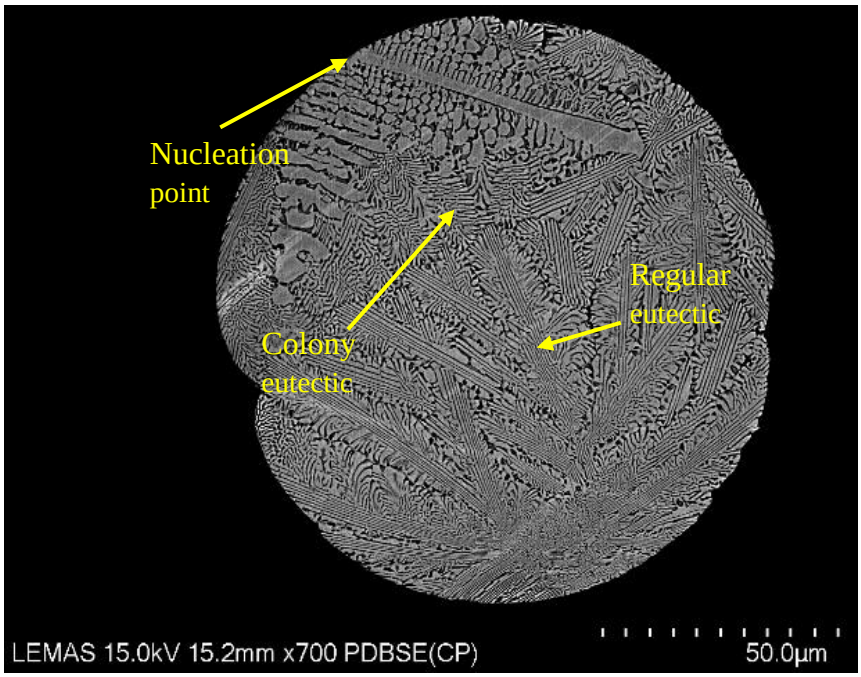

Figure 3.43 Particle from 75 – 106 µm size fraction with clear nucleation point leading to dendritic region. Colony and regular eutectic regions are also visible.

By analysing the $AlCoCrFeNi_{2.1}$ powders using TEM, it is observed that the rapid cooling achieved via drop-tube processing is sufficient to inhibit $L1_2$ ordering at relatively low cooling rates. This is shown by the TEM analysis in Figure 3.45, where the SAD patterns of particle from the 500 - 850 µm and 38 - 53 µm size fractions are presented. Figure 3.45a presents the regions from which the SAD patterns are taken in the 500 - 850 µm particle, whereby the pattern in Figure 3.45c shows that B2 ordering is retained (see superlattice spots) and Figure 3.45d shows that $L1_2$ ordering is lost. Figure 3.45b presents the regions from which the SAD patterns are taken in the 38 - 53 µm particle. Figure 3.45e shows that B2 ordering is lost in a particle from the 38 - 53 µm size fraction. As expected, $L1_2$ ordering is also inhibited in this particle as well (see Figure 3.45f), as it experiences a larger cooling rate than the 500 - 850 µm particle. As such, it can be concluded that a cooling rate of 650 K s^{-1} can lead to disorder trapping of the $L1_2$ phase but a higher cooling rate is required for disorder trapping of the B2 phase.

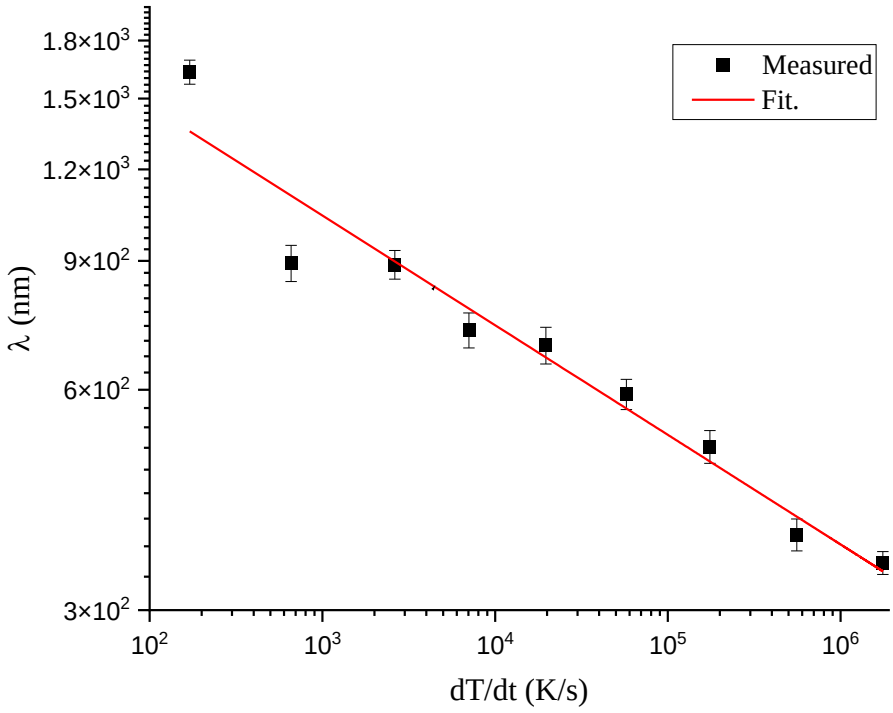

Figure 3.44 Interlamellar spacing versus cooling rate for $AlCoCrFeNi_{2.1}$ powders.

A morphology unobserved previously in $AlCoCrFeNi_{2.1}$ is worth noting and appears in particles of size $d < 212$ µm (shown in Figure 3.46a), where a dark dendritic phase appears to have nucleated as the primary phase. From this dark dendritic phase, a lighter dendrite has nucleated and is observed growing around its perimeter. Although the light, Cr-rich, dendrites have previously been observed in rapidly cooled $AlCoCrFeNi_{2.1}$ [117][124], this is, as far as the author is aware, the first instance of dendrites of the darker BCC phase being observed in dendritic form.

Figure 3.46b shows that this dark, Al-Ni rich phase can grow to dominate the microstructure, with the light phase forming the interdendritic region. Therefore, it is noted that some particles are observed to only have FCC dendrites (see any of Figures 3.39, 3.40, 3.42 and 3.43) and others to have only BCC dendrites. The EDX scan in Figure 3.47 shows that the dark dendrites are the Al-Ni rich, BCC phase, whereas Figure 3.48 shows a lighter-contrast dendrite depleted in aluminium and nickel in the microstructure of a particle from the 53 - 75µm size fraction. It must be noted that FCC dendrites remain

the dominant primary solidification microstructure, suggesting that they are the fastest growing primary. Nevertheless, the growth of BCC dendrites may be attributed to a critical undercooling at which disorder trapping occurs, causing the growth velocity of the A2 phase to compete with the FCC phase.

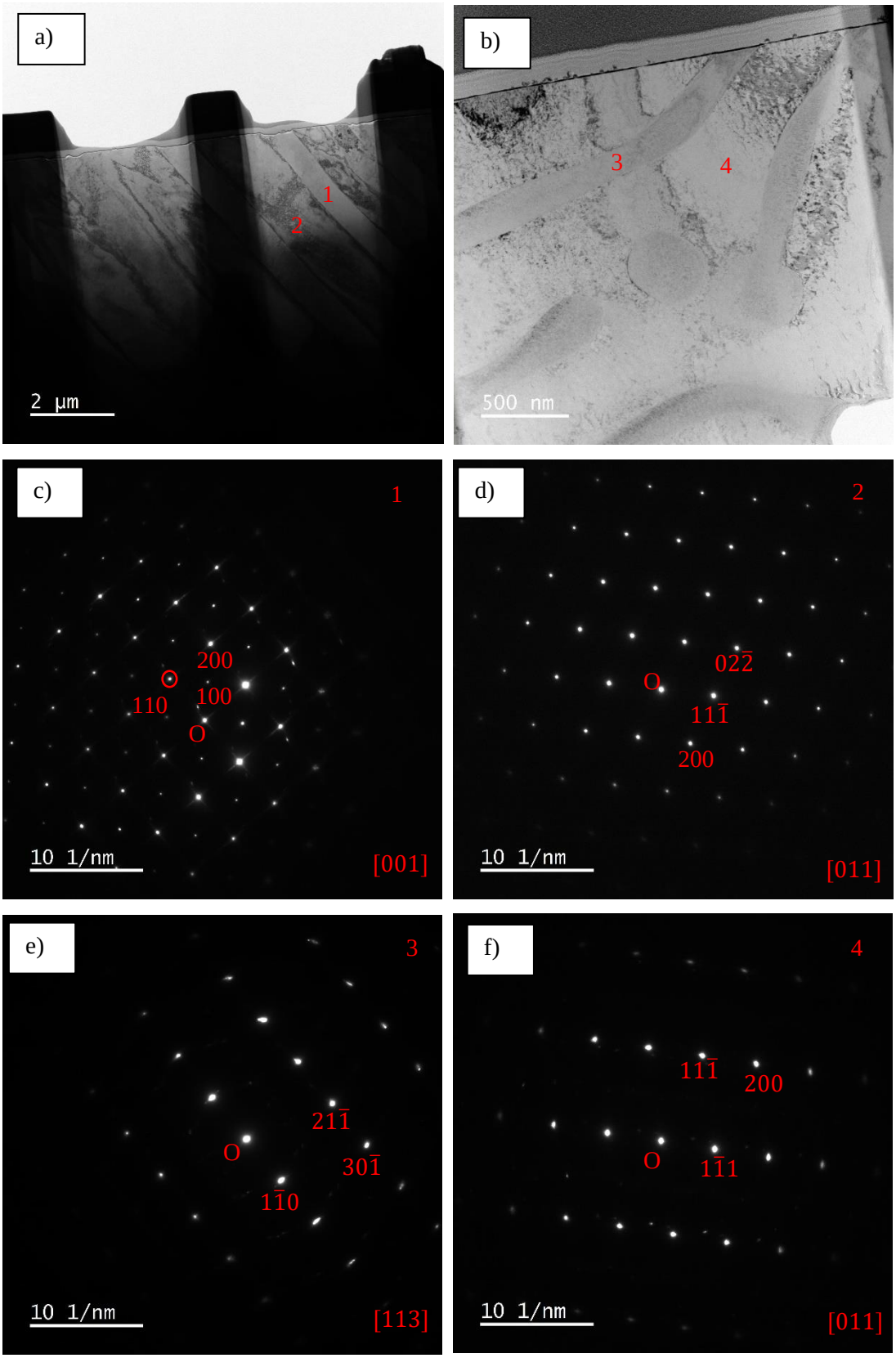
a)
1
2
2 µm
b)
3
4
500 nm
c)
1
200
110
100
O
10 1/nm
[001]
d)
2
022̄
O
11̄1
200
10 1/nm
[011]
e)
3
21̄1̄
O
301̄
1̄10
10 1/nm
[113]
f)
4
11̄1̄
200
O
1̄11
10 1/nm
[011]

Figure 3.45 a Lamellar region from 500 - 850µm size particle, with corresponding SAED patterns showing ordered B2 and disordered FCC structures in regions labelled 1 and 2, respectively. **Figure 3.45 b** Irregular lamellae from 38 – 53 µm size particle, with corresponding SAED patterns showing disordered BCC and disordered FCC structures in regions labelled as 3 and 4, respectively.

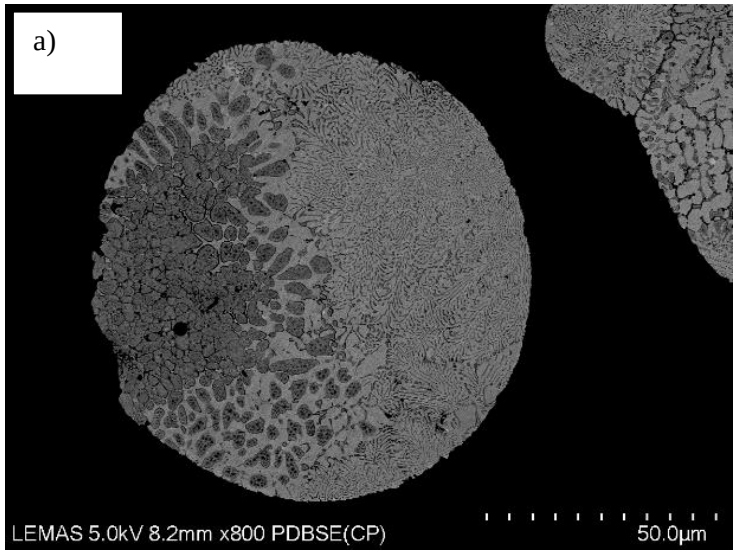

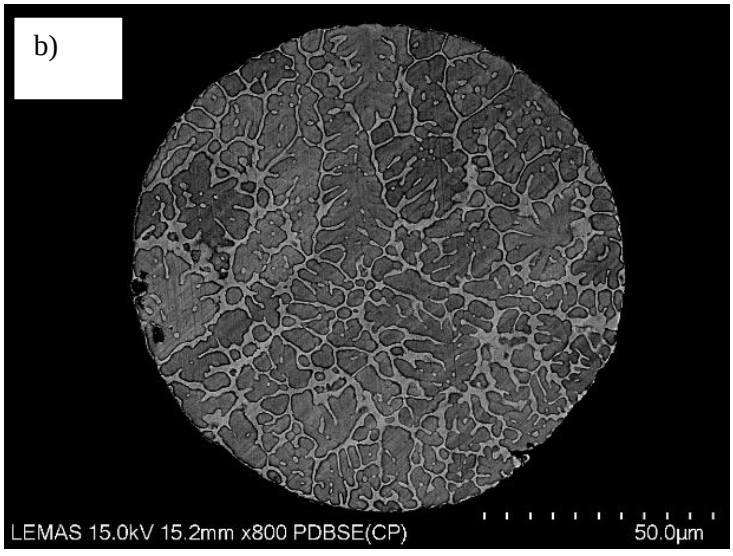

Figure 3.46 a BCC dendrites observed within particles of 75 – 106 µm size fraction **Figure 3.46 b** BCC dendrites extending beyond localized region and occupying full microstructure.

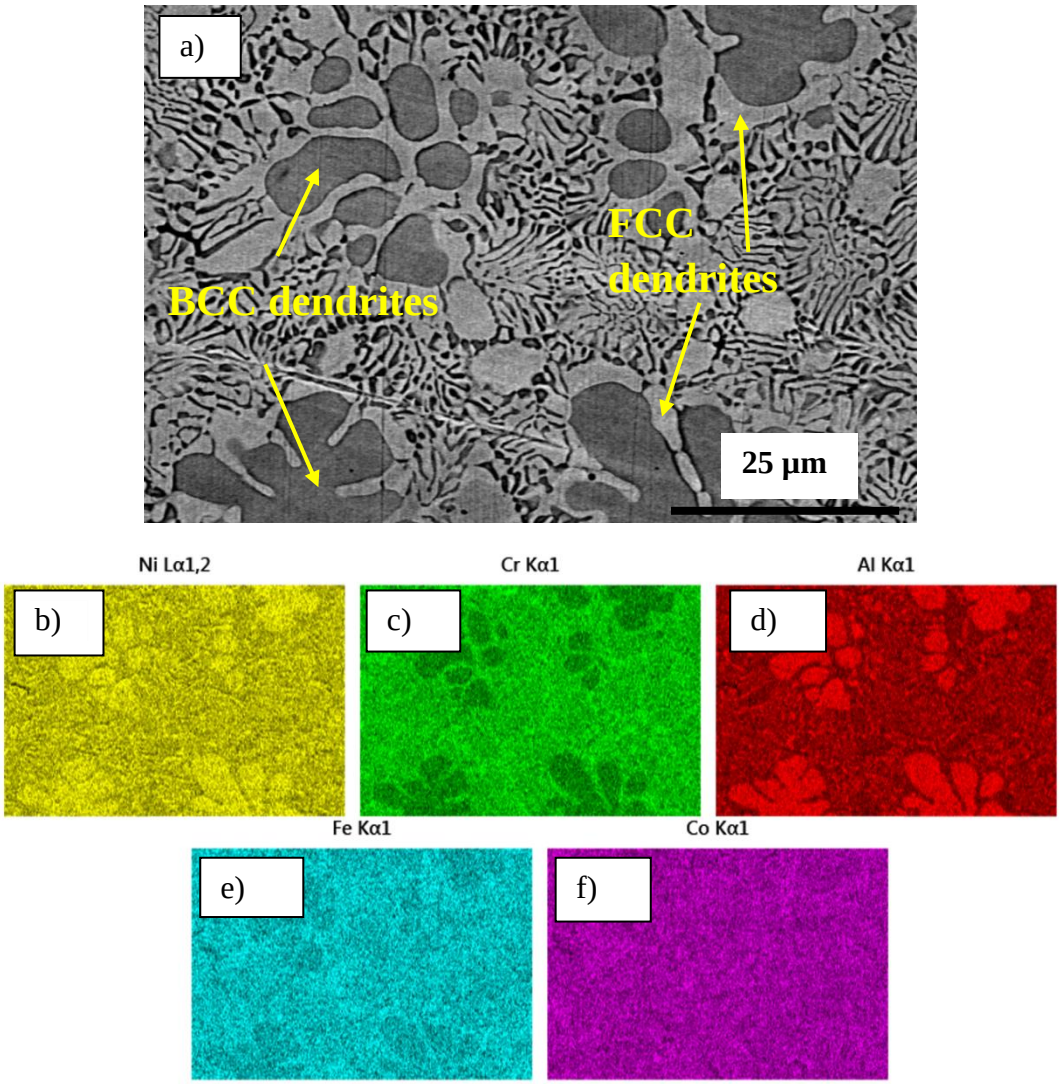

Figure 3.47 Al and Ni rich (BCC) dendrites of parasite-like phase observed within the 106 µm < *d* < 150 µm and 150 µm < *d* < 212 µm powder-size fractions.

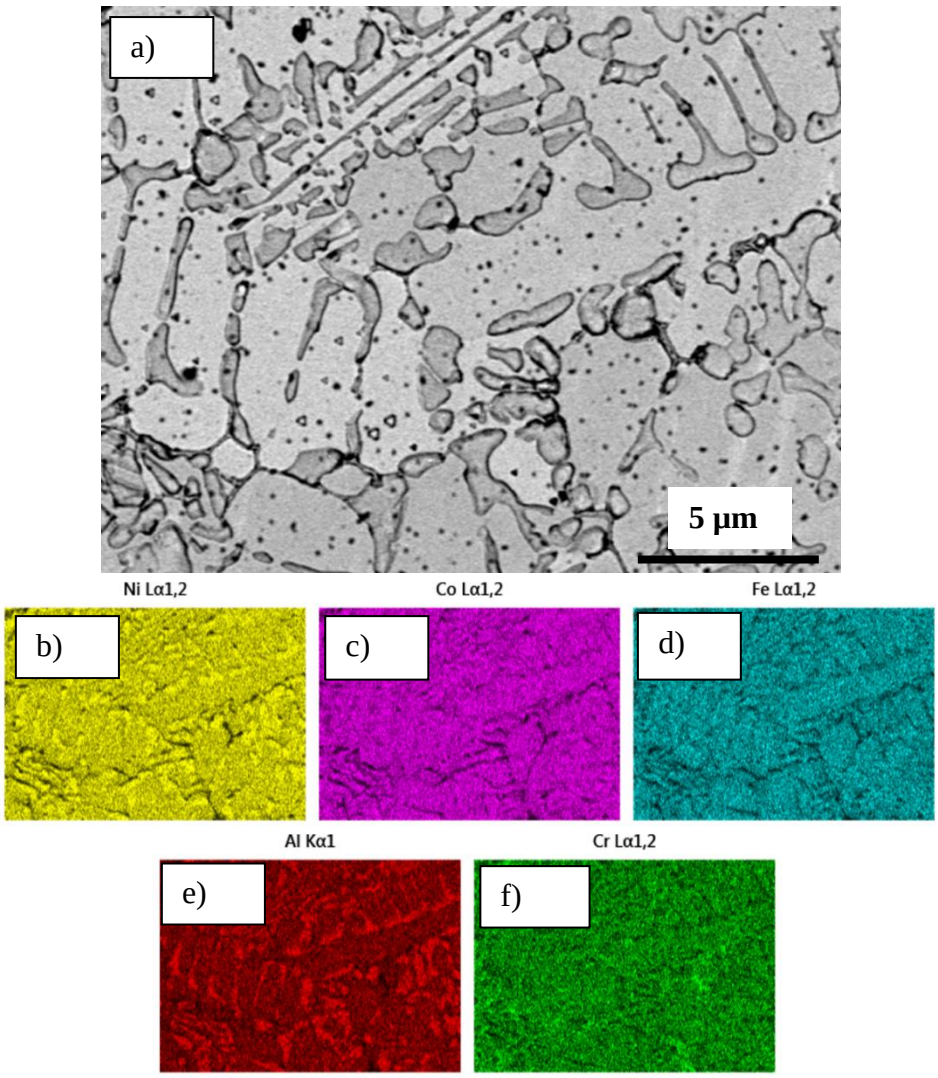

Figure 3.48 Al and Ni depleted (FCC) dendrite observed within a particle from the smallest powder-size fraction (38 µm < *d* < 53µm).

3.3.2 Microhardness

With relation to microhardness, the drop-tube-processed $AlCoCrFeNi_{2.1}$ powders show a weak Hall-Petch relation. The powders' microhardness does not vary greatly from an average value of around 340 $Hv_{0.03}$, even though the lamella spacing varies by a factor of 4.5 over this range of particle sizes. This unexpected result is discussed in detail in Section 3.1.3. The main argument, however, is that the increasing FCC volume fraction counteracts any mechanical benefits from grain refinement. Powders from the 150 - 212 µm size-fraction were chosen to be annealed for 30 minutes at 700 ºC, in order to investigate the effect on microhardness. The annealed powders showed an average microhardness that is 32 % higher than the non-annealed powders of the same size range (see Figure 3.49). However, the annealed powders are in fact expected to show reduced microhardness, as lamellar spacing increases by an average of 200 nm due to annealing. Figure 3.50 shows a micrograph of the annealed sample, where the slightly coarsened λ values are displayed.

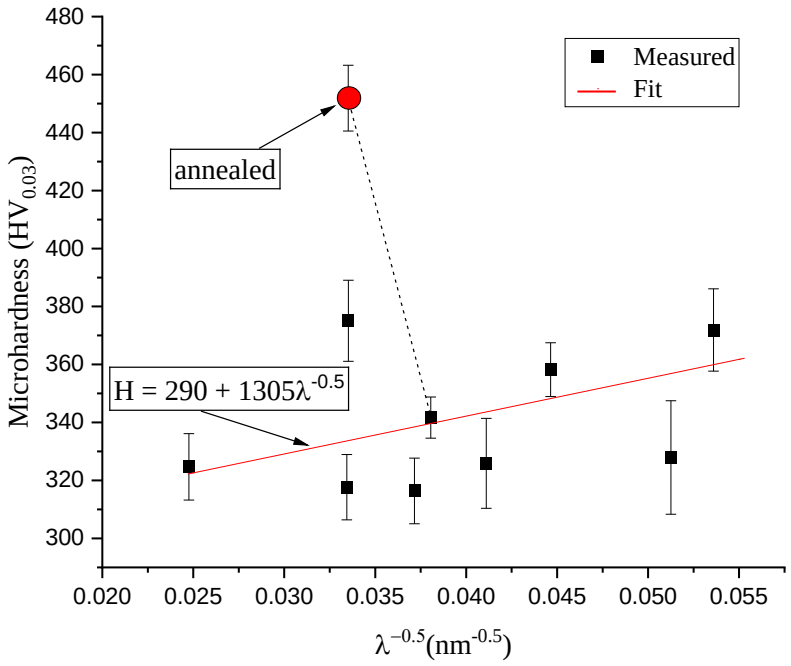

Figure 3.49 Microhardness of $AlCoCrFeNi_{2.1}$ powders as a function of lamellar spacing in a Hall-Petch plot.

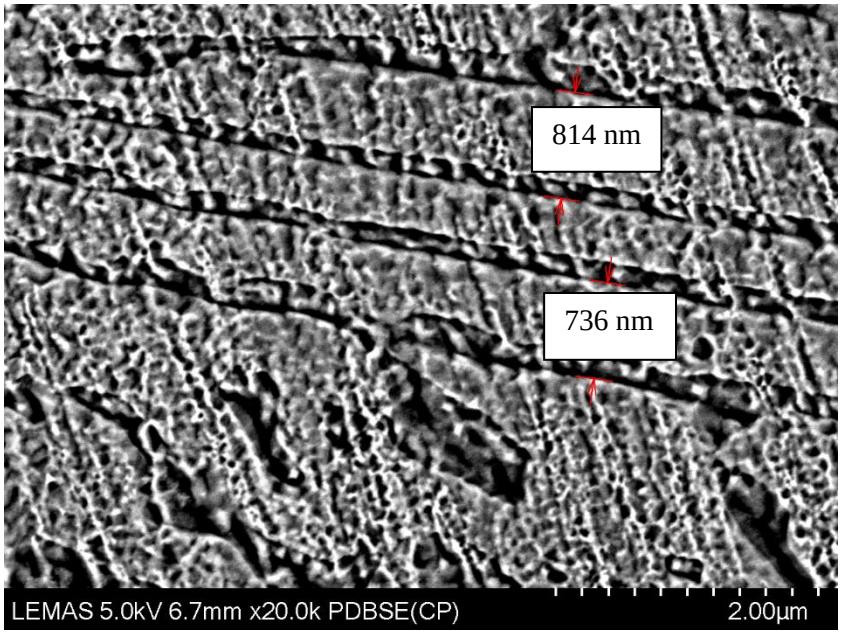

Figure 3.50 Backscattered SEM image of annealed particle from 150 - 212 µm size-fraction.

3.3.3 Discussion

In this section, drop-tube-processed powders of the $AlCoCrFeNi_{2.1}$ EHEA were presented. The sizes of the retrieved powders ranged from > 850 µm to 38 µm, with a corresponding range of cooling rates from 114 K s^{-1} to 1.75×10^{6} K s^{-1}. With increased cooling rate and decreased powder size, several notable features were observed in the $AlCoCrFeNi_{2.1}$ powders, which are: dendritic growth/departure from eutectic growth, growth of BCC dendrites, growth of cellular eutectic colonies and elimination of interdendritic eutectic. Prior to the appearance of those features, the microstructure largely retained the regular eutectic structure seen in the as-cast alloy, differing only with refined lamellar spacing.

Lesser cooling rates are required for the growth of the colony eutectic structure than for dendritic growth. A rapid solidification study by Rios et al. [177] on AlNbNi observes a transition from a regular eutectic to a colony eutectic very similar to the one observed in Figure 3.38b. Rios et al. make no observation of dendritic growth, although this is likely

to be due their method (Bridgman solidification) and a relatively low cooling rate (1000 K/s), which in turn does not achieve the required undercooling for the eutectic to dendritic transformation. Although the alloy of Rios et al. is not a HEA, it may support the observation that colony eutectic structures are formed more readily with rapid cooling than other morphologies.

Departure from eutectic growth is observed at cooling rates around 10^4 K/s, indicating that sufficient undercooling is achieved at this cooling rate for the eutectic to dendritic transformation to occur. Theoretically, it is expected that at sufficiently high driving force all eutectic systems will undergo an eutectic to dendritic transition. This reflects both the limited rate at which solute diffusion can facilitate eutectic growth and the fact that the eutectic spacing cannot be reduced indefinitely, leading to a situation in which, at sufficiently high undercooling, a dendritic front can outgrow the eutectic [178]. A study on the rapid solidification of the AgCuGe (ternary eutectic alloy) achieves a similar cooling rate of 9.3×10^3 K/s, although it was shown in this alloy that the undercooling in this condition is not sufficient for departure from eutectic growth [179]. Unlike the $AlCoCrFeNi_{2.1}$ alloy, an anomalous eutectic is observed in AgCuGe at intermediate cooling rates prior to dendritic growth.

Analysing the $AlCoCrFeNi_{2.1}$ powders using TEM unveiled that a relatively low cooling rate is sufficient to inhibit $L1_2$ ordering. This was proved by the analysis in Figure 3.45a, where the SAD patterns of a particle from the 500 - 850 µm size fraction show the loss of $L1_2$ ordering and that B2 ordering is retained. It is further shown that B2 ordering is lost in a particle from the 38 - 53 µm size fraction, wherein as expected due to the large cooling rate of 1.75×10^6 K s^{-1}, $L1_2$ ordering is also inhibited. It can therefore be deduced that a cooling rate of 650 K s^{-1} can lead to disorder trapping of the $L1_2$ phase. Although disorder trapping of the $L1_2$ phase may also be possible at a lower cooling rate (in larger powders), it is not feasible to conduct TEM and SAED analysis on all samples. It is also evident that a higher cooling rate is required for disorder trapping of the B2 phase. It may be possible that the B2 – A2 transformation can be achieved at lower cooling rates than 1.75×10^6 K s^{-1}, although as with the $L1_2$ phase, further TEM analysis would be required to reveal a closer estimate of the cooling rate required for this. This observation is in accord with the argument of Ding et al. that the B2 – A2 transformation requires larger

cooling rates to be achieved than the $L1_2$ – FCC transformation [117]. Ding et al. also argue that disorder trapping of the B2 phase is expected for $AlCoCrFeNi_{2.1}$ gas atomised powders 20 - 80 µm in size. Although Ding et al. do not support their argument by TEM analysis, Figure 3.45b confirms that the statement of Ding et al. is a reasonable one, as B2 ordering is retained for $AlCoCrFeNi_{2.1}$ particles of 500 - 850 µm.

It was shown in Figure 3.46 that BCC dendrites were observed where $d < 212$. To explain the occurrence of the BCC dendrites, the undercooling of the particles must be considered as follows. At most undercoolings the BCC phase will grow as its B2 variant, which will give the disordered FCC phase a growth advantage, it being known that disordered phases grow significantly faster than ordered phases [180]. However, if the undercooling is sufficient for disorder trapping in the BCC phase (i.e. a B2 – A2 transition) the growth advantage of the FCC phase will be much reduced, wherein a suitable heterogenous nucleant may favour the growth of BCC dendrites over FCC. Moreover, if recalescence leads to a reduction in undercooling during growth, a transition back to B2 growth would significantly reduce the BCC growth rate, leading to overgrowth of the BCC phase by FCC dendrites, as appears to be the case in Figure 3.46a and Figure 3.47a. Given this explanation for the appearance of BCC dendrites, it may be reasoned that the undercooling experienced by the 150 – 212 µm is enough for the B2 – A2 transition. The SAD pattern from Figure 3.45d had confirmed the disorder trapping of the B2 phase at the largest cooling rate, but the observation of BCC dendrites may be a more accurate indication of the conditions required for the B2 – A2 transformation. FCC dendrites were previously observed in gas-atomized [117] and air-cooled [124] $AlCoCrFeNi_{2.1}$, but BCC dendrites have never been reported prior to our disclosed drop-tube experiment. This further affirms that a critical undercooling is required for the competitive effect between the BCC and FCC dendrites.

Furthermore, it was observed that with increasing cooling rate, the primary FCC volume fraction increased monotonically, reaching an average maximum of 85% in powders of the 38 - 53 µm size-fraction. As such, faster cooling rates in $AlCoCrFeNi_{2.1}$ powders appear to favour the formation of the FCC phase over the BCC. It is also evident that faster cooling rate leads to departure from eutectic growth, leading to dendritic microstructures with a eutectic in the interdendritic regions. Despite the BCC dendrites

observed where $d < 212$ μm, FCC dendrites remained the dominant primary solidification microstructure. This suggests that FCC dendrites are the fastest growing primary. As long as the critical undercooling is not attained and B2 ordering is retained, the FCC phase retains the advantage of higher growth velocity.

Considering the lamellar as-cast structure, smaller $AlCoCrFeNi_{2.1}$ powders would be expected to have superior microhardness values as per the Hall-Petch relation i.e. $\sigma_y = \sigma_0 + \kappa_H \lambda^{-0.5}$; where σ_y is the yield strength of the material, σ_0 is the friction stress, κ_H is Hall-Petch coefficient and λ is the interlamellar spacing. Figure 3.49 showed that the Hall-Petch effect is observed in $AlCoCrFeNi_{2.1}$ powders, although it is a weak relation, where the values of microhardness do not vary greatly from an average value of around 340 $Hv_{0.03}$. The Hall-Petch relation may have been observed more strongly if the microhardness tests were intentionally conducted on lamellar regions of the powders. However, such microhardness values would be unrepresentative of $AlCoCrFeNi_{2.1}$ powders and are likely to create a distorted idea of the true overall microhardness of the powders. For those reasons, the microhardness values presented in this work are obtained with the indentations being made in randomly chosen locations of the droplets.

This observation may be explained by the dominance of the primary FCC phase in smaller droplets. As the FCC phase is the softer phase, its increased presence with increased cooling rate is expected to counter the strengthening due to scale refinement which would otherwise be observable. Meanwhile, it is worth drawing back on the inhibited atomic ordering due to the large cooling rates. As the disordered phases have more slip planes [181], disorder-trapping may also be a factor which hinders the alloy powders' hardness. As both phenomena occur in conjunction, ambiguity arises in identifying which of them has a more detrimental effect on the microhardness of the powders. However, for the powders in the 850 - 1000 μm size-fraction, it is likely that disorder trapping is the main factor contributing to the lower-than-expected microhardness value. This is because the phase volume fractions in the droplets of this size do not differ significantly from the as-cast alloy. Yet, the average microhardness in this size fraction is 12 % smaller than that of the as-cast alloy. As such, this drop in microhardness could be attributed to the disorder

trapping of the $L1_2$ phase. As such, disorder trapping seems likely to soften the microstructure and counter the strengthening effect of grain refinement.

Considering that annealing increases the microhardness of $AlCoCrFeNi_{2.1}$ powders (see Figure 3.49) despite coarsening, it could be justified that the disordered phases in the powders may be metastable. Namely, annealing the powders is expected to supply the driving force required for the disorder to order transformations to take place, thus improving the microhardness due to the reduced number of slip planes in ordered phases. Overall, however, the powders do show a Hall-Petch relationship (albeit a weak one) despite the impacts of disorder trapping and increased FCC volume fraction. This is consistent with the occurrence of grain refinement but with the mechanical benefits being countered by these two effects.

As far as the microstructure morphology of the powders is concerned, it can be concluded that the microstructure evolves from regular/irregular eutectic to cellular/colony eutectic, followed by a dendritic structure with regular eutectic in the interdendritic region. Finally, at the highest cooling rate, a predominantly dendritic structure may be observed with no eutectic observed in the interdendritic region.

4. Conclusions

1. The neural network referred to throughout the work as NN1 operated with a dataset including atomic percentage data only and yielded an average prediction accuracy of 92%. As far as the authors are aware, the predictive accuracy of NN1 is only 1% less than the highest accuracy achieved by researchers to date. The fact that NN1 performs with such accuracy has significant implications as it shows that the complete abandonment of HR parameters is not only possible but also advantageous. This result comes as no surprise, since atomic percentage data does not require estimations to be made (unlike thermodynamic and HR features), thus leading to datasets that are more consistent and less prone to errors. Due to the current saturation in the number of predictive parameters, a lean and accurate approach such as that of NN1 is crucial in achieving models that are scalable for rapid use by researchers.

2. The $Al_xCrCuFeNi$ system was found, using a neural network, to have a critical Al atomic percentage of 1.4 beyond which the alloy's microstructure becomes dominant with intermetallic phases. The x = 1.0, x = 1.3, x = 1.5 and x = 2.0 alloys were manufactured using an arc-melter to confirm the predictions obtained from the neural networks. The x = 1.0 and x = 1.3 compositions were confirmed to comprise SS+IM microstructures with the IM phase adhering to the vicinity of the dendrites.

3. The x = 1.5 alloy in $Al_xCrCuFeNi$ showed a significantly more complex microstructure, in which a "Chinese script" IM was observed in addition to a "sunflower structure" comprising a lamellar eutectic surrounding nano-scale preciptates appearing to have formed via spinodal decomposition. The x = 2 composition yields an alloy that is very brittle in nature, and its microstructure shows the clear presence of coarse spherical IM precipitates in the ID region, together with much finer spherical and needle shaped precipitates decorating the dendrite boundaries.

4. The growth of a needle-like phase is observed in the ID region of as-cast, equimolar AlCrCuFeNi, together with spinodally decomposed precipitates in its dendrites. The needle-like phase is found to be Cr-Fe rich, comprising a B2 ordered lattice with a parameter of 2.63 Å. The precipitates are Al-Ni rich and B2 ordered, with a lattice parameter of 2.42 Å. The rapid cooling of AlCrCuFeNi was carried out to explore the possibility of inhibiting the growth of these features, wherein it was found that their formation is inhibited only at the highest attained cooling rate of 1.13×10^6 K/s. Due to a core characteristic of HEAs that is sluggish diffusion, it would be expected that the solid-state spinodal decomposition which gives rise to Al-Ni precipitates would be suppressed at cooling rates of a lower magnitude. Nevertheless, this finding shows that at higher cooling rates simpler microstructures can be obtained and the extension of the solid-solution of HEAs is possible via RSP. On the other hand, the FCC structure in AlCrCuFeNi, which is found in its ID matrix, is inhibited at a cooling rate of only 112 K/s (d > 850 µm powders).

5. The XRD traces of AlCrCuFeNi powders are in accord with the observation that FCC growth is suppressed. However, weak FCC peaks remain which are attributed to the Cu nano-precipitates (globular and plate-like) observed in the TEM analysis. These spherical and plate-like copper nano-precipitates arise due to the small bonding energy of Cu with Cr and Fe which are the dominant elements in the ID region.

6. The microhardness of the AlCrCuFeNi droplets is probed and found to increase with cooling rate from 519 $HV_{0.03}$ in the slowest cooled powders to 805 $HV_{0.03}$ in the fastest cooled powders. A stark increase is observed between the d < 850 µm and the 500 – 850 μm powder size-fractions, which is attributed to the loss of the FCC structure. As the FCC is the softer phase in the alloy, its early suppression means that the hardness of the alloy is enhanced. Generally, a Hall-petch relation is observed in the AlCrCuFeNi powders, confirming that grain refinement improves the microhardness of the powders.

7. The $AlCoCrFeNi_{2.1}$ EHEA was also chosen for drop-tube processing in order to investigate the effect of cooling rate on eutectic growth. TEM analysis confirmed that phases in as-cast $AlCoCrFeNi_{2.1}$ are ordered B2 and $L1_2$ phases that are Al-Ni rich and Cr-Fe-Ni rich, respectively. It was found that disorder trapping of the $L1_2$ structure is observed at 650 K/s, whereas the B2 ordered structure requires higher cooling rates to undergo the B2 – A2 transformation. In this work, disorder trapping of the B2 structure is achieved at 1.75×10^6 K/s. It may be possible that this can be achieved at lower cooling rates, although further TEM analysis would be required to reveal a closer estimate of the cooling rate required for the B2 – A2 transformation.

8. With increasing cooling rate, the primary FCC volume fraction increased monotonically, reaching an average maximum of 85% in powders of the 38 - 53 μm size-fraction. As such, faster cooling rates in $AlCoCrFeNi_{2.1}$ powders appear to favour the formation of the FCC phase over the BCC. However, if the undercooling is sufficient for disorder trapping in the B2 phase (i.e. a B2 – A2 transition) the growth advantage of the FCC phase will be much reduced, wherein a suitable heterogenous nucleant may favour the growth of BCC dendrites over FCC. Faster cooling rates were also shown to lead departure from eutectic growth, resulting in dendritic microstructures with a eutectic in the interdendritic regions.

9. The microhardness of the powders shows a weak Hall-Petch relation, where the values of microhardness do not vary greatly from an average value of around 340 $Hv_{0.03}$. This is explained by the increasing FCC volume fraction with increasing cooling rate. Disorder trapping is also suggested to soften the microstructure and counter the strengthening effect of grain refinement.

10. As far as the microstructure morphology of $AlCoCrFeNi_{2.1}$ powders is concerned, it can be concluded that the microstructure evolves from regular/irregular eutectic to cellular/colony eutectic, followed by a dendritic structure with regular eutectic in the interdendritic region. Finally, at the highest cooling rate, a predominantly dendritic structure is observed with no eutectic observed in the interdendritic region. Although the highest cooling rates are unlikely to be achieved at scale, this project sheds light on the potential of RSP on extending the envelope of functional HEAs. Equally, this work has highlighted the usefulness of HEA powder metallurgy, in that largely attainable cooling rates may lead to significant improvements in microstructure and mechanical properties.

Future work

This project has made observations that are relevant to today's landscape of HEA research, the most notable of which are the use of an elemental approach to predict HEAs (rather than HR features) and the successful use of RSP to extend the solid-solution window of HEAs. Equally, this project sheds light on further questions that must be investigated to achieve a more complete understanding of the alloys in this work and in turn, the field as a whole. These points are highlighted below:

1. Although it has become evident that machine learning techniques are promising in unveiling novel HEAs, the limiting factor for progress on this front is the accuracy of HEA datasets. Until today, the role of processing in HEA formation has been largely ignored. As seen in this work, departure from equilibrium in HEA processing may largely influence the HEA's properties and microstructure. As such, a crucial point in moving forward is the construction of datasets that include processing information. Another important task on this front is the use of techniques such as phase-field simulations to predict how departure from equilibrium influences HEA formation.

2. This project has shown that RSP using a drop tube facility can extend the solid solution of the equimolar $Al_xCrCuFeNi$ system. More generally, this project has shed light on the extent to which RSP can be used to extend the SS-window across a wide range of HEA compositions. Not just limited to drop-tube, this work is relevant to the whole field of powder metal production by atomization, influencing the entirety of the additive manufacturing landscape. Given that increasing Al content results in a lower-density alloy but also complicates the microstructure, it would be of interest to explore the largest percentage of Al which can be used in the alloy while still being able to achieve a simple solid solution post-RSP. Exploring the drop tube processing of the $x = 1.5$ composition is suggested, as it is easy to observe the potential simplifications in its microstructure (inhibition of Chinese Script and sunflower structures should be

expected) and is also closer to the solid-solution window than any other composition where $x > 1.5$.

3. In $AlCoCrFeNi_{2.1}$ powders, disorder trapping of the B2 structure is confirmed at 1.75×10^6 K s^{-1}. However, it is likely that the B2 – A2 transformation may be achieved at lower cooling rates, as there will be a critical undercooling for the competitive effect observed between the BCC and FCC dendrites. As such, further TEM analysis is suggested to reveal an accurate estimate of the cooling rate needed for the B2 – A2 transformation.

References

[1] J.W. Yeh, Y.L. Chen, S.J. Lin, S.K. Chen, High-Entropy Alloys – A New Era of Exploitation, Mater. Sci. Forum. 560 (2007) 1–9. https://doi.org/10.4028/www.scientific.net/msf.560.1.

[2] Y. Zhang, Y.J. Zhou, Solid Solution Formation Criteria for High Entropy Alloys, Mater. Sci. Forum. 561–565 (2007) 1337–1339. https://doi.org/10.4028/www.scientific.net/msf.561-565.1337.

[3] F. Otto, A. Dlouhý, C. Somsen, H. Bei, G. Eggeler, E.P. George, The influences of temperature and microstructure on the tensile properties of a CoCrFeMnNi high-entropy alloy, Acta Mater. 61 (2013) 5743–5755. https://doi.org/10.1016/j.actamat.2013.06.018.

[4] H. Zhang, Y. Pan, Y.Z. He, Synthesis and characterization of FeCoNiCrCu high-entropy alloy coating by laser cladding, Mater. Des. 32 (2011) 1910–1915. https://doi.org/10.1016/j.matdes.2010.12.001.

[5] J.P. Couzinié, G. Dirras, L. Perrière, T. Chauveau, E. Leroy, Y. Champion, I. Guillot, Microstructure of a near-equimolar refractory high-entropy alloy, Mater. Lett. 126 (2014) 285–287. https://doi.org/10.1016/j.matlet.2014.04.062.

[6] B. Zhang, M.C. Gao, Y. Zhang, S. Yang, S.M. Guo, Senary refractory high entropy alloy MoNbTaTiVW, Mater. Sci. Technol. (United Kingdom). 31 (2015) 1207–1213. https://doi.org/10.1179/1743284715Y.0000000031.

[7] M.C. Gao, D.E. Alman, Searching for Next Single-Phase High-Entropy Alloy Compositions, Entropy. 15 (2013) 4504–4519. https://doi.org/10.3390/e15104504.

[8] K.M. Youssef, A.J. Zaddach, C. Niu, D.L. Irving, C.C. Koch, A novel low-density, high-hardness, high-entropy alloy with close-packed single-phase nanocrystalline structures, Mater. Res. Lett. 3 (2014) 95–99. https://doi.org/10.1080/21663831.2014.985855.

[9] F. Otto, Y. Yang, H. Bei, E.P. George, Relative effects of enthalpy and entropy

on the phase stability of equiatomic high-entropy alloys, Acta Mater. 61 (2013) 2628–2638. https://doi.org/10.1016/j.actamat.2013.01.042.

[10] J.W. Yeh, Physical Metallurgy of High-Entropy Alloys, Jom. 67 (2015) 2254–2261. https://doi.org/10.1007/s11837-015-1583-5.

[11] M. Beyramali Kivy, M. Asle Zaeem, S. Lekakh, Investigating phase formations in cast AlFeCoNiCu high entropy alloys by combination of computational modeling and experiments, Mater. Des. 127 (2017) 224–232. https://doi.org/10.1016/j.matdes.2017.04.086.

[12] S. Zhang, C.L. Wu, C.H. Zhang, Phase evolution characteristics of FeCoCrAlCuVxNi high entropy alloy coatings by laser high-entropy alloying, Mater. Lett. 141 (2015) 7–9. https://doi.org/10.1016/j.matlet.2014.11.017.

[13] T. Yang, S. Xia, S. Liu, C. Wang, S. Liu, Y. Zhang, J. Xue, S. Yan, Y. Wang, Effects of AL addition on microstructure and mechanical properties of AlxCoCrFeNi High-entropy alloy, Mater. Sci. Eng. A. 648 (2015) 15–22. https://doi.org/10.1016/j.msea.2015.09.034.

[14] Y. Lu, Y. Dong, S. Guo, L. Jiang, H. Kang, T. Wang, B. Wen, Z. Wang, J. Jie, Z. Cao, H. Ruan, T. Li, A promising new class of high-temperature alloys: Eutectic high-entropy alloys, Sci. Rep. 4 (2014). https://doi.org/10.1038/srep06200.

[15] Y. Lu, Y. Dong, H. Jiang, Z. Wang, Z. Cao, S. Guo, T. Wang, T. Li, P.K. Liaw, Promising properties and future trend of eutectic high entropy alloys, Scr. Mater. 187 (2020) 202–209. https://doi.org/10.1016/j.scriptamat.2020.06.022.

[16] C.M. Liu, H.M. Wang, S.Q. Zhang, H.B. Tang, A.L. Zhang, Microstructure and oxidation behavior of new refractory high entropy alloys, J. Alloys Compd. 583 (2014) 162–169. https://doi.org/10.1016/j.jallcom.2013.08.102.

[17] Y. Lu, X. Gao, L. Jiang, Z. Chen, T. Wang, J. Jie, H. Kang, Y. Zhang, S. Guo, H. Ruan, Y. Zhao, Z. Cao, T. Li, Directly cast bulk eutectic and near-eutectic high entropy alloys with balanced strength and ductility in a wide temperature range, Acta Mater. 124 (2017) 143–150. https://doi.org/10.1016/j.actamat.2016.11.016.

[18] Z.Q. Xu, Z.L. Ma, M. Wang, Y.W. Chen, Y.D. Tan, X.W. Cheng, Design of novel low-density refractory high entropy alloys for high-temperature applications, Mater. Sci. Eng. A. 755 (2019) 318–322. https://doi.org/10.1016/j.msea.2019.03.054.

[19] B. Cantor, K.B. Kim, P.J. Warren, Novel multicomponent amorphous alloys, in: Mater. Sci. Forum, 2002: pp. 27–32. https://doi.org/10.4028/www.scientific.net/msf.386-388.27.

[20] Y. Zhang, Z.P. Lu, S.G. Ma, P.K. Liaw, Z. Tang, Y.Q. Cheng, M.C. Gao, Guidelines in predicting phase formation of high-entropy alloys, MRS Commun. 4 (2014) 57–62. https://doi.org/10.1557/mrc.2014.11.

[21] J.W. Yeh, Recent progress in high-entropy alloys, Ann. Chim. Sci. Des Mater. 31 (2006) 633–648. https://doi.org/10.3166/acsm.31.633-648.

[22] W. Steurer, Single-phase high-entropy alloys – A critical update, Mater. Charact. 162 (2020). https://doi.org/10.1016/j.matchar.2020.110179.

[23] M. Calvo-Dahlborg, S.G.R. Brown, Hume-Rothery for HEA classification and self-organizing map for phases and properties prediction, J. Alloys Compd. 724 (2017) 353–364. https://doi.org/10.1016/j.jallcom.2017.07.074.

[24] E. Menou, F. Tancret, I. Toda-Caraballo, G. Ramstein, P. Castany, E. Bertrand, N. Gautier, P.E.J. Rivera Díaz-Del-Castillo, Computational design of light and strong high entropy alloys (HEA): Obtainment of an extremely high specific solid solution hardening, Scr. Mater. 156 (2018) 120–123. https://doi.org/10.1016/j.scriptamat.2018.07.024.

[25] B. Chanda, P.P. Jana, J. Das, A tool to predict the evolution of phase and Young's modulus in high entropy alloys using artificial neural network, Comput. Mater. Sci. 197 (2021). https://doi.org/10.1016/j.commatsci.2021.110619.

[26] L. Qiao, Z. Lai, Y. Liu, A. Bao, J. Zhu, Modelling and prediction of hardness in multi-component alloys: A combined machine learning, first principles and experimental study, J. Alloys Compd. 853 (2021).

https://doi.org/10.1016/j.jallcom.2020.156959.

[27] K. Kaufmann, K.S. Vecchio, Searching for high entropy alloys: A machine learning approach, Acta Mater. 198 (2020) 178–222. https://doi.org/10.1016/j.actamat.2020.07.065.

[28] Q. Wu, Z. Wang, X. Hu, T. Zheng, Z. Yang, F. He, J. Li, J. Wang, Uncovering the eutectics design by machine learning in the Al–Co–Cr–Fe–Ni high entropy system, Acta Mater. 182 (2020) 278–286. https://doi.org/10.1016/j.actamat.2019.10.043.

[29] J. Joseph, M. Imran, P.D. Hodgson, M.R. Barnett, D.M. Fabijanic, Towards the large-scale production and strength prediction of near-eutectic AlxCoCrFeNi2.1 alloys by additive manufacturing, Manuf. Lett. 25 (2020) 16–20. https://doi.org/10.1016/j.mfglet.2020.06.002.

[30] Y. Cai, L. Zhu, Y. Cui, K. Geng, S.M. Manladan, Z. Luo, J. Han, Strengthening mechanisms in multi-phase FeCoCrNiAl1.0 high-entropy alloy cladding layer, Mater. Charact. 159 (2020). https://doi.org/10.1016/j.matchar.2019.110037.

[31] Y. Yin, Z. Chen, N. Mo, D. Kent, A.R. Candella, K.E. Koey, Q. Tan, M. Bermingham, M.X. Zhang, High-temperature age-hardening of a novel cost-effective Fe45Ni25Cr25Mo5 high entropy alloy, Mater. Sci. Eng. A. 788 (2020). https://doi.org/10.1016/j.msea.2020.139580.

[32] W.Y. Chen, X. Liu, Y. Chen, J.W. Yeh, K.K. Tseng, K. Natesan, Irradiation effects in high entropy alloys and 316H stainless steel at 300 °C, J. Nucl. Mater. 510 (2018) 421–430. https://doi.org/10.1016/j.jnucmat.2018.08.031.

[33] D. Castro, P. Jaeger, A.C. Baptista, J.P. Oliveira, An overview of high-entropy alloys as biomaterials, Metals (Basel). 11 (2021). https://doi.org/10.3390/met11040648.

[34] V. Geantă, T. Cherecheș, P. Lixandru, I. Voiculescu, R. Ștefănoiu, D. Dragnea, T. Zecheru, L. Matache, Virtual testing of composite structures made of high entropy alloys and steel, Metals (Basel). 7 (2017).

https://doi.org/10.3390/met7110496.

[35] M. Dada, P. Popoola, S. Adeosun, N. Mathe, High Entropy Alloys for Aerospace Applications, in: Aerodynamics, 2021. https://doi.org/10.5772/intechopen.84982.

[36] S. Xiang, J. Li, H. Luan, A. Amar, S. Lu, K. Li, L. Zhang, X. Liu, G. Le, X. Wang, F. Qu, W. Zhang, D. Wang, Q. Li, Effects of process parameters on microstructures and tensile properties of laser melting deposited CrMnFeCoNi high entropy alloys, Mater. Sci. Eng. A. 743 (2019) 412–417. https://doi.org/10.1016/j.msea.2018.11.110.

[37] D.B. Miracle, O.N. Senkov, A critical review of high entropy alloys and related concepts, Acta Mater. 122 (2017) 448–511. https://doi.org/10.1016/j.actamat.2016.08.081.

[38] C.C. Tung, J.W. Yeh, T. tsung Shun, S.K. Chen, Y.S. Huang, H.C. Chen, On the elemental effect of AlCoCrCuFeNi high-entropy alloy system, Mater. Lett. 61 (2007) 1–5. https://doi.org/10.1016/j.matlet.2006.03.140.

[39] O.N. Senkov, J.D. Miller, D.B. Miracle, C. Woodward, Accelerated exploration of multi-principal element alloys with solid solution phases, Nat. Commun. 6 (2015). https://doi.org/10.1038/ncomms7529.

[40] W. Kucza, J. Dąbrowa, G. Cieślak, K. Berent, T. Kulik, M. Danielewski, Studies of “sluggish diffusion” effect in Co-Cr-Fe-Mn-Ni, Co-Cr-Fe-Ni and Co-Fe-Mn-Ni high entropy alloys; determination of tracer diffusivities by combinatorial approach, J. Alloys Compd. 731 (2018) 920–928. https://doi.org/10.1016/j.jallcom.2017.10.108.

[41] T. Tsao, Y. Chang, K. Chang, J. Yeh, M. Chiou, S. Jian, C. Kuo, W. Wang, H. Murakami, Developing New Type of High Temperature Alloys–High Entropy Superalloys, Int. J. Metall. Mater. Eng. 1 (2015). https://doi.org/10.15344/2455-2372/2015/107.

[42] D.L. Beke, G. Erdélyi, On the diffusion in high-entropy alloys, Mater. Lett. 164 (2016) 111–113. https://doi.org/10.1016/j.matlet.2015.09.028.

[43] M.H. Tsai, Physical properties of high entropy alloys, Entropy. 15 (2013) 5338–5345. https://doi.org/10.3390/e15125338.

[44] K.Y. Tsai, M.H. Tsai, J.W. Yeh, Sluggish diffusion in Co-Cr-Fe-Mn-Ni high-entropy alloys, Acta Mater. 61 (2013) 4887–4897. https://doi.org/10.1016/j.actamat.2013.04.058.

[45] J. Dąbrowa, M. Zajusz, W. Kucza, G. Cieślak, K. Berent, T. Czeppe, T. Kulik, M. Danielewski, Demystifying the sluggish diffusion effect in high entropy alloys, J. Alloys Compd. 783 (2019) 193–207. https://doi.org/10.1016/j.jallcom.2018.12.300.

[46] Q. He, Y. Yang, On lattice distortion in high entropy alloys, Front. Mater. 5 (2018). https://doi.org/10.3389/fmats.2018.00042.

[47] L.R. Owen, N.G. Jones, Lattice distortions in high-entropy alloys, J. Mater. Res. 33 (2018) 2954–2969. https://doi.org/10.1557/jmr.2018.322.

[48] Z.P. Lu, H. Wang, M.W. Chen, I. Baker, J.W. Yeh, C.T. Liu, T.G. Nieh, An assessment on the future development of high-entropy alloys: Summary from a recent workshop, Intermetallics. 66 (2015) 67–76. https://doi.org/10.1016/j.intermet.2015.06.021.

[49] O.N. Senkov, J.D. Miller, D.B. Miracle, C. Woodward, Accelerated exploration of multi-principal element alloys for structural applications, Calphad Comput. Coupling Phase Diagrams Thermochem. 50 (2015) 32–48. https://doi.org/10.1016/j.calphad.2015.04.009.

[50] F. Zhang, C. Zhang, S.L. Chen, J. Zhu, W.S. Cao, U.R. Kattner, An understanding of high entropy alloys from phase diagram calculations, Calphad Comput. Coupling Phase Diagrams Thermochem. 45 (2014) 1–10. https://doi.org/10.1016/j.calphad.2013.10.006.

[51] S. Gorsse, J.P. Couzinié, D.B. Miracle, From high-entropy alloys to complex concentrated alloys, Comptes Rendus Phys. 19 (2018) 721–736. https://doi.org/10.1016/j.crhy.2018.09.004.

[52] Q.F. He, Y.F. Ye, Y. Yang, Formation of Random Solid Solution in Multicomponent Alloys: from Hume-Rothery Rules to Entropic Stabilization, J. Phase Equilibria Diffus. 38 (2017) 416–425. https://doi.org/10.1007/s11669-017-0560-9.

[53] M. Feuerbacher, M. Heidelmann, C. Thomas, Hexagonal High-entropy Alloys, Mater. Res. Lett. 3 (2014) 1–6. https://doi.org/10.1080/21663831.2014.951493.

[54] S. Guo, C. Ng, J. Lu, C.T. Liu, Effect of valence electron concentration on stability of fcc or bcc phase in high entropy alloys, in: J. Appl. Phys., 2011. https://doi.org/10.1063/1.3587228.

[55] Z. Leong, Y. Huang, R. Goodall, I. Todd, Electronegativity and enthalpy of mixing biplots for High Entropy Alloy solid solution prediction, Mater. Chem. Phys. 210 (2018) 259–268. https://doi.org/10.1016/j.matchemphys.2017.09.001.

[56] D.B. Miracle, J.D. Miller, O.N. Senkov, C. Woodward, M.D. Uchic, J. Tiley, Exploration and development of high entropy alloys for structural applications, Entropy. 16 (2014) 494–525. https://doi.org/10.3390/e16010494.

[57] U. Mizutani, Hume-Rothery rules for structurally complex alloy phases, MRS Bull. 37 (2012) 169–169. https://doi.org/10.1557/mrs.2012.45.

[58] H. Jiang, K. Han, X. Gao, Y. Lu, Z. Cao, M.C. Gao, J.A. Hawk, T. Li, A new strategy to design eutectic high-entropy alloys using simple mixture method, Mater. Des. 142 (2018) 101–105. https://doi.org/10.1016/j.matdes.2018.01.025.

[59] E. Paul, L.J. Swartzendruber, The Fe-Nb (Iron-Niobium) system, Bull. Alloy Phase Diagrams. 7 (1986) 248–254. https://doi.org/10.1007/BF02869000.

[60] E. Sugawara, H. Nikaido, Properties of AdeABC and AdeIJK efflux systems of Acinetobacter baumannii compared with those of the AcrAB-TolC system of Escherichia coli, 2014. https://doi.org/10.1128/AAC.03728-14.

[61] S. Mukherjee, Z. Zhou, W.L. Johnson, W.K. Rhim, Thermophysical properties of Ni-Nb and Ni-Nb-Sn bulk metallic glass-forming melts by containerless electrostatic levitation processing, J. Non. Cryst. Solids. 337 (2004) 21–28.

https://doi.org/10.1016/j.jnoncrysol.2004.03.102.

[62] M. Venkatraman, J.P. Neumann, The Cr-Nb (Chromium-Niobium) system, Bull. Alloy Phase Diagrams. 7 (1986) 462–466. https://doi.org/10.1007/BF02867811.

[63] F. He, Z. Wang, P. Cheng, Q. Wang, J. Li, Y. Dang, J. Wang, C.T. Liu, Designing eutectic high entropy alloys of CoCrFeNiNbx, J. Alloys Compd. 656 (2016) 284–289. https://doi.org/10.1016/j.jallcom.2015.09.153.

[64] W. Huo, H. Zhou, F. Fang, X. Zhou, Z. Xie, J. Jiang, Microstructure and properties of novel CoCrFeNiTax eutectic high-entropy alloys, J. Alloys Compd. 735 (2018) 897–904. https://doi.org/10.1016/j.jallcom.2017.11.075.

[65] S.W. Wu, G. Wang, Y.D. Jia, J. Yi, Q.J. Zhai, C.T. Liu, B.A. Sun, H.J. Chu, J. Shen, P.K. Liaw, T.Y. Zhang, Enhancement of strength-ductility trade-off in a high-entropy alloy through a heterogeneous structure, Acta Mater. 165 (2019) 444–458. https://doi.org/10.1016/j.actamat.2018.12.012.

[66] S. Gorsse, M.H. Nguyen, O.N. Senkov, D.B. Miracle, Database on the mechanical properties of high entropy alloys and complex concentrated alloys, Data Br. 21 (2018) 2664–2678. https://doi.org/10.1016/j.dib.2018.11.111.

[67] I.S. Wani, T. Bhattacharjee, S. Sheikh, Y.P. Lud, S. Chatterjee, P.P. Bhattacharjeea, S. Guo, N. Tsujib, Ultrafine-grained AlCoCrFeNi2.1 eutectic high-entropy alloy, Mater. Res. Lett. 4 (2016) 174–179. https://doi.org/10.1080/21663831.2016.1160451.

[68] I. Baker, F. Meng, M. Wu, A. Brandenberg, Recrystallization of a novel two-phase FeNiMnAlCr high entropy alloy, J. Alloys Compd. 656 (2016) 458–464. https://doi.org/10.1016/j.jallcom.2015.09.264.

[69] H.W. Yao, J.W. Qiao, M.C. Gao, J.A. Hawk, S.G. Ma, H.F. Zhou, Y. Zhang, NbTaV-(Ti,W) refractory high-entropy alloys: Experiments and modeling, Mater. Sci. Eng. A. 674 (2016) 203–211. https://doi.org/10.1016/j.msea.2016.07.102.

[70] Z. Li, K.G. Pradeep, Y. Deng, D. Raabe, C.C. Tasan, Metastable high-entropy

dual-phase alloys overcome the strength-ductility trade-off, Nature. 534 (2016) 227–230. https://doi.org/10.1038/nature17981.

[71] M.R. Chen, S.J. Lin, J.W. Yeh, S.K. Chen, Y.S. Huang, M.H. Chuang, Effect of vanadium addition on the microstructure, hardness, and wear resistance of Al0.5CoCrCuFeNi high-entropy alloy, Metall. Mater. Trans. A Phys. Metall. Mater. Sci. 37 (2006) 1363–1369. https://doi.org/10.1007/s11661-006-0081-3.

[72] C.J. Tong, M.R. Chen, S.K. Chen, J.W. Yeh, T.T. Shun, S.J. Lin, S.Y. Chang, Mechanical performance of the AlxCoCrCuFeNi high-entropy alloy system with multiprincipal elements, in: Metall. Mater. Trans. A Phys. Metall. Mater. Sci., 2005: pp. 1263–1271. https://doi.org/10.1007/s11661-005-0218-9.

[73] J.Y. He, W.H. Liu, H. Wang, Y. Wu, X.J. Liu, T.G. Nieh, Z.P. Lu, Effects of Al addition on structural evolution and tensile properties of the FeCoNiCrMn high-entropy alloy system, Acta Mater. 62 (2014) 105–113. https://doi.org/10.1016/j.actamat.2013.09.037.

[74] M. Zhang, X. Zhou, D. Wang, W. Zhu, J. Li, Y.F. Zhao, AlCoCuFeNi high-entropy alloy with tailored microstructure and outstanding compressive properties fabricated via selective laser melting with heat treatment, Mater. Sci. Eng. A. 743 (2019) 773–784. https://doi.org/10.1016/j.msea.2018.11.118.

[75] S. Gangireddy, B. Gwalani, V. Soni, R. Banerjee, R.S. Mishra, Contrasting mechanical behavior in precipitation hardenable AlXCoCrFeNi high entropy alloy microstructures: Single phase FCC vs. dual phase FCC-BCC, Mater. Sci. Eng. A. 739 (2019) 158–166. https://doi.org/10.1016/j.msea.2018.10.021.

[76] C.M. Lin, H.L. Tsai, Evolution of microstructure, hardness, and corrosion properties of high-entropy Al0.5CoCrFeNi alloy, Intermetallics. 19 (2011) 288–294. https://doi.org/10.1016/j.intermet.2010.10.008.

[77] A. Rollett, G.S. Rohrer, J. Humphreys, Recrystallization and Related Annealing Phenomena, Recryst. Relat. Annealing Phenom. (2017) 1–704. https://doi.org/10.1016/j.matchar.2020.110382.

[78] H. Sistla, J.W. Newkirk, F.F. Liou, Microstructural characterization and mechanical properties of laser deposited high entropy alloys, in: Mater. Sci. Forum, 2014: pp. 2370–2375. https://doi.org/10.4028/www.scientific.net/msf.783-786.2370.

[79] C. Zhang, F. Zhang, S. Chen, W. Cao, Computational thermodynamics aided high-entropy alloy design, Jom. 64 (2012) 839–845. https://doi.org/10.1007/s11837-012-0365-6.

[80] W.R. Wang, W.L. Wang, J.W. Yeh, Phases, microstructure and mechanical properties of AlxCoCrFeNi high-entropy alloys at elevated temperatures, J. Alloys Compd. 589 (2014) 143–152. https://doi.org/10.1016/j.jallcom.2013.11.084.

[81] V. Geantă, I. Voiculescu, B. Istrate, D.M. Vrânceanu, R. Ciocoiu, C.M. Cotruț, The influence of chromium content on the structural and mechanical properties of AlCr x FeCoNi high entropy alloys, Int. J. Eng. Res. Africa. 37 (2018) 23–28. https://doi.org/10.4028/www.scientific.net/JERA.37.23.

[82] B. Gludovatz, A. Hohenwarter, D. Catoor, E.H. Chang, E.P. George, R.O. Ritchie, A fracture-resistant high-entropy alloy for cryogenic applications, Science (80-.). 345 (2014) 1153–1158. https://doi.org/10.1126/science.1254581.

[83] M.H. Chuang, M.H. Tsai, W.R. Wang, S.J. Lin, J.W. Yeh, Microstructure and wear behavior of AlxCo 1.5CrFeNi1.5Tiy high-entropy alloys, Acta Mater. 59 (2011) 6308–6317. https://doi.org/10.1016/j.actamat.2011.06.041.

[84] C.Y. Hsu, J.W. Yeh, S.K. Chen, T.T. Shun, Wear resistance and high-temperature compression strength of Fcc CuCoNiCrAl0.5Fe alloy with boron addition, Metall. Mater. Trans. A Phys. Metall. Mater. Sci. 35 A (2004) 1465–1469. https://doi.org/10.1007/s11661-004-0254-x.

[85] S. qin Xia, Z. Wang, T. fei Yang, Y. Zhang, Irradiation Behavior in High Entropy Alloys, J. Iron Steel Res. Int. 22 (2015) 879–884. https://doi.org/10.1016/S1006-706X(15)30084-4.

[86] S.Q. Xia, X. Yang, T.F. Yang, S. Liu, Y. Zhang, Irradiation Resistance in AlxCoCrFeNi High Entropy Alloys, Jom. 67 (2015) 2340–2344. https://doi.org/10.1007/s11837-015-1568-4.

[87] Y. Lu, H. Huang, X. Gao, C. Ren, J. Gao, H. Zhang, S. Zheng, Q. Jin, Y. Zhao, C. Lu, T. Wang, T. Li, A promising new class of irradiation tolerant materials: Ti2ZrHfV0.5Mo0.2 high-entropy alloy, J. Mater. Sci. Technol. 35 (2019) 369–373. https://doi.org/10.1016/j.jmst.2018.09.034.

[88] A. Kareer, J.C. Waite, B. Li, A. Couet, D.E.J. Armstrong, A.J. Wilkinson, Short communication: 'Low activation, refractory, high entropy alloys for nuclear applications,' J. Nucl. Mater. 526 (2019). https://doi.org/10.1016/j.jnucmat.2019.151744.

[89] W.Y. Chen, M.A. Kirk, N. Hashimoto, J.W. Yeh, X. Liu, Y. Chen, Irradiation effects on Al0.3CoCrFeNi and CoCrMnFeNi high-entropy alloys, and 316H stainless steel at 500 °C, J. Nucl. Mater. 539 (2020). https://doi.org/10.1016/j.jnucmat.2020.152324.

[90] E.J. Pickering, A.W. Carruthers, P.J. Barron, S.C. Middleburgh, D.E.J. Armstrong, A.S. Gandy, High-entropy alloys for advanced nuclear applications, Entropy. 23 (2021) 1–28. https://doi.org/10.3390/e23010098.

[91] J.W. Cahn, Phase separation by spinodal decomposition in isotropic systems, J. Chem. Phys. 42 (1965) 93–99. https://doi.org/10.1063/1.1695731.

[92] E.P. Favvas, A.C. Mitropoulos, What is spinodal decomposition?, J. Eng. Sci. Technol. Rev. 1 (2008) 25–27. https://doi.org/10.25103/jestr.011.05.

[93] G. Spanos, W.T. Reynolds, Microstructure of Metals and Alloys, in: Phys. Metall. Fifth Ed., 2014: pp. 1073–1112. https://doi.org/10.1016/B978-0-444-53770-6.00010-1.

[94] R. Alert, P. Tierno, J. Casademunt, Formation of metastable phases by spinodal decomposition, Nat. Commun. 7 (2016). https://doi.org/10.1038/ncomms13067.

[95] S.V. Orlando, M.L.H. Victor, O.A.D. Erika, L.S.M. Maribel, C.C. Nicolas,

Analysis of spinodal decomposition in Fe-32 and 40 at.% Cr alloys using phase field method based on linear and nonlinear Cahn-Hilliard equations, Rev. Metal. 52 (2016). https://doi.org/10.3989/revmetalm.078.

[96] Z. Zhang, H. Zhang, Y. Tang, L. Zhu, Y. Ye, S. Li, S. Bai, Microstructure, mechanical properties and energetic characteristics of a novel high-entropy alloy HfZrTiTa0.53, Mater. Des. 133 (2017) 435–443. https://doi.org/10.1016/j.matdes.2017.08.022.

[97] W. Lu, X. Luo, Y. Yang, J. Zhang, B. Huang, Effects of Al addition on structural evolution and mechanical properties of the CrCoNi medium-entropy alloy, Mater. Chem. Phys. 238 (2019). https://doi.org/10.1016/j.matchemphys.2019.121841.

[98] Z. Rao, B. Dutta, F. Körmann, W. Lu, X. Zhou, C. Liu, A.K. da Silva, U. Wiedwald, M. Spasova, M. Farle, D. Ponge, B. Gault, J. Neugebauer, D. Raabe, Z. Li, Beyond Solid Solution High-Entropy Alloys: Tailoring Magnetic Properties via Spinodal Decomposition, Adv. Funct. Mater. 31 (2021). https://doi.org/10.1002/adfm.202007668.

[99] G. Radnóczi, E. Bokányi, Z. Erdélyi, F. Misják, Size dependent spinodal decomposition in Cu-Ag nanoparticles, Acta Mater. 123 (2017) 82–89. https://doi.org/10.1016/j.actamat.2016.10.036.

[100] C.J. Tong, Y.L. Chen, S.K. Chen, J.W. Yeh, T.T. Shun, C.H. Tsau, S.J. Lin, S.Y. Chang, Microstructure characterization of AlxCoCrCuFeNi high-entropy alloy system with multiprincipal elements, Metall. Mater. Trans. A Phys. Metall. Mater. Sci. 36 (2005) 881–893. https://doi.org/10.1007/s11661-005-0283-0.

[101] E.J. Pickering, H.J. Stone, N.G. Jones, Fine-scale precipitation in the high-entropy alloy Al0.5CrFeCoNiCu, Mater. Sci. Eng. A. 645 (2015) 65–71. https://doi.org/10.1016/j.msea.2015.08.010.

[102] Y. Zhang, Z. Chen, D. Cao, J. Zhang, P. Zhang, Q. Tao, X. Yang, Concurrence of spinodal decomposition and nano-phase precipitation in a multi-component AlCoCrCuFeNi high-entropy alloy, J. Mater. Res. Technol. 8 (2019) 726–736.

https://doi.org/10.1016/j.jmrt.2018.04.020.

[103] X. Wang, Y. Zhang, Microstructures and corrosion resistance properties of as-cast and homogenized AlFeNiCuCr high entropy alloy, Mater. Chem. Phys. 254 (2020). https://doi.org/10.1016/j.matchemphys.2020.123440.

[104] A. Manzoni, H. Daoud, R. Völkl, U. Glatzel, N. Wanderka, Phase separation in equiatomic AlCoCrFeNi high-entropy alloy, Ultramicroscopy. 132 (2013) 212–215. https://doi.org/10.1016/j.ultramic.2012.12.015.

[105] Q. Tian, G. Zhang, K. Yin, W. Wang, W. Cheng, Y. Wang, The strengthening effects of relatively lightweight AlCoCrFeNi high entropy alloy, Mater. Charact. 151 (2019) 302–309. https://doi.org/10.1016/j.matchar.2019.03.006.

[106] S. Guo, C. Ng, C.T. Liu, Sunflower-like solidification microstructure in a near-eutectic high-entropy alloy, Mater. Res. Lett. 1 (2013) 228–232. https://doi.org/10.1080/21663831.2013.844737.

[107] Z. An, S. Mao, T. Yang, C.T. Liu, B. Zhang, E. Ma, H. Zhou, Z. Zhang, L. Wang, X. Han, Spinodal-modulated solid solution delivers a strong and ductile refractory high-entropy alloy, Mater. Horizons. 8 (2021) 948–955. https://doi.org/10.1039/d0mh01341b.

[108] L.A. Jacobson, J. McKittrick, Rapid solidification processing, Mater. Sci. Eng. R. 11 (1994) 355–408. https://doi.org/10.1016/0927-796X(94)90022-1.

[109] D.M. Herlach, Dendrite growth kinetics in undercooled melts of intermetallic compounds, Crystals. 5 (2015) 355–375. https://doi.org/10.3390/cryst5030355.

[110] M.C. Flemings, Solidification processing, Metall. Trans. 5 (1974) 2121–2134. https://doi.org/10.1007/BF02643923.

[111] T. Suzuki, Fundamentals of solidification phenomena, Trans Tech Publications, 1996. https://doi.org/10.2464/jilm.46.156.

[112] D.A. Porter, K.E. Easterling, K.E. Easterling, Phase Transformations in Metals and Alloys (Revised Reprint), 2009. https://doi.org/10.1201/9781439883570.

[113] R. Trivedi, Interdendritic Spacing: Part Ii. a Comparison of Theory and Experiment., in: Metall. Trans. A, Phys. Metall. Mater. Sci., 1984: pp. 977–982. https://doi.org/10.1007/bf02644689.

[114] G. Meyrick, G.W. Powell, Phase Transformations in Metals and Alloys, CRC press, 1973. https://doi.org/10.1146/annurev.ms.03.080173.001551.

[115] K. Hunt, JD Jackson, Binary eutectic solidification, Trans. Metall. Soc. Aime. 236 (1966) 843–852.

[116] N. Haque, R.F. Cochrane, A.M. Mullis, Morphology of order-disorder structures in rapidly solidified L12 intermetallics, in: Miner. Met. Mater. Ser., 2017: pp. 729–736. https://doi.org/10.1007/978-3-319-51493-2_70.

[117] P. Ding, A. Mao, X. Zhang, X. Jin, B. Wang, M. Liu, X. Gu, Preparation, characterization and properties of multicomponent AlCoCrFeNi2.1 powder by gas atomization method, J. Alloys Compd. 721 (2017) 609–614. https://doi.org/10.1016/j.jallcom.2017.06.020.

[118] W.L. Wang, Z.H. Kong, Phase separation and microhardness of rapidly solidified high-entropy CoCrFeNiCux alloys, J. Alloys Compd. 853 (2021). https://doi.org/10.1016/j.jallcom.2020.156451.

[119] R. Wei, H. Sun, C. Chen, Z. Han, F. Li, Effect of cooling rate on the phase structure and magnetic properties of Fe26.7Co28.5Ni28.5Si4.6B8.7P3 high entropy alloy, J. Magn. Magn. Mater. 435 (2017) 184–186. https://doi.org/10.1016/j.jmmm.2017.04.017.

[120] C. Song, G. Li, G. Li, G. Zhang, B. Cai, Tensile creep behavior and mechanism of CoCrFeMnNi high entropy alloy, Micron. 150 (2021). https://doi.org/10.1016/j.micron.2021.103144.

[121] P. Wang, J.F. Qi, Z.W. Chen, C.S. Lao, T.B. He, T.W. Lu, P. Gargarella, S. Scudino, Microstructure and mechanical properties of novel high-entropy alloy particle reinforced aluminum matrix composites fabricated by selective laser melting, J. Alloys Compd. 868 (2021).

https://doi.org/10.1016/j.jallcom.2021.159197.

[122] J. Lehtonen, Y. Ge, N. Ciftci, O. Heczko, V. Uhlenwinkel, S.P. Hannula, Phase structures of gas atomized equiatomic CrFeNiMn high entropy alloy powder, J. Alloys Compd. 827 (2020). https://doi.org/10.1016/j.jallcom.2020.154142.

[123] S. cheng ZHOU, P. ZHANG, Y. fei XUE, F. chi WANG, L. WANG, T. qing CAO, Z. TAN, B. yuan CHENG, B. peng WANG, Microstructure evolution of Al0.6CoCrFeNi high entropy alloy powder prepared by high pressure gas atomization, Trans. Nonferrous Met. Soc. China (English Ed. 28 (2018) 939–945. https://doi.org/10.1016/S1003-6326(18)64728-4.

[124] T. Nagase, M. Takemura, M. Matsumuro, T. Maruyama, Solidification microstructure of AlCoCrFeNi2.1 eutectic high entropy alloy ingots, Mater. Trans. 59 (2018) 255–264. https://doi.org/10.2320/matertrans.F-M2017851.

[125] T. Nagase, M. Takemura, M. Matsumuro, Microstructure of rapidly solidified melt-spun ribbon in AlCoCrFeNi2.1 eutectic high-entropy alloys, in: Mater. Sci. Forum, 2017: pp. 1350–1354. https://doi.org/10.4028/www.scientific.net/MSF.879.1350.

[126] J. Li, W. Jia, J. Wang, H. Kou, D. Zhang, E. Beaugnon, Enhanced mechanical properties of a CoCrFeNi high entropy alloy by supercooling method, Mater. Des. 95 (2016) 183–187. https://doi.org/10.1016/j.matdes.2016.01.112.

[127] J. Wang, T. Guo, J. Li, W. Jia, H. Kou, Microstructure and mechanical properties of non-equilibrium solidified CoCrFeNi high entropy alloy, Mater. Chem. Phys. 210 (2018) 192–196. https://doi.org/10.1016/j.matchemphys.2017.06.037.

[128] A.F. Andreoli, O. Shuleshova, V.T. Witusiewicz, Y. Wu, Y. Yang, O. Ivashko, A.C. Dippel, M. v. Zimmermann, K. Nielsch, I. Kaban, In situ study of non-equilibrium solidification of CoCrFeNi high-entropy alloy and CrFeNi and CoCrNi ternary suballoys, Acta Mater. 212 (2021). https://doi.org/10.1016/j.actamat.2021.116880.

[129] L. Hu, L. Wang, M.J. Lin, B. Wei, Single Crystal Growth and Chemical Disorder

Trapping of Refractory MoNbReTaW High-Entropy Alloy Solidified Under Electrostatic Levitation State, Metall. Mater. Trans. A Phys. Metall. Mater. Sci. 52 (2021) 167–180. https://doi.org/10.1007/s11661-020-06050-2.

[130] Y. Li, K. Zhou, P. Tan, S.B. Tor, C.K. Chua, K.F. Leong, Modeling temperature and residual stress fields in selective laser melting, Int. J. Mech. Sci. 136 (2018) 24–35. https://doi.org/10.1016/j.ijmecsci.2017.12.001.

[131] Y. Kok, X.P. Tan, P. Wang, M.L.S. Nai, N.H. Loh, E. Liu, S.B. Tor, Anisotropy and heterogeneity of microstructure and mechanical properties in metal additive manufacturing: A critical review, Mater. Des. 139 (2018) 565–586. https://doi.org/10.1016/j.matdes.2017.11.021.

[132] J. Joseph, T. Jarvis, X. Wu, N. Stanford, P. Hodgson, D.M. Fabijanic, Comparative study of the microstructures and mechanical properties of direct laser fabricated and arc-melted AlxCoCrFeNi high entropy alloys, Mater. Sci. Eng. A. 633 (2015) 184–193. https://doi.org/10.1016/j.msea.2015.02.072.

[133] H.R. Sistla, J.W. Newkirk, F. Frank Liou, Effect of Al/Ni ratio, heat treatment on phase transformations and microstructure of AlxFeCoCrNi2-x (x=0.3, 1) high entropy alloys, Mater. Des. 81 (2015) 113–121. https://doi.org/10.1016/j.matdes.2015.05.027.

[134] K. Zhou, J. Li, Q. Wu, Z. Zhang, Z. Wang, J. Wang, Remelting induced fully-equiaxed microstructures with anomalous eutectics in the additive manufactured Ni32Co30Cr10Fe10Al18 eutectic high-entropy alloy, Scr. Mater. 201 (2021). https://doi.org/10.1016/j.scriptamat.2021.113952.

[135] D. Cui, J. Zhang, Y. Ren, X. Luo, H. Wang, Rapid solidification of undercooled FeCoNiCu multi-principal element alloy: Mechanical and tribological properties, J. Alloys Compd. 890 (2022). https://doi.org/10.1016/j.jallcom.2021.161806.

[136] N. Islam, W. Huang, H.L. Zhuang, Machine learning for phase selection in multi-principal element alloys, Comput. Mater. Sci. 150 (2018) 230–235. https://doi.org/10.1016/j.commatsci.2018.04.003.

[137] Y.J. Chang, C.Y. Jui, W.J. Lee, A.C. Yeh, Prediction of the Composition and Hardness of High-Entropy Alloys by Machine Learning, Jom. 71 (2019) 3433–3442. https://doi.org/10.1007/s11837-019-03704-4.

[138] R. Jain, S.K. Dewangan, V. Kumar, S. Samal, Artificial neural network approach for microhardness prediction of eight component FeCoNiCrMnVAlNb eutectic high entropy alloys, Mater. Sci. Eng. A. 797 (2020). https://doi.org/10.1016/j.msea.2020.140059.

[139] Y. Zeng, M. Man, K. Bai, Y.W. Zhang, Revealing high-fidelity phase selection rules for high entropy alloys: A combined CALPHAD and machine learning study, Mater. Des. 202 (2021). https://doi.org/10.1016/j.matdes.2021.109532.

[140] Y. Zhang, C. Wen, C. Wang, S. Antonov, D. Xue, Y. Bai, Y. Su, Phase prediction in high entropy alloys with a rational selection of materials descriptors and machine learning models, Acta Mater. 185 (2020) 528–539. https://doi.org/10.1016/j.actamat.2019.11.067.

[141] Y. Li, W. Guo, Machine-learning model for predicting phase formations of high-entropy alloys, Phys. Rev. Mater. 3 (2019). https://doi.org/10.1103/PhysRevMaterials.3.095005.

[142] D. Dai, T. Xu, X. Wei, G. Ding, Y. Xu, J. Zhang, H. Zhang, Using machine learning and feature engineering to characterize limited material datasets of high-entropy alloys, Comput. Mater. Sci. 175 (2020). https://doi.org/10.1016/j.commatsci.2020.109618.

[143] W. Huang, P. Martin, H.L. Zhuang, Machine-learning phase prediction of high-entropy alloys, Acta Mater. 169 (2019) 225–236. https://doi.org/10.1016/j.actamat.2019.03.012.

[144] L. Zhang, H. Chen, X. Tao, H. Cai, J. Liu, Y. Ouyang, Q. Peng, Y. Du, Machine learning reveals the importance of the formation enthalpy and atom-size difference in forming phases of high entropy alloys, Mater. Des. 193 (2020). https://doi.org/10.1016/j.matdes.2020.108835.

[145] S.Y. Lee, S. Byeon, H.S. Kim, H. Jin, S. Lee, Deep learning-based phase prediction of high-entropy alloys: Optimization, generation, and explanation, Mater. Des. 197 (2021). https://doi.org/10.1016/j.matdes.2020.109260.

[146] Z. Zhou, Y. Zhou, Q. He, Z. Ding, F. Li, Y. Yang, Machine learning guided appraisal and exploration of phase design for high entropy alloys, Npj Comput. Mater. 5 (2019). https://doi.org/10.1038/s41524-019-0265-1.

[147] C. Wen, Y. Zhang, C. Wang, D. Xue, Y. Bai, S. Antonov, L. Dai, T. Lookman, Y. Su, Machine learning assisted design of high entropy alloys with desired property, Acta Mater. 170 (2019) 109–117. https://doi.org/10.1016/j.actamat.2019.03.010.

[148] U. Bhandari, C. Zhang, C. Zeng, S. Guo, A. Adhikari, S. Yang, Deep learning-based hardness prediction of novel refractory high-entropy alloys with experimental validation, Crystals. 11 (2021) 1–14. https://doi.org/10.3390/cryst11010046.

[149] Y. Yan, D. Lu, K. Wang, Accelerated discovery of single-phase refractory high entropy alloys assisted by machine learning, Comput. Mater. Sci. 199 (2021). https://doi.org/10.1016/j.commatsci.2021.110723.

[150] Y.F. Ye, Q. Wang, J. Lu, C.T. Liu, Y. Yang, High-entropy alloy: challenges and prospects, Mater. Today. 19 (2016) 349–362. https://doi.org/10.1016/j.mattod.2015.11.026.

[151] S. Guo, C.T. Liu, Phase stability in high entropy alloys: Formation of solid-solution phase or amorphous phase, Prog. Nat. Sci. Mater. Int. 21 (2011) 433–446. https://doi.org/10.1016/S1002-0071(12)60080-X.

[152] O. Oloyede, R.F. Cochrane, A.M. Mullis, Effect of rapid solidification on the microstructure and microhardness of BS1452 grade 250 hypoeutectic grey cast iron, J. Alloys Compd. 707 (2017) 347–350. https://doi.org/10.1016/j.jallcom.2016.08.214.

[153] E. Atkins, Elements of X-ray Diffraction, Phys. Bull. 29 (1978) 572–572.

https://doi.org/10.1088/0031-9112/29/12/034.

[154] M.J.J. Douglass, Book Review: Hands-on Machine Learning with Scikit-Learn, Keras, and Tensorflow, 2nd edition by Aurélien Géron, Phys. Eng. Sci. Med. 43 (2020) 1135–1136. https://doi.org/10.1007/s13246-020-00913-z.

[155] D.P. Mandic, A generalized normalized gradient descent algorithm, IEEE Signal Process. Lett. 11 (2004) 115–118. https://doi.org/10.1109/LSP.2003.821649.

[156] S.H. Brown, Multiple Linear Regression Analysis : A Matrix Approach with MATLAB, Alabama J. Math. (2009) 1–3. http://ajmonline.org/2009/brown.pdf.

[157] Y.F. Ye, Q. Wang, J. Lu, C.T. Liu, Y. Yang, Design of high entropy alloys: A single-parameter thermodynamic rule, Scr. Mater. 104 (2015) 53–55. https://doi.org/10.1016/j.scriptamat.2015.03.023.

[158] M. Zheng, W. Ding, W. Cao, S. Hu, Q. Huang, A quick screening approach for design of multi-principal element alloy with solid solution phase, Mater. Des. 179 (2019). https://doi.org/10.1016/j.matdes.2019.107882.

[159] Y.F. Ye, Q. Wang, J. Lu, C.T. Liu, Y. Yang, The generalized thermodynamic rule for phase selection in multicomponent alloys, Intermetallics. 59 (2015) 75–80. https://doi.org/10.1016/j.intermet.2014.12.011.

[160] O.N. Senkov, D.B. Miracle, A new thermodynamic parameter to predict formation of solid solution or intermetallic phases in high entropy alloys, J. Alloys Compd. 658 (2016) 603–607. https://doi.org/10.1016/j.jallcom.2015.10.279.

[161] M. Bahramyan, R. Taherzadeh Mousavian, D. Brabazon, Determination of atomic-scale structure and compressive behavior of solidified AlxCrCoFeCuNi high entropy alloys, Int. J. Mech. Sci. 171 (2020). https://doi.org/10.1016/j.ijmecsci.2019.105389.

[162] Y. Sui, S. Gao, X. Chen, J. Qi, F. Yang, F. Wei, Y. He, Q. Meng, Z. Sun, Microstructures and electrothermal properties of AlxCrFeNi multi-component alloys, Vacuum. 144 (2017) 80–85.

https://doi.org/10.1016/j.vacuum.2017.07.026.

[163] P. Jinhong, P. Ye, Z. Hui, Z. Lu, Microstructure and properties of AlCrFeCuNi x (0.6≤x≤1.4) high-entropy alloys, Mater. Sci. Eng. A. 534 (2012) 228–233. https://doi.org/10.1016/j.msea.2011.11.063.

[164] G. Yuan, M. Liu, Q. Wang, Y. Zhu, W. Ding, Microstructure refinement of Mg-Al-Zn-Si alloys, Jinshu Xuebao/Acta Metall. Sin. 38 (2002) 1105–1108.

[165] J.Y. Hwang, H.W. Doty, M.J. Kaufman, The effects of Mn additions on the microstructure and mechanical properties of Al-Si-Cu casting alloys, Mater. Sci. Eng. A. 488 (2008) 496–504. https://doi.org/10.1016/j.msea.2007.12.026.

[166] A.M. Manzoni, S. Haas, H. Daoud, U. Glatzel, C. Förster, N. Wanderka, Tensile behavior and evolution of the phases in the Al10Co25Cr8Fe15Ni36Ti6 compositionally complex/high entropy alloy, Entropy. 20 (2018). https://doi.org/10.3390/e20090646.

[167] N. Derimow, R. Abbaschian, Liquid phase separation in high-entropy alloys-a review, Entropy. 20 (2018). https://doi.org/10.3390/e20110890.

[168] F. Müller, B. Gorr, H.J. Christ, H. Chen, A. Kauffmann, S. Laube, M. Heilmaier, Formation of complex intermetallic phases in novel refractory high-entropy alloys NbMoCrTiAl and TaMoCrTiAl: Thermodynamic assessment and experimental validation, J. Alloys Compd. 842 (2020). https://doi.org/10.1016/j.jallcom.2020.155726.

[169] S. Guo, C. Ng, C.T. Liu, Anomalous solidification microstructures in Co-free Al xCrCuFeNi2 high-entropy alloys, J. Alloys Compd. 557 (2013) 77–81. https://doi.org/10.1016/j.jallcom.2013.01.007.

[170] S. Singh, N. Wanderka, B.S. Murty, U. Glatzel, J. Banhart, Decomposition in multi-component AlCoCrCuFeNi high-entropy alloy, Acta Mater. 59 (2011) 182–190. https://doi.org/10.1016/j.actamat.2010.09.023.

[171] R. Wang, K. Zhang, C. Davies, X. Wu, Evolution of microstructure, mechanical and corrosion properties of AlCoCrFeNi high-entropy alloy prepared by direct

laser fabrication, J. Alloys Compd. 694 (2017) 971–981. https://doi.org/10.1016/j.jallcom.2016.10.138.

[172] Y. Wang, R. Li, P. Niu, Z. Zhang, T. Yuan, J. Yuan, K. Li, Microstructures and properties of equimolar AlCoCrCuFeNi high-entropy alloy additively manufactured by selective laser melting, Intermetallics. 120 (2020). https://doi.org/10.1016/j.intermet.2020.106746.

[173] A. Vattré, B. Devincre, A. Roos, Dislocation dynamics simulations of precipitation hardening in Ni-based superalloys with high γ′ volume fraction, Intermetallics. 17 (2009) 988–994. https://doi.org/10.1016/j.intermet.2009.04.007.

[174] L. Wang, C. Yao, J. Shen, Y. Zhang, T. Wang, Y. Ge, L. Gao, G. Zhang, Microstructures and room temperature tensile properties of as-cast and directionally solidified AlCoCrFeNi2.1 eutectic high-entropy alloy, Intermetallics. 118 (2020). https://doi.org/10.1016/j.intermet.2019.106681.

[175] L. Cao, P. Hou, A. Nassar, A.M. Mullis, Dendritic growth of rapid-solidified eutectic high-entropy alloy, in: Mater. Sci. Forum, 2021: pp. 46–50. https://doi.org/10.4028/www.scientific.net/MSF.1035.46.

[176] T. Wang, M. Komarasamy, S. Shukla, R.S. Mishra, Simultaneous enhancement of strength and ductility in an AlCoCrFeNi2.1 eutectic high-entropy alloy via friction stir processing, J. Alloys Compd. 766 (2018) 312–317. https://doi.org/10.1016/j.jallcom.2018.06.337.

[177] C. Triveño Rios, M.F. Oliveira, R. Caram, W.J. Botta F, C. Bolfarini, C.S. Kiminami, Directional and rapid solidification of Al-Nb-Ni ternary eutectic alloy, Mater. Sci. Eng. A. 375–377 (2004) 565–570. https://doi.org/10.1016/j.msea.2003.10.187.

[178] R. Trivedi, P. Magnin, W. Kurz, Theory of eutectic growth under rapid solidification conditions, Acta Metall. 35 (1987) 971–980. https://doi.org/10.1016/0001-6160(87)90176-3.

[179] N. Wang, B. Wei, Rapid solidification behaviour of Ag-Cu-Ge ternary eutectic alloy, Mater. Sci. Eng. A. 307 (2001) 80–90. https://doi.org/10.1016/S0921-5093(00)01954-7.

[180] R. Ahmad, R.F. Cochrane, A.M. Mullis, Disorder trapping during the solidification of βni 3Ge from its deeply undercooled melt, J. Mater. Sci. 47 (2012) 2411–2420. https://doi.org/10.1007/s10853-011-6062-y.

[181] S. Samal, M.R. Rahul, R.S. Kottada, G. Phanikumar, Hot deformation behaviour and processing map of Co-Cu-Fe-Ni-Ti eutectic high entropy alloy, Mater. Sci. Eng. A. 664 (2016) 227–235. https://doi.org/10.1016/j.msea.2016.04.006.

Appendix

For the database of 391 alloys used in Chapter 3 please visit the link:

https://www.sciencedirect.com/science/article/pii/S0927025621004821#m0005